

DOCTOR OF PHILOSOPHY

Identifying the Relationship Between Occupant Injuries and Vehicle Mass; An Innovative Approach to Maximising Crashworthiness Efficiency and Inter-Category Compatibility

Harrison, Andrew

Award date:
2022

Awarding institution:
Coventry University

[Link to publication](#)

General rights

Copyright and moral rights for the publications made accessible in the public portal are retained by the authors and/or other copyright owners and it is a condition of accessing publications that users recognise and abide by the legal requirements associated with these rights.

- Users may download and print one copy of this thesis for personal non-commercial research or study
- This thesis cannot be reproduced or quoted extensively from without first obtaining permission from the copyright holder(s)
- You may not further distribute the material or use it for any profit-making activity or commercial gain
- You may freely distribute the URL identifying the publication in the public portal

Take down policy

If you believe that this document breaches copyright please contact us providing details, and we will remove access to the work immediately and investigate your claim.

**Identifying the Relationship Between
Occupant Injuries and Vehicle Mass;
An Innovative Approach to
Maximising Crashworthiness Efficiency
and
Inter-Category Compatibility.**

By

Andrew Harrison

October 2021

***A thesis submitted in partial fulfilment of the University's requirements for the
Degree of Doctor of Philosophy***

Coventry University



Certificate of Ethical Approval

Applicant: Andrew Harrison
Project Title: Minimalizing Occupant Injury and Vehicle Mass by Time-History Based Optimisation: An Analytical Relationship of Vehicle Parameters and Occupant Injury Scores for Heavy Quadricycles with Autonomous Driving Assisted Systems

This is to certify that the above named applicant has completed the Coventry University Ethical Approval process and their project has been confirmed and approved as Low Risk

Date of approval: 07 Jan 2021
Project Reference Number: P108027

Acknowledgements

I am extremely grateful to my supervisory team, Dr. Jesper Christensen, Dr. Christophe Bastien, and Dr. Alexis Wilson. Their expertise and keen insight were invaluable to improving my skills and shaping this research to what it is today. It is safe to say that without their tutelage and consistent guidance, this thesis would not exist today. A special mention is deserved for their support that was offered throughout a difficult time in my life, their character and willingness to go beyond duty is greatly admired.

I would also like to thank Dr. Stratis Kanarachos for notifying me of this wonderful opportunity and the support he provided in the early stages of the project. It is safe to say that his belief in me and constant encouragement throughout undergraduate years provided the foundations that led to this thesis.

To my family, particularly my parents, thank you for your love, support and unwavering belief in me. Without you, I would not be the person I am today.

Above all else, I would like to thank my wife Alina for her love and understanding throughout the last three years. Even more so the past few months, in which, despite everything, was still there for me. Without her, I am sure I would not have stayed sane. So, thank you for being my friend, thank you for trusting in an old turtle, thank you for believing in me. I owe you everything.

Table of Contents

I.	List of Sourced Figures	i
II.	List of Sourced Equations	vi
III.	Abstract.....	vii
1	Introduction	1
2	Road Safety	5
2.1	A Brief History.....	5
2.2	Environmental Target Interaction	8
2.2.1	Vehicle Architecture	11
2.3	Vehicle Safety	16
2.3.1	Vehicle Impact Regulations	16
2.3.2	Consumer Program Safety Assessments	31
2.4	Vehicle Passive Crashworthiness.....	37
2.4.1	Cross-Sectional Designs	41
2.4.2	Filling materials.....	49
3	Problem Definition.....	57
3.1	Current Situation	57
3.2	Change of Velocity.....	60
3.3	Hypothesis	60
3.4	Aim and Scope	61
4	Mass Relationship Exploration	63
4.1	Scenario Configuration	64
4.2	Finite Element Construction.....	65

4.2.1	Experiment Model Selection	65
4.2.2	Injury data Extraction and Calculation	72
4.2.3	Experiment Procedure.....	74
4.3	Mass Relationship Exploration Results.....	77
4.3.1	Occupant Head Acceleration	79
4.3.2	Occupant Body Acceleration	81
4.3.3	Thorax Injury Metrics	88
4.4	Mass Relationship Exploration Discussion	97
5	Crash Safety Light-Weighting.....	102
5.1	Scope and Operational Boundaries of the RMR.....	102
5.2	RMR Development	104
5.2.1	RMR Parameter and Criteria Creation.....	105
5.2.2	RMR Criteria Ranking and Execution	117
5.3	RMR Venza Light-weighting Assessment.....	124
5.3.1	Light-weighted Venza Vehicle Data	125
5.3.2	Light-weighted Venza Crash Performance	127
5.3.3	Performance of RMR Conclusion.....	146
6	Inter-Category Compatibility	151
6.1	Inter-Category Compatibility Scope	152
6.2	Inter-Category Compatibility Methodology	153
6.3	Inter-Category Compatibility Results	158
6.3.1	Occupant Results	158

6.4	Inter-Category Compatibility Conclusion	175
7	Discussion.....	178
8	Conclusions	182
9	References.....	185
10	Appendices.....	201

I. List of Sourced Figures

Figure 1. Volvo 360c (left) and Westfield Technology Group's Pod (right) (Gitlin 2018, Westfield Technology Group 2022).....	3
Figure 2. M-Category Crash Regulations of Europe, United Nations, USA, China, and India.....	17
Figure 3. USA FFRB Regulation (FMVSS 208) (carhs.training 2021)	20
Figure 4. FMVSS 214 Test Procedure (NHTSA 2012: 21)	23
Figure 5. Energy Absorbing Methods	37
Figure 6. Multi-cell Performance Summary (Reddy, Rao, and Narayanamurthy 2018).....	43
Figure 7. Crashworthiness indicators at various angles (Qiu et al. 2015)	44
Figure 8. Exterior Wall Performance Summary	47
Figure 9. Foam Filling Performance Summary	51
Figure 10. PCF and SEA comparison of hollow and foam-filled tubes (Gao et al. 2016).....	52
Figure 11. Accident at Junction.	58
Figure 12. Research Overview	61
Figure 13. Conflict points at junctions and roundabouts (European Commission 2021b)	64
Figure 14. Microcab Dimensions (Door Omitted)	67
Figure 15. AE-MDB Barrier Dimensions (Ellway 2013, Krebs and Bhalsod 2012)	68
Figure 16. Carriage and Barrier face of AE-MDB	69
Figure 17. Adapted Mass AE-MDB Centre of Gravity.....	70
Figure 18. Restraint System Fitted onto the Occupant Model.....	71
Figure 19. ISO View WSID Data Extraction Locations.....	72
Figure 20. AE-MDB and H-point Alignment in the Vertical Plane	75
Figure 21. MDB Interaction with Microcab Sill.....	76
Figure 22. R1.0 Energy Curve.....	77
Figure 23. HIC ₁₅ and Maximum Head Acceleration	80
Figure 24. Time-History Head Acceleration vs Time	81

Figure 25. T4 lateral Acceleration.....	83
Figure 26. Time-History T4 Lateral Acceleration	84
Figure 27. T12 lateral Acceleration.....	85
Figure 28. Time-History T12 Lateral Acceleration	86
Figure 29. Pelvic lateral Acceleration	87
Figure 30. Time-History Pelvic Lateral Acceleration.....	88
Figure 31. WSID Rib Designation	89
Figure 32. Maximum Rib Acceleration by Region (Normalised).....	90
Figure 33. Maximum Rib Compression by Region (Normalised).....	91
Figure 34. Maximum Rib Velocity by Region (Normalised)	92
Figure 35. Viscous Criterion.....	94
Figure 36. Thoracic Trauma Index by Thoracic Rib (Normalised).....	97
Figure 37. Normalised Injury Metric Correlation to Mass-Ratio	98
Figure 38. RMR Process Overview	104
Figure 39. Longitudinal CofG Parameter Boundaries with estimated reference planes of occupant H-Point* (XZ)	108
Figure 40. Longitudinal CofG Parameter Boundaries with estimated reference plane of occupant H-Point (XY)	108
Figure 41. Transverse CofG Parameter Zones (YZ)	110
Figure 42. Transverse CofG Parameter Zones (XY).....	111
Figure 43. Vertical CofG Parameter Boundaries with estimated reference planes of occupant H-Point* (XZ)	112
Figure 44. Venza CofG Parameter Combination Overlay	119
Figure 45. RMR Omitted Parts, Isometric view (Venza)	123
Figure 46. RMR Omitted Parts, Undercarriage view (Venza)	123
Figure 47. LLD Components with high Hourglass Energy	128
Figure 48. VLH Venza Energy Curve.....	129

Figure 49. Venza Comparison of Leading Component IE (XZ)	130
Figure 50. Venza Comparison of Leading Component IE (ISO)	131
Figure 51. Driver Side Venza Occupant Compartment Velocity.....	133
Figure 52. Venza Occupant Compartment Acceleration Comparison (x)	135
Figure 53. Venza Models Dynamic Crush Comparison.....	136
Figure 54. Venza Crush Deformation	137
Figure 55. Venza Undercarriage Crush Deformation	138
Figure 56. Venza Components Crush Kinematics	139
Figure 57. Venza Instrumental Panel and Footwell Panel Measurement Locations.....	140
Figure 58. Venza Footwell Intrusions Comparison	142
Figure 59. Footwell Panel Resultant Intrusion	143
Figure 60. Steering Column Relative Displacement	144
Figure 61. Vertical Plane Alignment of Bullet and Target Vehicle.....	154
Figure 62. Group-S Resultant Head Acceleration (CFC 180).....	161
Figure 63. Group-Y Head Acceleration	162
Figure 64. Group-S T12 Lateral Acceleration.....	164
Figure 65. Group-Y T12 Lateral Acceleration.....	165
Figure 66. Door Response to Groups S and Y	167
Figure 67. Group-S Lateral Pelvis Acceleration	168
Figure 68. Group-S Resultant Pelvic Acceleration	169
Figure 69. Group-Y Lateral Pelvic Acceleration	169
Figure 70. Group-Y Resultant Acceleration	170
Figure 71. R1.5 Energy Curve.....	202
Figure 72. R2.0 Energy Curve.....	203
Figure 73. R2.5 Energy Curve.....	203
Figure 74. R3.0 Energy Curve.....	204

Figure 75. R3.5 Energy Curve.....	204
Figure 76. Energy Curve.....	205
Figure 77. R4.5 Energy Curve.....	205
Figure 78. R5.0 Energy Curve.....	206
Figure 79. Intrusion of Lower Impact Beam	207
Figure 80. Intrusion of Upper Impact Beam	207
Figure 81. Door Intrusion Rates for Mass Relationship Exploration	208
Figure 82. Engine Sensor Locations	214
Figure 83. Baseline Venza Energy Curve (25mph).....	214
Figure 84. LLD Venza Energy Curve	215
Figure 85. VLL Venza Energy Curve	215
Figure 86. VLH Venza Energy Curve.....	216
Figure 87. BL Dynamic Crush	216
Figure 88. LLD Venza Dynamic Crush	217
Figure 89. VLL Venza Dynamic Crush.....	217
Figure 90. VLH Venza Dynamic Crush.....	218
Figure 91. BL Occupant Compartment Intrusion.....	218
Figure 92. LLD Venza Occupant Compartment Intrusion	219
Figure 93. VLL Occupant Compartment Intrusion.....	219
Figure 94. VLH Venza Occupant Compartment Intrusion	220
Figure 95. Baseline Venza Occupant Compartment Acceleration	220
Figure 96. LLD Venza Occupant Compartment Acceleration	221
Figure 97. VLL Venza Occupant Compartment Acceleration	221
Figure 98. Rev2 Venza Occupant Compartment Acceleration	222
Figure 99. Baseline Venza Occupant Compartment Velocity.....	222
Figure 100. LLD Venza Occupant Compartment Velocity.....	223

Figure 101. VLL Venza Occupant Compartment Velocity.....	223
Figure 102. VLH Venza Occupant Compartment Velocity	224
Figure 103. Baseline Venza Longitudinal Engine Displacement	224
Figure 104. LLD Venza Longitudinal Engine Displacement.....	225
Figure 105. VLL Venza Longitudinal Engine Displacement	225
Figure 106. VLH Venza Longitudinal Engine Displacement	226
Figure 107. Venza Driver Velocity Comparison	226
Figure 108. Venza Passenger Velocity Comparison.....	227
Figure 109. Venza Driver Acceleration Comparison.....	227
Figure 110. Venza Passenger Acceleration Comparison	228
Figure 111. Venza Driver Dynamic Crush Comparison.....	228
Figure 112. Venza Passenger Dynamic Crush Comparison	229
Figure 113. Venza Driver Footwell Intrusion Comparison.....	229
Figure 114. Venza Driver Toepan Intrusion Comparison	230
Figure 115. Venza Toepan Centre Intrusion Comparison	230
Figure 116. Venza Passenger Toepan Intrusion Comparison	231
Figure 117. Venza Engine 'Bottom' Displacement Comparison.....	231
Figure 118. Venza Engine 'Top Displacement Comparison	232
Figure 119. Group-S Head Acceleration (CFC1000).....	232
Figure 120. Group-S T12 Lateral Acceleration.....	233
Figure 121. Group-S T12 Resultant Acceleration	233

II. List of Sourced Equations

Equation 1. Head Injury Criterion (HIC)	28
Equation 2. Viscous Criterion	28
Equation 3. Delta-V Simplified.....	60
Equation 4. Head Injury Criterion 15ms (HIC ₁₅).....	73
Equation 5. Viscous Criterion for World-SID	74
Equation 6. Thoracic Trauma Index.....	74

III. Abstract

To achieve Vision Zero, road safety is at the forefront of concern, especially considering the development of new vehicle designs and application of Advanced Driving Assistance Systems (ADAS). Despite the effectiveness of ADAS in reducing the quantity and severity of rear-end crashes, high risk scenarios are likely to remain within urban environments until fully connected vehicle and city infrastructure is established. The market share projection is divided between larger passenger vehicles (M_1) and lightweight microcars (L7e) for future transport hubs and the 'next generation' of mobility. The differences between the structural designs and masses of the vehicle, in relation to occupant safety, are of great concern as the smaller vehicle is at 10-times the risk of sustaining injuries.

The research conducted throughout this thesis took an analytical approach to examine and explore the effects of vehicle masses and vehicle mass-ratios to combat the upcoming crash compatibility issues. The first study examined the relationship between vehicle mass-ratios and occupant injury. Measures were taken to manage the influence of other compatibility factors. The results of the first study were indicative of a relationship between vehicle mass-ratio and occupant injuries sustained and showed that occupant injury metrics likely begin to plateau at a bullet vehicle to target vehicle mass ratio of 3:1, reaching the maximum by 4:1. This study identified a pre-liminary relationship between the masses of bullet (M_1) vehicle and the injury metrics of the L7e occupant, which was then used to define a 'favourable' vehicle mass ratio for the benefit of the L7e occupant.

A novel method of light-weighting with respect to occupant injuries was developed. The mass reduction procedure adopted a unique approach to crash safety and crashworthiness efficiency by prioritising and ranking vehicle components by segment location, thickness, and material selection in relation to occupant positioning with respect to high-risk scenarios. The partnered approach objectively reduced vehicle mass whilst increasing vehicle-to-vehicle compatibility for a lateral impact. The unique method adopted provided results that highlight the feasibility of increasing compatibility by a function of vehicle mass and improvement to more practical placement and focus of protective structures.

1 Introduction

There are many benefits to the development of connected and autonomous vehicles; in the UK alone it is predicted that by 2030, £51 billion per year will have been added to the UK economy, as well as the creation of 320,000 new jobs (KPMG 2015: 12). The European Commission (EC) is actively supporting the electrification and development of digital technologies, as over 70% of Greenhouse gases are produced by road transport alone (European Commission 2016). Connected and Automated Mobility (CAM) will help to achieve the emissions targets by reducing road congestion and vehicle fuel requirements through constant inter-vehicle communication and the application of fleet-management methods known as platooning (Syed and Abadin 2020). Moreover, CAM holds significant value to the consumer and pedestrian alike; 94% of road collisions are caused by driver error, with 85% of collisions comprising of recognition, decision, and performance error (NHTSA 2015). This suggests that fully autonomous vehicles could reduce the number of road casualties and fatalities per annum (recorded by the Great British Department for Transport) down to 7,874 and 95 respectively (Department for Transport 2021: 1). However, current evidence provides scepticism in their ability to do so. There have been numerous instances with autonomous vehicle trials and systems already in active use that have failed to prevent collisions, injuries or even fatalities to those involved. Such instances occurred within the ongoing trials of completely autonomous vehicles in California in which minor vehicle damage often occurred (Favaro et al. 2017). More distressingly, however, instances of partially autonomous vehicles have been involved in fatal crashes in Taiwan and Texas (Sankaran 2021, Templeton 2020). The Insurance Institute for Highway Safety (IIHS) categorises driver error into five causes:

- Sensing and perceiving
- Predicting
- Planning and deciding
- Execution and performance
- Incapacitation

Of the 5,000 case studies examined, it was found that only 33% of the crashes could have been avoided or mitigated whilst assuming fully operational autonomous systems (IIHS HLDI 2020). This suggests that even in 'ideal' circumstances of autonomous operation, road traffic accidents will still be present due to the

unpredictability of road traffic and the planning of a possible outcome or event. This is more worrisome during the intermediary stage, during which highly autonomous vehicles are operating alongside conventional vehicles and vehicles fitted with Advanced Driving Assistance Systems (ADAS), as the predictability of road traffic will remain as it is today or even worse due to the perceivable abnormal behaviour of Autonomous Vehicles (AV) in comparison to human operators.

Currently, ADAS improves collision mitigation rates and collision severity; Autonomous Emergency Braking (AEB) has helped to reduce the occurrence of rear-end collisions by 39% and injuries by 42% (Cicchino 2017, Fildes et al. 2015). Despite this, the number of road traffic accidents are remaining relatively constant over recent years (Dhani 2019). Of all the reported road traffic accidents, vehicle occupants currently contribute to 46% of all reported fatalities and 58% of all reported casualties (European Commission 2018: 2, Dhani 2019: 5). Therefore, despite the improvements made by collision avoidance technology in reducing impact severity and the occurrence of specific types of collision arrangements, vehicle occupants still form the majority of reported road fatalities and injuries. As the vehicle occupant category is the largest individual category of road fatalities and injuries, this demonstrates a requirement for improved vehicle safety from the viewpoint of effect mitigation, rather than crash prevention, to aid in achieving Vision Zero targets (Hughes, Anund, and Falkmer 2015, European Commission 2019). By looking at the immediate future of vehicle concepts, the risks to occupants are inherently greater due to the vast array of designs and functions. A comparative example are the differences between the Westfield Technology Group Pod and the privately owned Volvo 360c concept. The Westfield POD (Pod On Demand) is developed to transport groups of people with space for standing passengers, in a similar style to a compact bus. On the other hand, the Volvo 360c concept aims to permit multiple functions for the occupants by providing various or changeable seating positions and functions throughout operation, including bed-style seating arrangements whilst retaining a 'conventional' shape similar to that of vehicles today. (Volvo 2021, Westfield Technology Group 2022). The Volvo 360c and Westfield POD are shown in Figure 1.

This item has been removed due to 3rd Party Copyright. The unabridged version of the thesis can be found in the Lanchester Library, Coventry University.

Figure 1. Volvo 360c (left) and Westfield Technology Group's Pod (right) (Gitlin 2018, Westfield Technology Group 2022).

Although the Westfield POD and Volvo 360c were designed with autonomous driving systems, it is expected that all vehicles sold by 2030 will include safety performance technology to help reduce the 50 million global injuries per year. In the interim years between now and when full automation is achieved, the emergence of heavy quadricycles and ultra-light-weight vehicles to the market further increase the demand for sufficient occupant safety (KPMG 2015). The quadricycle market alone is expected to have a 5% growth in Europe by 2029, this growth does not include the potential market growth of light weight M1 category vehicles which may arise to conform to environmental incentives and consumer requirements (PMR 2019, ICCT 2019). Due to the infrastructure changes to cities, consumer incentives, and country initiatives set by the European Commission and the European Union, the market growth of quadricycles and light-weight vehicles could grow exponentially (European Commission 2016, Council of the European Union 2017). Therefore, safety concerns should be addressed immediately as it can be assumed that collisions between light-weight vehicles and heavier counterparts will become more and more frequent as the market share changes, signifying a greater risk to the occupants of the lower mass vehicle (Kahane 2003, Santucci, Pieve, and Pierini 2016). Taking this into account, it can be proposed that the heavy quadricycle tests conducted by Euro NCAP in 2014 and 2016 are insufficient to predict the injury outcomes in a crash scenario with a vehicle of M1 categorisation as the mass differences between the two vehicle categories had not been accounted for (Euro NCAP 2014a, 2014b). It can be expected that a collision between a heavy quadricycle and M1 vehicle would result in detrimental

crashworthiness performance of the heavy quadricycle largely due to the force of the greater mass vehicle overwhelming the compartment and structural strength of the smaller vehicle, inducing a compartmental collapse, fatal forces, and accelerations to the occupants of the heavy quadricycle. This can be described as crash incompatibility, a 'mismatch' of one or multiple factors, specifically: mass, stiffness or geometry between the colliding vehicles (Sadeghipour 2017, Delannoy et al. 2004). Each factor is apparent in heavy quadricycle and light-weight vehicle collisions, thereby increasing the injury risk 10-fold to the occupant of the light-weight vehicles.

Technological advancements and changing vehicle demographics force diversions from the current accident trends and associated vehicle geometry, rendering some vehicle crash assessments obsolete or poorly representative of real scenarios. This is especially true when considering heavy quadricycles and light-weight passenger vehicles; the anticipated variety of vehicle designs and respective autonomy within the next 10 years necessitates research to identify new risks, accident metrics and the associated capability of achieving inter-category compatibility, as highlighted previously.

2 Road Safety

The governance of road vehicles and how best to operate them is a fundamental part of road safety. Principally, this describes the degree of security and protection provided in an accident, and the ability to avoid an accident entirely. Over the course of 90 years, road traffic laws have developed alongside technological advancements to ensure progression towards reducing the number of accidents and injuries. Consequently, this includes infrastructure changes, vehicle development and new laws that have affected various types of road users. Throughout Chapter 2, a brief history of road safety and the developments made over the past years will be introduced (2.1). Following this, section 2.2 discusses environmental targets and their influence on vehicle design and developments. Section 2.3 presents the current road safety regulations and tests as well as how they are being adapted for the evolving automotive market. Finally, section 2.4 showcases and discusses newly developed crash structure designs and methodologies that could greatly enhance passive crashworthiness performance.

2.1 A Brief History

The first highway code as part of the 'Road Traffic Act' was introduced in 1931 and is described by the Driver & Vehicle Standards Agency (2019) to have mainly consisted of road etiquette and advertisements. Before 1950, it had often been thought by many countries that road traffic accidents were a result of bad luck and that the driver had sole blame in any circumstance (Hakkert and Gitelman 2014: 139, Hagenzieker, Commandeur, and Bijleveld 2014: 151). Over time knowledge-based institutions began directing their attention to 'why' a road traffic accident occurred instead of just 'what happened'; this change in thought process ultimately led to 'how' can an accident be prevented or mitigated. This is reflected in the developments throughout history of the Highway code and Road Traffic Act by the introduction of driving agencies, changes in the licensing to operate vehicles, and the introduction of mandatory seatbelt use by the year 1983 (DVSA 2019, Department for Transport and Hammond 2013).

By examining Netherland's history in policy making and research focus it is revealed that the collaboration between knowledge institutes (e.g. Universities, Research groups) and policymakers (e.g. Ministry of Transport) is pivotal to the successful reduction in road injuries and fatalities (Wegman, Aarts, and Bax 2008). Throughout the development, the research institute helped identify possible causes or plans to facilitate in the future, such as the 'Stichting Wetenschappelijk Onderzoek Verkeersveiligheid', providing a base for road safety measures (introduced as policy in 1983) and identifying crashes as having multiple causes instead of one cause. Research organisations, along with SWOV, also developed the strategic vision 'Sustainable Safety', which has now been revised and implemented in the road safety policy plans of 2006 and 2008 as 'Advancing Sustainable Safety' (Wegman, Aarts, and Bax 2008: 133). Similarly, other countries have adopted strategies to improve the road driving practice, accident data collection and quality of road infrastructure. Namely, these are 'Vision Zero', 'Strategic Road Safety Framework' and the 'National Road Safety Strategy' for Sweden, the UK and Australia respectively (Hughes, Anund, and Falkmer 2015: 173).

Countries that have incorporated strategies into policies have shown substantial decreases in annual road deaths. Between the years 2000-2019 the annual road fatalities in the UK had decreased by 49%; of this statistic, 47% of the decline in fatalities were achieved by 2010. After 2010, the rate of reduction in road fatalities slowed, resulting in only 7.8% fewer fatalities in 2019 in comparison to 2011 (International Transport Forum 2020a: 2). Similarly, other European countries shared comparable results to the UK, showing 64% reduction of road fatalities in France and 60% reduction in Germany between the years 2000 and 2019. However, the rate of fatality reduction showed significant decline after 2013 in these countries (International Transport Forum 2020b: 2, 2020c: 2). In 2019 the group constituting the most to road fatalities were passenger car occupants, constituting 44, 45 and 50 percent of road fatalities recorded in the UK, France, and Germany respectively. The other road user groups are motorcyclists, moped riders, cyclists, pedestrians, and others (including unknown). Except for the recorded pedestrian fatalities in the UK (28%), the fatalities recorded by any road user group (other than those of passenger car occupants) form less than a quarter of total recorded

fatalities and less than half of the recorded fatalities of passenger car occupants (International Transport Forum 2020a: 3, 2020b: 4, 2020c: 5). The steady increase of registered vehicles on the road year by year may have influenced the rate of fatality reduction, the introduction of emerging technologies and increasing of popularity of other road user groups would also decrease the rate of injury and mortality reduction, making it harder for Vision Zero to be achieved. For instance, the increasing popularity of cycling and alternative modes of transport (such as e-bikes) has given rise to an increase in cyclist mortality rates and injuries in 11 of 17 cities examined by the International Transport Forum (2020d: 27). It can be speculated that other factors are indirectly affecting mortality rates, such as the EU directive 2008/50/EC for better ambient air quality and cleaner air for Europe helping to support changes to vehicle architecture and vehicle-type adoption rates (DIRECTIVE 2008/50/EC 2015). The subsidiary effect of environmental directives leads to an increase in electric vehicle uptake as well as alternative modes of transport, especially when the EU regulation 2019/631 regarding CO₂ emission performance is considered (REGULATION (EU) 2019/631 2019). The increasing commitment to alternate modes of transport provides further challenges for road safety, most notably in densely populated urban environments in which injury and mortality rates have decreased less than other road networks between the years 2000 and 2019 (International Transport Forum 2020a: 6, 2020b: 6, 2020c: 6). As a result, the urban environment held the greatest share of road mortalities in 2019, providing approximately 50% of all recorded road fatalities. As the highest percentage of fatalities occurred within an urban environment, of which were mostly passenger car occupants, the statistics suggest that there are difficulties in improving road safety, especially within an urban environment. However, reducing injuries and mortalities of passenger car occupants in an urban environment would have a greater impact in reducing overall road fatalities in comparison to any other group or road network, thus helping to increase the rate of road fatality reduction on the path to Vision Zero (International Transport Forum 2020d: 33).

City infrastructure is also changing in conjunction with clean air initiatives and alternate fuel infrastructure, to meet the demands and requirements of the upcoming vehicle fleets (Directive 2014/94/EU on the Deployment

of Alternative Fuels Infrastructure 2020). Further infrastructure changes acted as incentives (such as allowing electric vehicles to use the bus lanes) but also helped reduce congestion in an attempt to reach EU emissions and clean air targets (BMW 2020, Burgess 2016). However, these changes are not likely to be permanent and could lead to a rise in recorded road traffic incidents and put vulnerable road users at greater risk, due to a greater variety of driving scenarios than drivers are accustomed to. Furthermore, the effects of imposed policies and directives to road safety are hard to identify in urban environments, especially in regard to drastic changes to vehicle design and performance. Therefore, section 2.2 explores the developments attempting to meet 'green' targets, and how this interacts with the shift towards electric mobility and related road safety concerns.

2.2 Environmental Target Interaction

Whilst countries are acting independently to develop their land and cities to cater for the electric vehicle market and alternative modes of transport, an emphasis has been placed on homogenisation to allow global use of these vehicles (KPMG International 2019). This is especially important when considering dynamic driving assistance systems, automated technology and connected cities (which are discussed in more detail in section 2.3.2, 'Advances in Crash Avoidance & Mitigation Technology'). A challenge for the construction of globally standardised infrastructure surfaces when individual city requirements, country requirements and pre-existing infrastructure are accounted for. Therefore, individual city developments and policies will be mentioned when applicable.

Major effort has been made to ensure electric-drive train readiness in Norway, Austria, Spain, Germany, Netherlands, France, USA, China, and the UK. For instance, China's charging network has grown approximately 50% per year since 2017 and is the country with the highest number of charging stations (2.2 million) and electric vehicles (EV) sales (Doll 2021, Kane 2021, Li 2020). However, a surge of electric vehicle uptake was identified in Europe throughout 2020 (137% increase) whilst Germany became the second largest market of EV sales, taking 1 in 8 of global sales (Irle 2021). To match the demand and surge of EV and PHEV market share,

the number of charge stations is vitally important, in addition to the strategic location, charging speed and the charge stations publicly available per EV. An example presented within a briefing document created by (Hirst, Winnett, and Hinson 2020) stated there are already 7630 rapid charger connections located near major roads, and a projected budget of £16.7 billion to fulfil requirements of 2.8 million charge points by 2035 (Hirst, Winnett, and Hinson 2020: 32). Due to the size of the UK, the strategy would result in a fast charge point every 20 miles of travel (of 95% of highway network), easily providing sufficient charging points to encourage early uptake and use of EV within the UK.

Aside from the construction of charging infrastructure to support the increasing demand of electric vehicles, governmental incentives have been introduced. Studies have been conducted by (Plötz, Gnann, and Sprei 2016, Davies et al. 2016b, Yong and Park 2017) that researched various factors impacting the market growth of electric vehicles. These can be identified as either technology, policy (law and economics) or environmental (including social) factors. It was found by Davies et al. that factors and incentives are expected to have varying effectiveness between regions across Europe (2016b: 2577–2582). This is largely due to differing opinions and drives by the government and public. An example is presented as the difference between the cost of fuel and electricity, including taxation. It was found that while a strong relationship was present in Austria, it held little influence in Spain or the UK (Davies et al. 2016b: 2578). Evidence for the lack of policies and incentives in regard to fuel taxation is shown by a respondent in the study that stated, ‘there are neither policies encouraging recharging networks nor active policies to discourage the use of combustion vehicles’ (Davies et al. 2016b: 2578). Many countries are actively applying taxation incentives to vehicles to encourage electric drive, as it has been shown that a positive correlation (indirect) is present between an increase in fuel-price and the adoption of hybrid or electric vehicles (Plötz, Gnann, and Sprei 2016: 3). However, this approach would not be sustainable as there would be a limit to the increase of prices, otherwise it could spark public unrest and defiance. Due to this, other incentives are applied to encourage the use of battery powered vehicles, especially within an inner-city environment.

These incentives take the form of reduced motoring cost, purchase subsidies and priority driving or special access (Yong and Park 2017, Davies et al. 2016b, Plötz, Gnann, and Sprei 2016, Amsterdam Roundtable Foundation and McKinsey & Company 2014: 14–17). Although countries offer the same benefits to each user, some of the incentives would not positively influence the uptake of EV when the location within that specific county is considered. For instance, an EV driver benefits from no congestion charge in London, but this will not hold any sway with potential buyers in more rural areas or towns that do not implement a congestion charge. Therefore, incentives are often placed together to ensure a larger market is reached, such as a one-time purchase subsidy and access to bus and taxi lanes for smaller electric vehicles (Wappelhorst et al. 2020).

A common incentive across countries and demographics are subsidised cost on vehicle tax or vehicle purchase. Although this is useful for the uptake of electric vehicles, it will not be sustainable once electric powered vehicles form the majority of vehicle fleet registrations. Environmental concerns regarding the disposal of battery cells could negatively affect consumer uptake, though with research and development, emerging technologies and alternative vehicle architecture may be preferred (Cano et al. 2018). For example, there is less power demand by a lighter vehicle which allows for a smaller battery system whilst maintaining range requirements for inner-city use. In contrast, larger vehicles have the capability to store larger and more battery cells, thus maintaining the range and power input to the drivetrain. Therefore, a region that offers short distances between charge stations would likely favour a smaller BEV. On the other hand, regions with sparsely located or too few charging stations would favour vehicles with greater range. In either case, future vehicle development not only relies on the infrastructure available, but on consumer expectations and requirements. The combination of environmental influences, available infrastructure and consumer requirements could lead to a larger variance and distribution of vehicle types and architectures. Therefore, section 2.2.1 examines direction of the vehicle market and the respective categories of vehicle types likely to arise in the future.

2.2.1 Vehicle Architecture

Attempting to accomplish zero emission fleet targets and reducing road fatalities, whilst maintaining consumer interest and acceptance, has led to changes in vehicle market share and a greater variety of vehicle designs. Whilst the market share of PHEV and EVs continue to grow, so does the average weight of a vehicle across Europe. For instance, the average vehicle weight in Germany is 1582kg; 185kg above the European average. However, the overall purchase trend in countries such as the Netherlands shows a reduction in vehicle fleet weight, averaging 68kg lighter than the European average (ICCT 2019: 10: 7). This is not suggestive of consumers actively opting for lighter vehicles, but it does indicate that lighter vehicles satisfy the consumer requirements in the Netherlands. Although the difference in vehicle weight between the countries may not seem significant, due to the predominantly premium market across Europe and strong research and development investment by automotive manufacturers, Germany holds the largest market share and manufactures more vehicles than any other country in Europe, thus shifting the average weight of the European vehicle fleet towards the heavier side of the spectrum (GTAI 2020). Additionally, statistics shown by the International Council for Clean Transportation Europe (2019: 14) reflect a substantial growth of the SUV market share in 2018, reaching approximately 33%. The market share growth of SUVs coincides with the increasing vehicle weight average. Interestingly, 'mini' vehicles have maintained their respective market share in 2018, which is likely to increase in the coming years (Santucci, Pieve, and Pierini 2016).

The architecture of vehicles is beginning to splinter off from the 'norm', largely owing to the introduction of Battery Cells (for powertrain use) and the implementation of smart technologies. A reason for the diversity of vehicle architectures usually arises with designs for specific functions, such as range. This is apparent with EVs often having their battery pack encompassing the floor plan of the vehicle with the controller over the drive axle, whereas PHEV have a battery pack towards the rear axle and the ICE towards the front axle (U.S Department of Energy n.d., n.d.). As the PHEV does not require as much charge capacity as an EV, the battery pack can be smaller and lighter. However, as battery packs commonly weigh 230kg and require larger package

space than the PHEV counterpart, it limits the available locations to store the battery pack; as well as limiting the vehicle mass, this could be a contributing factor for the increased number of SUVs manufactured and the increase in average fleet weight (Tostengard 2015). The restrictions are represented by the Mercedes-Benz EQC 400 4MATIC in which the vehicle floor is formed of the battery pack and housing covers (Mercedes-Benz 2019). Subsequently there has been investment into battery cell research to improve important factors such as performance, sustainability and recycling to fit a range of vehicle model types, and permitting application into various vehicle categories, designs and operational requirements by 2030 (EUCAR 2019). Notably, a method of improving the performance and range of a battery is by vehicle light-weighting.

As previously stated, vehicle market direction is divided between SUVs and smaller passenger vehicles. Though, there has been greater exposure and more research funding towards much smaller vehicles for use within city roads as they provide numerous benefits to larger counterparts, such as affordability, potential to reduce congestion and reduced road damage. The Horizon 2020 project shown the potential in the 'next generation of electrified, cost and energy-efficient light urban vehicles' and a project called 'Efficient Urban Light Vehicles' was formed, in which the various possible concept designs of future mobility were showcased (EU-LIVE n.d.). The Lutz Pathfinder, which was developed to promote autonomous systems and low carbon urban transport, highlights the alternative design solutions for densely populated areas when personal or private transport is desired (Catapult 2016). On the other hand, a 'people mover' was developed by Westfield Technology Group as a full electric autonomous bus (2022). The dissimilarity between vehicle designs provides distinctive looks, which are favoured by manufacturers due to the competitive market. Despite differences in designs throughout the automotive market, road legal vehicles open for public use must adhere to specific regulations within a defined category. The regulations applied to automotive design for purposes of categorisation are detailed below in 'Automotive Categorisation.'

Automotive Categorisation

Road vehicles are categorised by the European Commission so that specific licenses, technical requirements, safety tests, administrative protocols for type approval and other legislation can be applied homogeneously within specific categories and sub-categories of vehicles. This allows manufacturers to benefit from the EU Single Market and the Global Market under the United Nations Economic Commission for Europe (UNECE) (Regulation (EU) 2018/ 858 2018). The legislative is extensive, and therefore only information relevant to inter-category differences that are pertinent to occupant safety of passenger vehicles will be discussed. Similarly, vehicles with special functions (e.g., ambulance) are excluded due to their unique requirements and allowances. Adhering to these requirements results in two main categories of vehicle: the 'M' and 'L' categories.

M-Category Vehicles

Passenger vehicles form 85% of all vehicles on public roads across Europe (ACEA 2019). Passenger vehicles are categorised as 'M-category' and defined by the European Union as 'motor vehicles designed and constructed primarily for the carriage of passengers and their luggage' (Regulation (EU) 2018/ 858 2018: 14, European Commission n.d.). The M-category is divided into three subcategories named M₁, M₂ and M₃, each with their own restrictions.

- M₁ sub-category: The number of seats is limited to a maximum of 9 seating positions (inclusive of the driver seating position) and no allowance for standing passengers.
- M₂ sub-category: The motor vehicle will not exceed 5 tonnes and has greater than 9 seating positions, standing passengers are allowed.
- M₃ sub-category: The motor vehicle has a maximum mass exceeding 5 tonnes, more than 9 seating positions and standing passengers are allowed.

Notably, the classification criteria for M-category vehicles and respective subcategories are the number of seating positions and total mass constraints. The classification criteria provides ample room for architectural differences between two vehicles of the same subcategory. For instance, the smart fortwo EQ coupé has a

kerb weight of 1,095kg and length, width and height of 2.69m, 1.66m and 1.55m respectively (smart 2021). The Mercedes-Benz G 63's dimensions are 4.87m, 1.98m and 1.97m in length, width and height respectively, with a kerb weight of 2,560 kg (Daimler n.d.). Both vehicles fall within the M₁ category, despite the Mercedes-Benz G 63 being 2.33 times heavier and 1.81 times longer than the smart fortwo EQ coupé.

The differences are not limited to the basic dimensions and weight of the vehicles; both example vehicles mentioned above passed the type approval of Regulation (EU) 2019/2144 (2019) which sets specific requirements on equipment functionality and vehicle safety. Compliance to the regulations can help shape M₁ vehicle architecture due to specific requirements involving occupant and vulnerable road-user safety. However, this is focused upon self-achievement rather than homogenisation between vehicle categories or sizes, therefore still permitting a range of structure types, technology and materials used that may not benefit drivers and passengers of other vehicles. The safety tests of M₁ vehicles are discussed in section 2.3. It is of notable importance that none of the regulations listed in Regulation (EU) 2019/2144 apply to motorised vehicles within L7 and L6 categorisation, despite their primary function and design also being intended for passenger transport.

L-Category Vehicles

The 'next generation' of vehicles are categorised as L-category, which are defined as two, three and four wheeled powered vehicles (European Commission n.d., EU-LIVE n.d.). The safety legislation, environmental policies and approval of L-category vehicles are detailed in Regulation (EU) No 168/2013 (2013), and Regulation (EU) No 901/2014 (2014) details the administrative requirements and templates for type approval as described by article 72 in (EU) No 168/2013. It is worth noting that these have been further amended by Regulation (EU) 2019/129 (2019) and Regulation (EU) 2020/239 (2020) to ensure administrative and test requirements are met to fulfil the conditions set by Euro 5 and Euro 5+ emissions targets.

The L-category contains many restrictions that relate to the architecture of the vehicle group. For the purposes of passenger vehicles which are emerging into smart vehicle technology and multi-transport sectors, only L6 and L7 vehicles will be considered. A summary of the classification criteria for L-category vehicles, in accordance to Regulation (EU) No 168/2013 and all relevant amendments, are presented in Table 1. Greater description and classification of categories L6e and L7e are provided in Appendix I, Table 69.

Table 1. Architectural Classification Criteria of L-Category Vehicles (Quadricycles) (Regulation (EU) No 168/2013 2013: 94–101)

Sub-Category	Max. Mass (kg)	Max. Dimensions (L, W, H) (m)	Max. Continuous Power (kW)	Max. Design Speed (km/h)	Transport Function
L6e-A	425	4, 2, 2.5	4	45	
L6e-B	425	3, 1.5, 2.5	6	45	Utility or Passenger use
L7e-A	450	4, 2, 2.5	15	N/A	Passenger only
L7e-B	450/ 600	4, 2, 2.5	B1: N/A B2: 15	B1: 90 B2: N/A	Passenger/ Utility
L7e-C	450/ 600	3.7, 1.5, 2.5	15	90	Passenger/ Utility

The dimensions and weight limits of the L6e and L7e vehicle (for passenger transport) permit a mixture of design interpretations, as seen by various ‘pod’ or ‘car like’ designs. Additionally, as L6e and L7e vehicles have greater fuel efficiency (or battery efficiency) than their M1 counterparts, their operational and manufacturing lifespan is relatively unhindered by the upcoming ban to diesel engines and stricter emission targets for vehicles, thereby encouraging more radical and light-weight designs which implement new technologies and futuristic vehicle shapes (Regulation (EC) No 715/2007 2007). However, the constraints placed upon this category for type approval are disadvantageous for the performance and applicability of adequate safety measures and features (discussed in section 2.3). The lack of ample safety performance consequently damages the public perception of L-category vehicles, possibly hindering vehicle uptake and market share (Edwards et

al. 2014). Subsequently, this could result in clean air targets within cities and overall fleet emission targets being harder to achieve with the current battery and EV technology available.

2.3 Vehicle Safety

This section examines the vehicle safety in the aspect of crash avoidance and mitigation to vehicle occupants and passengers, as well as general occupant safety. The UN Regulations published in the Official Journal of the European Union will be presented, as well as public consumer program testing, and will be reviewed for their effectiveness and influence on manufacturers and governing bodies (if applicable). Furthermore, global tests will be presented together with their respective methods and where they differ from European testing programs.

2.3.1 Vehicle Impact Regulations

There are over 100 regulations that cover different aspects of vehicle and road-user safety; Figure 2 shows the regulations and rules in place set by regulators in their respective region and the location of the vehicle they apply to. The list of regulators and their associated acronyms and regions are:

- Federal Motor Vehicle Safety Standards (FMVSS), USA.
 - Enforced by the National Highway Traffic Safety Administration (NHTSA)
- United Nations Economic Commission for Europe (UN), Europe.
- Japanese Industrial Standards Committee (JIS), Japan.
 - Utilise Regulations of UNECE unless specified.
- China Compulsory Certification (CCC), China.
 - Products must comply with national GB standards.
- Automotive Industry Standards (AIS), India.
- Korean Motor Vehicle Safety Standards (KMVSS), South Korea
- Australian Design Rules (ADR), Australia.

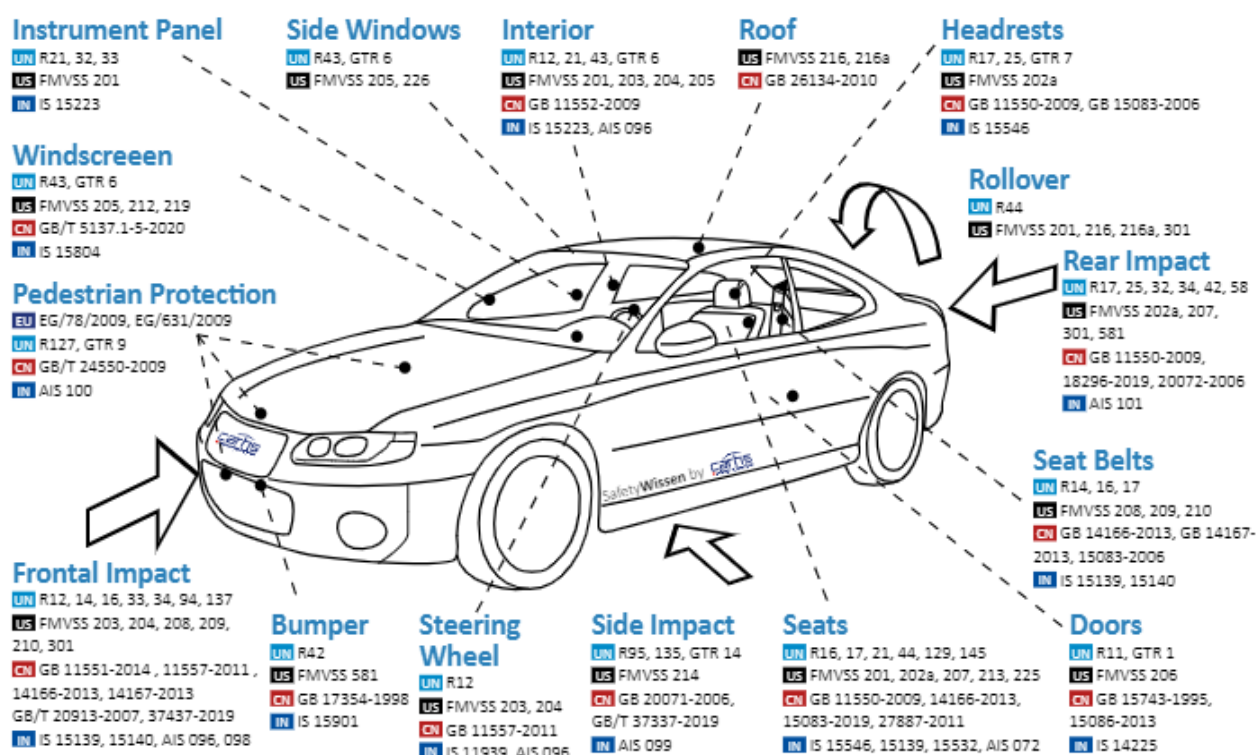


Figure 2. M-Category Crash Regulations of Europe, United Nations, USA, China, and India

Although there are many regulations concerning vehicle performance upon impact, or those regarding specific devices and systems, they do not analyse occupant safety. The main regulations set by various regions that analyse occupant safety in a full vehicle dynamic test are summarised in Table 2. All regulations are currently enacted with the exception of UN Regulation 135 and UN Regulation 137 which come into force in 2022 for new vehicles (Regulation (EU) 2019/2144 2019). Other dynamic regulations incorporate pedestrian safety, rear impact, head impact, vehicle rollover and child safety. Although these are important regulations for road and occupant safety, the regulations revolve around technical units or equipment and their performance, rather than the overall vehicle. For instance, the rollover laboratory test procedure for roof crush resistance establishes the strength requirements of the passenger compartment, in the event that the test vehicle does not conform to the rollover requirements of FMVSS 208 (NHTSA 2006: 1).

Table 2. Brief Summary of Vehicle Dynamic Test Configurations (carhs.training 2021)

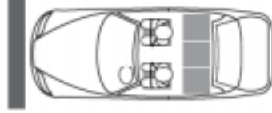
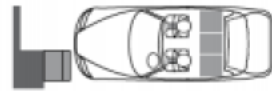
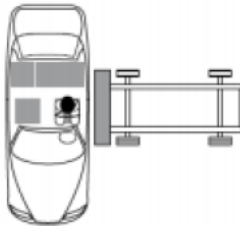
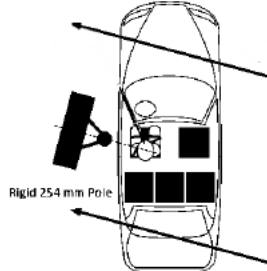
Test type and Abbreviation	Regulation(s) & Rule(s)	Region(s)	Test Synopsis	Dummy Model(s)	Simplified Illustration
Full Width Rigid Barrier (FFRB)	FMVSS 208, UN R137, Art. 18 & Att. 23, GB 11551-2014, KMVSS 102-3, ADR 69/00	USA, Europe, Japan, China, South Korea, Australia	Vehicle travels directly into a rigid wall that spans width of test vehicle.	HIII-50 & HIII-5	
40% Frontal Offset Deformable Barrier (ODB)	FMVSS 208, UN R94, Article 18, GB/T 20913-2007, AIS-098, ADR 73/00	USA, Europe, Japan, China, India, Australia	0° impact of vehicle driving direction into deformable barrier (40% overlap) on driver side.	HIII-50 & HIII-5	
Side Impact with Moving Deformable Barrier (MDB)	FMVSS 214, UN R95, Art. 18 & Att. 24, GB 20071-2006, AIS-099, KMVSS 102, ADR 72/00	USA, Europe, Japan, China, India, South Korea, Australia	Trolley with a deformable barrier impacts the driver side of the test vehicle.	ES-1 & ES-2 re & SID IIs	
Pole Side Impact (PSI)	FMVSS 214, UN R135, KMVSS 102-4, ADR 85/00	USA, Europe, Japan, South Korea, Australia	Test vehicle impacts 254mm rigid pole at 75° angle into occupant's H-point on driver side.		

Table 2 highlights that the vehicle tests are similar between world regions, however there are small differences between regulation test procedures and/or analysis tools. Details of the tests listed in Table 2 are presented in Table 3, Table 4, Table 5 and Table 6 for FFRB, ODB, MDB and SP respectively.

Table 3. Full Frontal Rigid Barrier Test Details by Region

FFRB	Region						
	USA	Europe	Japan	China	India	South Korea	Australia
Number of Tests	4	1	1	1	-	1	1
Number of Dummy models	2	2	2	2	-	2	2
Dummy Model(s) Type	<u>Tests 1&4:</u> HIII 50% <u>Tests 2&3:</u> HIII 5%	Driver HIII 50%, Passenger HIII 5%	Driver HIII 50%, Passenger HIII 5%	HIII 50%	-	HIII 50%	HIII 50%
Angle of Rigid Wall to Vehicle Direction	<u>Test 1:</u> 0° <u>Tests 2&3:</u> ± 5° <u>Test 4:</u> ± 30°	0°	0°	0°	-	0°	0°
Vehicle Velocity (km/h)	<u>Tests 1&2:</u> 56 <u>Tests 3&4:</u> 32-40	50	50	50	-	50	48

Table 3 presents the FFRB of world regions aspiring to global harmonisation to UNECE regulations. It is noticeable that all regions that conduct this test have velocities within 2km/h of one another and all drivers are represented by the Hybrid III 50% percentile (HIII) dummy. However, the passenger is represented by the HIII 5% in Europe and Japan. Similarly, the USA also tests with the HIII 5% and HIII 50% of the passenger and drivers, though these are the same as each other in each test, as illustrated in Figure 3. The FMVSS 208 is the only regulation across the regions that applies angles to the rigid wall as well as applying multiple velocities across the range of tests.

This item has been removed due to 3rd Party Copyright. The unabridged version of the thesis can be found in the Lanchester Library, Coventry University.

Figure 3. USA FFRB Regulation (FMVSS 208) (carhs.training 2021)

Table 4. Offset Deformable Barrier Test Details by Region

ODB	Region						
	USA	Europe	Japan	China	India	South Korea	Australia
Number of Tests	1	1	1	1	1	-	1
Number of Dummy models	2	2	2	2	2	-	2
Dummy Model(s) Type	HIII 5%	HIII 50%	HIII 50%	HIII 50%	HIII 50%	-	HIII 50%
Angle of Impact Location to Vehicle Direction	0°	0°	0°	0°	0°	-	0°
Percentage Offset of Barrier to Vehicle	40%	40%	40%	40%	40%	-	40%
Barrier Offset Location	Driver Side	Driver Side	Driver Side	Driver Side	Driver Side	-	Driver Side
Vehicle Velocity	40	56	56	56	56	-	56

All regulations across the regions that adhere to ODB testing are undertaken with 40% overlap of the deformable barrier to the front of the test vehicle at 0° impact angle. Additionally, all tests have a driver and passenger dummy model of the same variety within their corresponding examination. Excluding the USA, all regions also observe use of the HIII 50% dummy model and an impact velocity of 56km/h. The USA makes use of the HIII 5% crash test dummy whilst also applying a smaller velocity of 40km/h upon impact.

Table 5. Moving Deformable Barrier Test Details by Region

MDB	Region						
	USA	Europe	Japan	China	India	South Korea	Australia
Number of Tests	1	1	1	1	1	1	1
Number of Dummy models	2	1	1	1	1	1	1
Dummy Position	Driver and Rear Passenger (on Driver Side)	Driver	Driver	Driver	Driver	Driver	Driver
Dummy Model Type	<u>Driver:</u> ES-2 re <u>Passenger:</u> SID IIs	ES-2	ES-2	ES-2	ES-1/ES-2	ES-1/ES-2	ES-2
Angle of Impact Location to Vehicle Direction	63° skew (barrier and vehicle longit. axes are perpendicular at time of impact)	90°	90°	90°	90°	90°	90°
Barrier Impact Location	Left edge of barrier contacts vehicle horizontal axis + 940mm. MDB central longit. axes 0.5 length of wheelbase from rear wheels.	Longit. axis of MDB in line with vehicle front seat R-point	Longit. axis of MDB in line with vehicle front seat R-point	Longit. axis of MDB in line with vehicle front seat R-point	Longit. axis of MDB in line with vehicle front seat R-point	Longit. axis of MDB in line with vehicle front seat R-point	Longit. axis of MDB in line with vehicle front seat R-point
Barrier Type	MDB	MDB EEVC	MDB EEVC	MDB EEVC	MDB EEVC	MDB EEVC	MDB EEVC
Barrier Weight (kg)	1368	950	950	950	950	950	950
Barrier Velocity	48 perpendicular to vehicle drive direction, 54 at 63°	50	50	50	50	50	50

Table 5 summarises the MDB test across world regions, the abbreviation 'longit.' is short for longitudinal. Similarly to other regulations, the USA is the only region to have major differences in their procedure in comparison to the other world regions. All member regions apply regulations to vehicle performance in lateral collisions, all but the USA apply the same test procedure in terms of MDB mass, travel direction and impact velocity. In addition, although the use of the latest iteration of the ES-crash test dummy family (ES-2) is

preferred, South Korea and India permit use of ES-1 as well. Despite this, the collaboration between member states is highlighted by the identical MDB testing procedures across Europe, Japan, India, China and South Korea, as well as the use of the MDB European Enhanced Vehicle Safety Committee (EEVC) which was developed to provide better consistency, repeatability and reproducibility than the older form of MDB (Lowne 2001).

The USA has many differences for their MDB test in comparison to other regions. For example, the mass of the MDB is 418kg heavier than other regions, it has a skewed angle of impact and the test includes a rear passenger. It is important to note that this is not an oblique impact due to the vehicle side trim and barrier being parallel at time of impact. The variance in the MDB test procedures across regions are due to the differences in driving manoeuvres allowed on the roads and due to statistically common or high-risk collision arrangements. An example of a different manoeuvre is shown by some states across America in which it is permitted to turn right at intersection whilst the traffic light is red. The differences between driving manoeuvres from region to region could lead to a similar analogy of tests presented in Figure 4 as defined for the FMVSS 214(NHTSA 2012).

This item has been removed due to 3rd Party Copyright. The unabridged version of the thesis can be found in the Lanchester Library, Coventry University.

Figure 4. FMVSS 214 Test Procedure (NHTSA 2012: 21)

Figure 4 demonstrates the impact method of FMVSS 214. The impact location is designated by the left-hand side of the MDB face, which is set to intersect the test vehicle at half of the vehicle's wheelbase plus 940mm (from rear wheel central axis). This differs from the other tests in which the centreline vertical plane of the MDB is aligned with the vertical plane of the R-point (seat reference location provided by the manufacturer). Furthermore, the angle of approach of the MDB in FMVSS 214 procedure is 117° from the test vehicle's central longitudinal vertical plane (clockwise) and the MDB is rotated 153° (clockwise) from the vertical plane of travel direction. This ensures perpendicular contact between the barrier face and vehicle side. This induces a purely lateral impact velocity of 48km/h (due to 54km/h at 27°).

Table 6. Side Pole Impact Test (Oblique) Details by Region

This item has been removed due to 3rd Party Copyright. The unabridged version of the thesis can be found in the Lanchester Library, Coventry University.

1: Reduced to 26km/h if vehicle width is equal to or less than 1.5metres (UN Regulation 14 2013)

Table 6 shows that oblique pole side impacts across the member states and regions use the same impact velocity, pole dimensions, angle of impact and must all pass through the Centre of Gravity (CofG) of the dummy model's head. The only difference between regions and member states for the Side Pole impact is that the USA utilises the SID IIs or the ES-2 instead of the World-SID 50%. The World-SID has greater bio-fidelity for side

impacts compared to the ES-2, as examined by Stahlschmidt and Gromer (2010). The ES-2 shows stiffer rib responses in comparison to the World-SID as well as being more influenced by the arm positioning throughout the crash pulse. Interestingly, an alteration to this test procedure presents itself if the subject vehicle possesses a width of 1.5m or less and is therefore classified as a 'small' vehicle. In which case, the impacting velocity is reduced to 26km/h. Whilst some regulations are constrained to vehicles within a certain mass, this is the only full vehicle dynamic procedure that is modified dependant on the vehicle dimensions.

Electrical Safety

Hybrid and electric vehicles also have safety requirements to achieve with respect to the Rechargeable Energy Storage System (REESS). The safety requirements of the REES are implemented to M-category vehicles with a design speed exceeding 25km/h. The safety requirements are divided into two sections, but both apply to the REESS when it is used as a primary power source for the vehicle drivetrain (not auxiliary systems). Part 1 of UN Regulation No. 100 (2013) focuses upon insulation and protection from direct contact to electrical components of any electrical system in operation, whereas part 2 lists the requirements of REESS with regard to its safety, inclusive of post-crash requirements. Vibration, thermal shock and cycling, overcharge and discharge protection, emission criteria, external short circuit protection and fire resistance laboratory examinations are conducted as part of UN R100. The manufacturer can opt for a component-based test or full vehicle dynamic test to analyse the REESS's safety performance for mechanical shock and integrity. The full vehicle examinations include performing UN Regulations 94 or 12 for frontal impact (manufacturers choice) and UN Regulation 95 for side impact assessments. The assessment criteria of the REESS safety are identical between frontal and lateral impacts. The acceptance criteria is as follows (Regulation No. 100 2013):

- No evidence of fire or explosion.
- No electrolyte leakage into passenger compartment for 30 minutes after impact.
- No more than 7% of electrolyte capacity to spill out of REESS.
 - 5 litre maximum is applied to open type traction batteries.
- No penetration of external* REESS compartments into occupant compartment.

- * Initially located/installed outside of occupant compartment pre-crash.
- At least 100Ω per Volt of isolation resistance for high-voltage REESS.

The electrical safety of hybrid and electric vehicles are partially reliant on the crashworthiness performance of the vehicle. For example, extensive external damage to the vehicle could rupture the REESS or cause major internal intrusions of the REESS into the occupant compartment. Therefore, the acceptance criteria and optional test procedures ensure that severe consequences of the battery cells and REESS system are adequately intact upon an impact. However, UN Regulation 100 only applies to vehicle categories of M and N. This could be a cause of concern if L-category vehicle registrations increase in the near future and become more popular on the road.

Occupant Metrics by Test Procedure

Each vehicle and occupant model is prepared to the instructions listed in UN Addendum - Regulation 137 (2016), including the seatbelt anchorage specifications (Addendum 13: UN Regulation No. 14 2020) and restraint systems (Addendum 15: UN Regulation No. 16 2020). But the approval criteria of the regulations described in section 2.3.1 differ between each impacted zone of vehicle for occupant safety. The criteria for type approval requires recorded data of the occupant models to be within a specified threshold.

The real values of each criterium are recorded throughout the test; a Channel Frequency Class (CFC) is applied to each value which is specific for that metric. If the recorded values of the occupant model in each criterium are under the maximum specified value, then the results are deemed satisfactory. Additionally, if there is no contact of the occupant head to any vehicle part, then the HIC calculation is not performed and is deemed satisfactory. In addition to occupant metrics, vehicle measurements are taken and assessed. These are consistent throughout all procedures unless stated and are as follows:

- Displacement of steering wheel hub is less than 80mm and 100mm in the upward vertical and backward horizontal directions, respectively.
- No door shall open or lock.

- No evidence of interior component detachment or deformation that visibly increases injury risk to the occupants (such as sharp intrusions).
- The following should be possible post-impact:
 - 1) To open at least one door per row of seats (or gain access to via a door)
 - 2) To release the dummies from the restraint system with a maximum of 60N force applied to the release control.
 - 3) To remove the dummies from the vehicle without seat adjustments.
- Limited fuel leakage of 30 grams per minute for liquid-fuel propelled vehicle. Electrical safety requirements and measurements are enacted (detailed in section 2.3.1, 'Electrical Safety').

Full Frontal Rigid Impact

Table 7 provides the evaluation criteria and corresponding values for the dummy models used in UN Addendum - Regulation 137 (2016). All values are for the HIII 50% male dummy model except within the square brackets, which symbolises the value threshold for the HIII 5% female dummy (front passenger seat). The Viscous Criterion (VC) and Femur's axial force are not recorded for the driver (HIII 50% male) in this test.

Table 7. Occupant Criteria for UN Regulation 137 (FFRB)

Section	Criterium	Max. Value	Unit	Time	CFC
Head	HIC ₃₆	1000	-	-	1000
	Resultant Acceleration	80	g	X > 3ms duration	1000
Neck	Moment, extension (M _y)	57	Nm	-	600
	Tension (F _z)	3.3 [2.9]	kN	-	1000
	Shearing (F _x)	3.1 [2.7]	kN	-	1000
Chest	Deflection	42 [34]	Mm	-	180
	Viscous Criterion (VC)	[1]	m/s	-	-
Femur	Axial Force	[7]	kN	-	600

The Head Injury Criterion (HIC) criteria is a measure of the likelihood of the occupant suffering a head injury due to prolonged acceleration. The HIC is evaluated between 15ms and 36ms which is signified by the subscript numbering. A higher value of HIC is typically found with the vehicle impact causing contact between the occupant head and the vehicle interior, resulting in a large increase to head acceleration. For this reason, the HIC is marked as satisfactory if the head does not contact any vehicle component throughout the test, though it is noted as 'non-contact' in the results. The formula for calculating HIC is presented in Equation 1.

$$HIC_x = \left[\frac{1}{t_2 - t_1} \int_{t_1}^{t_2} a(dt) \right]^{2.5} (t_2 - t_1)$$

Equation 1. Head Injury Criterion (HIC)

Within Equation 1, 'a' is the resultant head acceleration, ' $t_2 - t_1$ ' is less than or equal to the time interval in milliseconds (as defined by the subscript 'x') and is selected to maximise the HIC value. The acceleration of the head that exceeds 3ms (by one or multiple peaks) has the CFC 1000Hz applied before the calculation is conducted for the resultant. Similarly, the VC does not show a CFC as the filtering is applied to the rib compression before the VC is calculated. The VC is calculated by the product of the relative rib compression and the rate of compression, which are both derived from the measurement of the rib deflection, to which the filtering is applied. The VC formula differs slightly between dummy models as the relative distance is calculated by the rib extremities and the centre of the dummy spine. The general calculation for VC is shown in Equation 2.

$$VC(t)_i = V(t)_i * C(t)_i$$

Equation 2. Viscous Criterion

In Equation 2, $V(t)_i$ is the relative velocity of rib_i at time t and $C(t)_i$ is the relative compression of rib_i at time t . The calculation of the relative compression, $C(t)_i$, varies depending on the dummy model used due to differences in rib sizes, the calculation method for the World Side Impact Dummy 50th Percentile (WSID50th) is presented in Equation 5.

Offset Deformable Barrier

Both regulations that manage frontal impacts have shared vehicle metrics and performance criteria. However, as shown in Table 8, the occupant criteria for the ODB differs to that of the FFRB.

Table 8. Occupant Criteria for UN Regulation 94 (ODB)

Section	Criterium	Max. Value	Unit	Time	CFC
Head	HIC ₃₆	1000	-	-	1000
	Resultant Acceleration	80	G	X < 3ms duration	1000
Neck	Moment, extension (M _y)	57	Nm	-	600
	Tension (F _z)	3.3 _{a1}	kN	a ₁ = 0ms	1000
		2.9 _{a2}		a ₂ = 35ms	
		1.1 _{a3}		a ₃ ≥ 60ms	
	Shearing (F _x)	3.1 _{b1}	kN	b ₁ = 0ms	1000
		1.5 _{b2}		b ₂ = 25-35ms	
		1.1 _{b3}		b ₃ ≥ 45ms	
Chest	Deflection	42	mm	-	180
	Viscous Criterion (VC)	1	m/s	-	-
Femur	Axial Force	9.07 _{c1}	kN	c ₁ = 0ms	600
		7.58 _{c2}		c ₂ ≥ 10ms	
Knee	Displacement	15	mm	-	CFC
Tibia	Tibia Index (TI)	1.3	-	-	1000
	Axial Force Compression	8	kN	-	1000

The head criterium and measuring procedure remains the same between the FFRB and ODB, including the automatic pass for no impact to vehicle components. However, the ODB incorporates timeframes for recorded values throughout the test in the neck (tension and shearing) and the axial force within the Femur. The initial values (time = 0) are the equivalent to that of the FFRB test and decrease throughout the crash pulse to ensure

there is reduced acceleration throughout. As only half of the vehicle's crash structure is engaged during this crash mode, there are increased forces and intrusions which could negatively affect the occupant compartment. Therefore, the ODB occupant criteria has additional metrics of the Knee and Tibia to help assess the load-path of forces by engagement of 40% of the vehicle width.

Moving Deformable Barrier

Table 9. Occupant Criteria for UN Regulation 95 (MDB)

Section	Criterium	Max. Value	Unit	CFC
Head	HIC ₃₆	1000	-	1000
Chest	Deflection	42	mm	180
	Viscous Criterion (VC)	1	m/s	-
Abdomen	Abdominal Peak Force (APF)	2.5 _{internal} 4.5 _{external}	kN	600
Pelvis	Pelvic Symphysis Peak Force (PSPF)	≤ 6	kN	600

Table 9 presents the occupant criteria for the pure lateral impact by a MDB EEVC according to UN Addendum 94: Regulation No. 95 (2014). In contrast to the FFRB and ODB criteria, the MDB lateral impact has far fewer criterion as it omits criterions of the leg, but it does include abdominal and pelvic forces. The PSPF is recorded within the dummy by a load cell, but the APF can be recorded externally. The APF is the maximum sum of three transducers, which can be placed 39mm below the surface of the impacted side (in relation to the MDB)(Addendum 94: Regulation No. 95 2014: 26). The MDB vehicle metrics possess no limitation on the allowable displacement of the steering wheel, but all other metrics are equivalent to those of the FFRB and ODB tests.

Oblique Pole Side Impact

Table 10. Occupant Criteria for UN Regulation 135 (PSI)

Section	Criterium	Max. Value	Unit	CFC
Head	HIC ₃₆	1000	-	1000
Shoulder	Peak Lateral Force	3	kN	600
Chest	Thorax Rib Deflection	55	mm	600
Abdomen	Abdominal Rib Deflection	65	mm	600
Lower Spine	Resultant Lower Spine Acceleration	75	g	180
Pelvis	PSPF	3.36	kN	600

The PSI utilises the World-SID 50% which permits the measurement of thoracic rib deflections (upper, middle, and lower) and abdominal rib deflections (upper and lower), improving the study of the effects of a crash in human kinematics to older counterparts such as the ES-2. Therefore, the rib deflections have been divided into the sections of chest and abdomen. The occupant criteria of the ODB also measures the peak lateral force of the shoulder and resultant spinal acceleration due to the impact location. The resultant lower spinal acceleration is calculated at the T12 vertebrae by the squared sum of accelerations in all axes that exceed a 3ms (millisecond) timeframe. Each acceleration peak is individually filtered by a CFC of 180Hz before the resultant acceleration is calculated.

2.3.2 Consumer Program Safety Assessments

Consumer programs such as NCAP and IIHS develop rigorous tests that explore and analyse the crashworthiness of a vehicle and sub-systems involved, specifically for new vehicle designs and technology. This method aids in the developments of amendments and adoption to regulations by providing an increased understanding of vehicle performance, via research in vehicle safety and applied technology. Moreover, the assessment programs employ a scoring-based system for the vehicles and accompanying equipment which allows comparisons to be made by the public consumer market between vehicle models and manufacturers in relation to safety. Each New Car Assessment Program (NCAP) contains members from nationwide

administrative capabilities from multiple countries (Euro NCAP n.d.). Programs conducted by NCAP cover the aspects of adult, child and vulnerable road-user protection as well as safety assistance systems. A summary of active protocols of Euro NCAP are provided in Table 11.

Table 11. Euro NCAP Protocol Listing

Protocol	Adult Occupant Protection	Child Occupant Protection	Vulnerable Road User Protection	Safety Assist
Assessment	Y	Y	Y	Y
Frontal MPDB Test	Y	Y		
Frontal Full Width Test	Y			
Knee Mapping Sled Test	Y			
Side AE-MDB Test	Y	Y		
Side Oblique Pole Test	Y			
Far Side Test	Y			
Whiplash Test	Y			
Rear Whiplash Test	Y			
Rescue, Extrication & Safety Test	Y			
AEB Vulnerable Road User Test			Y	
Pedestrian Test			Y	
SAS Test				Y
AEB Car-to-Car Test				Y
LSS Test				Y

The frontal full width test is equivalent to the FFRB (UN) presented in Table 3. However, the Mobile Progressive Deformable Barrier (MPDB) has replaced ODB since 2020 to better represent the collision between two vehicles (Euro NCAP 2020a). Likewise, the MDB used in legislation has been developed further to better represent the current front-end stiffness present in today's passenger fleet; the Advanced European Mobile Deformable Barrier (AE-MDB) is utilised in the lateral impact test. It is worth noting the occupant assessment criteria differs to those of regulation by number of areas assessed as well as the limiting value. Scores are applied to each area of assessment and collated to provide overall vehicle safety performance, whilst still highlighting areas which may have performed poorly. Furthermore, NCAP test procedures use a variety of

different occupant models. Those that are equivalent to a test in legislation, such as the FFRB and Full Width Frontal, conform to the build and preparation of the relevant occupant model.

In addition to improving upon regulation procedures and applying a scoring system for consumers, NCAP also tests vehicles and systems not currently covered by legislation. Vehicles categorised as L7e or L6e only have three Regulations of the United Nations enforced by law, which govern the use of head rests, fitting of glazed glass and emissions targets (Addendum 15: Regulation No. 16 2020, Addendum 42: Regulation No. 43 2020, Addendum 24: Regulation No.25 2015). In 2014 Euro NCAP developed and applied testing protocols for heavy quadricycles (L7e-category vehicles) for frontal and lateral impact (Euro NCAP 2014a, 2014b). The tests were conducted in 2014, then after recommendations to improve their safety, had tested L7e vehicles again in 2016. The results of the tests are discussed in the subsection titled 'Heavy Quadricycle Crashworthiness Performance' within section 2.3.2.

In addition to testing vehicles not covered by regulations, other protocols are designed to test the effectiveness of systems or specific areas of a vehicle, such as the AEB, Speed Assist System (SAS) and pedestrian protection protocols which too, are not currently under legislative law.

Advances in Crash Avoidance & Mitigation Technology

In 2020 NHTSA announced that the voluntary effort by 20 automotive manufacturers to install low speed AEB and FCW systems to all new vehicles by 2023 is progressing three years ahead of schedule. By 2019, Tesla and Volvo had achieved 100% of their fleet fitted with these systems, whilst Mercedes and Audi had 99%. By December 2020, 15 of the manufacturers have installed AEB and FCW in over 50% of their vehicle fleet (NHTSA 2020). The voluntary commitment by automotive manufacturers such as Tesla, Nissan, Toyota, Mercedes-Benz, BMW, Audi, Subaru, Volkswagen, Mazda, Hyundai and Volvo (which implemented FCW and AEB in over 95% of their vehicle fleet by 2020) highlights the global industrial preference to employ greater safety measures than what is mandatory by federal ruling.

In addition to AEB and FCW, other Advanced Driving Assistance Systems (ADAS) are being researched, known as Reverse Collision Warning System (RCW), Adaptive Cruise Control (ACC), Collision Mitigation System (CMS) and Lane Keeping Devices (LKD) (European Commission 2021a). Typically, complete vehicle ADAS is formed of numerous individual assistance systems, such as the combination of FCW and AEB. The effectiveness of these technologies has been studied by Cicchino (2017), in which it was predicted that FCW reduced front to rear crash rates by 27% and AEB systems reduced front to rear crashes rates by 45%. Further to this, the combination of FCW and AEB systems reduced front to rear crash rates by 50% (5% more than AEB alone) and reported injury rates by this mode of crash by 56% (11% more than AEB alone).

On the other hand, early warning systems such as FCW and LDW are more advantageous on an open road with fewer obstructions to their 'vision' as this provides ample time for the driver to respond to stimulus provided by the system. Furthermore, the systems are developed assuming nominal operation of the vehicle. Namely, good tyre and brake system operation within a clear and dry environment. Thus, in adverse weather conditions, such as wet or icy roads, or with substantial tyre degradation, the systems are less likely to prevent the accident. This is because there is an increased stopping distance which is not factored into the systems calculations at time of initial and partial braking (Christ 2020). For instance, wet weather increases the likelihood of road accidents by 150% (Jaroszweski and McNamara 2014).

Euro NCAP is actively testing the performance of ADAS, specifically systems that aid in speed management, emergency braking (including vehicle detection) and lane keeping systems (Euro NCAP 2021). The testing protocols involve assessing the mitigation or avoidance of car-to-car impact scenarios whilst the secondary vehicle is driving forward, driving backward, stopped, or crossing path at an intersection. However, all tests require dry conditions with temperatures between 5°C and 40°C, with no obstructing features. Although the assessment gauges the performance of when and how the ADAS operates, it may not be representative of real scenarios, given the more chaotic nature of urban environments and adverse weather conditions. Especially if

the UK's 'roundabout' road network is considered. The driving behaviour and lane manoeuvres at a roundabout are significantly different to that of the intersection laboratory testbed, therefore a roundabout junction could induce premature braking by the system.

Heavy Quadricycle Crashworthiness Performance

Consumer programs aim to represent real-world scenarios for accident prevention and crashworthiness performance. Thus, statistical data of accident and injury reports provides data that help shape and develop test procedures. Due to the projected market growth and support by the European Commission for smaller and electric vehicles, Euro NCAP had assessed L7e vehicles for their crashworthiness performance and occupant safety. However, despite improvements being suggested by European NCAP to the manufacturers, there were no significant changes to the occupant's safety within two years (Euro NCAP 2016a). The vehicles that were tested had scored very poorly in both front and side impacts, only scoring a maximum of 2 stars overall. Table 12 provides a summary of the information and scores achieved by the subject vehicles.

Table 12. Crashworthiness Performance of Quadricycles in 2014 and 2016 (Euro NCAP 2016b, 2016c, 2016d, 2016e, 2014c, 2014d, 2014e, 2014f)

Vehicle	Kerb Weight (kg)	Number of Seats	Front Score (16 max)	Side Score (16 max)	Stars
Aixam Crossover GTR	440	4	2	10	1
Bajaj Qute	400	4	4	6	1
Microcar M.GO Family	425	4	4	6	1
Chatenet CH30	390	2	6	6	2
Tazzari ZERO	542	2	4	8	1
Renault Twizy 80	474	2	6	7	2
Club Car 2+2 Villager LSV	541	4	2	9	0
Ligier IXO JS Line 4 Places	465	4	2	7.9	0

It should be noted that the tests conducted upon the L7e category vehicles differ to that of a passenger vehicle in the M1-category (Euro NCAP 2014a, 2014b). The main differences were the use of a deformable barrier for the full width frontal impact test (instead of a rigid wall) and a reduced trolley mass for the lateral impact test

(350kg less). Although the tests were prepared in a similar fashion to those applied to the M1-category as described in UN Addendum - Regulation 137 and Addendum 94: Regulation No. 95, it can be speculated that the procedures are not representative of a real-world scenario. An assumption can be made that it is more likely for an L7e vehicle to impact, or be impacted by, an M1 vehicle, especially in the introductory phase to public roads. Therefore, the trolley's reduced mass does not characterise a vehicle within the M1-category.

Despite the trolley mass reduction, Table 12 shows that only three vehicles achieved greater than 50% scoring in the MDB test assessment. Furthermore, despite using the deformable barrier for the full-frontal impact assessment, no vehicle achieved greater than 6 of the available 16 allocated points. In both load cases the occupants had suffered severe injuries to numerous regions of their body, often critical areas. Many of these were the result of high acceleration, component intrusions and occupant contact to the vehicle. Therefore it can be expected that a collision between an L7e and M1 vehicle would result in detrimental crashworthiness performance of the heavy quadricycle due to crash incompatibility and overwhelming forces afflicted by the larger vehicle (Edwards et al. 2014, Baker et al. 2008). It is stated by Davis et al. (2016a) that within the introductory stages of L7e vehicles to the public sector, collisions with larger vehicles should be of major concern. Road incidents often occur between two or more vehicles rather than a single vehicle incident. This type of collision incurs much greater risk to the occupants within the lower mass vehicle. For instance, a head on collision of two vehicles (one with double the mass of the other) could lead to an estimated fatality risk ten times greater for the occupants of the smaller vehicle. This results in the smaller vehicle experiencing a change of velocity double to that of its partner. Furthermore, as shown by the results in Table 12, it is expected that an L7e vehicle does not have a suitable structure that effectively reduces intrusions and sufficiently absorbs energy from an M1 vehicle.

To provide better protective measures for smaller vehicles, research into new crash structures and methodologies was conducted. This was done to discern the feasibility of implementing suitable crash structures within a L7e vehicle despite the constraints applied to the vehicle category.

2.4 Vehicle Passive Crashworthiness

Occupant safety heavily relies on the performance of the passive crash structures within the vehicle when an impact occurs. A lot of research has been accomplished to ascertain the best structures to absorb the energy of the collision whilst maintaining suitable deformation distances and deceleration. The evolution of vehicle design and test regulations has led to a need for innovative designs and methods of developing crashworthy structures. Recent developments have been aptly categorized by Zahran et al. (2018) as either configuration methods or imperfection methods. The full tree is shown in Figure 5.

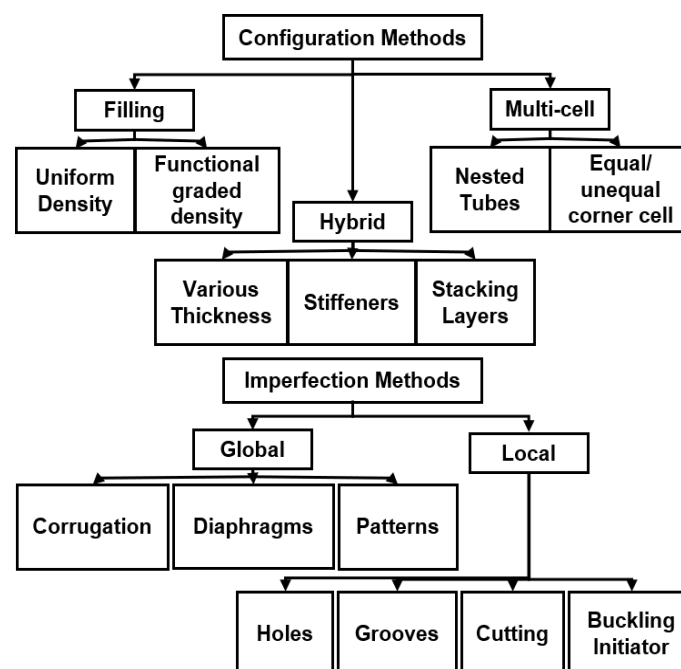


Figure 5. Energy Absorbing Methods

Configuration methods could be defined as an arrangement of elements into a particular form to achieve specific goals; accordingly, this method incorporates multi-cell and foam structures. Although ‘imperfection’ usually has negative connotations of undesirable features, the definition can be manipulated for application to crash structures. For instance, an imperfection could be viewed as a cut, hole or other ‘deformity’ to a regular section of material. As such, this type of method incorporates initiation triggers, grooves, holes and other face changes such as corrugation. It was found through literature that imperfection methods were very efficient at reducing the peak force and developing stable folds, however this came at a cost to the amount of energy absorbed (Zahran et al. 2018, Asanjarani, Dibajian, and Mahdian 2017). Although this is beneficial for

occupant safety as it reduces the instantaneous load to the occupant, it poses problems in terms of energy absorption for smaller vehicles due to small crush distance allowance. Furthermore, initiation triggers are highly specific to impact velocity as they are related to the fold wavelength of material, which can reduce the performance of the component if a different velocity of impact occurs. In contrast, configuration methods have been shown to drastically increase the EA of a structure for an equivalent counterpart of the same mass (discussed further in section 2.4.1 and 2.4.2), but also increase the peak force. This has been shown in numerous instances, inclusive of multiple angles of impact (with varying efficiency). Due to the adaptability of configuration methods, a greater focus towards these systems has been made recently. Some of these incorporate imperfection methods in attempt to ensure stable collapse modes along with reducing the peak force. Therefore, this section will discuss the most recent developments in advanced crash structures available today. It includes filling techniques, variable thicknesses, multi-cell applications as well as combinations of all three.

Common measurements (and their respective constraints) that are taken during analysis of the structures are shown in Table 13. These are common for all literature and relate to the vehicle's structure, where the models are evaluated and validated experimentally or numerically. It should be noted that some metrics have significant impact upon the occupant, such as the Peak Crush Force (PCF) and Mean Crush Force (MCF). In addition, more constraints could be added depending on the scenario and model that has been simulated, an example of which is an intrusion constraint for lateral impact.

Table 13. Typical Measurements of Crashworthiness

Name	Abbreviation	Formula	Ideal	Constraint
Energy Absorption	EA	$\int_0^{\delta} F(x)dx$	Max	PCF & crush δ
Specific Energy Absorption	SEA	$\frac{EA}{M}$	Max	PCF & crush δ
Mean Crush Force	MCF	$\frac{\int_0^{\delta} F(x)dx}{\delta}$	Near PCF, small fluct.	Min & Max
Peak Crush Force	PCF	N/A	Balan.	Max
Crush Force Efficiency	CFE	$100 \left(\frac{F_{mean}}{F_{max}} \right)$	Max	Min

Where F , δ and M are the force (kN), crush displacement (metres) and the mass (kg) respectively. The abbreviated 'fluct.' and 'Balan.' signifies 'fluctuation' and 'balanced' respectively. Inopportunately, many of the assorted designs that will be discussed do not provide a direct comparison to each other despite having common measurements; this is due to minor changes in the modelling procedures, material property differences, or even load-case variances. In addition to this, it was found that relevant research of new design procedures for side impacts are quite scarce. Nonetheless, where applicable, the theory and application will be noted accordingly.

Firstly, it is apt to summarise the various load-cases that were analysed in literature. Table 14 provides an overview of the analysis performed; each row corresponds to a single paper released by the respective author. The letters 'Y' and 'N' correspond to yes and no respectively, whilst 'P' signifies partial or an approximation to.

Table 14. Analysis overview

Author(s)	Impact(s) type:			
	Axial	Oblique	Lateral	Multiple Velocity
Nagel (2005) Nagel	Y	Y	N	Y
Zhang, Wen, and Zhang (2014)	Y	N	N	N
Sun et al. (2017)	Y	N	N	N
Fang et al. (2017)	Y	N	N	N
Ito, Yokoi, and Mizuno (2014)	N/A	N/A	N/A	Y
Lee and Park (2017)	P	N	P	N
Gao et al. (2016)	Y	Y	N	N
Qiu et al. (2015)	Y	Y	N	N
Noversa and Peixinho (2013)	Y	N	N	N
Asanjarani, Dibajian, and Mahdian (2017)	Y	N	N	N
An et al. (2015)	Y	N	Y	N
Sun et al. (2017b)	Y	N	N	N
Reddy, Rao, and Narayanamurthy (2018)	Y	N	N	N
Kamran et al. (2017)	Y	N	N	N
Hou et al. (2015)	Y	N	N	N
Ma et al. (2015)	Y	N	N	N
Ahmad Mujahid, Lang, and Ahmad Firdaus (2010)	N	N	Y	Y
Zhu et al. (2017)	Y	Y	Y	N
Kohar et al. (2016)	Y	N	N	N
Kohar et al. (2015)	Y	N	N	N
Omer et al. (2017)	Y	N	N	N
Schlosser et al. (2017)	N	N	Y	N
Li et al. (2018)	Y	N	N	N
Sun et al. (2017a)	Y	N	N	N
Zahran et al. (2018)	Y	N	N	Y
Xu et al. (2016)	Y	N	N	Y
Nia and Chahardoli (2016)	Y	N	N	P
Zhang, Bai, and Bai (2018)	Y	N	N	N
Reddy, Abbasi, and Fard (2015)	Y	N	N	N

It is clear to see in Table 14 that there is a severe lack of multiple cases analysed by a single paper, rendering it extremely difficult to isolate an optimum design that caters for multiple impacts. For development of crush structures, it is imperative that future designs encompass multiple velocities, oblique impacts, and lateral impacts, as these are expected to be the most common crash scenario and hold the largest risk for L7e

category vehicles and autonomous pods (Subit et al. 2017, Favarò et al. 2017). Despite this, claimed improvements of the most promising literature will be highlighted in each section. These are multi-cell, exterior walls, foam filling, and filling by an internal structure.

2.4.1 Cross-Sectional Designs

In this section comparisons are made of literature that examines the effects of changing cross-sectional profiles, and the effect this has on crashworthiness performance. It was found that the most popular methods were multi-cell designs or changes to the exterior wall of the component.

Multi-Cell

To define a multi-cell structure, a delve into the origin of the word could be made. Cell originates from the Latin 'Cella' which means 'small chamber'. Much like a chamber or room, this could either be open or closed. In relation to crash structures, this definition can be easily carried over. For instance, a closed cell structure would have walls present at each side of the shape, whereas an open cell structure could have one or two walls missing, typically the 'roof' or 'floor' of the chamber. Thus, multi-cells could be thought of as many combined chambers to make a structure. It has been found through literature that the usual multi-cell structures used within longitudinal rails are 'open'. This permits the rails to be manufactured by an extrusion process. Although the following studies primarily focus upon vehicle light-weighting and the use of extrusions, it should be noted that the multi-cell structures do not have to be regular in shape, nor do they have to be of a continuous profile throughout the depth of the structure.

As mentioned, many studies have been conducted upon multi-cell extrusions, primarily with aluminium extrusions. A swarm optimization was conducted by Fang et al. (2017) to obtain a cross-sectional design of a longitudinal rail; this constraint driven algorithm highlighted the trend of the material being pushed towards the corners of the member. This was identified to aid in the increase of energy absorption by inducing more folds under the crush load (Fang et al. 2017). By ensuring that there is a connection between the outer and inner walls of the multi-cell cross section, a stable fold condition is induced with a narrow force fluctuation

range (Ma et al. 2015). This is an important feature to have for a crash rail as this configuration helps reduce the likelihood of fracture under these load conditions, demonstrated by Sun et al. (2017b, 2017c) and Omer et al. (2017) via quasi-static and dynamic tests. Thus, it can be deduced by this alone that an increase in the number of corners (or more regions capable of large plastic deformation) holds the potential to vastly improve crashworthiness. Accordingly, it appears relevant to summarise the claimed effectiveness of multi-cell designs found throughout literature.

The numbers within Table 15 are percentage changes to a baseline comparison and they highlight the 'best' result contained in a study, these are shown graphically within Figure 6. Due to selecting the best obtained results, many of the design variations in each study will not be presented. Please note that all these designs underwent a crush displacement of a typical crush-rail as discussed by Reddy, Rao, and Narayanamurthy (2018).

Table 15. Multi-Cell Performance Summary (Reddy, Rao, and Narayanamurthy 2018)

S ^{no.}	PCF	EA	SEA	MCF	CFE	Mass
1	+7.1	+45	+45	-	+20	-
2	+27	+26.7	+4.6	+22	-2.5	+21
3	+66	+68	+21	+68	+1.1	+40

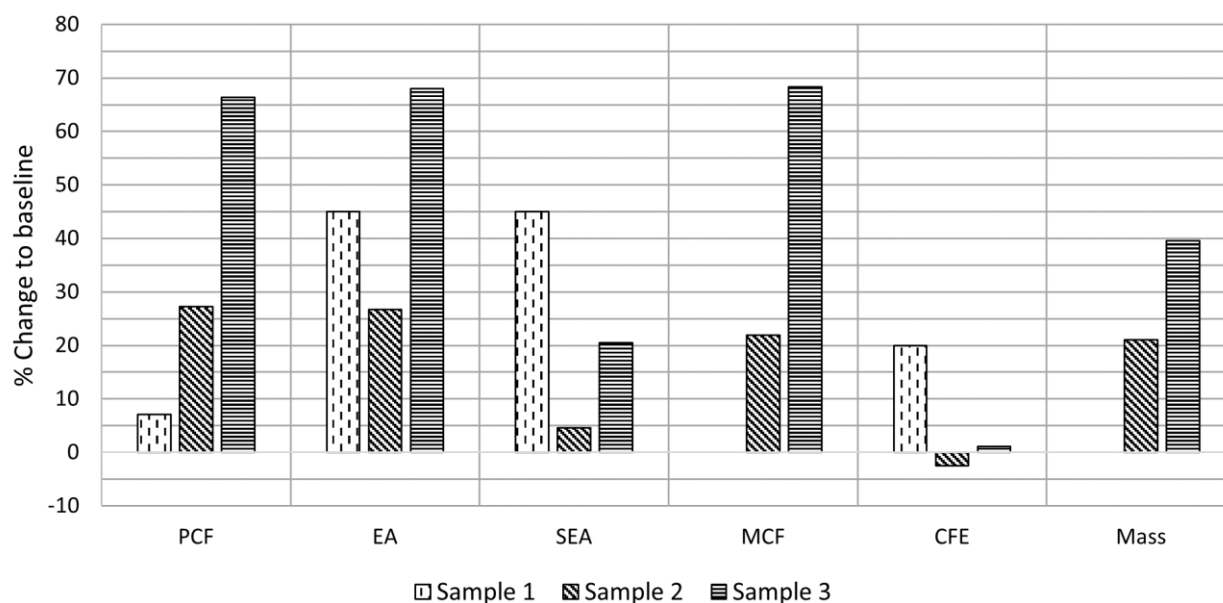


Figure 6. Multi-cell Performance Summary (Reddy, Rao, and Narayanamurthy 2018)

All specimens within Table 15 are compared to a hollow counterpart or baseline specimen of their respective study - it should also be noted that the cross-sectional geometry may vary between each paper. For instance, Qiu et al. only utilizes hexagonal profiles whereas authors Zhang, Bai, and Bai evaluates between square, hexagonal and octagonal (Qiu et al. 2015, Zhang, Bai, and Bai 2018). Unfortunately, some studies could not be included as there had not been a baseline or counterpart to allow comparison. It can be seen in Table 15 and Figure 6 that the mass of a structure heavily influences the energy absorbed, yet it does not always result in a better performance (in terms of crush force efficiency and SEA) for the amount of added mass.

A study by Kohar et al. (2016) utilized two base-line crush cans of a 7 and 6 series aluminium rail in addition to a 4-cell configuration of the 6-series aluminium alloy. Through a dynamic crash sled test, it was found that the 7-series aluminium had the highest crush performance of the 3 configurations, however this is to have been expected as it had a higher mass. It was also decided to optimize the SEA in this study as this would directly impact the crush efficiency. It was found that the walls closest to the corners of the cross section were most sensitive to parameter changes, leading to a high change in SEA with changes in wall thickness or mass.

Despite efforts to improve the performance of crush members for high velocity impacts, the effects of multiple load cases are relatively understudied. However,, the effects of different loading angles on multi-cell configurations were studied by Qiu et al. in which a 600kg rigid block at 15m/s (33.5mph) was impacted into various multi-cell designs of a longitudinal crash rail. The simulated impact was conducted at 0° (purely axial crush) to 30° in 10° intervals (Qiu et al. 2015). Each configuration maintained the same component mass as the hollow configuration by reducing the outer and inner wall thickness accordingly. (Qiu et al. 2015). Figure 7 illustrates the cross-sectional design of each of the seven tubes and their respective performance in each test-case. Note that the Crush Load Efficiency (CLE) is equivalent to the Crush Force Efficiency (CFE) defined in Table 13.

This item has been removed due to 3rd Party Copyright. The unabridged version of the thesis can be found in the Lanchester Library, Coventry University.

1 51 52 53 54 55 56 57 ■

Figure 7. Crashworthiness indicators at various angles (Qiu et al. 2015)

Multi-cell designs appear to typically improve the EA in an axial load, whilst some also decrease the maximum peak force. This suggests that multi-cell designs should be taken with great scrutiny, as it may not actually improve performance and will often lead to greater manufacturing costs as they are more complex. Then again, by specifically observing the results of S4 and S7 as shown in Figure 7, the EA and CFE obtained are far superior in comparison to the hollow tube, S1. It is shown in the study that in these cases that a stable fold condition is still present at a 10° angle, it is clear that the interconnecting ribs induced smaller folds and progressed more axially than other counterparts. When the angle is increased further, this axial progression is completely lost as global bending dominance proceeds, rendering the inner ribs near useless in controlling the deformation. The multi-cell designs shown in Figure 7 could be improved further by varying the thickness of specific walls or inter connecting ribs, thus increasing the resistance to global bending (Kohar et al. 2015). It can be speculated that the orientation of the internal structures is important to induce axial folding, whilst a longitudinally changing internal profile would benefit at greater impact angles to resist the global bending. In essence, ‘pulling’ the structure to collapse by fold progression.

Furthermore, an approximate drop in EA performance of 20% between 0 and 10° of impact is noticeable, the largest of which was found to be of the square profile with 36% loss (Gao et al. 2016). A severe drop of PCF is noticeable with an increase of impact angle; a major drop was found in all profiles between the first interval of impact angle, with only minor drops in PCF with the remaining 10° intervals to 30°. Gao et al.’s study, despite different cross-sectional profiles to Kohar et al.’s hexagonal design, still proves the usefulness of interconnecting ribs. It can be deduced that different profile shapes influence the crush efficiency (Gao et al. 2016, Kohar et al. 2016).

Exterior wall

Changes to the exterior wall include the cross-sectional profile as well as wall thickness gradients. Table 16 provides a summary of performance metrics that show the percentage change of a studies’ ‘best’ profile to its ‘worst’ or baseline. The smaller changes in SEA were typically found in profiles that employed a graduated

thickness, or where mass had not been considered. Larger differences were noticeable when the profile had completely different geometry to one-another.

However, these results should be taken with care as the results listed are all considering an axial compression. Thus, an oblique impact could drastically affect the efficiency of the structure, or the location that the structure is impacted (such as the short side of an ellipses in comparison to the longer side). Furthermore, sample 5 (Table 16) has such a high increase due to a complete change of geometry, however there was no observable consideration to mass or other parameters. Due to no consideration of mass, this could render the spline design that Sun et al. discusses inapt for quadricycles and light-weight vehicles (Sun et al. 2017a).

Table 16. Exterior Wall Performance Summary

S ^{no.}	PCF	EA	SEA	MCF	CFE	Mass
1	-56	+9.6	+9.6	-	-	Equivalent
2	-10	-	+53	-	-	-
3	-	-	-35	-	57	-
4	+27	-	+204	+203	+36	-
5	-	+61	+63	-	-	-1.2

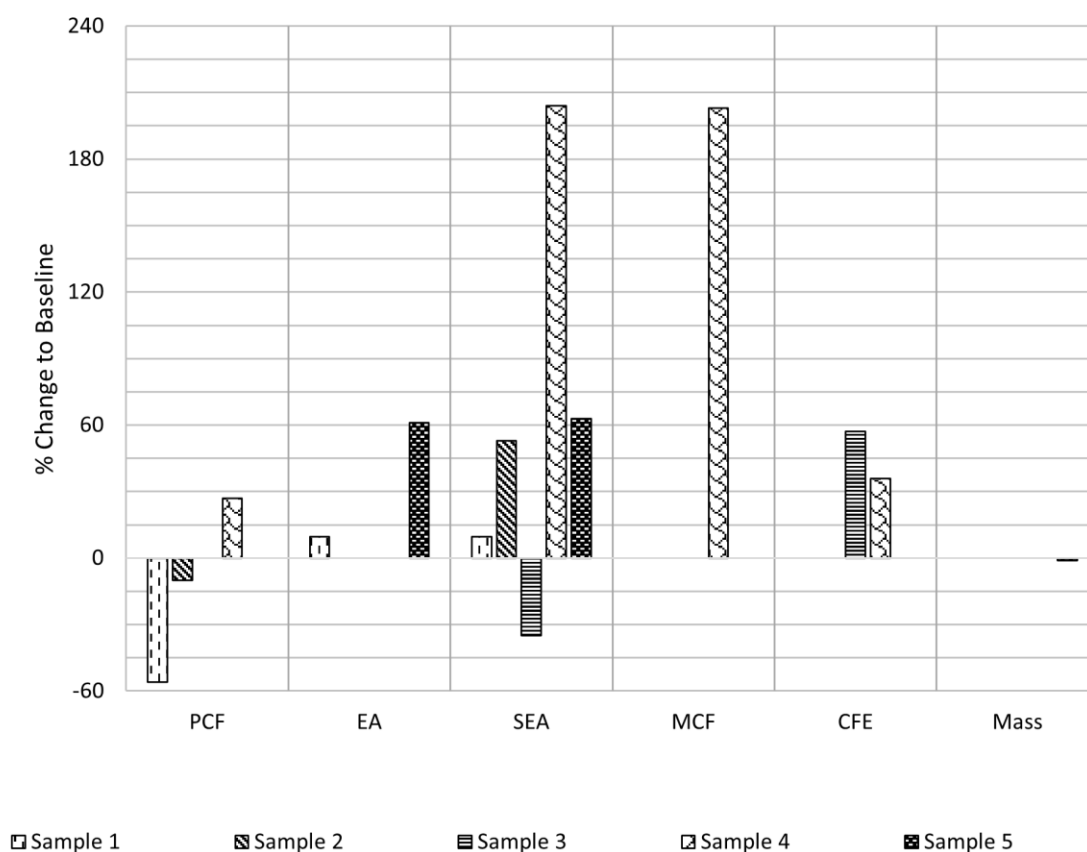


Figure 8. Exterior Wall Performance Summary

A study by Zhang et al. varied the thickness of the metal laterally (variable cross-sectional thickness). Two designs were used for the experiments: single-surface gradient (SSG) and double-surface gradient (DSG). The main difference of these is that the SSG had a fixed outer-wall dimension whilst the DSG achieved the thickness gradient by ‘thinning’ the metal symmetrically towards the centreline of each wall. The main drive for this study was to demonstrate that uniform crash structures are not fully utilizing the limited material available, thus attempting to show that for the same mass (or less) a structure that holds a higher EA and MCF could be designed. It was found that both the SSG and DSG improve the EA and MCF in comparison to the uniform thickness tube. However, it must be mentioned that in practicality, a gradient too large would provoke tearing at the weaker sections of the tube, thereby reducing the energy absorbing capacity. Despite tearing, the SSG managed to obtain 29.3% higher EA, 23.3% increase in MCF and a reduction in PCF of 1.2%, all with a 2.4% decrease in mass. In addition to this, it was found that the DSG’s lobe formation does not have a large enough

amplitude to cause tearing but offers very similar results in terms of performance to the SSG. For instance, with a mass change of less than 0.2% a 27.9% increase to EA, 1.4% reduction of PCF and a 26.2% increase in MCF was observed (Zhang, Wen, and Zhang 2014).

A study by Sun et al. could be regarded as a continuation of this work by also comparing the laterally functional graded thickness (LFGT) against axially functional graded thickness (AFGT) tubes (Sun et al. 2017b). Sun et al. (2017b) implemented initiation triggers to ensure fold initiation and progression of the different tubes so that they could be adequately compared by quasi-static testing. It was found that the AFGT tube reduced the PCF by 27.3% in comparison to the uniform thickness (UT) tube, whilst the LFGT increased this value by 2.5%; these results suggest that the AFGT may perform better. However, the LFGT did hold a SEA value (by experimentation) 17.2% higher than that of the AFGT tube, inclusive of a higher average MCF.

It is noticeable that the MCF increases with each fold progression within the AFGT (due to the larger thickness of the wall as the crush displacement progresses). This not only increases the MCF and the SEA throughout progression but could lead to the PCF being located at the latter stages of deformation instead of the instantaneous moment of impact (Yin et al. 2016). Sun et al. confirms this by discovering that the EA of the AFGT tube dramatically increased after 80mm of deformation. Although this would suggest this tube is more suitable for longer deformation zones of a vehicle, the material thickness at the impacting end could be increased, or the gradient of thickness could be increased. Although this would lead to a larger PCF, it is expected that this will still provide a reduction to the value achieved by the UT tube, thus also inducing a higher SEA at shorter deformation length (Sun et al. 2017b).

It is evident that by changing these parameters the performance in different crashworthiness criteria is significantly affected. A possible improvement to the AFGT tube is the incorporation of a multi-cell cross-sectional design as conducted by Yin et al. (2016). Although this study had the primary focus of assessing the

functionality of an adaptive radial basis function for optimization, it still shed some light on the capability of incorporating a multi-call design to an AFGT tube. The performance was greatly affected by the addition of connecting ribs. For instance, a slight gradient change of thickness reduced the PCF by 41.17%, whilst only reducing the SEA by 22.13%. Unfortunately, the effect of different loading angles on this specimen are unknown, however it can be assumed that the performance would be better than that of the LFGT tube or hollow tube. This is apparent as more resistance to the global buckling dominance is present. However, care should be taken as this may require more component mass, which is an important parameter to consider for super-light-weight vehicles.

2.4.2 Filling materials

Mimicking section 2.4.1, direct comparison between literature will be made to evaluate performance of crash tubes using filling techniques. Numerous filling techniques were utilized; most commonly foams were selected, however other filling techniques present themselves as structural and multi-tubular design.

Foam

Foam filling was opted for in many studies due to the characteristics of it being light-weight and holding a lot of potential to absorb energy without altering the collapse mode. Due to the nature of this analysis, it is often the case that foam filled tubes can be directly compared to their hollow counterpart. These comparisons are shown in percentages within Table 17. The results shown in Table 17 are only representative of results from an axial collapse or pure lateral bending corresponding to the same cross-sectional profile. The lateral bending tests are samples 6 to 9. A graphical representation of the percentage changes presented in Table 17 are presented in Figure 9.

Table 17. Foam Crashworthiness Performance Summary

S ^{no}	PCF	EA	SEA	MCF	CFE	Mass
1	+21.6	+38	+38	-	-	Equivalent
2	+14.7	+45	+45	-	-	Equivalent
3	+13	+64.7	+64.7	-	-	Equivalent
4	+18.3	+40.6	+40.6	-	-	Equivalent
5	+0.3	+16.6	+16.6	-	-	Equivalent
6	-3.3	+7.9	+7.9	N/A	N/A	Equivalent
7	-	+25	-	N/A	N/A	-
8	-	+10.9	-	N/A	N/A	-
9	-	+20	-	N/A	N/A	-

For equivalent mass, a foam filling increases the EA greater than it does PCF. This suggests that foam filling could be particularly useful in increasing EA in a short crush distance, whilst the PCF could be managed and kept within limits by other methods such as notches or grooves. Unfortunately, none of these studies gave values regarding the MCF, therefore it is not possible to gain knowledge of the CFE of these rails.

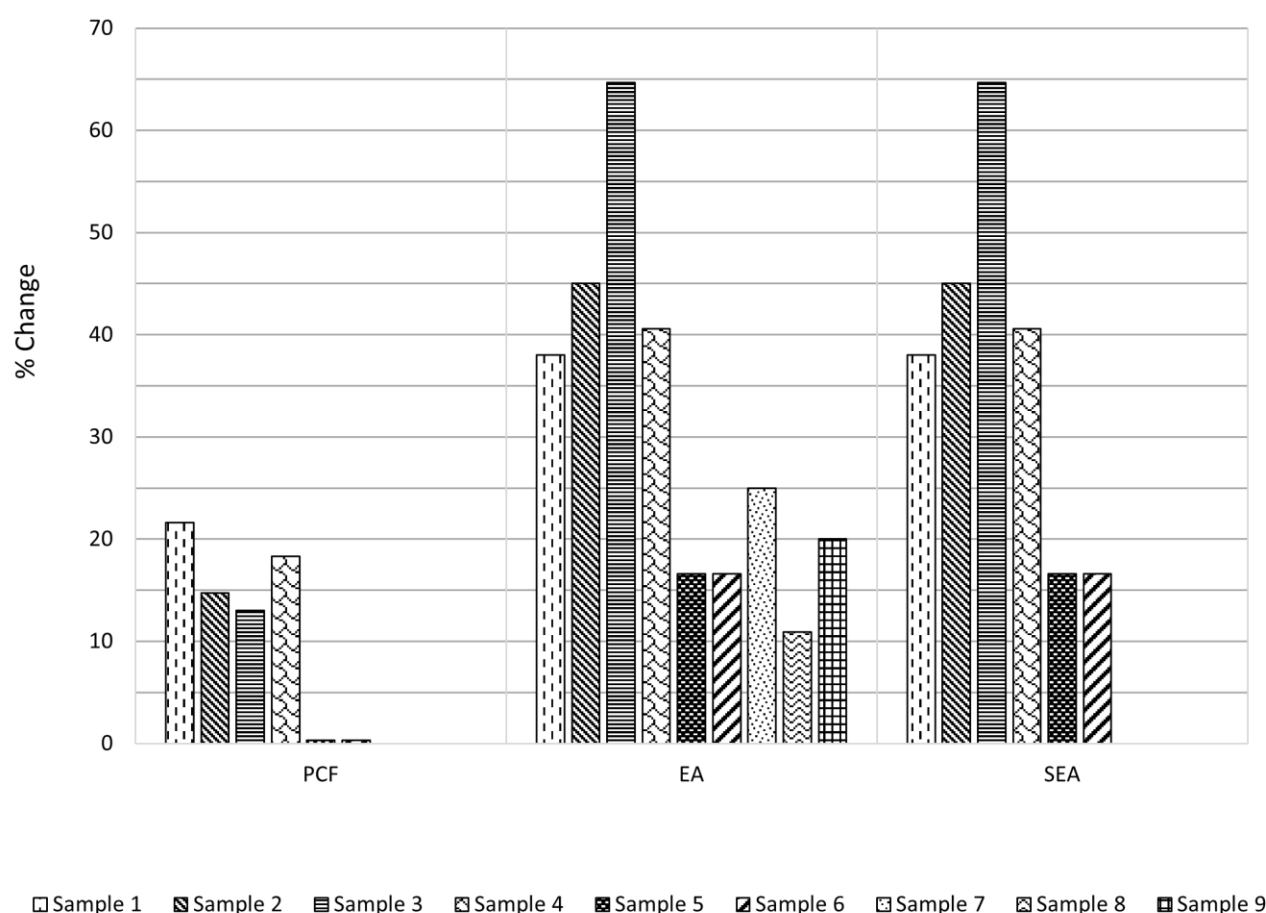


Figure 9. Foam Filling Performance Summary

A study by An et al. utilized LFGT tubes with foam filling to compare the performance difference against a UT counterpart for axial crush and lateral bending. Inopportunately, this study did not analyse the effects between a foam filling to a hollow section, nor did it ascertain an optimal foam density. However, it does show that the LFGT tube does not always exceed the performance (in relation to the peak force obtained) of a UT counterpart, especially for a lateral bending condition (Sun et al. 2017c). However, much of the data obtained could be due to the influence of the foam filling rather than the exterior wall, thus a more in-depth study is required to identify the efficacy of foam filling.

This is accomplished by Gao et al. as the authors considered different cross-sectional geometries with varying impact angles for both hollow and foam filled specimens. It is worth noting that the foam material used in this

study consisted of an isotropic uniform material model generated by Deshpande and Fleck in the commercially available software, LS-DYNA. It is evident in Figure 10 that the foam filling does not always improve the performance of the member under crushing, especially at larger angles. A specific case that shows this is the SEA obtained by the foam-filled tubes at 20° and 30°. It appears from Figure 10 that the performance is less than that of the hollow counterpart for all geometries. It can also be noticed that the foam-filling has varying amounts of efficiency in respect to PCF at all angles.

This item has been removed due to 3rd Party Copyright. The unabridged version of the thesis can be found in the Lanchester Library, Coventry University.

Figure 10. PCF and SEA comparison of hollow and foam-filled tubes (Gao et al. 2016)

Despite apparent improvements, it is shown by a quasi-static test conducted by Ma et al. that foam structures are highly unpredictable in manufacturing. Often leaving air pockets or an inconsistent porosity that results in highly unpredictable responses (Ma et al. 2015). This unpredictability is not represented by an isotropic foam

model that is often used in analysis, resulting in a large overestimate of performance by computational methods.

Nonetheless, foam filling can effectively increase the SEA of a structure at varying impact velocities (Ahmad Mujahid, Lang, and Ahmad Firdaus 2010). A 15% kenaf (*Hibiscus cannabinus*) foam density composite could increase the EA achieved by approximately 21% at a 30m/s (67.1mph) velocity, however, a severe performance decrease presents itself with densities above 15%. The EA is notably dependent on the foam density and impact velocity. Literatures demonstrate that filling materials such as aluminium foam could be useful for increasing the energy absorbed by a structure. However, it is also evident that the effectiveness is highly dependent on the density, the outer profile, the impacting velocity and Poisson's ratio. The Poisson's ratio is defined as the ratio of strain perpendicular to the strain caused by loading stress of uniaxial loading. Simply put, it describes the ratio of how much a material would expand or contract under compression or tension, a useful metric to consider in crash tubes. Thus, these studies show the significance of utilizing all available space and that an internal structure is desirable, even for small crush lengths. It can be declared that these studies show viable promise for the implementation of foam to the vehicle architectures of the future due to their light-weight design and small packaging requirements. On the other hand, the lack of predictability of foam production and implementation cannot be neglected. Therefore, a cleverly designed internal structure that offers similar benefits to foam (with greater reliability) is more appealing.

Structural & Multi-Tubular

As this method of enhancing the crash structure is relatively new, not many designs could be located for discussion. Albeit the few studies that have been published offer invaluable insight into the latest developments and effectiveness of these new crash structures.

An interesting idea was put forward by Li et al. that based the internal core design on a lotus plant's root. Under conditions of same mass, the lotus root design core offers a significant increase in EA compared to the

hollow counterpart, whilst reducing the PCF substantially. Seven pairs of tubes were analysed in this study, each pair consisted of a hollow and filled tube. The variations between each pair were the wall thicknesses, therefore each pair had a different mass to one-another. The greatest improvements are noticeable with the lowest and highest mass tubes (0.4kg and of 0.7kg respectively); suggesting that the thickness of the walls has a large influence on crash beam behaviour and performance (Li et al. 2018). However, the outer-wall thickness is not specified for these structures for each change of mass. In addition to this, no validation of the mesh has been specified throughout the literature and so comparisons and validity of the study cannot be made against true data.

The obvious advantage of a structural design is the capability to be built for varying and numerous load-cases. In effect, Nia and Chahardoli (2016), Zahran et al. (2018) had accomplished this by implementing numerous internal tubes that exhibit greater stiffness values through the progression of collapse. Multi-Stage Square Tubes (MSSQ) boast an improvement of 59%, 17.8 and 20.7% for SEA, MCF and CFE against the conventional square tube, respectively. Further to this, study of nestled cylindrical tubes provided evidence that a similar CFE could be achieved. In addition to this, if overlap between the tubes is permitted, it reduces the length of collapse whilst providing a slight increase in energy absorbed.

Due to the high crush efficiency, short crush distance and small packaging potential, structurally designed or multi-tabular components offer valuable insight to what could be implemented to quadricycles and pods to effectively protect the occupants and components.

To ascertain the most effective structures and components, numerous simulation methods were adopted throughout literature. It is typical for a design to start as a benchmark that would allow improvements to be made by various methods such as optimization or sensitivity analysis (or even both). It is suggested that for

future vehicle component designs, the most current design methodologies should be adopted, including an appropriate method of optimization.

Few studies have been conducted that analyse the effects of an out-of-position stance during an impact. This will become more relevant with the concepts of future vehicles having capability to rotate the chairs during travel. Further work should be conducted that analyses the effects of an out-of-position stance and a frontal crash pulse impacting the side of a vehicle. This would gain preliminary data on what could be expected in a typical crash scenario of future 'unconventional' vehicle architecture.

In addition, given the statistical data of expected crash scenarios, current research and advancements of crash structures do not cater for the effects of oblique, lateral and multiple velocity impacts. Despite this, crash rails with an internal structure offer the most promising properties to apply to future vehicles. Compared to their hollow counterparts, it is often the case that the filled structures have a greater energy absorption capability, lower PCF and greater CFE (typically between 20-60%). Despite the simulated benefits of other filling techniques such as foam filling, the modelling of this material used within the studies discussed would exhibit better performance than that of real-world. Due to the unforgiving constraints applied to L7e vehicles, this would result in foam not being preferable if similar styles of absorbers are used as with vehicles today. However, unconventional designs would offer the use of foam where the low mass and high energy absorbing capability can be most effective, such as combined with a novel architecture of multi-stage members, designed for the numerous cases of loading.

The crashworthiness design of super-light-weight vehicles and autonomous pods will differ significantly from standard vehicle structures. Functionally graded vehicles structures could potentially fill the safety gap that currently exists. To this end, advanced design methods based on nonlinear numerical optimization techniques, which can solve computationally expensive problems fast and reliably, could be required. Alternatively,

greater examination into the cause and effects of occupant injuries with regard to L7e vehicles could encourage development of harmonised crash structures between vehicle designs and categories, without the requirement of expensive structural designs.

3 Problem Definition

Although many advancements have been made throughout the years to improve road safety, continuous progress must be pursued to achieve Vision Zero by 2050. Advanced driving systems and connected and autonomous technologies show promise of realising this idea, however throughout the interim years whilst this technology is being developed and implemented, an increasing risk to consumers of alternative and light-weight mobility has begun to surface. For that reason, section 3.1 identifies and summaries the concerns of occupant safety that require research. The information provided by section 3.1 forms the objectives and scope of conducted research.

3.1 Current Situation

In view of the increasing divide between the weights of passenger vehicles, alongside the adoption of electric drivetrain, examination of likely and high-risk road traffic incidents is essential to achieve Vision Zero. Especially for occupants of Heavy-Quadricycles (L7e) and microcars that adopt the 'car like' designs for the consumer market as the designs of these vehicles often possess a short distance between the occupant compartment and the exterior surface. The risk of injury to the occupants of smaller vehicles are significantly greater than larger vehicles, mostly owing to the reduced distance to employ a sufficient crash structure that efficiently engages the impacting vehicle's crash-structure (Fujimura 2015, Davies et al. 2016a). Further to this, unconventional seating appears to be desirable for future vehicles, as shown by autonomous and 'pod' vehicle concepts (IDEO n.d.). The alterations to occupant positioning increase the risk of severe injuries due to the change of occupant kinematics (Bastien, Blundell, and Neal-Sturgess 2017, Gierczycka, Watson, and Cronin 2015). Restraint and internal protective systems are designed for particular crash pulses, thus the protective systems (such as airbags) could induce injuries or offer little protection should the occupant be out of position (Gaylor, Junge, and Abanteriba 2017, Jeong et al. 2017). For alternate seating arrangements of future vehicles, the effectiveness of the crash-structure is of vital importance to protect the occupant and maintain compartmental integrity.

The technological advancements collectively known as Collision Mitigation Systems (CMS) and Advanced Driving Assistance Systems (ADAS) are constantly being improved and implemented to new vehicles for improved safety (NHTSA n.d.). These technologies, twinned with other systems, provide the hope of fully autonomous vehicles being deployed on public roads within the years of 2025-2030 (Singapore Government 2017; Bjoern 2014; Brownlee 2014; Czarnecki 2017; Grayling 2018). CMS and ADAS have already shown their effectiveness in avoiding vehicular collisions and reducing impact severity (Mikusova 2017, Favaro et al. 2017). Unfortunately, CMS often struggles to prevent many lateral impacts occurring at junctions, this is reflected by the accident statistics of an autonomous vehicle trial in California (Svensson et al. 2014, Favaro et al. 2017). This study revealed that 80% of all reported accidents were on suburban and city roads (48% and 32% respectively), 89% of which occurred at a junction, as illustrated in Figure 11.

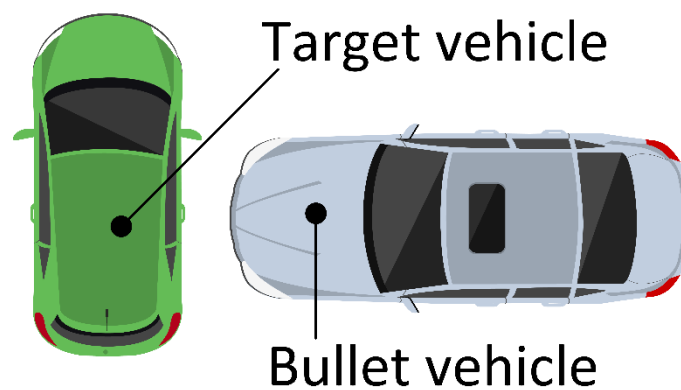


Figure 11. Accident at Junction.

Obstruction to the 'vision' of detecting equipment (sensors and cameras) and lack of manoeuvrability to perform evasive driving are the likely sources of the high percentage of reported accidents being located at junctions. In addition, there is a reduced time to process data and respond accordingly at a junction when compared to other road networks such as motorways (Harald et al. 2016, Dixit, Chand, and Nair 2016, Lee, Kim, and Kim 2019). Unfortunately, the potential to reduce occupant injury is relatively low on motorways in comparison to city streets, this provides prominence of improved vehicle safety in an urban environment (European Commission 2021a).

Due to the observed inefficacy of ADAS functionality at a junction or heavily obscured area, most of the vehicle's crash performance must be provided by passive safety structures. In this regard, lateral impacts pose a significant risk to the occupant due to the restricted space for effective crash structures, even more so if the bullet vehicle's size and mass are much larger than the target vehicle (Zeng, Wen, and Huang 2016, Baker et al. 2008, Harrison et al. 2020). The differences between L7e and M₁ vehicle architecture presents prominent safety concerns to the occupants of L7e vehicles and microcars, owing to the inherent crash incompatibility between these vehicle types. The risk is further enhanced to occupants of L7e as there is lack of legislative documents applied to this category which relates to occupant safety and crashworthiness performance (carhs 2021). In contrast, legislative requirements are enforced to M₁ passenger vehicles. Inopportunately, the safety requirements imposed are focused on self-performance and do not consider vehicles of markedly different construction. As discussed previously in section 2.3.1, deformable barriers have been introduced into regulatory tests to provide a better representation of current vehicle fleet stiffness. In terms of stiffness, the AE-MDB provides a good likeness to M₁ category vehicles of today. Therefore, the AE-MDB is a suitable representative for the bullet vehicle in a lateral impact scenario. However, SUV kerb-weight can be approximately 2.5 tonnes, over 5-times that of the maximum permissible mass of L7e vehicles, which would mean the MDB would require specific scaling should it be built to represent specific vehicle types (Mercedes-Benz 2020: 19). The data recorded by crashworthiness assessment methods, namely the occupant metrics, can be applied to an estimation of injury severity probability to a body region. This is useful for assessing performance towards achieving 'Vision Zero', but it is not a necessary for identifying occupant metric improvements and relationships. Another method for predicting overall injury risk of an occupant is the change of velocity, commonly referred to as delta-v. This injury predictor provides a good estimate to the overall risk to occupant injuries by using statistical data. The delta-v is described in chapter 3.2, followed by the research hypothesis (3.3) and research scope (3.4).

3.2 Change of Velocity

The change of velocity of a vehicle is governed by Newton's law of conservation of momentum. Thus, the change of velocity (delta-V) is dictated by the vehicle masses, impact speeds and impact angle. The simplified relationship is formulated in Equation 3.

$$\Delta V = \frac{m_1}{m_1 + m_2} \sqrt{V_1^2 + V_2^2 - 2V_1V_2 \cos \phi}$$

Equation 3. Delta-V Simplified

Where ΔV is the change of velocity of the vehicle, m_1 and m_2 are the masses of the bullet and target vehicle respectively, with V_1 and V_2 being their impact velocities, whilst ϕ denotes the angle between the central axis of the vehicles in their travel direction. Other factors such as stiffness, brake application, vehicle rotation, restitution and impact location can alter the delta-v calculation (Jurewicz et al. 2016). However, through accident analysis and predictive statistical modelling, the delta-v has been proven to provide a decent estimate to the absolute risk to driver injury. Whilst the influence of mass ratio is present in predictive modelling it does not cater for individual injury metrics of a driver nor the vehicle size and shape (Tolouei, Maher, and Titheridge 2013).

Therefore, to calculate and identify injury relationship with vehicle mass-ratio, the variables presented in the calculation of delta-v must be limited. Such that the impact location, impact velocity, impact angle and structure stiffness are maintained.

3.3 Hypothesis

A relationship between occupant injury metrics and vehicle mass-ratios can be determined to provide an ideal vehicular mass-ratio between bullet and target vehicle, allowing for objective light-weighting procedures targeting occupant safety and bodily regions thereof. Improvements to crash efficiency can be made by identification of critical structural regions for defined impact scenarios, providing better inter-category compatibility.

3.4 Aim and Scope

Due to the large differences in vehicle mass and crash structures between M_1 and L7e vehicles, the research aims to explore methods of maximising the crash compatibility of an Ultra-light-weight vehicle by method of maximising passive crush-structure efficiency. An overview of the aims and objectives are provided in Figure 12, the left most box contains the overall aim whilst the objectives are listed from 2-4 as how this is accomplished. Correspondingly, the direction of right to left is the 'why' these objectives must be completed to complete the aim.



Figure 12. Research Overview

The scope of the project is focused toward light-weight vehicles, in particular L7e. Goods carrying vehicles and straddle-seated positions are not accounted for due to future concept designs and market projection of L-category vehicles, as highlighted throughout section 2.2. Similarly, only speeds and locale of the intended operational environment of L7e vehicles will be considered. The urban environment provides greater potential to reduce occupant injury severity whilst maintaining consumer expectations of the vehicle. Therefore, if a road traffic incident were to occur, it is likely that an L7e vehicle will be involved in a road traffic incident with

an M₁ vehicle as approximately 92% of vehicles currently registered in Europe and the UK are categorised as small or larger M₁ vehicles, 35% of which are SUVs (ICCT 2019: 15). Due to implementation of AEB, rear-end crashes are less likely to occur and possess less risk. As evidence has shown that intersections provide difficulties for the advanced driving assistance systems to respond accordingly, a lateral impact into the L7e vehicle will be investigated. The L7e will not be considered as the bullet vehicle for occupant injury assessments since there is a greater risk of severe injuries (40%) whilst acting as the recipient of a driver-side lateral impact within urban speed limits (Jurewicz et al. 2016).

4 Mass Relationship Exploration

The first stage of improving inter-category vehicle crashworthiness is to examine the direct effects of vehicle mass-ratio upon the occupant. Occupant injury risk, in relation to vehicle mass, has been predicted by numerous statistical approaches (utilising reported accident data) but is subject to error in the data recorded at the incident as well as vehicle parameters. Solely using predictive measures such as Delta-v as an approach to identify vehicle mass-ratio relationship to occupant injuries does not suffice because a close examination and assessment of component properties and interactions throughout time is required. To appropriately explore the effects of vehicle mass-ratio on specific occupant injury metrics, influencing factors other than vehicle mass must be controlled or limited, namely:

1. Impactor width, height, and effective area
2. Impact location and angle
3. Stiffness of bullet and target vehicle structure
4. Closing Velocity and Pre-crash braking
5. Occupant positioning and stance

To provide a basis for comparison, the methodology followed enabled repeatability and represented the predominant vehicle fleet in a real-world accident scenario. The information obtained should be taken directly from the occupant sensors to provide accurate injury metrics for each criterion, enabling direct comparison between occupant injury data with various vehicle mass-ratios. Considering the various aspects to occupant injury influences, the requirements of the injury to vehicle-mass-ratio examination are listed as:

- i. Representative of the identified Road Traffic Incident (RTI) and the modern vehicle fleet.
- ii. Consistent and representative occupant positioning.
- iii. Reliable and consistent data extraction and experiment procedures.

- iv. Management of Bullet and Target vehicle parameters (stiffness, height, angle, velocity, effective area, mass).

Each requirement listed can be fulfilled using a Finite Element Model (FEM). Therefore, the Oasys Suite is utilised for pre-processing, processing, and post-processing data. The software suite is comprised of PRIMER v17.0 for pre-processing and model creation, LS-DYNA r11.0 for explicit calculation, T/HIS v17.0 for post-processing and data consolidation, and D3PLOT v17.0 for visual output (Oasys n.d.). Each requirement listed (i.-iv.) is achieved by further defining the scenario (4.1) and constructing the conclusions into a FEM for numerical analysis (4.2). Following this, the results of the experiments are presented in section 4.3 and the discussion and conclusion of mass-ratio effects on occupant injuries are presented in section 4.4.

4.1 Scenario Configuration

To fulfil the requirement 'i. Representative of the identified Road Traffic Incident (RTI) and the modern vehicle fleet' multiple stages are applied to construct the scenario. Firstly, the scenario defined in chapter 3 is applied as the configuration framework. Specifically, a lateral impact by an M_1 vehicle into the driver-side of a lightweight (L7e) vehicle at a maximum speed of 30mph (48km/h) with no preventative manoeuvres conducted by either party. The diverse junction types provide many impact possibilities through diverging, merging, or crossing traffic. Conflicts that would be categorised as lateral impacts are present in Figure 13, lateral collisions can occur in all traffic scenarios at a junction.

This item has been removed due to 3rd Party Copyright. The unabridged version of the thesis can be found in the Lanchester Library, Coventry University.

Figure 13. Conflict points at junctions and roundabouts (European Commission 2021b)

Driving behaviours and vehicle positioning are dependent on the road infrastructure, incidents at the junctions shown in Figure 13 would often result in an oblique impact between the bullet and target vehicle. However, “hook and turn” junctions, driver familiarity with the road or vehicle turning arc provide too much variation to accurately predict a consistent angle of impact. Therefore, a compromise is made by selecting a lateral collision of 90° to represent the RTI. The 90° lateral RTI scenario provides a suitable representation to the modern vehicle fleet as the effectiveness of ADAS technology is reduced, furthermore, it provides the benefit of allowing parallels to Euro NCAP testing and assessment procedures to be made (Favaro et al. 2017). Although the mass range of the M_1 passenger vehicles varies greatly. The popular vehicle types operating in an urban environment provide the range of masses to be considered in the experiment. Mostly, the vehicles range from examples such as the 820kg Smart Fortwo to the 2,295kg Mercedes-Benz GLE Coupé (Harald et al. 2016, Diaz et al. 2021, Mock 2019, Sanchez n.d., Mercedes-Benz AG 2019). As the L7e category has a maximum permissible mass of 450kg, the mass ratio between bullet and target vehicles ranges between 1.8:1 and 5.2:1 (Edwards et al. 2014, Regulation (EU) No 168/2013 2013).

4.2 Finite Element Construction

The scenario described in 4.1 is translated into PRIMER v17 to enable explicit analysis. Details and justification for model utilised in the experiment are provided in 4.2.1, injury data and calculation methods are presented in 4.2.2 and the process of conducting the experiments is discussed in 4.2.3.

4.2.1 Experiment Model Selection

Microcab

The target vehicle used throughout the experiments was Coventry University’s Microcab which has a mass of 931.4kg, approximately twice that allowed by the L7e category classifications. Despite the vehicle mass exceeding the allowance, the architecture and dimensions are representative of an L7e vehicle (Edwards et al. 2014). The complete Microcab’s specifications are provided in Table 18, with a comparison to the Ligier IXO Heavy-Quadricycle.

Table 18. Microcab and Ligier IXO Specifications (Ligier Group 2013: 9)

Attribute	Unit	Microcab	Ligier IXO
Vehicle Length	mm	3390	3148
Vehicle Width	mm	1545	1524
Vehicle Height	mm	1650	1497
Seat Height	mm	666	600
Wheelbase	mm	2154	-
Wheeltrack (front/rear)	mm	1361/1401	-
Finite Element Mass	kg	935.9	-
Vertical CofG (from floor)	mm	525	-
Transverse CofG (from mid-point of width)	mm	21	-
Longitudinal CofG (from mid-point of length)	mm	41	-

Despite the mass of the Microcab exceeding the limit of the L7e category it still meets the criteria in all other aspects. Due to the similar vehicle architecture to other microcars and Heavy-Quadricycles, namely the seating position and occupant position within the cabin, it is expected that similar occupant responses will be achieved to those that participated in the Euro NCAP Heavy-Quadricycle tests (Euro NCAP 2014d, 2014c, 2014e, 2014f, 2016d, 2016e). Table 18 shows that the difference in seat height between the Microcab and Ligier IXO is just 66mm, thus showing that the higher seating position and novel seat-design of the Microcab is still representative of vehicles within the L7e category. Figure 14 shows the dimensions of the Microcab with the driver-side door omitted.

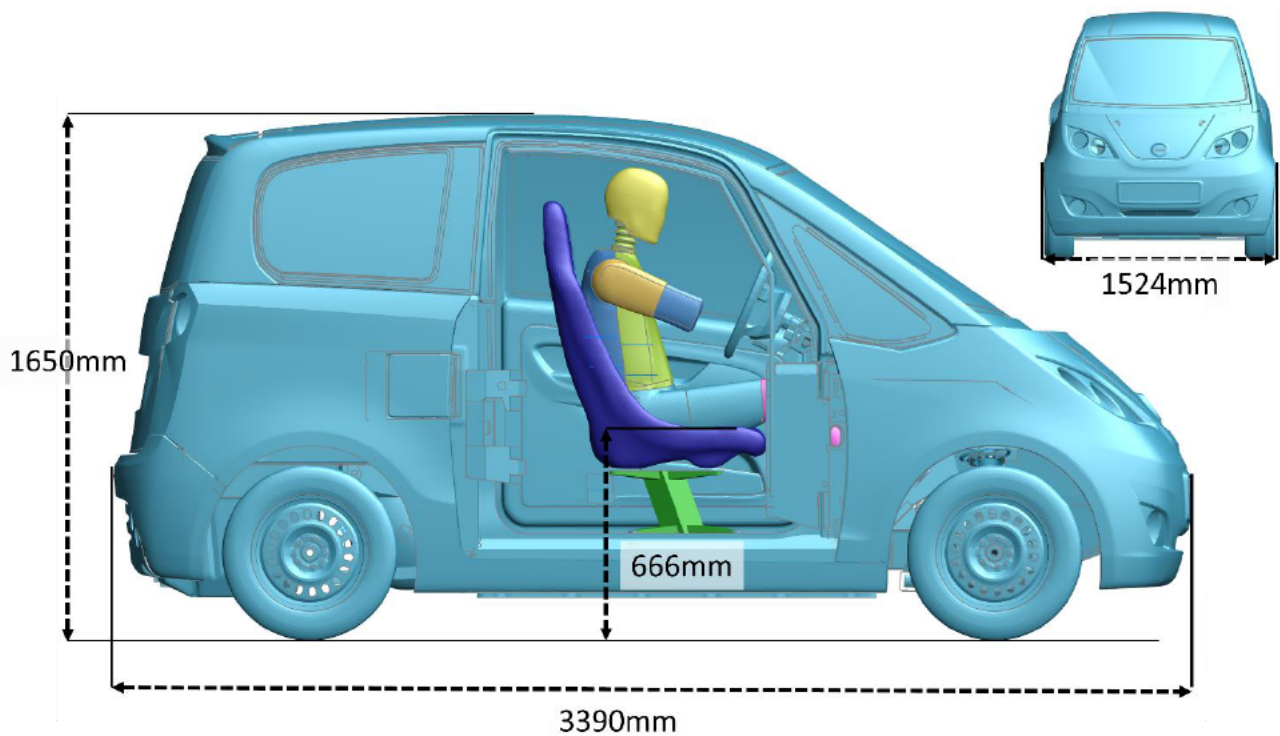


Figure 14. Microcab Dimensions (Door Omitted)

The Microcab consists of 553 parts and the element data is provided in Table 19.

Table 19. Microcab Element Data

Section Type	Section Quantity	Element Type	Element Quantity	ELFORM(s)	Hourglass Type	Number of Nodes
Shell	513	Shell	1561073	2, 16	1, 8	4
Discrete	6	Discrete	10	-	-	2
Beam	20	Beam	466	-	-	2
Solid	14	Solid	38342	1, 2	-	8

All shell elements had 5-integration points throughout the thickness, the Belytschko-Tsay warping stiffness flag was applied across the model with re-computation of the shell normal at every cycle. The solid elements predominantly utilise the 'ARUP_Adhesive' material model and properties (Feucht, Haufe, and Pietsch 2007).

To ascertain the correct mass-ratio for the vehicle-to-vehicle collision, either the mass of the Mircocab must be reduced or the mass of the bullet vehicle must be increased accordingly. However, achieving large differences in vehicle mass ratio whilst maintaining constant stiffness for fair comparison is a complex task. Simply changing the gauge thickness, materials or geometry of a vehicle between experiments would distort the resulting analysis due to the change in structural stiffness. This was overcome by employing the Version 2, Revision 3.9.250912 AE-MDB created for FE analysis (Krebs and Bhalsod 2012).

AE-MDB

The barrier face (Figure 15) maintains the stiffness representation of a modern vehicle fleet whilst permitting mass changes to the affixed carriage. The Finite Element AE-MDB has been validated by method of rigid wall impact and force-displacement corridors (Krebs and Bhalsod 2012).

This item has been removed due to 3rd Party Copyright. The unabridged version of the thesis can be found in the Lanchester Library, Coventry University.

Figure 15. AE-MDB Barrier Dimensions (Ellway 2013, Krebs and Bhalsod 2012)

As the carriage (Figure 16) is formed of 8-node rigid elements and is symmetrical across the width (by mass), changes to the carriage do not cause undesirable effects to the dynamic performance throughout between experiments. The alterations were completed by a total mass procedure within Primer (Option1_Intertia on Part Card).

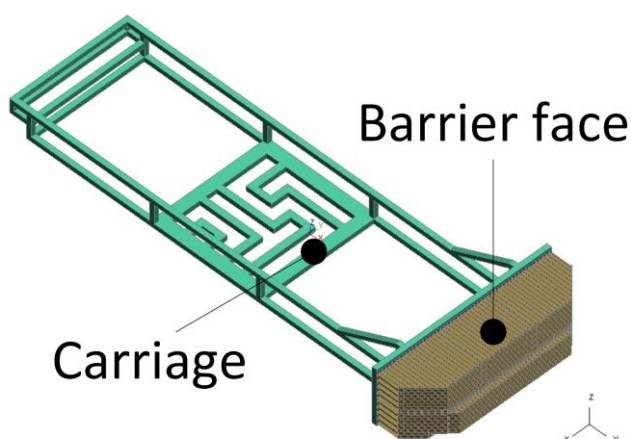


Figure 16. Carriage and Barrier face of AE-MDB

The position of the centre of gravity and the moment of inertia of the impacting vehicle could induce different vehicle responses, such as rollover. To minimise the difference in vehicle response due to inertial properties between experiments, the AE-MDB must adhere to the following Euro NCAP criteria:

- i. The centre of gravity shall be situated in the longitudinal median vertical plane within 10mm,
- ii. The centre of gravity shall be $1000 \pm 30\text{mm}$ behind the front axle,
- iii. The centre of gravity shall be $500 \pm 30\text{mm}$ above the ground and
- iv. The distance between the front face of the impactor and the centre of gravity of the barrier shall be $2000 \pm 30\text{mm}$ (Ellway 2013: 1).

Table 20 shows the mass of the minimum and maximum mass because of the mass changing procedure of the AE-MDB and the respective locations of the barrier's CofG in global co-ordinates.

Table 20. AE-MDB Centre Of Gravity with Mass Changes (Global Coordinates)

Complete MDB Mass (kg)	Centre of Gravity (mm)		
	Transverse (x-direction)	Longitudinal (y-direction)	Vertical (z-direction)
934.17	-40.16	-1083.1	346.44
4670.9	-40.16	-1063.0	360.49

No changes are presented to the transverse coordinates between the two barrier masses. However, in comparison to the lowest barrier mass, the CofG of the barrier with the maximum mass moves towards the barrier face and upwards from the floor by 20.1mm and 14.05mm respectively. The changes to the CofG in each axis are deemed acceptable as they satisfy the criteria defined by Euro NCAP AE-MDB specifications as presented in i.-iv (Ellway 2013: 1). Figure 17 presents a visual representation of the transverse, longitudinal and vertical CofG of the minimum and maximum mass barriers, using the reference locations and planes as described in the list of criteria *i.-iv* above. The black text signifies the CofG location of the greatest mass barrier (4671kg) and the red text signifies the CofG of the lowest mass barrier (934kg).

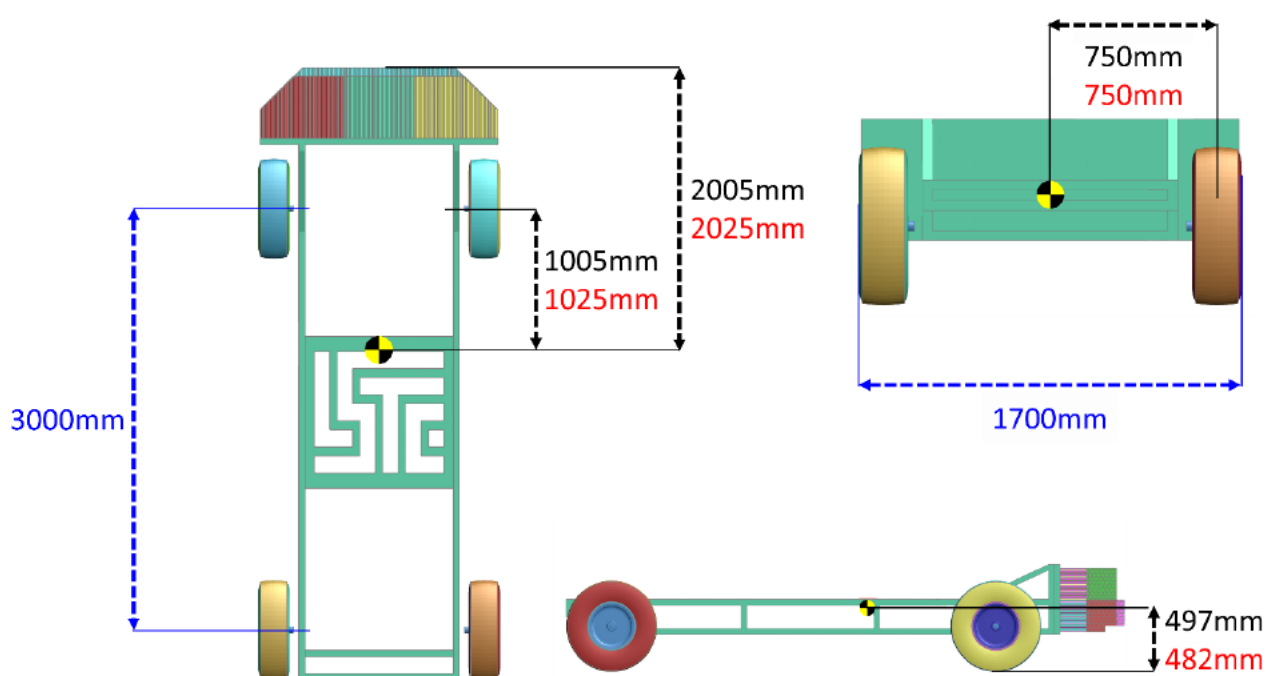


Figure 17. Adapted Mass AE-MDB Centre of Gravity

WorldSID 50th

The occupant model was selected to coincide with approved dummies that are already in use or are to be implemented in future years. Therefore, the WorldSID50th occupant model has been selected as it has been utilised by UN Regulations and Euro NCAP side testing protocols (Euro NCAP 2020b, UN Addendum 134 - Regulation No. 135 2015). DYNAMore developed the WorldSID50th and has been validated with material, component and sled tests; at the time of the research the model iteration available was v1.1 (Gromer, Stahlschmidt, and D'Souza 2009: 31). The occupant was positioned to correctly sit within the style of the driver seat. This was accomplished by assigning positions of the dummy assembly and performing a Seatsquash procedure within PRIMER. A 3-point-seatbelt was fitted across the occupant model, utilising 1D seatbelt elements for the ends of each segment and 2D Shell Elements (*MAT_34 Fabric) for all segments that contact the occupant model as shown in Figure 18.

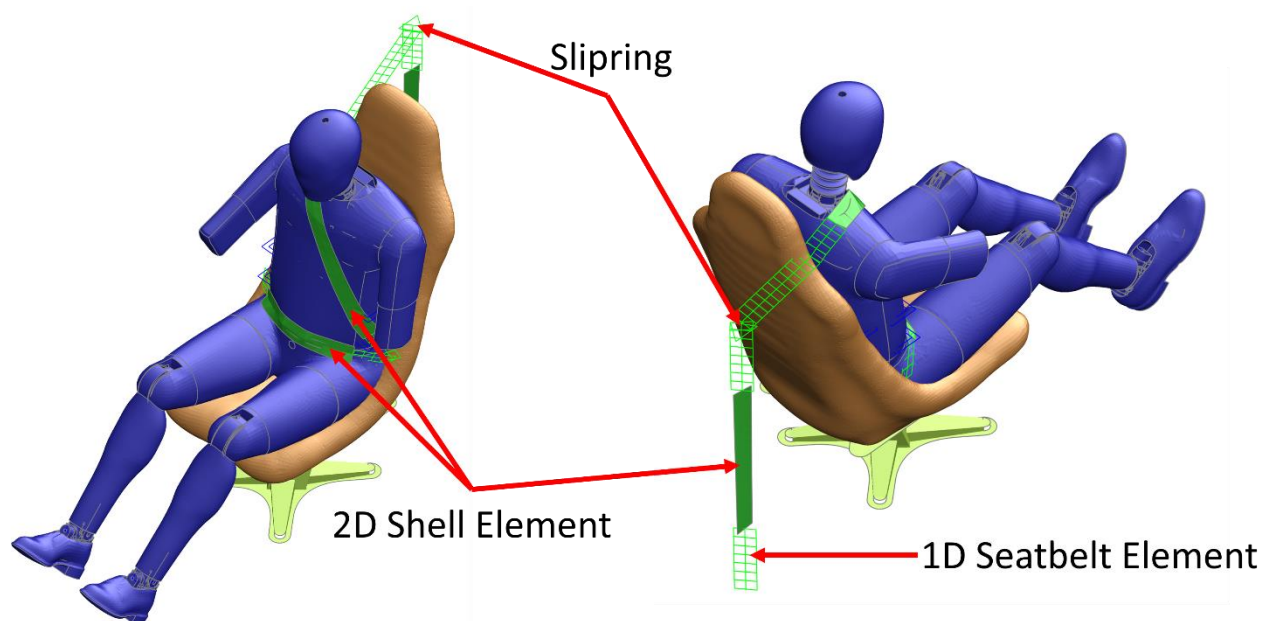


Figure 18. Restraint System Fitted onto the Occupant Model

The door-side arm was rotated to accommodate for the driver having one hand on the steering-wheel whilst driving across or on an intersection (Viano, Patel, and Ciccone 1989).

4.2.2 Injury data Extraction and Calculation

The injuries that could be recorded by the WSID are limited to the calibrated extraction fields as described by the LSTC documentation concerning the first FE WSID model (LSTC 2018). The extraction fields within the WSID record varying data, accelerations are obtained in the head, upper spine (T4), lower spine (T12) and the pelvis whilst the relative displacement of the ribs are extracted at the shoulder, thorax region (3 ribs) and abdominal region (2 ribs). The accelerometers are labelled in Figure 19.

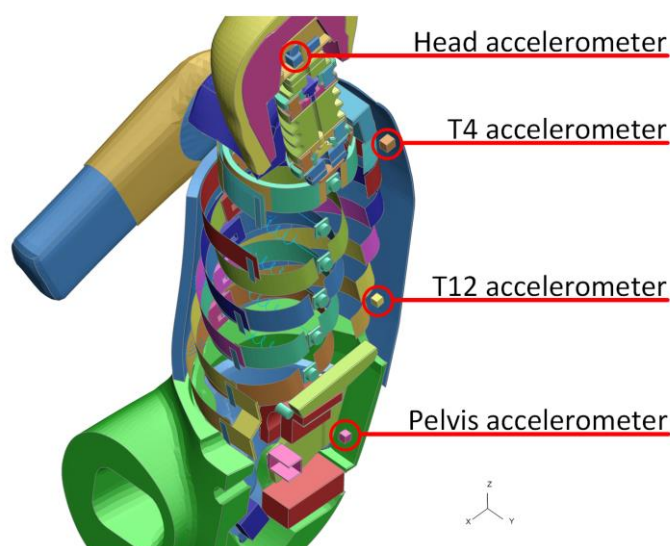


Figure 19. ISO View WSID Data Extraction Locations

The data that can be extracted by the accelerometers and springs allow calculations of the Head Injury Criterion (HIC), Thoracic Trauma Index (TTI), Viscous Criterion (VC) and the respective rib velocities and accelerations. It has also been shown by S.Kuppa (2004) that the Average Spinal Acceleration (ASA) often shows strong correlation in predicting injuries in the thorax. However, as this study does not look at the specifics of injury, rather the relationship of the 'mass factor', the ASA is redundant because the TTI can be calculated separately. Unfortunately, version 1.1 of the Finite Element model does not have a reliable manner to extract further data, such as the pubic symphysis force, however the kinematic response of the occupant will be examined to identify observable differences in the crash behaviour.

The data is extracted by the sensors and springs for application of the corresponding Channel Frequency Class (CFC) filter in T/HIS, as specified in the documentation for the WSID50th occupant model (Humanetics Innovative Solutions 2018). The filter frequency of sensor data is presented in Table 21. The velocity and acceleration of the ribs were filtered by CFC180 after differentiation of the compression.

Table 21. Occupant Injury Criteria Filter Specification (LSTC 2018)

Extraction Sensor(s)	Head	T4	T12	Pelvis	Rib Compression	Rib Velocity	Rib Acceleration
Measurement Unit	m/s ²	m/s ²	m/s ²	m/s ²	m	m/s	m/s ²
CFC Filter	1000	180	180	180	600	180	180

Injury Criteria Calculations

The extraction fields provide the raw data required to calculate the injury metrics. Compression and acceleration values require no further calculation but are used in the calculation of the HIC₁₅, VC and TTI. The formulae of which are presented in Equation 4, Equation 5 and Equation 6 respectively.

Head Injury Criterion

Equation 4 presents the HIC₁₅ formula, the subscript '15' signifies a maximum time interval equal to 15 milliseconds.

$$HIC_{15} = \left[\frac{1}{t_2 - t_1} \int_{t_1}^{t_2} a \, (dt) \right]^{2.5} (t_2 - t_1)$$

Equation 4. Head Injury Criterion 15ms (HIC₁₅)

Within Equation 4, 'a' is the resultant head acceleration, ' $t_2 - t_1$ ' is less than or equal to 15ms and is selected in attempt to maximise HIC. Primarily, a large HIC is caused by the head contacting the vehicle (commonly the B-Pillar) in a lateral impact. It should be noted that the head of the WSID did not collide with the vehicle in any of the subsequent simulations unless specifically mentioned. This was judged to be due to the seating position of the occupant within the target vehicle.

Viscous Criterion

The VC is a rate dependant injury criterion typically used for soft tissue damage. It is usually used to complement the crushing injury mechanism. The calculation for the VC varies between occupant models, the specific calculation for the World-SID is shown in Equation 5.

$$VC(t)_i = V(t)_i * \frac{D(t)_i}{0.17}$$

Equation 5. Viscous Criterion for World-SID

Within Equation 5, $V(t)_i$ is the velocity of rib_i at time t and $D(t)_i$ is the displacement of rib_i at time t .

Thoracic Trauma Index

Another thoracic injury metric is the TTI, which is defined as a measure of the potential for a chest injury. For purely comparative studies, the age term can be omitted from Equation 6, however true values of TTI require the addition of the age function. The TTI only uses the maximum acceleration of one of the three thoracic ribs present in the WSID50th as it excludes the shoulder and abdominal region. As this study is identifying a trend with vehicle mass ratios utilising the WSID, the age term is set to unity and the mass term set to 75; thus, providing a factor of 1 (75/75 in Equation 6).

$$TTI = 1.4 \cdot age + \frac{(rib_{max} + T12_{max})}{2} \cdot \frac{Mass}{75}$$

Equation 6. Thoracic Trauma Index

Within Equation 6: rib_{max} is the maximum peak acceleration of either the (4th rib-1.3)-2.02 or the maximum peak acceleration of the 8th rib, age is equal to the occupant age in years, and $Mass$ is the dummy mass in kg.

4.2.3 Experiment Procedure

The AE-MDB was assigned an initial velocity of 13.33m/s (48km/h) in the global Y-axis target vehicle is stationary and perpendicular to the bullet vehicle's travel direction. An Automatic Surface to Surface contact was used between the Microcab tyres and the ground. A Static and Dynamic friction coefficient of 0.8 and 0.7 was selected to characterise the forces present on a good quality asphalt road (MFES 2007). The dynamic

friction coefficient for the bullet vehicle's wheels to ground remained at 0.15 as the vehicle is in motion and no rotational velocity to the wheels of the carriage were applied (Krebs and Bhalsod 2012).

Model Alignment

Figure 20 shows that the occupant's H-Point aligns with the central vertical plane of the AE-MDB in alignment with consumer program and regulation protocols. However, the AE-MDB was lowered by 130mm to engage with the target vehicle sill. The vehicle sill is the most protective structure that is common across numerous vehicle designs, thus making the comparison less dependent on vehicle specific architecture. Lowering the AE-MDB preserves a common vehicle's ground clearance, which can range from 225 to 365mm (Reichert et al. 2018: 4). Figure 21 shows AE-MDB in its lowered position and alignment to the sill of the Microcab.

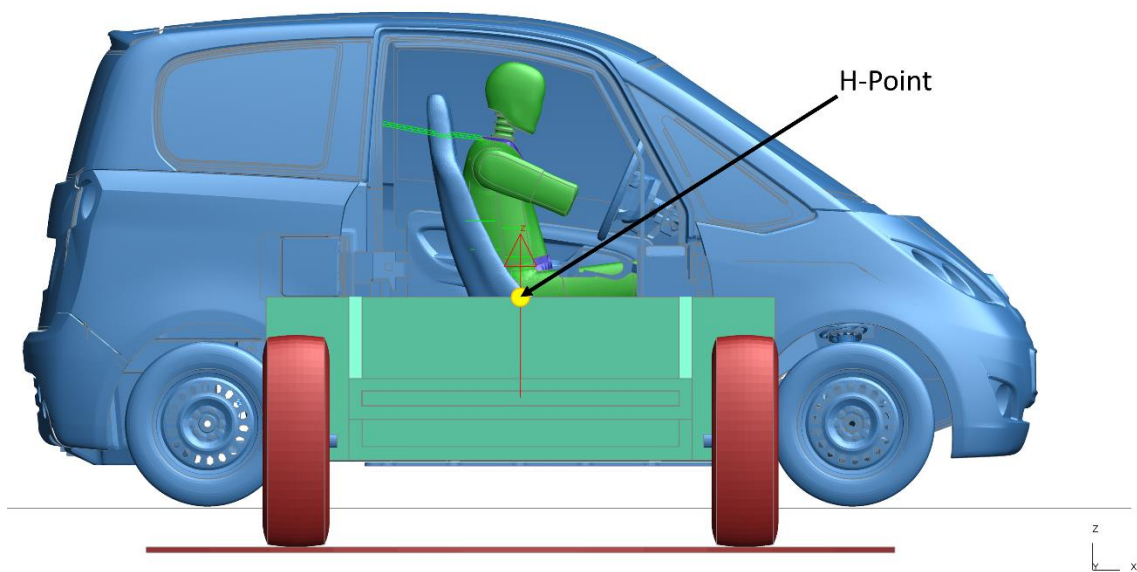


Figure 20. AE-MDB and H-point Alignment in the Vertical Plane

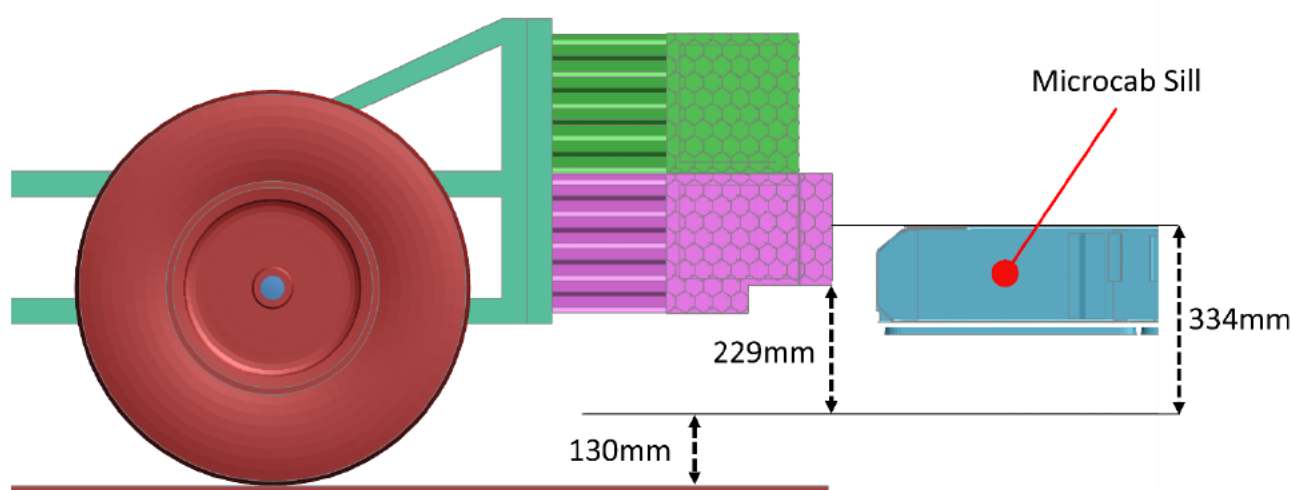


Figure 21. MDB Interaction with Microcab Sill

Mass scaling and Observation Methods

The final change to the AE-MDB was the overall mass reduction of the model. This was required as the AE-MDB and the Microcab have an initial mass of 1,302kg and 934kg respectively. To obtain a baseline model for comparison the mass of the AE-MDB was reduced to equal the Microcab. Thereby providing the baseline model a 1:1 mass ratio between bullet and target vehicle. Note that the 1:1 ratio (named R1.0) represents a base scenario that essentially presents a two-car-collision of the L7e category. The mass of the MDB carriage was incrementally increased by a factor of 0.5 of the Microcab mass (467.2kg) up to achieve the desired 5:1 bullet to target vehicle mass ratio.

Table 22. AE-MDB Mass Ratio to Target vehicle

Mass ratio	1:1	3:2	2:1	5:2	3:1	7:2	4:1	9:2	5:1
Experiment name	R1.0	R1.5	R2.0	R2.5	R3.0	R3.5	R4.0	R4.5	R5.0
AE-MDB mass (kg)	934.4	1401.3	1868.3	2335.4	2802.5	3269.2	3736.7	4203.8	4670.9

The injury scores obtained by the increase in mass of each mass ratio experiment will be compared against the results of the baseline R1.0 experiment. The injury metrics are calculated as detailed in section 4.2.2 and

then compared as a percentage change to the baseline results. D3plot is used to examine interactions of the vehicle to the occupant that may differ between experiments.

Stability and Performance Check

The performance of the vehicle has been deemed stable. Figure 22 presents the R1.0 energy curve throughout the crash duration. Energy curves of R1.5 to R5.0 are provided in Appendix II.

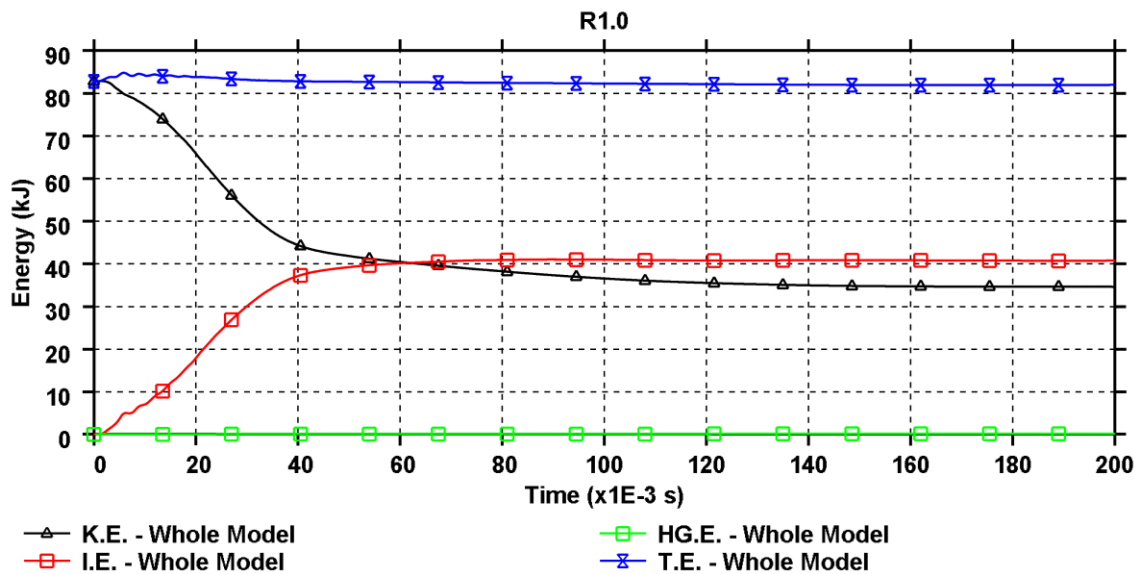


Figure 22. R1.0 Energy Curve

The slight increase at the beginning of the internal energy was identified as the airbag deployment within the bullet vehicle's barrier face, the remaining energy curves act as expected for a lateral impact scenario. Small increases are noticed within the sliding/interface energy, although this is to be expected as the ground was modelled as new asphalt by use of two rigid patches. The maximum energy ratio of all models (total energy/initial energy) increases from 1 to 1.001.

4.3 Mass Relationship Exploration Results

All injury predictions have been ascertained by the sensors and calculation methods described in 4.2.2. The baseline (R1.0) has been normalised for each criterion, the other mass-ratios (R1.5-R5.0) are compared to the baseline results. The approach of comparing each experiment to the baseline enables discovery of possible

relationships between each increment of mass-ratio to the respective percentage change to occupant injuries. By this method, correlations could be drawn for criteria that utilise just one metric, such as the lower spine (T12) acceleration, or metrics that utilise multiple criterion, such as the calculation of the TTI. The graphical representation of R1.0 is signified graphically by the horizontal red line within the column charts. The time-history plots are also presented if a particular trend is observed between experiments, although the time differences have not been normalised. Should injury trends between occupant injuries and vehicle mass-ratios be determined, it could allow for very fast computation and risk assessment in the development of new or existing vehicle models for occupant safety.

Each occupant criterion is examined separately by region and data obtained. Section 4.3.1 examines the Head acceleration and the HIC₁₅. Following this, section 4.3.2 investigates the accelerations witnessed at the upper spine, lower spine and the pelvis. Section 4.3.3 examines the rib compression, velocity and acceleration as well as the VC and TTI. Concluding remarks of the study and the results obtained throughout 4.3 are compiled and discussed in detail within section 4.4.

4.3.1 Occupant Head Acceleration

The results of maximum acceleration and the corresponding HIC values are provided in Table 23 with the 'R1.0' column acting as the baseline.

Table 23. Head Acceleration

Experiment	R1.0	R1.5	R2.0	R2.5	R3.0	R3.5	R4.0	R4.5	R5.0
Maximum Head Acceleration (G_y)	42.16	54.14	70.33	74.77	82.21	87.16	91.21	85.58	89.25
Maximum Head Acceleration (N)	1.00	1.28	1.67	1.77	1.95	2.07	2.16	2.03	2.12
t_m (s)	0.082	0.078	0.089	0.090	0.090	0.090	0.090	0.090	0.119
HIC₁₅, Normalised	1.00	2.06	3.07	3.88	4.39	4.75	4.96	5.00	5.28
HIC₁₅, Actual	114	235	350	442	501	541	565	570	602
(HIC) t₁ (s)	0.0708	0.0689	0.0690	0.0682	0.0678	0.0677	0.0674	0.0674	0.0673
(HIC) t₂ (s)	0.0858	0.0838	0.0839	0.0832	0.0827	0.0827	0.0824	0.0824	0.0823

Except for R5.0, all the times of the instantaneous maximum acceleration (t_m) are all within 5% of the baseline. In experiments R2.0 to R4.5 the head had made contact against the windowpane at 0.09 seconds, it had little effect on the head trajectory but spikes in acceleration are noticed in the time history plot of Figure 24. R5.0 had a secondary impact upon the windowsill at 0.119 seconds due to the vehicle trim raising upwards as the occupant torso rotated about the pelvis towards the impact location. Despite this, the largest HIC₁₅ in each experiment was achieved within very similar timeframes. The HIC₁₅ results obtained in the experiments presented here were unaltered by contact with the occupant cabin, a reliable comparison can still be made without notable influence by the vehicle structure.

In comparison to R1.0, the HIC_{15} increased by 206% at R1.5 and 307% at R2.0, providing a near linear progression with each mass-ratio interval. Following R2.0, the increase in HIC_{15} between each experiment is reduced with the increase in mass-ratio, correspondingly this appears to lead towards a convergence of approximately $515 \pm 5\%$, suggesting a maximum HIC_{15} would be achieved at a 5:1 mass-ratio or greater. This is only applicable if external factors such as the head impacting the vehicle and differing seatbelt operations do not influence the results. Alike HIC_{15} , the maximum head acceleration values revealed a trend of increasing magnitude that follows a polynomial of 2nd order up to approximately 206% of R1.0, which then begins to plateau with a perceptible maximum near 210%. The relationship between the maximum head acceleration and the HIC_{15} with increasing mass-ratio is illustrated in Figure 23.

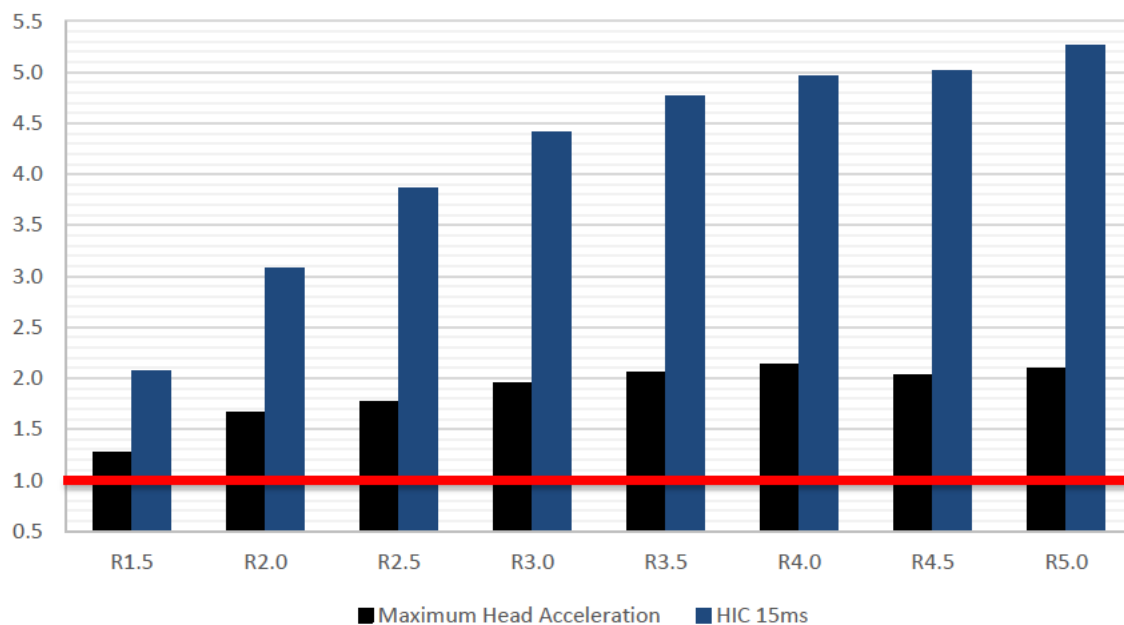


Figure 23. HIC_{15} and Maximum Head Acceleration

Another factor to consider with vehicle-to-vehicle collisions are the time at which the peak accelerations of the occupant occur. Identification of particular accelerations could help design safety systems to engage at specific times within the initial impact phase. For this reason, the time-history plot of the occupant's head accelerometer is provided in Figure 24.

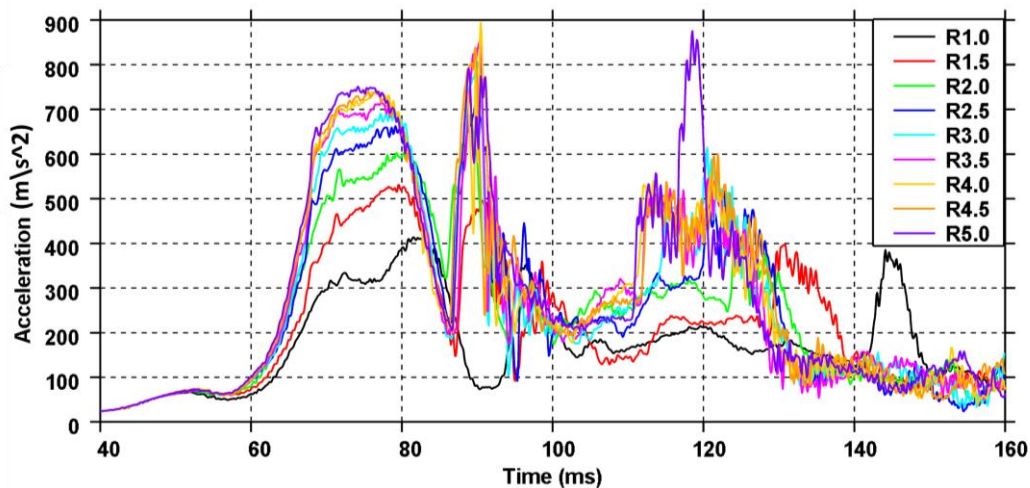


Figure 24. Time-History Head Acceleration vs Time

Figure 24 shows that experiments R2.0 to R5.0 have multiple large spikes in the acceleration recorded, but these peaks are caused by head to vehicle contact, so to keep the results comparable and applicable to all vehicle geometries, only the initial peak will be discussed. The time history plot in Figure 24 shows that the initial acceleration occurs slightly earlier (as well as the peak acceleration) with each increase to mass-ratio, the total time change between R1.0 to R5.0 constitutes to 5.9 milliseconds, additionally the acceleration becomes more 'rounded' with each increase to the mass-ratio. Thus, the noticeable small bump at 78ms of R1.0 becomes less prominent with each ratio increase. This signifies that the occupant experiences an earlier, larger and more sustained acceleration with increasing vehicle mass-ratios.

4.3.2 Occupant Body Acceleration

The World-SID has spinal accelerometers located at the 4th and 12th vertebrae and an accelerometer within the pelvis. The 4th and 12th vertebrae are located towards the top of the spine, just below the neck and towards the bottom of the spine within the thorax region. The pelvis accelerometer is located within the centre of the WSID50th between the hips (Figure 19). The data extracted by each accelerometer was conducted in the global axis and only considered the lateral acceleration.

Table 24 summarises the normalised maximum accelerations of the various accelerometers, the maximum increase for the T4, T12 and pelvis are 20.3%, 65.9% and 72.2% respectively, with the maximum T4 and pelvis being evident in R4.5 and the T12 in R4.0. The data without normalisation is provided in Appendix II.

The mass-ratio influence upon the T12 and pelvic accelerations are greater than T4, however this is expected as the vertical distance from the impact location of the bullet vehicle to the T4 accelerometer is far greater than that of the other two. The vertical distances of the T4, T12 and pelvic accelerometers to the top of the MDB-barrier face are 475mm, 227mm and 57mm respectively.

Table 24. Normalised Maximum Body Accelerations in Lateral Direction

Sensor Location	R1.0	R1.5	R2.0	R2.5	R3.0	R3.5	R4.0	R4.5	R5.0
T4	1	1.021	1.199	1.042	1.072	1.169	1.138	1.203	1.197
T12	1	1.234	1.496	1.455	1.520	1.524	1.659	1.626	1.611
Pelvis	1	1.241	1.490	1.547	1.515	1.553	1.652	1.722	1.712

For ease, each sensor located in the torso has been divided into their respective regions for discussion and graphical presentation.

T4 Acceleration

The T4 is located under the base of the neck of the occupant model. The data recorded is provided in Table 25 in the normalised format and in units of gravity.

Table 25. Lateral T4 Acceleration Data

Experiment	R1.0	R1.5	R2.0	R2.5	R3.0	R3.5	R4.0	R4.5	R5.0
Acceleration Normalized	1.00	1.02	1.20	1.04	1.07	1.17	1.14	1.20	1.20
Acceleration _(g)	45.01	45.93	53.95	46.88	48.24	52.61	51.21	54.15	53.87

The normalised acceleration is graphically represented in Figure 25. A large increase of approximately 7g is found within R2.0 to the neighbouring mass-ratios. However, as there is no discernible difference in the occupant response that could justify the R2.0 'divergence', it could be argued that the data recorded in R2.0 is an outlier to the general trend. Yet, the experiment results fluctuations make a clear T4-acceleration to vehicle mass-ratio relationship harder to identify. The impact location, seat design of the Microcab and the

vehicle rotational response are likely causes of data fluctuations for this criterion. Despite this, a loose trend appears towards a limit of recorded accelerations, this occurs by experiment R4.5 with an approximate 20% increase to that of R1.0.

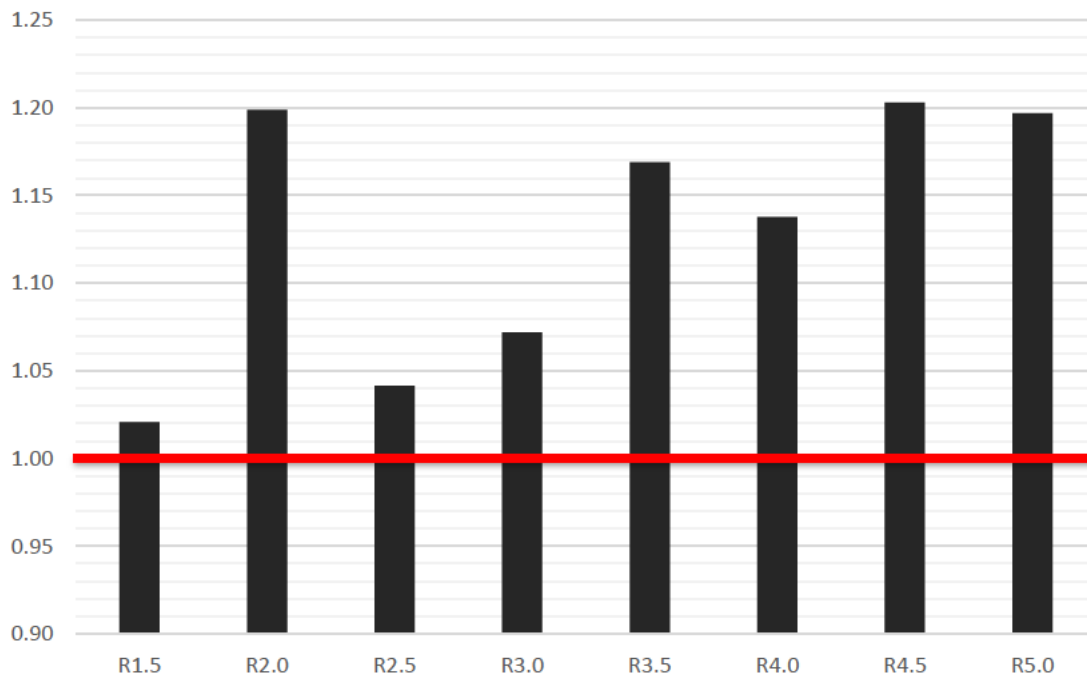


Figure 25. T4 lateral Acceleration

The trend is noticeable in Figure 25 in which a clear rise is presented from experiments R2.5 to R4.5 before a possible plateau, similar to the Head Acceleration.

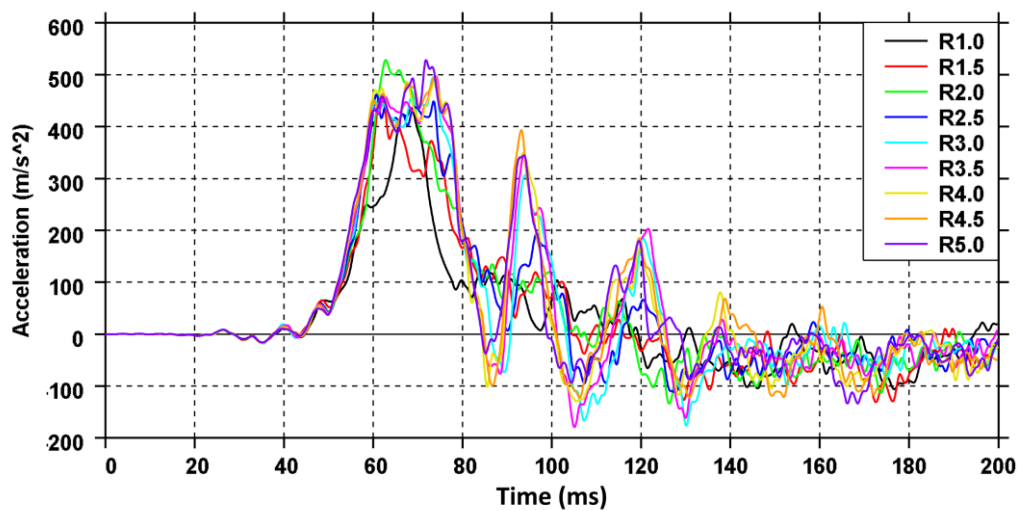


Figure 26. Time-History T4 Lateral Acceleration

Figure 26 provides a time history plot of the lateral acceleration recorded in the T4. The time of the initial acceleration peak had changed with varying mass-ratios, furthermore, the majority of the experiments possess a 'twin-peaked' shape apart from R1.0 and R2.0. Additionally, mass ratios below R3.5 have their maximum peaks closer to 0.06s, a 0.01s difference to R1.0, but mass-ratios greater than 3.5 have their peak 0.005s later than R1.0. Nevertheless, this first 'twin-peak' still occurs at 0.06s similarly to other mass-ratio experiments, showing that the occupant has an extended exposure to the level of acceleration that is achieved by mass-ratios less than R3.5 before a secondary increase in acceleration. This greater and extended level of acceleration would induce more force upon the occupant and signify a greater risk of withstanding injuries to which the WSID50th v1.1 cannot record. Furthermore, experiments R3.0 and above have a large spike at 0.095s which could signify a substantial bounce-back, whereas all other experiments reduce similarly to R1.0 and fluctuate with the same trend.

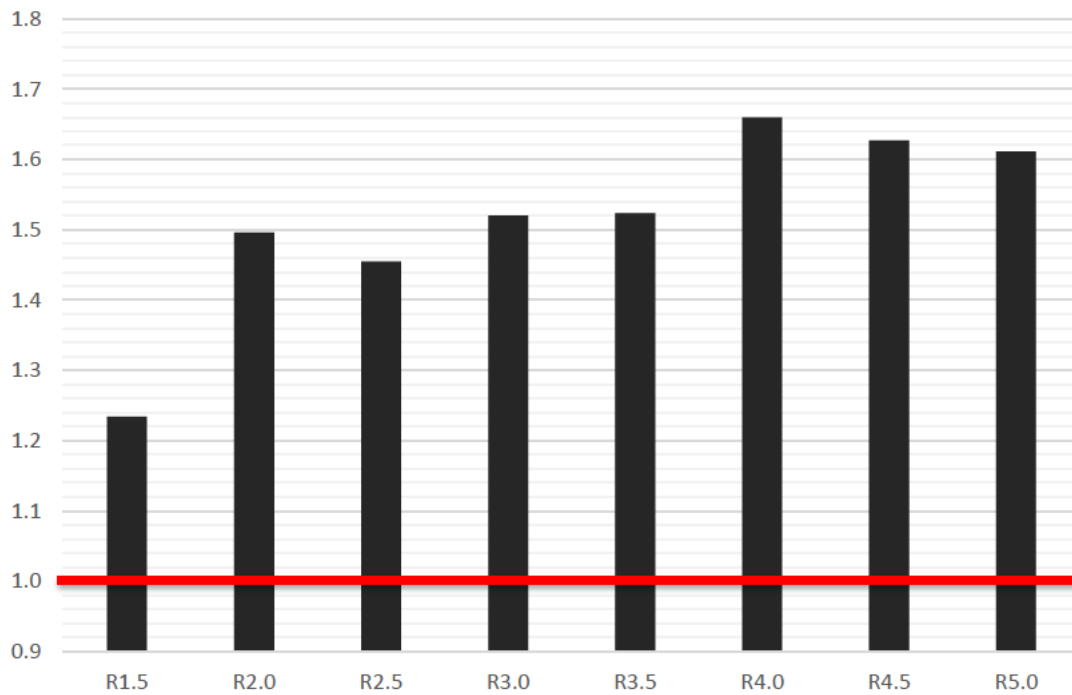
T12 Acceleration

Figure 27. T12 lateral Acceleration

The T12 results in Figure 27 show a large increase within the first mass-ratios (R1.5 and R2.0) of 23% and 50%. Between R2.0 and R3.5 the increase remains around $50\pm 5\%$ relative to R1.0 until another jump is witnessed with R4.0 that leads to a 66% increase in comparison to R1.0 in which R4.0 to R5.0 appear to converge around 1.63 times that of R1.0, as shown in Table 26.

Table 26. T12 Lateral Acceleration Data

Experiment	R1.0	R1.5	R2.0	R2.5	R3.0	R3.5	R4.0	R4.5	R5.0
Acceleration <small>Normalized</small>	1.00	1.23	1.50	1.45	1.52	1.52	1.66	1.63	1.61
Acceleration _(g)	31.18	38.48	46.65	45.36	47.40	47.50	51.75	50.72	50.25

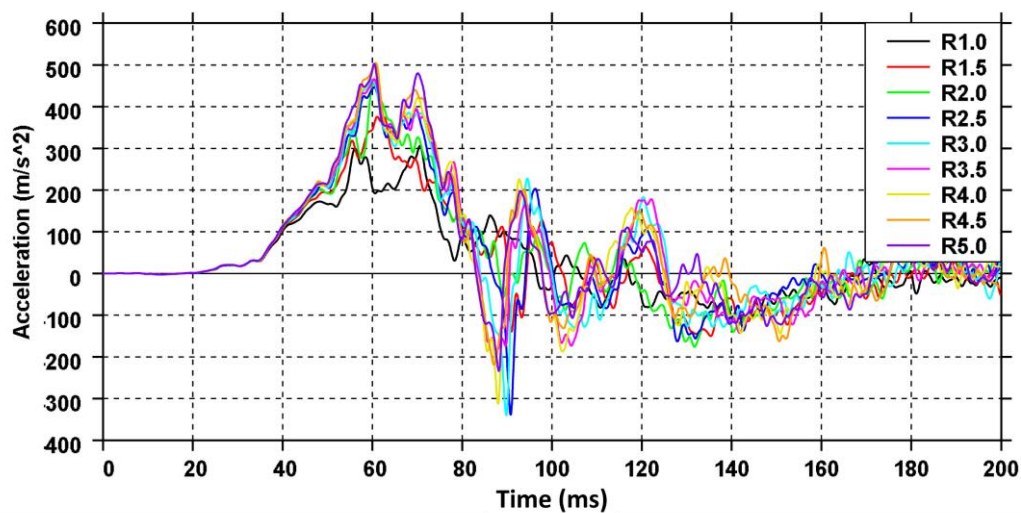


Figure 28. Time-History T12 Lateral Acceleration

Examination of the time-history plot (Figure 28) shows that the general trend of acceleration between all experiments are similar. However, a noticeable difference lies within the initial two peaks, R1.5 has a single peak at approximately 0.06s but does not have a central dip like the other experiments. After this instance, the rest of R1.5 follows the deceleration pattern of R1.0. The constant deceleration to 130ms is only presented in R1.0, suggesting the occupant experienced a 'shunt' effect in which the lower spine accelerated rapidly due to the initial impact and proceeded to rapidly decelerate after initial contact was made. Contrastingly, alongside an increase to mass-ratio, the trough between the two initial acceleration peaks becomes more abrupt and deeper, whilst still maintaining similar times of peak acceleration between of 0.06s and 0.07s.

Pelvic Acceleration

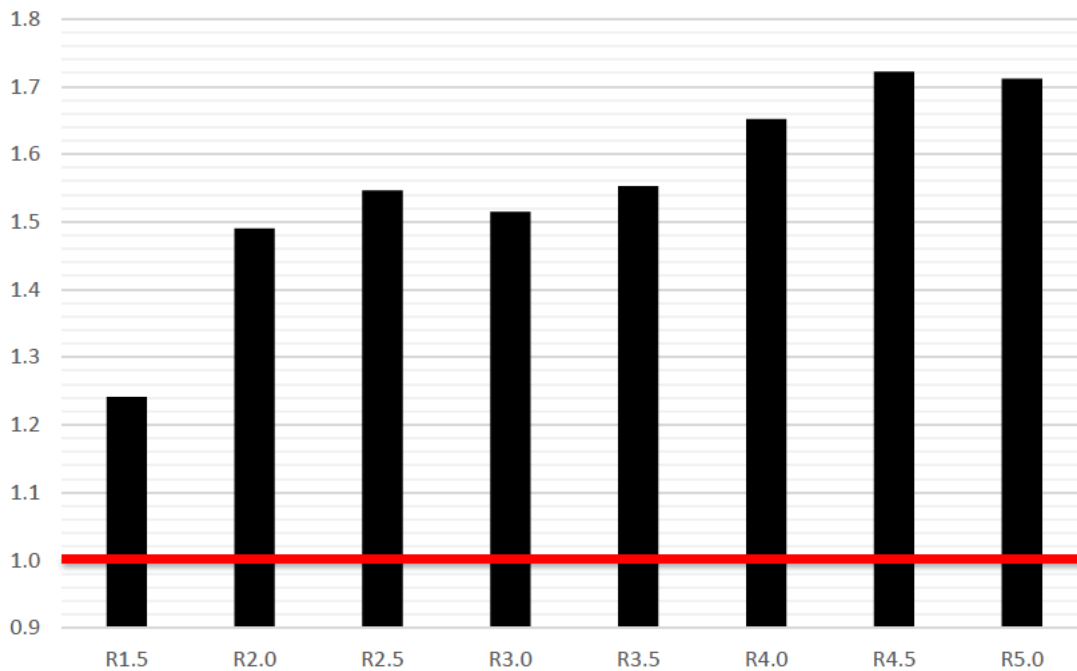


Figure 29. Pelvic lateral Acceleration

Figure 29 and Table 27 show that the pelvic acceleration has a large increase from R1.0 to R1.5 and R2.0. The overall pelvic acceleration continues to slightly increase between experiments after this mass-ratio, averaging 2% increase with each mass increment from R2.0 to R4.0. The mass-ratios of R2.0 to R3.5 remain relatively constant with small fluctuations; a similar pattern is revealed in experiments R4.0 to R5.0 at an approximate 70% increase. The results indicate that the pelvic acceleration begins to plateau by a mass ratio of 4:1. As with the T12, the pelvic acceleration shows that the lower mass-ratio impacts would provide the largest increase to the occupant response, but these are still substantially less than mass-ratios of 2:1 or greater.

Table 27. Pelvic Acceleration Data

Experiment	R1.0	R1.5	R2.0	R2.5	R3.0	R3.5	R4.0	R4.5	R5.0
Acceleration _{Normalized}	1.00	1.24	1.49	1.55	1.51	1.55	1.65	1.72	1.71
Acceleration _(g)	19.58	24.30	29.18	30.28	29.66	30.40	32.35	33.72	33.52

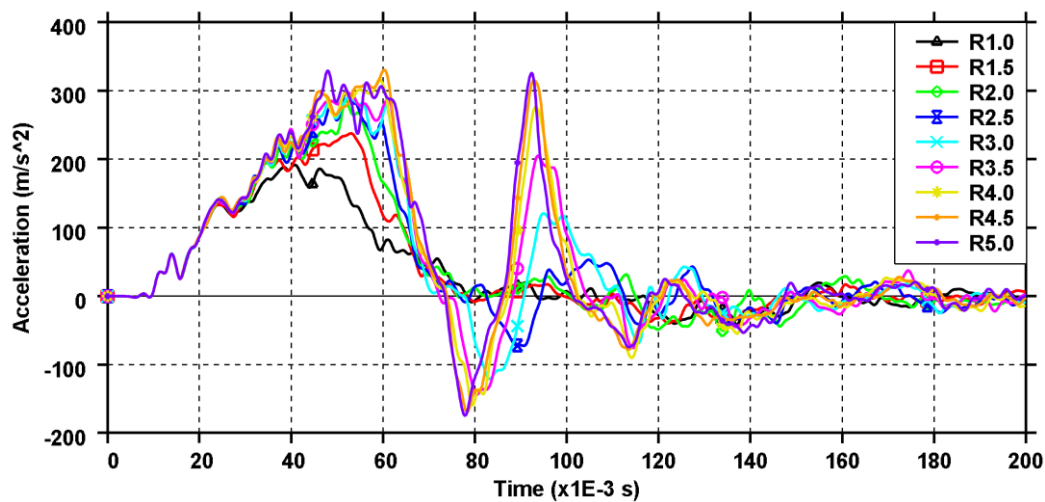


Figure 30. Time-History Pelvic Lateral Acceleration

Figure 30 provides the time-history plot of the lateral acceleration at the pelvis. With each increment of mass-ratio the acceleration is sustained for longer, with each peak arriving slightly later than the previous experiment. Furthermore, pelvic accelerations of R1.5 and R2.0 decrease at a similar rate to R1.0 and then follow the R1.0 curve closely. Larger differences are found with R2.5 as this experiment begins to diverge from the settled acceleration after 0.08s with larger oscillations, the same behaviour is noticeable with R3.0 and larger ratios. With each increase to the mass ratio greater than R2.0, the amplitude of the accelerations increases as well as the time between each peak (positive and negative). Again, a longer sustained acceleration and greater changes to the occupant's speed would induce further injuries that the WSID cannot record, especially if the occupant had already been injured within the initial acceleration phase up to 0.07s.

4.3.3 Thorax Injury Metrics

The thorax injury metrics calculable are limited to the VC and the TTI (Equation 5 and Equation 6 respectively). The rib accelerations are obtained by double differentiation of the rib compression data of the WSID50. The effects of vehicle mass-ratio on the rib deflections and accelerations are reviewed first, followed by the VC and TTI.

Rib Data Recorded

The ribs are separated into three main regions: shoulder, thorax and abdomen. The shoulder consists of one rib, thorax of three and abdomen of two, as shown in Figure 31.

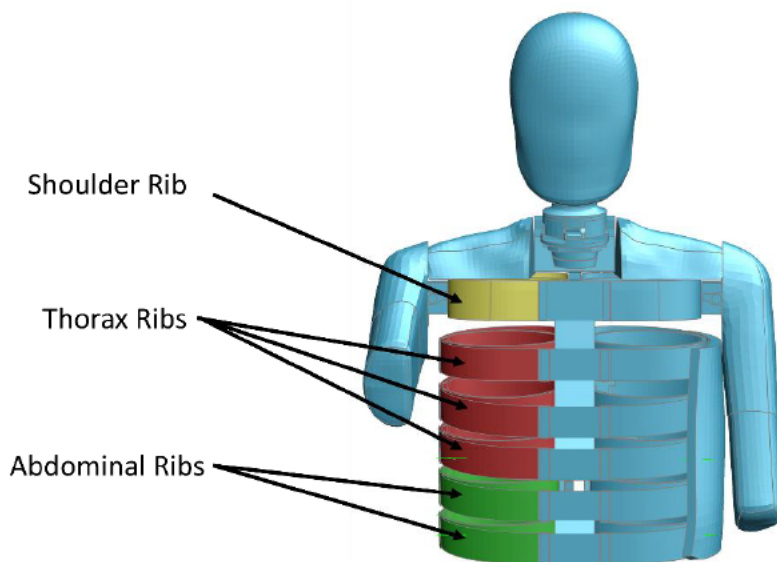


Figure 31. WSID Rib Designation

Table 28 shows the normalised maximum rib accelerations by region of the WSID50. Full data of individual rib compression, rate of compression and the acceleration is available in Appendix II, Table 71.

Table 28. Normalised Maximum Rib Acceleration by Region

WSID50 Rib Region	R1.0	R1.5	R2.0	R2.5	R3.0	R3.5	R4.0	R4.5	R5.0
Shoulder Region	1.00	1.03	1.35	1.31	1.41	1.20	1.48	1.34	1.53
Thorax Region	1.00	1.18	1.17	1.33	1.77	1.38	1.43	1.25	1.66
Abdominal Region	1.00	1.30	1.35	1.96	2.36	2.26	1.67	1.67	2.40

The shoulder region has very little increase from R1.0 to R1.5, R2.0 to R3.0 and between R4.0 and R5.0. A reduction to the previous mass-ratio experiment is noticed with R3.5 and R4.5 though these may be caused by a different occupant response due to the rest of the body rotating upon impact, thus engaging with the vehicle interior differently. Although the results fluctuate for the shoulder, they appear to progress upwards with an average of about 7.5% per incremental increase of mass-ratio. However, the trend could also suggest that groups of mass-ratios have little effect to the acceleration until a critical mass is reached, such that the acceleration increases in segments of complete mass-ratio increase (every two increments of 0.5).

The thorax region also shows a spike in acceleration of 177.1% within the experiment R3.0, a 49g difference to R1.0 to exceed 110g. Although the thoracic rib accelerations oscillate across the experiments, it is noticeable in Figure 32 that the greater mass-ratios provide less increases to R1.0 per increment. The third region, the abdominal region, shows large changes in R2.5, R3.0, R3.5 and R5.0 compared to R1.0. As the other experiments remain aligned with each-other (6% increase from R1.5 to R2.0, 0% change R4.0 to R4.5) it suggests that a 'critical' mass-ratio is present within the R2.5 to R3.5 range for rib acceleration. This would align with the jump in acceleration noticed within the thorax rib of R3.0.

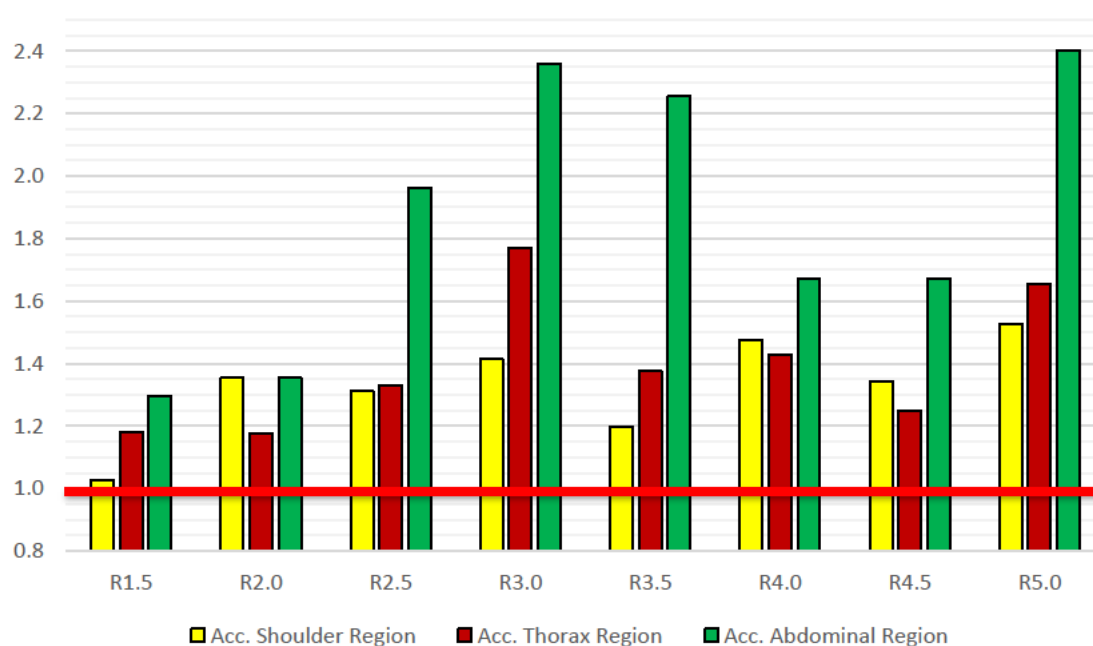


Figure 32. Maximum Rib Acceleration by Region (Normalised)

Figure 32 shows that the acceleration of the shoulder and thorax ribs are relatively predictable, however the abdominal region shows too large a variation to ascertain a clear relationship. Thus, these large acceleration increases may be due to a critical region or greater influenced by the proximity of the impact location of the bullet vehicle. Intriguingly, the rib deflections (Figure 33) show a clear convergence to a maximum (thoracic and abdominal ribs) and a minimum (shoulder rib) with no 'critical' region. Additionally, the thoracic rib has greater change with progressing mass-ratios in comparison to the abdominal region but the abdominal region still follows a similar trend. This is evident in Table 29 in which it is shown that the mass-ratios provided by

experiments R2.0 to R3.0 show an average difference between thoracic and abdominal rib compressions of 1.25%, whereas the difference grows to an average of 4.5% from a 5:2 ratio upwards.

Table 29. Normalised Maximum Rib Compression by Region

WSID50 Rib Region	R1.0	R1.5	R2.0	R2.5	R3.0	R3.5	R4.0	R4.5	R5.0
Shoulder Region	1.00	1.09	1.06	1.07	1.06	1.04	1.02	1.00	0.99
Thorax Region	1.00	1.37	1.51	1.62	1.69	1.74	1.77	1.78	1.80
Abdominal Region	1.00	1.39	1.52	1.62	1.67	1.68	1.73	1.73	1.76

This states that the thoracic region is more influenced by the mass-ratio, especially with greater differences between bullet and target vehicle, than the abdominal region. Despite the proximity of the abdominal region to the impact location. Conversely, the compression of the shoulder rib reduces with the growth of the mass-ratio, this aligns with the previous discussion that the greater mass-ratios begin to localise the effects upon the occupant's ribs.

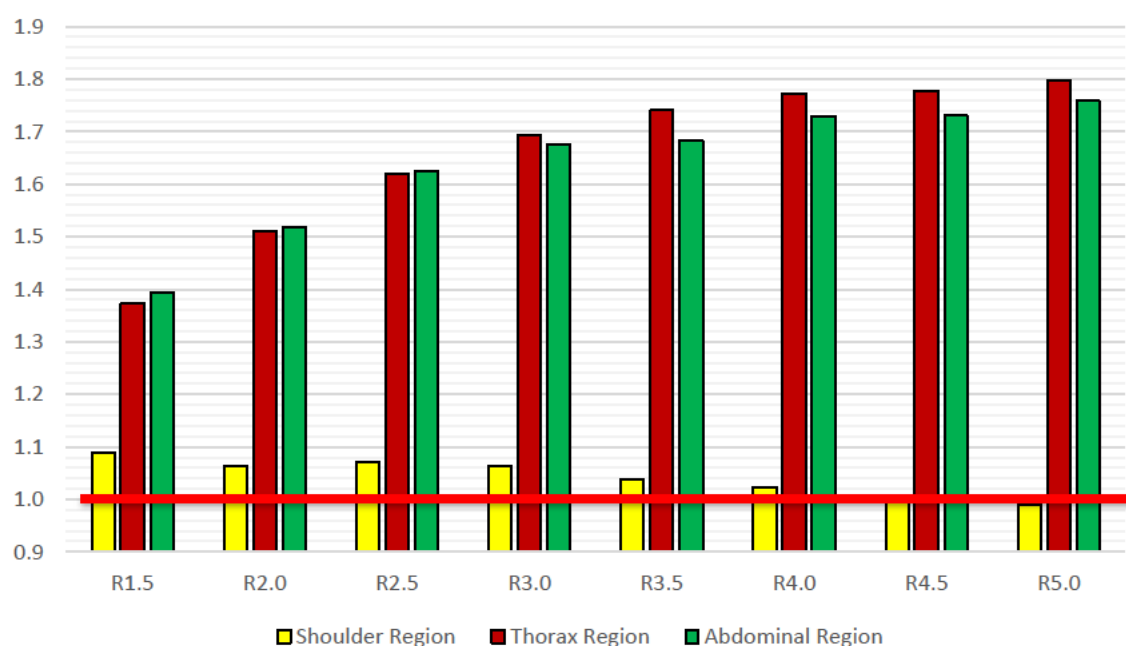


Figure 33. Maximum Rib Compression by Region (Normalised)

Although the compression of the thorax ribs was greater than the abdominal in relation to R1.0, the abdominal ribs had a far greater rate of compression. The rate of compression, or rib velocity, of the abdominal region rapidly grew with each experiment up to a near maximum at R3.0, at which point the growth halted at an

average increase of 233% to the rib velocity of R1.0. The abdominal rib velocity plateauing at R3.0 is not shared by the other ribs. Experiment R3.0 provides the mass-ratio in which the shoulder rib obtains maximum velocity and begins to decrease with greater mass-ratios. Although, there are small fluctuations with the results after the experiment R3.0 which surround a 50% increase. This would insinuate that mass-ratios above 2:1 do not significantly impact the velocity of the shoulder rib. Conversely, the thoracic ribs steadily increase up to experiment R3.0 with smaller percentage growth with each iteration from R1.0. However, the thoracic rib velocity fluctuates around a 71% increase between R2.5 and R4.0, suggesting that the mass-ratio in this range has little effect to the velocity of thoracic ribs. The normalised data of the rib velocity, by region, are presented in Table 30.

Table 30. Normalised Maximum Rib Velocity by Region

WSID50 Rib Region	R1.0	R1.5	R2.0	R2.5	R3.0	R3.5	R4.0	R4.5	R5.0
Shoulder Region	1.00	1.23	1.52	1.54	1.57	1.47	1.49	1.50	1.43
Thorax Region	1.00	1.29	1.50	1.62	1.75	1.67	1.78	1.89	1.85
Abdominal Region	1.00	1.69	1.88	2.26	2.37	2.32	2.27	2.31	2.38

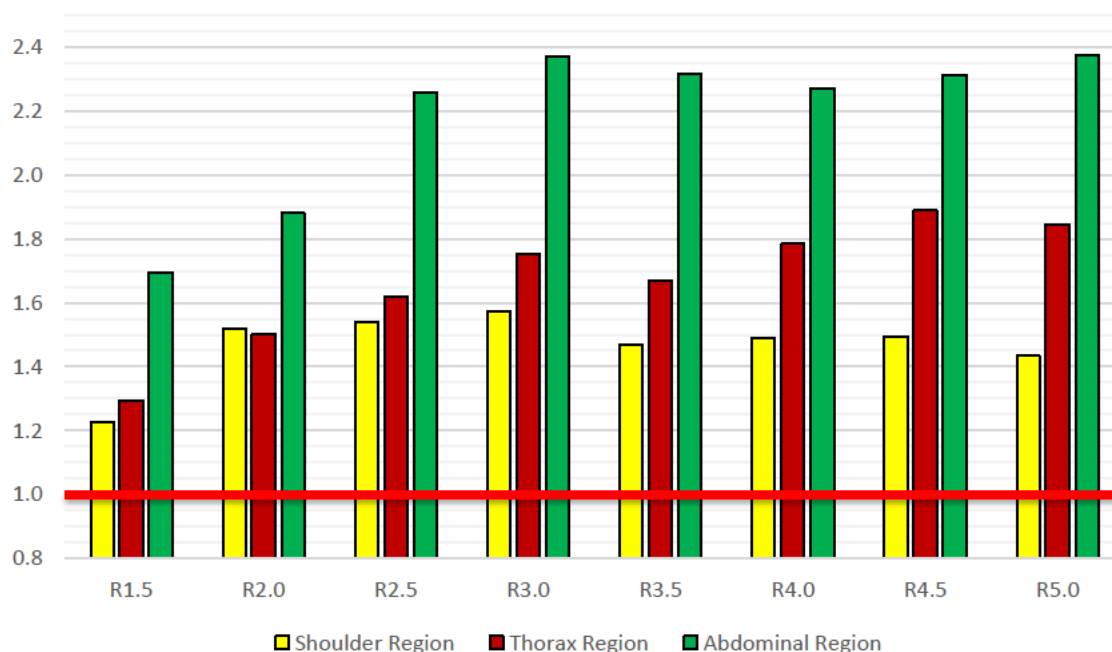


Figure 34. Maximum Rib Velocity by Region (Normalised)

The rib data by region suggests that mass-ratios not exceeding 2:1 provide a larger increase to the metrics of rib compression and velocity for the thoracic and abdominal regions. Following this, the increases to velocity and compression percentage per mass-ratio increase are substantially less, typically within 7%. The shoulder rib exhibits a similar response for velocity, although the compression steadily decreases as the mass-ratio increases. The rib acceleration shows no discernible relationship to mass-ratio as there were heavy fluctuations in the results. This could be caused by the sensitivity and capability of the WSID50 spring sensor or sporadic contact with the interior door panelling throughout the duration of experiments. Despite this, the injury metrics of the occupant model are calculated and less dependent on a single recorded metric, thus providing better insight to mass-ratio relationship with occupant injuries.

Viscous Criterion

The VC is a good indicator of an injury sustained in a lateral impact; this is owed to the calculation employing a rate dependant variable as shown in Equation 5. Normally the VC would be applied to the rib which holds the maximum velocity and displacement as to maximise the injury score, but for this comparison the normalised VC of each rib is provided in Table 31. The calculated values of VC, without standardisation, are available in Appendix II, Table 72. For ease, the shoulder, thorax and abdominal ribs have been categorised into regions in Figure 35 to aid in identification of relationships.

Table 31. Viscous Criterion

WSID Rib	R1.0	R1.5	R2.0	R2.5	R3.0	R3.5	R4.0	R4.5	R5.0
Shoulder Rib	1.00	1.34	1.61	1.65	1.67	1.52	1.53	1.49	1.42
Upper Thorax Rib	1.00	1.40	1.64	1.85	1.89	1.90	1.97	1.99	2.02
Middle Thorax Rib	1.00	1.78	2.27	2.62	2.97	2.91	3.16	3.36	3.32
Lower Thorax Rib	1.00	2.07	2.66	2.95	3.31	3.43	3.67	3.89	4.08
Upper Abdominal Rib	1.00	1.79	2.23	2.60	2.79	3.03	3.12	2.75	2.98
Lower Abdominal Rib	1.00	2.36	2.85	3.67	3.97	3.90	3.93	4.00	4.18

Table 31 shows the normalised data of the viscous criterion of each rib. Accordingly, most of the maximum VC changes are located within R5.0, exhibiting an increase ranging from 41.9% (shoulder) to 417.8% (lower

abdominal). The general trend appears to be that the lower the rib in the occupant, the higher increase of injury within the same mass-ratio experiment, however the upper abdominal rib is consistently lower than the lower thoracic rib across each experiment. Upon examination of the occupant response, the lower increases are due to less contact with the vehicle frame in comparison to the surrounding ribs, a similar reaction is observed with the shoulder region. Nonetheless, the comparison between each mass-ratio is still reliable as the VC will always take the maximum of the results to apply to the calculation, furthermore, having results with little to no contact with the cabin interior shows the expected injury increase per mass-ratio increment without influence by the occupant cabin interior. It should be noted that all L7e vehicle's passive protective structures within the near-side door would influence the VC results specific to that vehicle, although the specific architecture may differ from the target vehicle, the location of the most substantial door intrusion would lead to a similar change to the VC (as presented in Table 31) to the nearest rib.

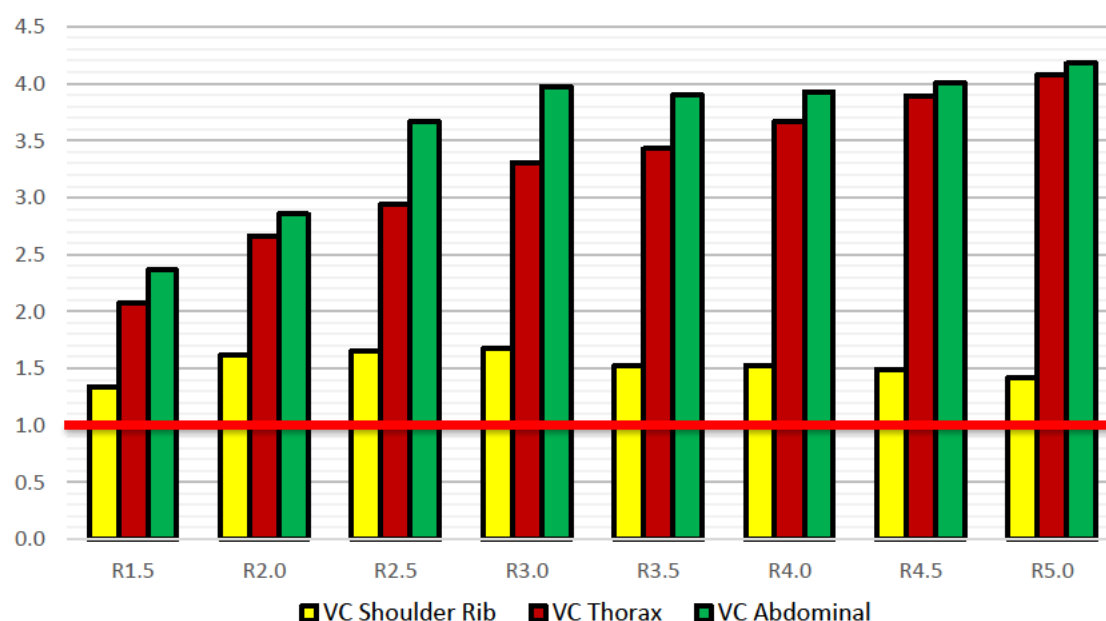


Figure 35. Viscous Criterion

Figure 35 provides a graphical representation of the VC from R1.0 with each mass-ratio. Firstly, it is evident that the shoulder region plateaus to a 50% increase from R3.5 onward, whilst the preceding ratios circulate a 65% increase to R1.0. The larger increases in VC with the mass-ratios between R1.5 and R3.0 would suggest

that the occupant sustains a better distributed force across all the ribs as opposed to it being concentrated upon a singular rib. This is reflected by the larger increases of all rib regions from R1.5 to R3.0 with each mass-ratio experiment, whilst R3.5 to R5.0 show a trend of lesser VC increase per mass-ratio increment, apart from individual ribs of each region as discussed following Table 31. Even though mass-ratios R1.5 to R3.0 provide larger increases to the VC result in comparison to larger mass-ratios, this would actually benefit the occupant as the average rate of displacement and deflection across all of the ribs would be less than one large impact on an individual rib, to which the VC is calculated.

A general relationship of VC by rib region can be identified by examining Figure 35; the abdominal region is faster to converge towards the 400% increase in comparison to experiment R1.0, achieving this by experiment R3.0. However, the thoracic region's progression is far steadier and closer to the abdominal VC increase with each mass-ratio experiment, therefore it is expected to reach an equivalent percentage increase as delivered by the VC of the abdominal ribs. This would suggest that the location of the impact plays a significant role in the relationship with mass-ratio. For instance, at first the abdominal region (which is closer to the primary impact) increases at a faster rate with each increase in mass compared to the other rib regions, following this, the thoracic region begins to converge on the increases exhibited by the abdominal region. Whereas the shoulder region has no significant change after the mass-ratio is large enough to overcome the protective structures of the Microcab and its ability to distribute the load.

Thoracic Trauma Index

The TTI is the most popular injury metric for lateral impact, though numerous studies have put the method under scrutiny due to numerous methods of calculation or for the accuracy and the greater sensitivity to unforeseen or uncontrollable factors that occur in the real world (Gierczycka, Watson, and Cronin 2015, Lai et al. 2012, Tencer et al. 2005, Gandikota et al. 2015). However, despite the sensitivity to specific factors such as the cabin interior and arm positioning, the TTI comparison is still valid for this study as only the mass of the bullet vehicle is altered and not the position of the occupant or impact location of the bullet vehicle. Thereby

permitting a dependable comparison across all experiments and the effects of vehicle mass-ratio difference to the TTI. Similarly to the VC, the TTI can be compared across each rib of the thorax within range of the 4th and 8th rib (as per Equation 6), permitting a deeper analysis and comparison to be made. Therefore, the normalised results of the upper, middle and lower thoracic ribs are presented in in Table 32 and shown graphically in Figure 36.

Table 32. Normalised Thoracic Trauma Index by Thoracic Rib

Thoracic Rib	R1.0	R1.5	R2.0	R2.5	R3.0	R3.5	R4.0	R4.5	R5.0
Upper Thorax	1.00	1.07	1.12	1.13	1.15	1.17	1.21	1.12	1.16
Middle Thorax	1.00	1.01	1.10	1.17	1.10	1.18	1.16	1.17	1.15
Lower Thorax	1.00	1.18	1.22	1.25	1.44	1.30	1.33	1.26	1.41

As the highlighted cells in Table 32 indicate, the maximum TTI is present in the lowest thoracic rib in each experiment. Additionally, the largest TTI is located in experiment R3.0, closely followed by R5.0. This outcome is expected due to the large rib accelerations found in the thorax within the rib metrics (Table 28). By comparing the acceleration in the Thorax region, Figure 32 and the pattern of the TTI, Figure 36, it can be seen that the TTI of the Lower Thorax Rib and the acceleration of the Thorax region follow the same pattern. With the exception of R3.0 and R5.0, the TTI and rib accelerations are within 7% of one another, despite the variance of the T12 acceleration between each experiment. A close relationship between the changes in the TTI to the changes in the rib acceleration and T12 are expected as both variables equally input to the TTI calculation. Therefore, discrepancies in the data of the Thoracic Rib acceleration or T12 acceleration would impact the TTI calculation.

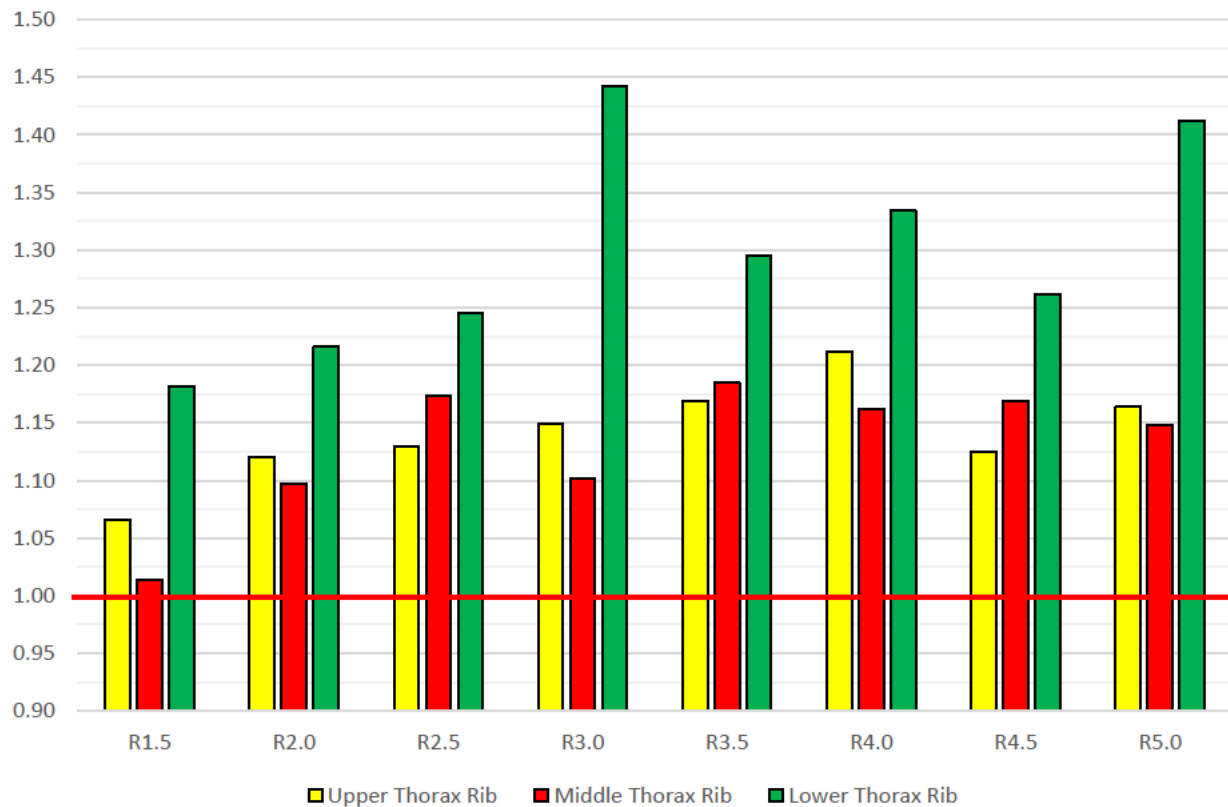


Figure 36. Thoracic Trauma Index by Thoracic Rib (Normalised)

Nonetheless, Figure 36 demonstrates a general increase of the TTI of an average 5% per mass increment, 2% less than the T12 and Thoracic Rib accelerations. Although it is difficult to ascertain how viable it is to assume that relationship due to the large fluctuations found across the experiments due to the rib accelerations, possibly caused by sensor capability or proximity to the impact location and vehicle interior.

4.4 Mass Relationship Exploration Discussion

The links between differing injury metric have been discussed throughout 4.3, however these have mainly focused within their respective category. By superimposing all the occupant metric data onto a single graph, indications of the relationship between each injury metric and possible influencers may be identifiable, adding regression equations allows a prediction to be made upon the injuries sustained by an occupant within the target vehicle for differing masses of bullet vehicle. It should be noted that despite the limited number of experiments, the relationship between occupant injury and vehicle mass-ratio is not linear, nor exponential, but could be a relationship of a 3rd or 4th order function, or even logarithmic. Thus, the regression lines and

equations are indications of pattern; to better ascertain whether the relationship is true, more experiments would have to be conducted.

Figure 37 provides the regression lines of each occupant injury metric discussed throughout section 4.3, whilst Table 33 provides the equation of the respective regression and their coefficient of determination (R^2). The shorthand “Accel.” signifies maximum acceleration for Figure 37 and Table 33.

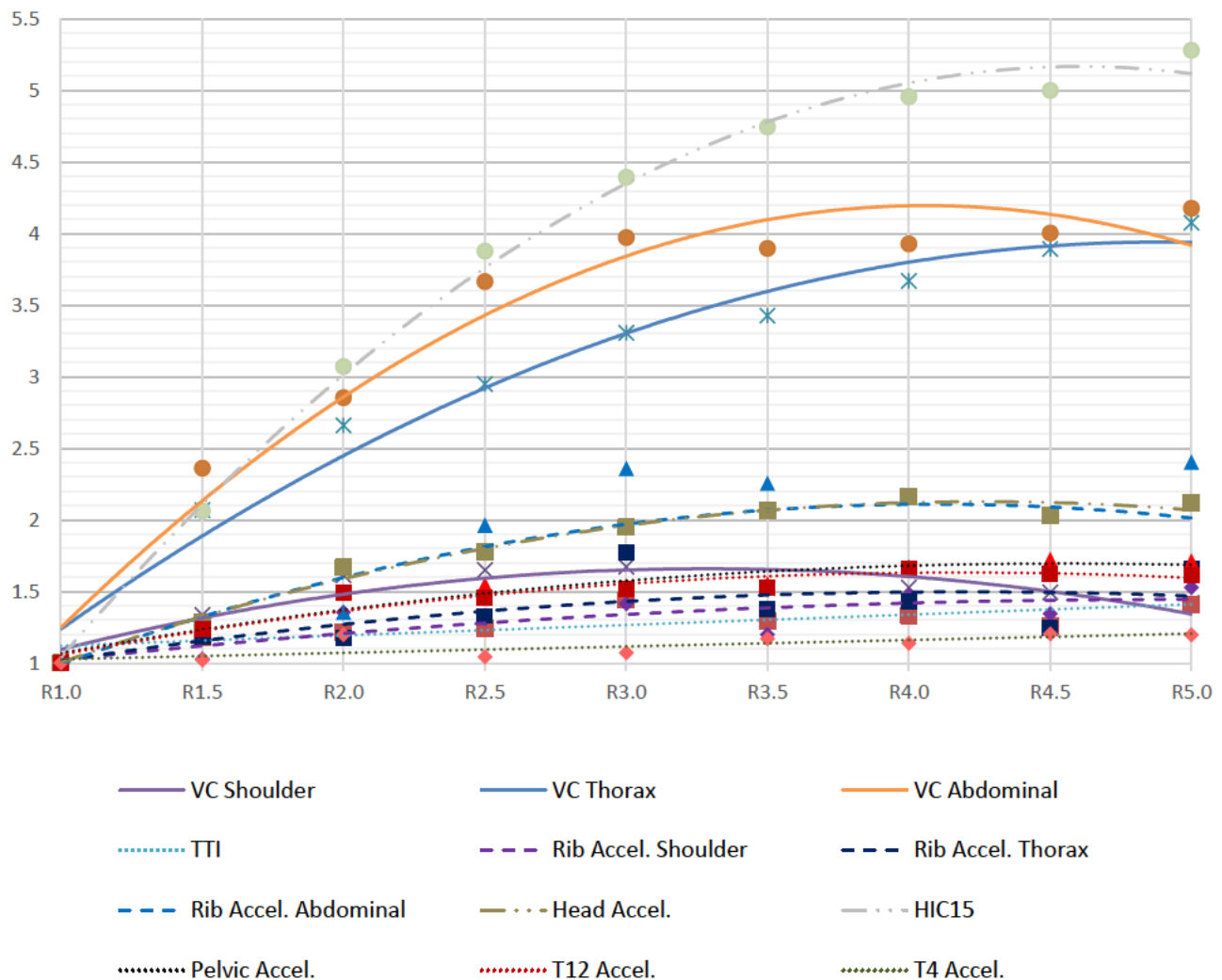


Figure 37. Normalised Injury Metric Correlation to Mass-Ratio

Examination of Figure 37 highlights that the HIC₁₅, VC abdominal and VC thorax are greatly influenced by the mass-ratio of bullet to target vehicle in comparison to other injury metrics. However, there is no evidence that injury metrics influence other results, apart from when they are included within the equation (such as the

TTI using the T12 acceleration). Despite this, Figure 37 provides a visual representation of the plateauing pattern that occurs in many injury metrics. Interestingly, all of the rib accelerations appear to maximise between R3.0 and R4.0 and then begin to decrease, to which the 2nd order function does not capture well. This is reflected by the value of R^2 held by the rib accelerations laying between 0.50-0.67, which is low in comparison to the other R^2 values achieved.

Table 33. Trend Equations for Injury Metrics

Injury Metric	R^2	Equation of Regression
VC Shoulder	0.82	$y = -0.027x^2 + 0.3008x + 0.8212$
VC thorax	0.97	$y = -0.0447x^2 + 0.7851x + 0.4964$
VC Abdominal	0.96	$y = -0.0787x^2 + 1.1209x + 0.2062$
TTI	0.73	$y = -0.0084x^2 + 0.1206x + 0.9294$
Rib Accel. Shoulder	0.67	$y = -0.0067x^2 + 0.1199x + 0.9067$
Rib Accel. thorax	0.50	$y = -0.0117x^2 + 0.1739x + 0.8543$
Rib Accel. Abdominal	0.61	$y = -0.0292x^2 + 0.4202x + 0.5998$
Accel. Head	0.98	$y = -0.0267x^2 + 0.3978x + 0.6269$
HIC ₁₅	0.99	$y = -0.08x^2 + 1.3092x - 0.1915$
T4 Accel.	0.55	$y = -0.0007x^2 + 0.0292x + 0.9913$
T12 Accel.	0.92	$y = -0.0142x^2 + 0.2092x + 0.8629$
pelvis Accel.	0.92	$y = -0.0124x^2 + 0.2009x + 0.8802$

The equations of regression provided in Table 33 had not been set to intercept with R1.0, thus may not provide an exact result of '1' if the input 'x' is equal to '1'. This was done to allow better alignment of the regression lines which could cater for minor discrepancies within the results. The equations provided in Table 33 are constructed so that the mass-ratio of the bullet to target vehicle acts as the input 'x', providing the percentage increase to the respective occupant injury metric in comparison to a 1:1 mass-ratio.

As mentioned in the opening paragraph of this section (4.4) the regression equations act as indicators to a pattern, whilst the R^2 shows how well the regression equation aligns with the resulting data. All of the regression equations within Table 33 are of a 2nd order function as these provide a satisfactory trend with the limited data points up to a 5:1 ratio. Arguably, a higher order function would provide a better coefficient of determination and manage to capture the large increases that are found within some curves (such as the abdominal rib acceleration), however without more numerical experiments between each ratio increment to provide more data, the higher order functions are not warranted.

By altering the mass of the bullet vehicle, a relationship between the mass-ratio of bullet and target vehicle to occupant injury was accomplished for numerous injury metrics. Many of the injury metrics recorded provide evidence of convergence to a maximum increase of occupant injuries, in comparison to a 1:1 mass ratio. Namely, the HIC_{15} , Viscous Criterion, T12 and pelvic accelerations, each of which appear to plateau at R4.0, R3.0, R4.0 and R4.0 respectively. The injury parameters most influenced by the vehicle mass-ratio are the HIC_{15} and the VC in the abdominal and thorax regions, each holding a maximum increase of 526%, 418% and 408% respectively. Additionally, the occupant's body accelerometers that are important for various injury calculations had substantial increases at the lower mass ratios, the T4, T12 and pelvis acceleration results then converged towards 120%, 166% and 172% respectively. However, per mass increase, the occupant injury metrics recorded experienced larger increases at the smaller ratios, making it difficult for an L7e vehicle to achieve safety standards comparable to a vehicle within the M_1 category. Although, it is important to note that an acceleration increase of 166% at the T12 vertebrae may not pose a huge risk to the occupant as it is dependent on the initial (mass ratio of 1:1) crashworthiness performance of the target vehicle.

Regardless of the actual injury data obtained, the experiments suggest that maximum occupant injuries fluctuate at a bullet to target vehicle mass ratio of 4:1. This translates to a laden mass of 1800kg for an M_1

vehicle. Therefore, to provide an L7e occupant with more beneficial circumstances to lessen injury likelihood and severity (in a lateral collision from a vehicle of greater mass) then the mass of the M_1 vehicle should be less than 4 times greater than the L7e vehicle. Generally, the increase of injury metrics per incremental mass increase reduces with ratios above 3:1. Consequently, each reduction of mass-ratio below 3:1 yields greater reductions of injury metrics than those above 3:1. However, the plateauing nature of the results is not prevalent in all injury metrics at the same vehicle mass-ratio. Thus, it may be possible to reduce the risk to the occupant by avoiding unfavourable mass-ratios or designing the target vehicle to better mitigate the effects of high-risk ratios to specific occupant regions. Another method is to attempt to attain mass-ratios of vehicles that minimise the aggressivity of the M_1 vehicle whilst maximising the energy absorption efficiency of the L7e vehicle for high-risk scenarios. To achieve this, a novel methodology of universal vehicle parameterisation was developed.

5 Crash Safety Light-Weighting

A method of achieving the most favourable vehicle mass ratios for occupant safety is to show the possibilities of vehicle light-weighting procedures which possess little cost increase. The viability of a procedure which incorporates no geometrical changes to the original vehicle design and construction is advantageous as this facilitates application to all vehicle designs and manufacturers. In a similar vein, Lotus Engineering Incorporation had performed an in-depth study into vehicle light-weighting and cost-analysis upon the 2009 Toyota Venza (2010). The functional objectives of this study are summarised as maintaining utility and driving performance of the Venza model throughout mass and cost optimisation. Occupant safety and adherence to FMVS standards and NCAP compliance were not considered, although the light-weight vehicles were assessed by FE analysis at a later date by the National Crash Analysis Center (NCAC 2014a, 2014b, 2014c). However, the methodology created and adopted in this research aims to reduce the overall vehicle mass whilst maintaining similar occupant safety performance to the original vehicle model, thus increasing the crashworthiness efficiency of the vehicle (by mass) and defining a rudimentary method of light-weighting vehicles to achieve a more sympathetic vehicle mass-ratio for vehicle-to-vehicle impacts.

The light-weighting procedure developed is named the Ranked Mass Reduction (RMR). The scope and operational limits of the RMR are discussed throughout section 5.1 before the development and application of the RMR is defined in section 5.2. Following this, a full comparison of the effectiveness of the RMR against the light-weighting procedure of the 2009 Venza vehicle model is presented in section 5.3.

5.1 Scope and Operational Boundaries of the RMR

First and foremost, the function of the Ranked Mass Reduction (RMR) is to identify vehicle components that permit mass reduction whilst not compromising the vehicle integrity for occupant safety. Secondly, for applicability and assessment on all passenger vehicles currently (or soon to be) in production, the RMR does not permit or produce geometrical changes to the vehicle architecture. For instance, incorporation of

functionally graded structures could benefit occupant safety, however, it is nonsensical to integrate these into the light-weighting procedure as functionally graded structures are tailored for specific components, locations and load-cases, all of which have different requirements to fulfil depending on the vehicle. Thus, incorporation of functionally graded structures to the procedure would limit the RMR's applicability to all passenger vehicles. Furthermore, the cost requirements of producing functionally graded components would likely increase the cost of the vehicle, possibly changing the targeted consumer audience. In effort of retaining the same consumer audience, the RMR does not make changes to components that are too expensive or impractical to produce or construct. The RMR utilises the expected crash scenario of the near future, the vehicle-to-vehicle lateral impact. The RMR prioritises the safety of the more vulnerable user for this scenario, as described in the problem statement within chapter 3. Therefore, the overarching scope and function of the RMR can be summarised as:

1. Vehicle mass reduction via component level alterations.
2. Prioritisation of L7e occupant safety in lateral collisions.
3. Only approved materials and manufacturing methods accepted.
4. No geometrical changes to components or assemblies permitted.

The RMR concentrates on structures and passive safety structures. Thus, the RMR does not cater for alterations to active safety systems installed within the occupant compartment. Although it is a limitation, firing times of airbags and seatbelt pre-tensioning and forces can be manipulated after a light-weighting procedure is performed. Another limitation is that the Noise, Vibration, and Harshness (NVH) of the subject vehicle is not considered. However, NVH targets can be accomplished by intelligent positioning of small reinforcements or vibration isolators at the source and transmission path within the vehicle at a later development phase (Mallick 2021: 426). As a result, the limitations affecting the RMR do not inhibit the applicability to varying vehicle types nor constrain the function of the RMR to reduce vehicle mass by parameterised component attributes.

5.2 RMR Development

The defined scope of the RMR provides the skeleton to which the RMR tool and associated research is developed. It is formed of six overarching stages shown in Figure 38 below, including the completion and assessment of vehicle and RMR performance. The acronyms 'SV' and 'BOM' represent the 'Subject Vehicle' and 'Bill of Materials' respectively. The subject vehicle is defined as the vehicle that the RMR and scenario is applied to. Accordingly, the 'Opposing attributes' are the aspects negatively affecting the subject vehicle, such as bullet vehicle dimensions and mass.

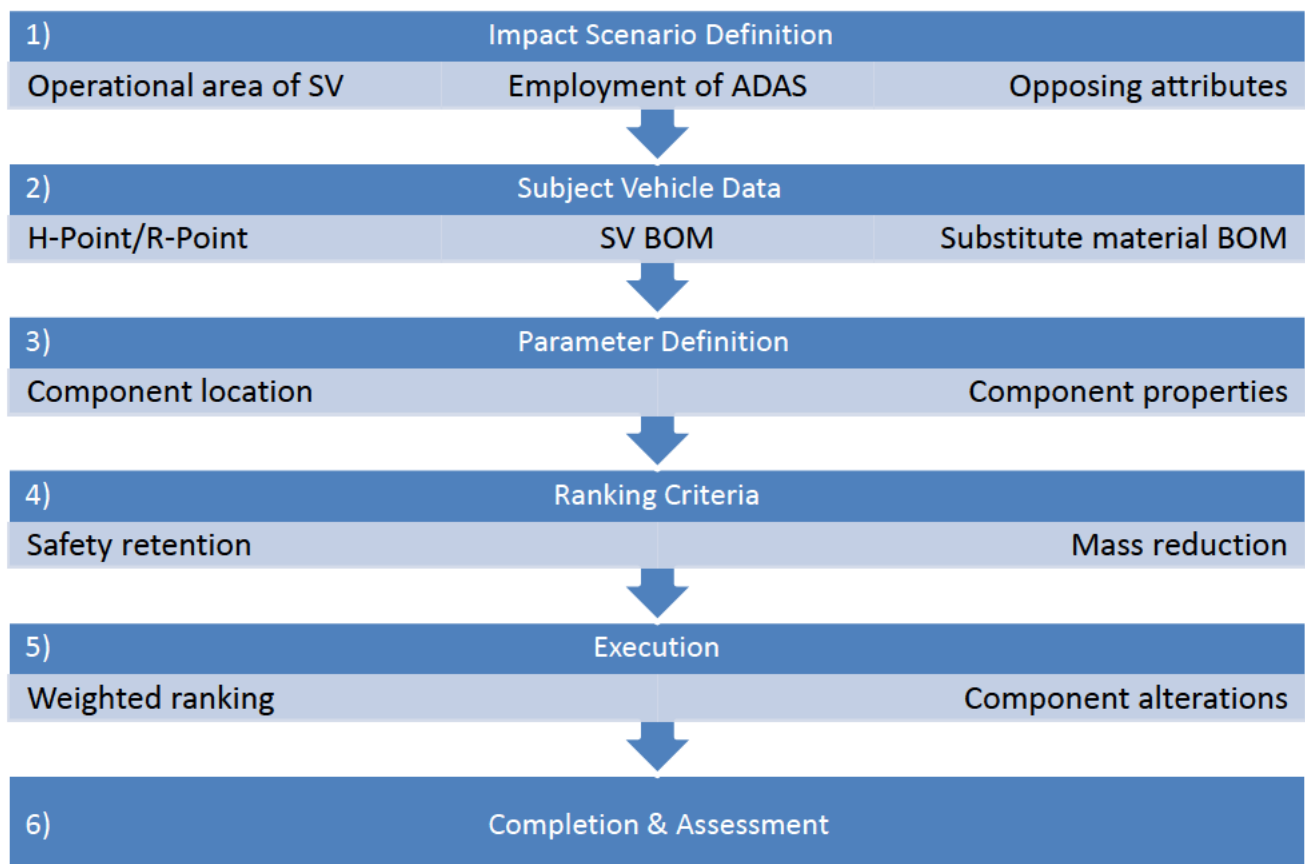


Figure 38. RMR Process Overview

As the performance of the Venza vehicle model after light-weighting procedures is compared between the methodology adopted by Lotus Engineering Inc. and the RMR, stage 1 of the process is pre-defined. The load-case to evaluate the performance of the RMR is equivalent to the test performed by NCAC on the Venza Baseline (VB) , Low Development (VLD) and High Development (HLD) vehicle models (NCAC 2014a, 2014b,

2014c). Similarly, the substitute materials used in the light-weight vehicle models of the Venza study are used for the RMR for a fair comparison between results as well as maintaining material cost requirements within an acceptable range of the VB model (Lotus Engineering Incorporation 2010: 244). In summary, the Venza load-case is a FFRW impact at 25mph (40.2km/h) with no pre-crash braking, more information regarding the test arrangement is disclosed in section 5.3. As process stages 1 and 2 (Figure 38) are vehicle specific, they are also included in section 5.3. Process stages 3 and 4, regarding the creation and designation of the component parameters, are detailed in section 5.2.1 and the parameter ranking process is discussed in section 5.2.2.

5.2.1 RMR Parameter and Criteria Creation

The method utilised by the RMR requires the identification of the load-case scenario, in keeping with the scope of the RMR procedure as outlined in section 5.1, the RMR prioritises safety of the L7e occupant against a lateral impact. By this manner, it can also be tailored to results in adjustments to the frontal crash rails of an M_1 bullet vehicle. However, to retain sufficient levels of occupant safety, limitations were implemented to the mass reduction procedure. These limitations form the basis of component parameters. Each parameter ranks the attributes of that field for mass reduction capability. The capability is defined as “the potential to remove mass without hindering the primary function or protective performance of the component to the occupant”. Each component of the subject vehicle has 6 parameters defining their respective attributes, each with a possible score of 1 to 3. A low score signifies poor mass reduction capability or that they are prominent in maintaining safety performance. Conversely, a higher score indicates better mass reduction capability and lower likelihood of undesirable safety implications after alterations. The component parameters have slightly differing emphases within the RMR procedure, the component attributes that form the parameters and their motivations are presented in Table 34.

Table 34. Component Parameter Definition Overview

Component Parameter	Definition Type	Scoring Method(s)	Motivation(s)
Centre of Gravity along the SV length (CofG _{long})	Zone Location	Longitudinal distance from R-Point/H-Point	Occupant safety retention
Centre of Gravity across the SV width (CofG _{trans})	Zone Location	Transverse distance of in-line crash rails for probable aggressivity of SV	Occupant safety retention for v-t-v impact for target vehicle
Centre of Gravity upwards from floor (CofG _{vert})	Zone Location	Vertical distance from R-Point/H-Point, likely impacting height	Occupant safety retention
Material	Fixed Selection	Specific strength, stiffness, absorption capability, deformation predictability	Mass reduction, crash performance, occupant safety retention
Gauge thickness	Percentage	Thickness of component in relation to function and average component thickness across the vehicle	Mass reduction
Mass	Percentage	Percentage of vehicle mass constituted by component	Scalar for weighted summation (section 5.2.2)

As Table 34 highlights, parameters have different motivations for the light-weighting procedure and scoring methods. The CofG parameters mainly focus on the retention of occupant safety in a vehicle to vehicle (v-t-v) impact and function by defining segments of maximum mass reduction and vice versa. Whereas the material and gauge parameters mainly target mass reduction. The gauge and mass parameter operate by a percentage coverage of the subject vehicle; therefore, these can be specifically tailored to any vehicle. The construction and definition of each parameter and their respective type are discussed individually throughout the following sub-sections in order of appearance of Table 34.

Centre of Gravity Parameter Definition

The restrictive measures of the CofG parameter are formed by defining zones along (CofG_{long}), across (CofG_{trans}) and upwards (CofG_{vert}) of the vehicle driving direction. These are formed in line with the defined crash scenario. The occupant H-Point or vehicle R-Point are reference locations for the CofG_{long} and the opposing attributes (Figure 38) define the zone boundaries for CofG_{trans} and CofG_{vert}. As described in section 5.2.1, the zones of the CofG parameters are scored between 1 and 3, denoting the mass reduction capability of that

zone. The zone location and boundaries are defined for initial impact but can be altered to cater for different load-cases and vehicles, such that the zone definition of $\text{CofG}_{\text{trans}}$ may be adapted for wider or narrower crash-rail placement. Additionally, specific components can be omitted from the RMR procedure by user-defined criteria (as demonstrated in section 5.2.2: RMR Employment) allowing for greater adaptability in mass reduction or inclusion of secondary impacts, such as roll-over. Furthermore, each zone boundary could contain multiple components that extend between multiple zones. In this case, only the CofG of the component is considered when stating the location within the vehicle. Each zone boundary and formulation is described below throughout the sub-sections, the definitions provided are for the 2009 Venza model (NHTSA 2014a).

Longitudinal Centre of Gravity Zone definition

The zones that divide the vehicle longitudinally are defined by the reference location of the H-Point. The zones represent the capability for component weight reduction and the inherent influence on the occupant injury metrics recorded. Each zone is ranked for the mass reduction capability so that the zone closest to the occupant and main safety structures are given the lowest number. Subsequent zones are provided in an incremental order to the maximum desired number of zones. For this study, three differing zones were implemented. The zones scored 1 (red), 2 (orange) and 3 (green) for longitudinal separation along the Venza vehicle model are depicted in Figure 39 and Figure 40 in the XZ and XY view respectively. The dashed blue lines represent the reference planes of estimated occupant H-point in the longitudinal (XY) and vertical (YZ) planes.

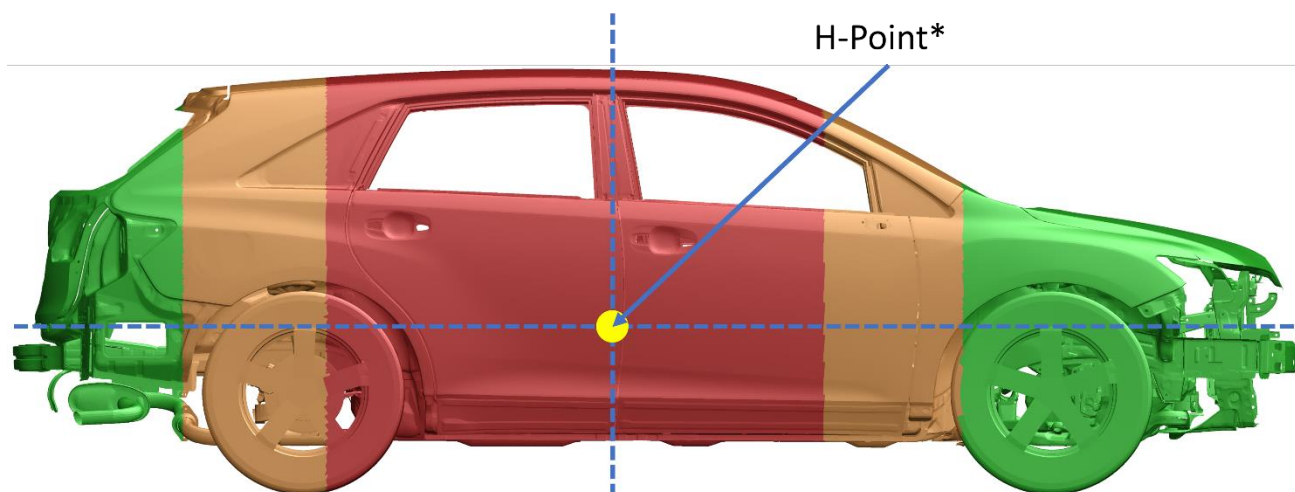


Figure 39. Longitudinal CofG Parameter Boundaries with estimated reference planes of occupant H-Point* (XZ)

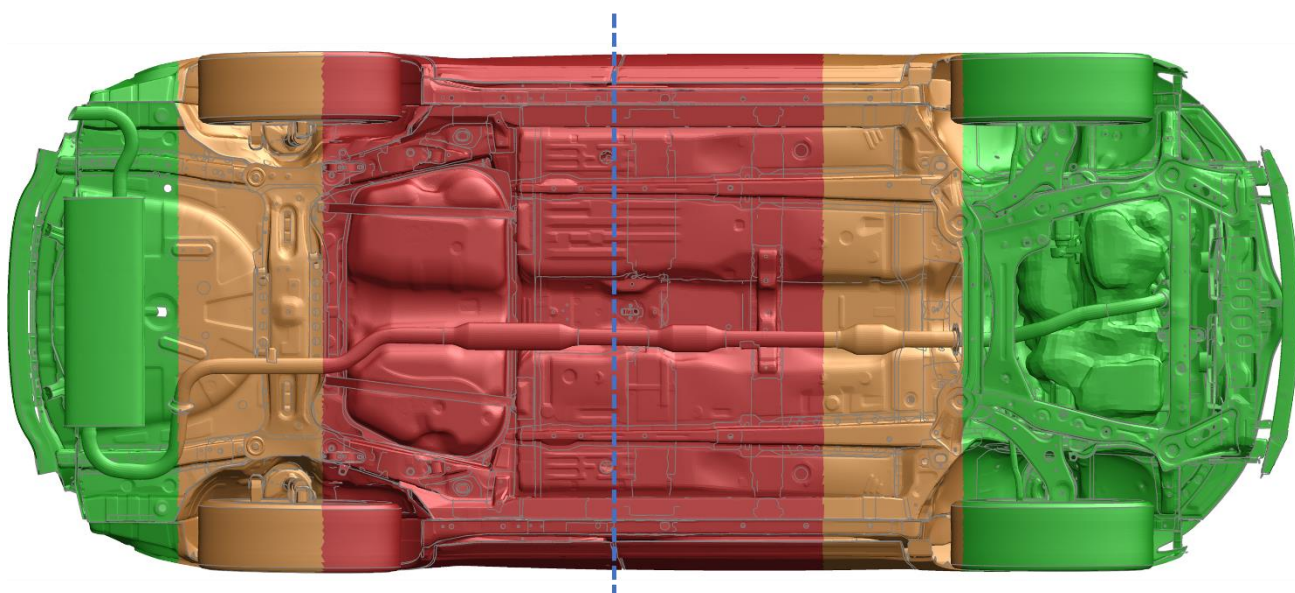


Figure 40. Longitudinal CofG Parameter Boundaries with estimated reference plane of occupant H-Point (XY)

The driving direction of the vehicle shown in Figure 39 and Figure 40 are in the positive x-direction. The reference location of the $CofG_{long}$ boundaries is provided by the occupant H-point point on the YZ reference plane and from the front of the vehicle in Table 35. Additionally, the total coverage of the zones is provided for the Venza vehicle model.

Table 35. Longitudinal CofG Parameter Boundaries (Venza)

Zone		Zonal Co-ordinates (x)		Total Zone Coverage (x)	
Colour	Score	Approx. H-Point Reference (mm)	Front of Vehicle Reference (mm)	Millimetre	Percentage
Red	1	$-1100 \leq x \leq 750$	$-3600 \leq x \leq -1750$	1850	39
Orange	2	$750 < x \leq 1265$ $-1635 \leq x < -1100$	$-4135 \leq x < -3600$ $-1750 < x \leq -1235$	1050	22
Green	3	$-2258 < x < -1635$ $1265 < x < 2500$	$x < -4135$ $x > -1235$	1858	39

The red zones presented on the Venza are extended backwards further from the H-point in consideration of rear occupancy. Similarly, orange zones cater for the rear occupants, resulting in the extension of the green zone at the front of the vehicle. The zone specifications and their respective limiting function in the RMR execution phase suggest a 'ramping' effect of strength throughout the crash pulse of the full-frontal load-case will be expected. On the other hand, the vehicle had already been designed to accommodate full frontal impacts where the 'ramping' effect is built into the crash rail design. Therefore, a greater crush distance is expected for the lighter-weight revisions by the sole application of the $CofG_{long}$ parameter of the Venza model until the orange and red zones are engaged. In accordance with the prioritisation and objectives of the RMR procedure, the zone segregation caters for the 'opposing attributes' of a lateral impact by M_1 categorised vehicles. For instance, the Citroën C1 has a total fender-to-fender width of 1615mm whilst a Land Rover Discovery Sport has a width of 1920mm (Automobiledimensions n.d.). Factoring in the average wheel width and assuming the frontal crash rails of the bullet vehicle are directly inset of the wheels, the largest width required to cover becomes 1475mm to 1780mm. As stated in Table 35, the red and orange zones provide adequate boundaries to cater for the bullet vehicle crash structures and vehicle extremities.

Transverse Centre of Gravity Zone definition

Transverse parameterisation for component positioning assumes the vehicle is acting as a bullet vehicle of the M_1 categorisation. The motivation of the $CofG_{trans}$ is to reduce the aggressivity of the bullet vehicle for v-t-v impacts to assist in decreasing the risk to occupant injuries sustained within an L7e vehicle. It is reasoned that in the near future, ADAS will render wall and full-frontal impacts obsolete, as expressed throughout section

2.3. As a result, it is expected that there will be less necessity for stiff frontal crash structures that are designed for high-speed impacts, as well as impacts into an unyielding barrier. This permits alterations to the crash structures of the subject vehicle to be made. Consequently, the $\text{CofG}_{\text{trans}}$ is highly dependent on the vehicle architecture as the frontal crash-rails and primary protective structures are priorities for mass reduction. The definition of the $\text{CofG}_{\text{trans}}$ for the Venza vehicle model is visually provided in Figure 41.



Figure 41. Transverse CofG Parameter Zones (YZ)

Figure 41 illustrates that the central column of the vehicle permits greater mass savings to be made whilst retaining the form of more external structures that are inherently weaker in a frontal collision. The $\text{CofG}_{\text{trans}}$ is calculated from the centreline of the vehicle, the classifications of the transverse zones are presented in Table 36.

Table 36. Transverse CofG Parameter Boundaries (Venza)

Zone		Zonal Co-ordinates (y)	Total Zone Coverage (y)	
Colour	Score	Vehicle Centreline Reference (mm)	Millimetre	Percentage
Red	1	$-950 < x \leq -725$ $725 \leq x < 950$	450	24
Orange	2	$-725 < x \leq -525$ $525 \leq x < 725$	400	21
Green	3	$-525 < x < 525$	1050	55

Due to symmetry of the vehicle, the $\text{CofG}_{\text{trans}}$ zones are equally divided across the vehicle. The percentage coverage of the vehicle presented by the 'green' zone is greater than that of the $\text{CofG}_{\text{long}}$ (Table 35), signifying larger changes are permitted by the $\text{CofG}_{\text{trans}}$ parameterisation scoring to achieve mass targets and reduce

aggressivity from localised mass of the frontal structures. Conversely, the $\text{CofG}_{\text{trans}}$ also partially counteracts the frontal and rear scoring of $\text{CofG}_{\text{long}}$, developing better segmentation and reduction suggestions once the CofG parameters are combined (5.2.2). The green zone was aligned with the centreline of the front crash rails of the Venza which extend under the occupant floor panelling as shown in Figure 42. The orange and red zones were defined by the location of supportive structures and protective structures for occupant safety respectively.

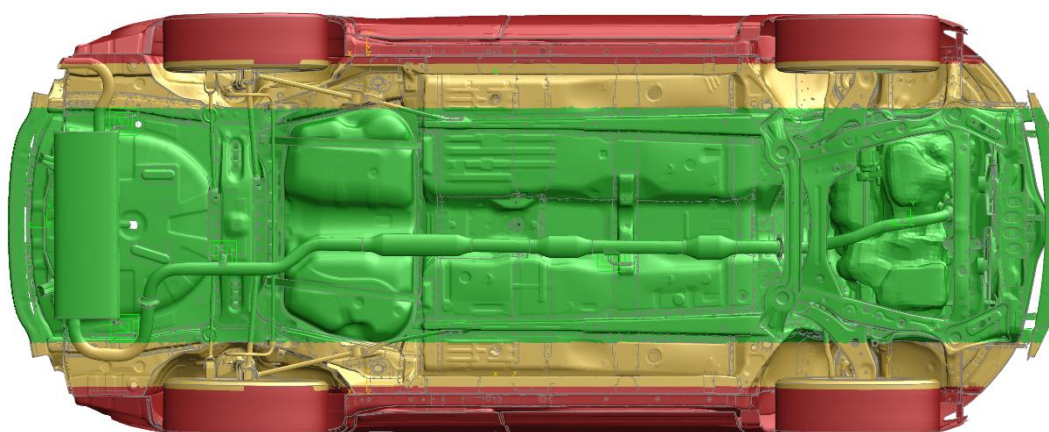


Figure 42. Transverse CofG Parameter Zones (XY)

Vertical Centre of Gravity Zone definition

Alike the $\text{CofG}_{\text{long}}$ parameter definition, the $\text{CofG}_{\text{vert}}$ is defined by protective structures and to counteract opposing attributes, such as the impacting height of a bullet vehicle. Figure 43 provides a visual portrayal of the $\text{CofG}_{\text{vert}}$ zones as defined in Table 37. The dashed blue lines signify the planes of the estimated H-point.

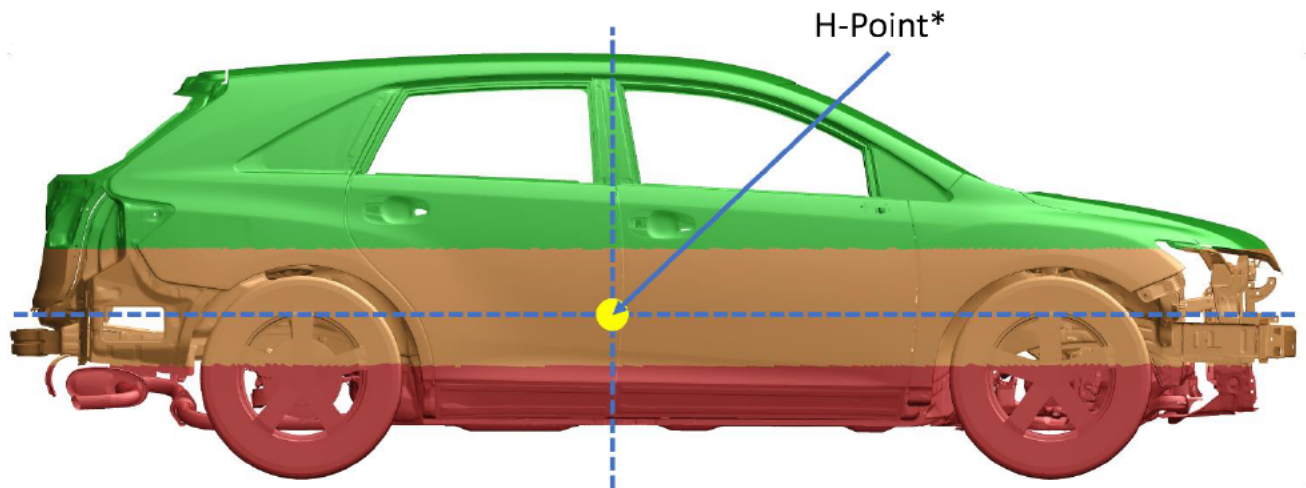


Figure 43. Vertical CoG Parameter Boundaries with estimated reference planes of occupant H-Point* (XZ)

The height of the red zone extends past the Venza sill and rests under the front and rear crash structures. More importantly, the red zone aligns within 10% of the central height of the extruded barrier face of the AE-MDB (Figure 15). Additionally, the combination of the red and orange zones extends vertically to a combined 850mm from the ground reference location which is sufficient to accommodate for varying heights of probable impact as identified throughout section 2.3.2.

Table 37. Vertical CoG Parameter Boundaries (Venza)

Zone		Zonal Co-ordinates (z)		Total Zone Coverage (z)	
Colour	Score	Approx. H-Point Reference (mm)	Floor Reference (mm)	Millimetre	Percentage
Red	1	$-674 \leq x \leq -259$	$x \leq 415$	415	27
Orange	2	$-259 < x \leq 176$	$415 < x \leq 850$	435	27
Green	3	$176 < x \leq 901$	$x > 850$	725	46

The percentage coverage of the red and orange zones for the CoG_{vert} constitutes to a combined total of 54%. The red and orange zones constitute the majority of the vehicle, thereby limiting the quantity of mass removed due to proximity of the occupant location and likely distribution of impact location and effective area. This is in contrast to the $\text{CoG}_{\text{trans}}$ that has a majority zonal coverage of 55% attained by the green zone. This expresses the different motives and procedures required for the definition of the zones upon subject vehicle. CoG_{long} and CoG_{vert} provide more limited regions to reduce mass and prioritise lateral safety as the target vehicle, whereas the $\text{CoG}_{\text{trans}}$ parameter provides greater regions for mass reduction as it is assumed that the vehicle

is acting as the bullet vehicle. The combination of the parameters, by essentially reducing aggressivity whilst simultaneously increasing localised protection, provides the framework of increasing crash efficiency and inter-category compatibility. The combination and application of the CofG parameters and their interaction with other parameters are clarified in section 5.2.2.

Component Material Parameter Definition

The material parameter primarily focuses on mass reduction by changing selective materials to suitable alternatives. The new materials must be available and still abide by the cost and manufacturing requirements of the subject vehicle to maintain market value and consumer audience. Alterations to the materials used for components must be able to provide a similar primary function to the original material. Such as changing Steel to Aluminium or a high-grade alternative. Despite the possible cost and gauge thickness increase alternative materials may incur, the possible lower density and gauge thickness requirement are advantageous. In summary, the benefits gained by changing the material must outweigh the severity of the downsides.

As opposed to other parameters, the material parameter utilises fixed values instead of percentage mass of the original component. This reflects that the changes to the material are absolute, and a variable percentage change is not feasible by altering the metal alloy or material. The material changes are defined by a predetermined list of materials that can be used for components. The material score for each component is evaluated by the density of the material used for the given component and the applicability of another material in its place. The criteria can be summarised as an observable improvement in predictability of plastic deformation, the strength to mass ratio of the material, packaging space and manufacturability for the desired need. Conversely, the material that is used in the subject component is ranked lowly if few criteria are met. This research utilises the materials that are defined in the 2010 Venza light-weight study as the material replacements used had a cost and performance evaluation (Lotus Engineering Incorporation 2010). By utilising the same materials provided, it allows a direct comparison in the performance of the RMR and to the process of application to be made. The FE materials designated for changing from the Venza baseline (BL) and their

associated scoring are provided in Table 38. The two 3-digit numbers signify the Yield and Tensile strength of that material.

Table 38. Material Parameter Scoring for Venza Baseline

FE Material Name	Description	Score	Potential Component Mass Reduction (%)	Number of Components	Representative Total Vehicle Mass (%)
Mild 140-270	Mild Steel	3	66	445	33.6
BH 210-340	Bake Hardened Steel	3		26	2.5
DP 350-600	Dual Phase Steel	3		1	0.1
DP 700-1000	Dual Phase Steel	2	45	5	0.6
HSLA 350-450	High Strength Low Alloy Steel	2		225	13.8
HSLA 490-600	High Strength Low Alloy Steel	1	12	52	3.3

All materials selected were alloys or treated Steel. The density of Steel is approximately 2.8 times greater than Aluminium, leading to a specific strength in the range of 40.5- 47.2 kNm/kg, 2.3 times greater than the specific strength of Mild Steel (17.8-26.8kNm/kg) (Ansys 2020). The HSLA and DP Steels provide a greater specific strength than Mild Steel and are therefore scored lower as replacement materials do not offer substantial differences in performance. The materials presented in Table 38 form 54% of the total Venza mass, providing ample opportunity to reduce overall vehicle mass by employing the alternative materials as presented in Table 39. The materials suggested in Table 39 form the basis of the potential mass reduction by material type in Table 38. This is estimated by the function of the material and the replacement. As such, a lighter Aluminium counterpart could easily replace the low strength steels. However, as the specific strength of the steel increases, the demand on the Aluminium to match the performance of the Steel increases in difficulty, which could result in a material thickness increase.

Table 39. Material Database for Venza RMR

FE Material Name	Description
al 6013-t6	Heat Treated Aluminium Series 6000
AL-6013-T6 sht - (Alcoa-Ed Forsythe 100927)	Heat Treated Sheet Aluminium Series 6000
240MPa aluminum	Stamped Aluminium
240MPa aluminum (25% failure)	Stamped Aluminium
AL-6061-T6 ext - (Alcoa-Ed Forsythe 100923)	Heat Treated Extrusion Aluminium Series 6000

The replacement materials are applied to vehicle components that facilitate a change. This safeguards against false implementation of material types into the Venza model. An additional 'check' method had also been employed when isolating the material parameter. The 'check' function highlights components that do not possess a material within Table 38. This assists in identifying assemblies and components that are omitted from the RMR process. The material database is subject to change if the RMR process is repeated as it is conditional on material availability and costing target/allowance. Furthermore, as the specific strength of the material increases, the component may require increased thickness with a lighter material to ascertain similar or desired performance.

Component Gauge Thickness Definition

The Gauge parameter is partially dependent upon the results and implementation of the material parameter. The gauge parameter is scored by the component potential to reduce mass via thinning the component wall with minimal change to occupant safety performance. However, material changes and the respective component function or manufacturable capability may not permit a particular gauge thickness, conversely the component could require a greater thickness to achieve the same performance or function after a material change. Therefore, the changes suggested by the gauge parameter can be applied before the material changes and once again after. This method allows identification of areas that require improvement in safety performance and can therefore be rectified or examined in the stage of the material change routine of the RMR. Usually, any excess material is typically reduced in post-processing in the design of the vehicle through optimisation methods, or it is limited by the manufacturing technique used. Nonetheless, this study examines the use of heavy-quadracycles and light-weight vehicles and their compatibility with other vehicle categories on future roads. By this reasoning, the novel designs that are already emerging on the market spearhead

changes and improvements in materials, their designs and the manufacturing methods used. Thereby, what are currently expensive components to manufacture may not be in the future once a greater demand is established, thus allowing more complex alloys and components to be made which can bare the reduced thickness and provide equal or better performance. However, functionally graded structures and similar designs are not assessed or utilised due to the current increased cost of manufacturing (in comparison to sheet or extrusions) as well as the variance and particular performance to load-cases, as examined throughout section 2.4. It is understood that specific components may benefit from such techniques and designs for protective structures, but the application of tailored geometry extends this study past the scope of investigating crash compatibility as a function of mass.

Table 34 described the definition of the gauge parameter as a percentage reduction. Each score within the gauge parameter has a potential mass reduction assigned to the components that fall within that category. The bounds and potential component mass reduction are presented in Table 40.

Table 40. Gauge Parameter Scoring for Venza Baseline

Gauge Score	Gauge Thickness Definition (mm)	Number of Components	Total Structural Mass (%)	Potential Component Mass Reduction (%)
1	$0.45 < x < 1.2$	714	54.7	10
2	$1.2 \leq x \leq 2.0$	348	23.3	18
3	$2.0 < x \leq 15$	246	22.0	50

It can be seen in Table 40 that the components that have a thickness less than 1.2mm constitute to nearly 55% of the total vehicle mass. Despite estimation of a 10% reduction per component within the score 1 category, mass savings in this zone could potentially reduce the vehicle mass by over 8kg alone. However, manufacturing constraints would limit many of the reductions within this category. The minimum gauge thickness is defined as 0.45mm to omit rigid shells and applied masses within the FE model. The potential component mass reduction is an idealistic mass saving, the gauge reductions would not be so severe due to manufacturing methods, material selections and component functions. This is imitated in the RMR process by the weighted sum of each category, discussed in 5.2.2, in which the component mass parameter plays an important role.

Component Mass Parameter Definition

As the component mass is controlled by the material and gauge parameter, the mass parameter serves as an identifying and scaling tool. It identifies the components that cannot be changed, such as the vehicle powertrain system or adhesive paste. Additionally, this parameter is useful in the application of the RMR when the parameter weighting system is applied, by providing heavier components (those that form the greater percentage of the vehicle's mass) a higher priority. The bounds for each mass ranking can change depending on the vehicle, as it is calculated by the most common and maximum weight across the vehicle components. Table 41 presents the scoring bounds for the mass parameter for the Venza baseline model.

Table 41. Mass Parameter Scoring for Venza Baseline

Mass Score	Mass Parameter Boundary (kg)	Number of Components	Total Structural Mass (%)
1	$0 < x \leq 1$	1154	38.3
2	$1 < x \leq 4$	163	28.4
3	$4 < x \leq 20$	46	33.3

Each category constitutes to approximately a third of the total vehicle mass, whilst the number of components reduces by one third with ascending score. The mass parameter does not provide an estimated mass reduction as the parameter is used in conjunction with other parameters throughout the ranking process of the RMR.

5.2.2 RMR Criteria Ranking and Execution

The RMR parameters operate together to produce suggested light-weighting methods whilst retaining localised occupant safety. The limiting parameters (CofG parameters) work in conjunction by segregating areas of the subject vehicle and ranking them in location prominence to occupant safety of an L7e vehicle. In a similar fashion, the gauge and material parameters work in conjunction to reduce the vehicle mass and maximise specific strength at a component level. Each parameter score defined throughout 5.2.1 are multiplied by a weighting factor and summed together to achieve an overall score which suggests the achievable total mass reduction.

RMR Weighting

Each parameter is weighted in order of importance for the objective of the RMR. Namely, this is to reduce the mass of the vehicle. However, the RMR's mass-reduction is regulated to maintain sufficient occupant safety performance. Therefore, for practical application of mass-reduction, the Material and Gauge Parameters were weighted the heaviest and equally to each-other. The CofG Parameters were weighted equally to one another too, as these are equally responsible for assigning safer regions for the mass reduction. Although, due to the combined application of the CofG parameters, they were assigned the least weight. The final parameter, Mass, is weighted greater than the CofG Parameters as the main function of the RMR in this study is to lower vehicle mass. Thus, the Mass scoring acts as a scalar for providing a greater score for the component at the end of the weighted sum-total, signifying the importance in reducing the component's weight. The parameter weight and maximum and minimum scorings for individual parameters are given in Table 42.

Table 42. Weighting Multiplier for RMR Parameter Ranking

Parameter	Weighting	Minimum Weighted Score	Maximum Weighted Score
CofG _{long}	1	3	9
CofG _{trans}	1		
CofG _{vert}	1		
Material	3	3	9
Gauge Thickness	3	3	9
Mass	2	2	6

Table 42 shows that the CofG parameters are combined. This is imperative to the operational rational of the RMR. The combination of the CofG parameters ensures that vehicle light-weighting is accomplished with minimal negative influence on occupant safety. The conjunctive use of CofG parameters generates 75 regional segments throughout the volumetric space of the subject vehicle as shown Figure 44.

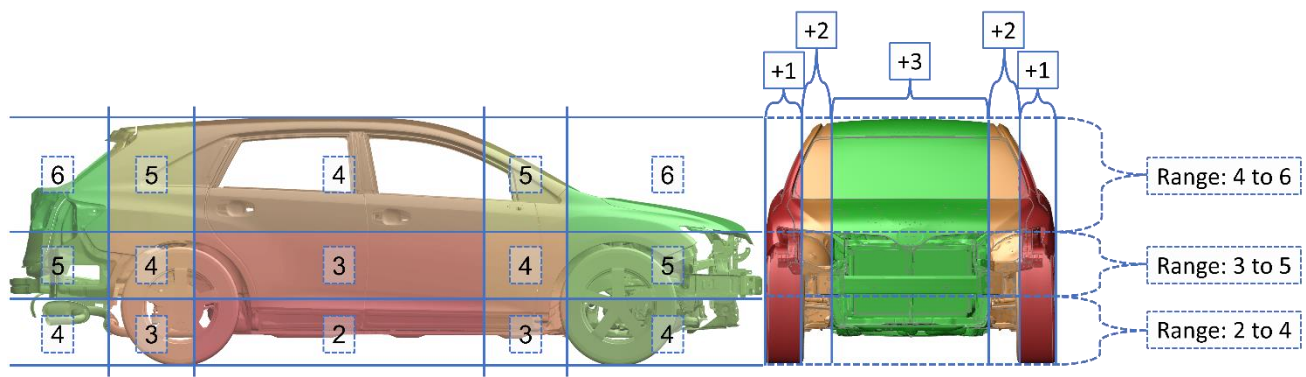


Figure 44. Venza CofG Parameter Combination Overlay

After the multiplication of component scoring by the weighted multiplier in Table 42, a score is achieved for the component by a summation of the component score and multiplier across each parameter. A high value may only be achieved if all categories provide advantageous location, material and component thickness for mass reduction. Consequently, this would not be possible should the component possess great potential within the Gauge parameter, but not in Material or CofG parameters. Further, even if the Material and Gauge parameters suggest a large mass reduction is possible, the lower values of both CofG combined would limit the overall score achieved by the component to 27. Hereby satisfactorily limiting the changes made to the selected component. The minimum total and maximum total achievable are 11 and 33 respectively. The combination and achievable values are shown in Table 43.

Table 43. RMR Scoring Values

Parameter(s)	Parameter Score	CofG Parameter Weighted Score Addition							Weighted Combined Score
		3	4	5	6	7	8	9	
		11	12	13	14	15	16	17	
Mass	2	13	14	15	16	17	18	19	
	3	15	16	17	18	19	20	21	
Gauge	2	14	15	16	17	18	19	20	
	3	17	18	19	20	21	22	23	
Material	2	14	15	16	17	18	19	20	
	3	17	18	19	20	21	22	23	
Mass + Gauge	2+2	16	17	18	19	20	21	22	
	3+2	18	19	20	21	22	23	24	
	2+3	19	20	21	22	23	24	25	
	3+3	21	22	23	24	25	26	27	
Mass + Material	2+2	19	20	21	22	23	24	25	
	3+2	21	22	23	24	25	26	27	
	2+3	19	20	21	22	23	24	25	
	3+3	21	22	23	24	25	26	27	
Gauge+ Material	2+2	17	18	19	20	21	22	23	
	3+2	20	21	22	23	24	25	26	
	2+3	17	18	19	20	21	22	23	
	3+3	23	24	25	26	27	28	29	
Mass + Gauge + Material	2+2+2	19	20	21	22	23	24	25	
	3+2+2	21	22	23	24	25	26	27	
	2+3+2	22	23	24	25	26	27	28	
	3+3+2	24	25	26	27	28	29	30	
	2+2+3	22	23	24	25	26	27	28	
	3+3+3	27	28	29	30	31	32	33	

The scoring methodology provides 175 different combinations to achieve the values shown in Table 43. Value ranges 19 to 24 each provide a distribution of 8% or higher in likelihood of attainment. The values at closer to the extremities steadily decrease near proportional. This highlights that the RMR ranking method follows closely to a normal distribution curve, denoting that the weighting criteria of each parameter is sufficient and does not heavily favour extreme mass reduction. The establishment of the RMR ranking and values enables implementation of the mass reduction procedure, utilising the material database and gauge thinning parameters as defined in section 5.2.1.

RMR Employment

The RMR requires the complete Bill of Materials (BOM) of the subject vehicle for setting and operating control of parameters. A complete list of each part or assembly and the relevant information for the RMR process is available in the BOM. These are namely:

- Part Identification Number (PID)
- Section Identification Number (SID)
- Material Identification Number (MID)
- Material Name
- Material Type
- Gauge Thickness
- Component CofG
- Component Structural and Part Mass

In addition to the listed items above, the BOM also provides other details pertinent to finite element modelling, namely the Hourglass (HG) ID, HG type, Number of Integration points through shell thickness (NIP) and Element Formulation (ELform). The finite element specific attributes aid in the management and control of elements and shells throughout the changes and application of the RMR process in which the previous HG type or Element formulation is not supported by the material or section properties.

The parameters and weighting attributes are applied to the BOM in MS Excel. The ranked result is used to filter components for targeting mass reduction. If component attributes lay outside of the defined parameters, as discussed in the 'Component Material Parameter Definition' sub-section, a value is not provided for that component. Table 44 provides the estimated mass reduction by component and vehicle level achievable by the RMR upon the Venza model.

Table 44. RMR Summated Bounds and Estimated Mass Reduction

SUM Bounds	$33 \geq x \geq 28$	$27 \geq x \geq 25$	$24 \geq x \geq 19$	$18 \geq x \geq 15$	$14 \geq x \geq 11$
Estimated Component Mass Reduction (%)	75	50	25	15	5
Estimated Vehicle Mass Reduction (%)	0.01	8.42	8.13	0.45	0.01
Total Mass Coverage (kg)	68.01	297.88	574.78	43.90	8.11
Total Vehicle Mass (%)	0.04	16.84	32.49	0.03	0.01

Table 44 shows that the total percentage of vehicle mass covered by the bounds of the RMR is approximately 49%, with an estimated total vehicle mass reduction of 17%. Consequently, it can be deduced that 395 components, totalling 776kg, form the remaining 51% of the Venza model. As defined by the scope of the RMR in section 5.1, drivetrain and packaged assemblies are omitted from the RMR procedure. The 'check function' of the material parameter definition (5.2.1) excludes numerous parts and assemblies from RMR listing by omission of material name, returning a 'FALSE' result in the weighted SUM. Only the components identified with a 'TRUE' value are considered. Many of the 'FALSE' components are formed of suspension systems, engine blocks, straps, bolts, radiator modules, adhesives and glass panes. The full list of the material names omitted from the RMR can be found in Appendix III, Table 73. Components omitted from the RMR procedure are visually represented in Figure 45 and Figure 46.

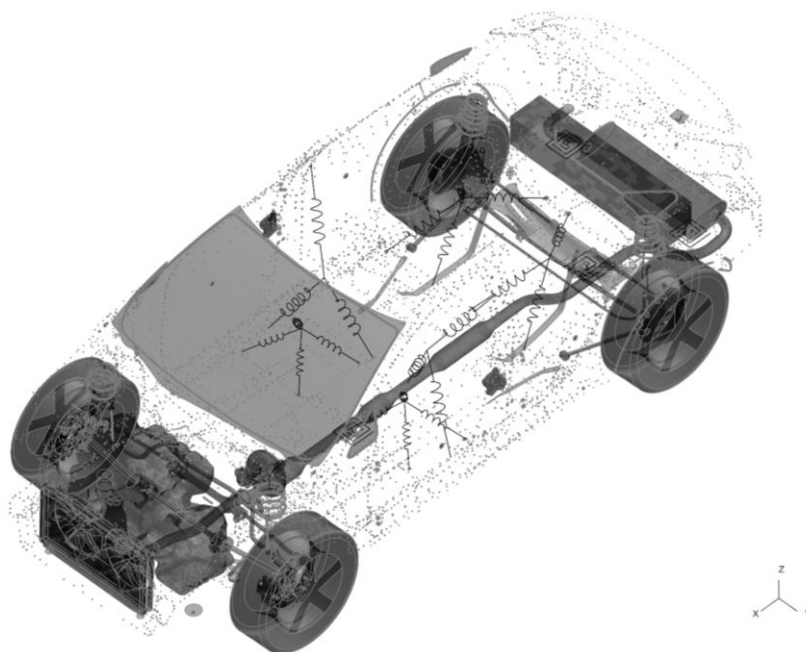


Figure 45. RMR Omitted Parts, Isometric view (Venza)

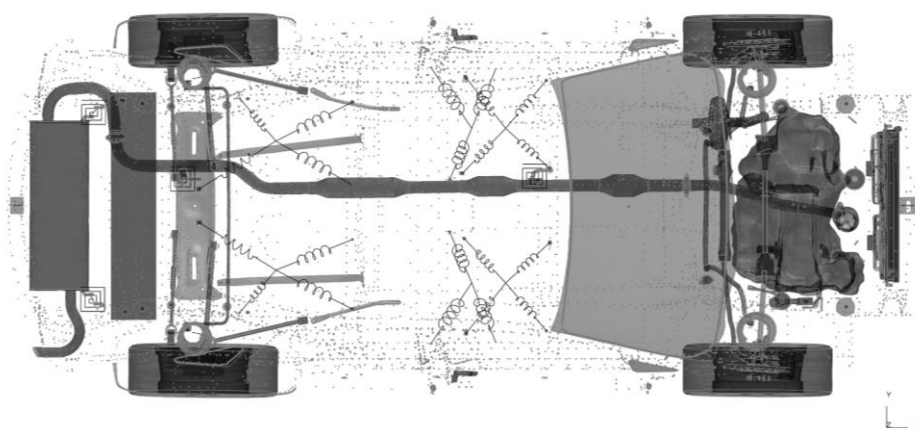


Figure 46. RMR Omitted Parts, Undercarriage view (Venza)

The changes to the BOM are executed in MS Excel for the material and gauge changes suggested by the RMR. This is imported into the BOM of the FE Venza Baseline model to provide the new component data. To assess the RMR and light-weighting possibilities of vehicles, as well as retaining crashworthiness performance in future crash scenarios, the RMR process and the corresponding results are examined and compared to the Light-weight study conducted by Lotus Engineering Inc. (Lotus Engineering Incorporation 2010, NCAC 2014a,

2014b, 2014c). Section 5.3 evaluates the RMR in aspects of time and Light-weighting achievement against the Venza study by Lotus Engineering Inc. Additionally, the crashworthiness performance of the Venza vehicle model post-RMR is examined and evaluated against the ability to retain crashworthiness performance.

5.3 RMR Venza Light-weighting Assessment

The Venza models achieved by the RMR light-weighting methodology are assessed against the Toyota Venza “Low Development Option”. The “High Development Option” does not align with the scope of the research due to the extensive geometrical changes to the chassis, wheelbase and wheeltrack (Lotus Engineering Incorporation 2010: 188-248). Despite the “Low Development” option making alterations to the powertrain, electrical systems and panelling, which is out of the scope of the Light-weighting study, the changes are deemed minor enough to still provide a valid comparison for crash performance and post-design light-weighting.

Unfortunately, the procedure of applying the RMR to established vehicle architecture cannot be compared to the methodology adopted for the “Low Development” and “High Development” vehicle models due to lack of quantitative data regarding labour time and staffing numbers. It can be assumed that the method adopted by Lotus Engineering Incorporation takes a sizable amount of time and labour due to manual examination of each part throughout the vehicle, as well as likely iterations to test the performance of suggested reinforcement panelling or systems. In comparison, the RMR is designed so that quick changes in easily accessible software (such as MS Excel) can be made whilst not altering vehicle geometry. Arguably, the labour intensity for both methodologies would be equivalent if it is assumed there is not a pre-designated material database and tooling method supplied. Regardless, the RMR is designed so that a database of ‘ready’ materials can be applied in the subject vehicle in bulk if the component satisfies the user-defined criteria and ranked-score requirement.

To assess the execution of the RMR, the vehicle data and crashworthiness performance is assessed. The light-weighting study aims to retain levels of crashworthiness and achieve a mass reduction that provides a more

beneficial vehicle mass-ratio for a L7e occupant, as defined in section 4.4. As the Venza has an approximate mass of 1800kg, nearly 4-times greater than a L7e vehicle, the total mass reduction achieved needs to be 24% of the Venza Baseline to lower the bullet to target vehicle mass ratio from 4:1 to 3:1, which is indicated to be the beginning of the injury plateau for L7e occupants.

Alongside the mass reduction accomplished, the vehicle is examined for the same test-case performed by NCAC (2014a). In addition to this, the same sensors and measurement procedures are used to ensure unbiased comparisons. A summary of the crash configuration is provided in Table 45.

Table 45. RMR Summary of Crash Composition

Crash Arrangement	Description	Occupant	Velocity (mph, km/h)	External systems	Evaluation Protocol	Assessment Duration (ms)
FFRW	Full Frontal Rigid Wall	None	25, 40.23	None	IIHS 2017, Euro NCAP 2015	150

No occupant data is available for the Venza, therefore structural performance is recorded. This includes intrusion distance and rate of the occupant cabin, the velocity and acceleration pulse throughout the impact phase and energy absorption with the associated load-path. The vehicle attributes of each Venza revision are provided in section 5.3.1. The results of the impact for the Light-weight Venza models are presented in section 5.3.2 and overall review of the Light-weighting possibilities of M₁ vehicles are provided in section 5.3.3.

5.3.1 Light-weighted Venza Vehicle Data

Vehicle data was extracted to provide a comparison between Venza revisions achieved by the RMR and Lotus method pre-crash. The RMR process is separated for multi-stage comparison. Stage 1 will examine the results obtained by only applying gauge alterations. Stage 2 performs the full RMR with material and gauge modifications.

Table 46 provides the mass and CofG of each vehicle revision, where:

- Venza Baseline: BL
- Venza “Low Development”: LLD

- Venza RMR, gauge changes only: **VLL**
- Venza RMR, gauge and material changes: **VLH**

The 'Allowable Mass Reduction' indicates the permissible mass which can be reduced via the parameters of the RMR whilst the 'Omitted Mass' is the quantifiable mass in which no changes could be made as discussed in section 5.2.2. The comparisons are made against the Baseline Venza Model (BL) regarding the percentage of mass reduction achieved. Blacked out cells are present when there is no applicable data.

Table 46. Venza Revisions Vehicle Data

Measurement Field	Unit	Vehicle Model			
		BL	LLD	VLL	VLH
Total Mass	kg	1768.7	1458.9	1576.4	1309.2
Omitted Mass				896.04	896.04
Allowable Mass Reduction				872.66	872.66
Mass Reduction of vehicle				291.1	192.3
Mass Reduction of vehicle	%			17	11
Mass Reduction of Authorised Components				22	52.7
Vehicle CofG _{long}	mm	-2164	-2075	-2154	-2078
Vehicle CofG _{trans}		-1	-1	-2	-4
Vehicle CofG _{vert}		586	565	573	554

Table 46 shows that the VLH retains the BL CofG within 5% (86mm) and 9% (32mm) in the longitudinal and vertical axis respectively. In comparison to LLD, the longitudinal displacement is 10mm more forward and the CofG lowers by 13mm. This has benefits to resisting roll-over and is caused by the preferences set in the CofG_{vert} parameter (5.2.1). The lateral CofG of the VLH model had shifted by -3mm in comparison to BL, this can be accounted for by the engine block and drivetrain not being repositioned during the RMR procedure. It can be seen in Table 46 that only applying stage-1 of the RMR yields 6% less mass reduction than the LLD and 15% less than VLH. This is to be expected as Table 38 and Table 40 suggest the greatest mass savings are obtainable by the material change and not the component thickness, despite greater vehicle coverage of the gauge parameter. Despite the reduced number of components for the RMR procedure in comparison to the LLD, the VLH had achieved a 26% overall vehicle mass reduction (52.7% of authorised components). Providing

9% more mass reduction than the LLD. Additionally, the mass ratio to an L7e vehicle was reduced from 3.9 (BL) to 3.5 (VLL) and 2.9 (VLH). As proposed in section 4.4, the decrease of an entire ratio suggests that the risk of injury to a L7e occupant could reduce by 30% in key criterion. However, vehicle light-weighting could introduce different interactions between components and may incur difficulties for crashworthiness performance for regulation and consumer testing. The performance of the RMR to reduce the vehicle mass and retain crash performance is assessed in section 5.3.2.

5.3.2 Light-weighted Venza Crash Performance

The crash configuration described in Table 45 is applied to all vehicle revisions. No changes were made to the BL or LLD model, nor changes to the material modelling provided by the NHTSA Venza FE models (NHTSA 2014b, NCAC 2014b, 2014c). Consistent data extraction methods were used across all vehicle models to identify the Energy, Crush Load-path, Crash Pulse and Velocity and Occupant Compartment Intrusions. Where applicable the results obtained in the sub-sections listed are used for Valuation by Consumer Testing.

Energy Balance

The energy balance across the vehicle models were examined to ensure validity and robustness. Establishing the same energy readings in the analysis as those provided by NCAC certifies the RMR models as comparable counterparts. All models provide a similar response curve for global energy readings as that presented in Figure 48. The initial 'wave' of total energy is provided by the initiation of pressure within the vehicle tyres by method of AIRBAG SIMPLE_PRESSURE_VOLUME. The energy ratio of each revision rests within acceptable boundaries of less than 10% variation from unity. However, the general guideline for HGE is that it should remain within 5% of the total energy of the model at any stage, which the LLD revision of the Venza vehicle model does not. Table 47 presents the Energy Ratio of each vehicle revision as well as the maximum Hourglass Energy (HGE) and how much Total Energy (TE) is formed by the HGE.

Table 47. Energy Ratio and Hourglass Energy of Venza Vehicle Revisions

Maximum Energy:	Model			
	BL	LLD	VLL	VLH
Ratio	1.03	1.059	1.016	1.025

Hourglass (kJ)	4.014	6.985	1.733	0.809
HE/TE (%)	3.4	7.1	1.7	0.9

The large HGE reported in the LLD may cause artificial stiffening in the results obtained and may not represent the true values that the vehicle would achieve. Nonetheless, the performance of the RMR is primarily focused upon the BL vehicle model, therefore comparisons to the BL model and an accurate assessment of the RMR's performance can be obtained. Comparison to the LLD model is also viable with visual and numerical inspection in components and vehicle regions that possess the higher HGE readings. Figure 47 shows the components of LLD that sum to 4.7% of the global HGE/TE. The list of parts as provided by the NHTSA Crash Simulation Vehicle Model (2014c) are provided in Table 74 within Appendix IV.

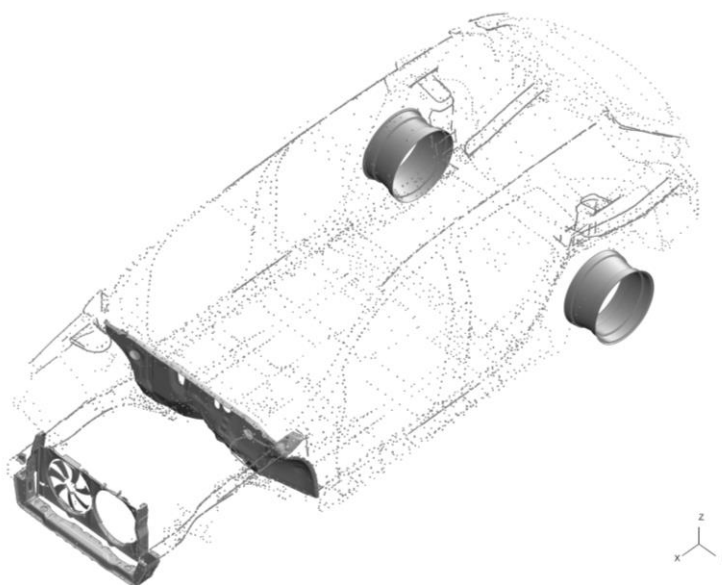


Figure 47. LLD Components with high Hourglass Energy

The global energy curves across all revisions of the Venza vehicle model are similar to those shown in Figure 48, all energy curves can be found in Appendix IV. The TE and initial Kinetic Energy (KE) are representative of the vehicle mass and starting velocity, so this ensures that there were no issues regarding point masses applied to the BL model during the RMR procedure.

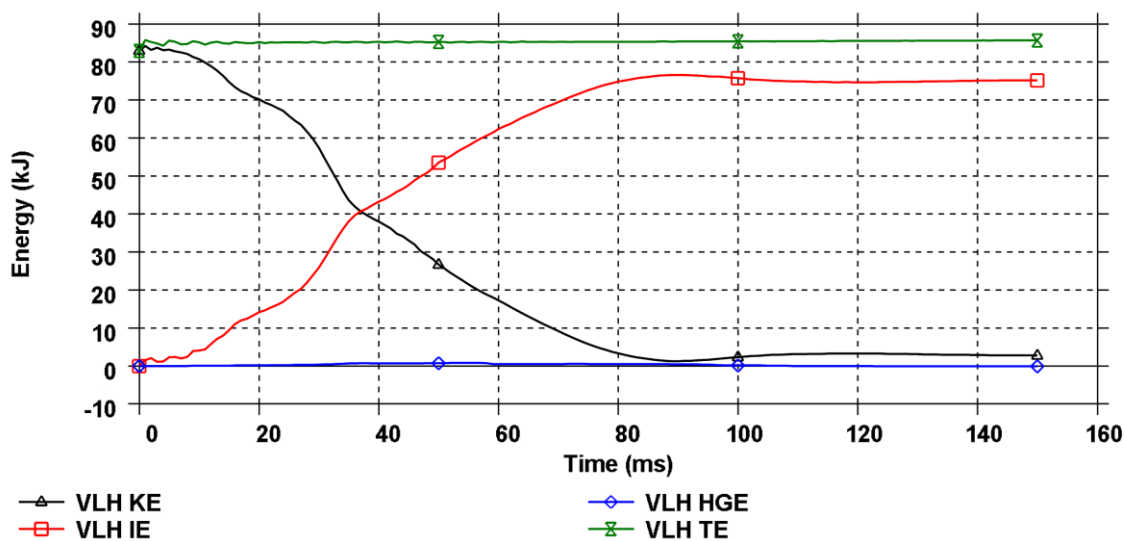


Figure 48. VLH Venza Energy Curve

The general trend of the KE is that it will decrease as the IE increases as shown in Figure 48, other energy forms such as the HGE, contact energy (sliding interface energy) and system damping energy all form the remainder of the energy difference between the Internal Energy (IE) and TE. However, the LLD energy curve has a visibly higher HGE which extends above the IE at 55ms into the simulation. This causes the total energy to rise by approximately 2.3kJ after the airbag deployment phase (0-20ms).

Crush Load-path

The direction and distribution of the loads during an impact are imperative to occupant safety and vehicle performance. The vehicle structures must be able to withstand extreme loads and yield in a desirable fashion, absorbing as much of the kinetic energy of the impact as possible. Front crash rails are typically formed for a progressive development that increases stiffness throughout the progression of the crushing process.. This prevents heavy accelerations being transferred to the occupant which would increase injury risk. Many methods are used to improve the efficiency of crush-rails or possibly change the load-path, as detailed throughout section 2.4. However, it is desirable for RMR to retain the designed load-path whilst reducing the strength of the frontal structures for reduced aggressivity. Therefore, the load-path and energy absorbed by the components in each model were examined. To identify the main load-path during crash progression, only

components that exhibited an IE of 0.35kJ or more were selected as the rate of IE recorded greatly increased in each model at this result. Limiting the threshold to 0.35kJ also provides an overview of component interactions and engagements between models. Figure 49 and Figure 50 shows the cut-sections, by model, of the components that possessed the greatest quantity of internal energy at any time within 150ms. The tyres were omitted due to the pressurisation of the wheels causing high initial IE recordings. The welds across the vehicle had also been dismissed as the weld IE was computed globally. The exclusion of the welds and tyres from the IE calculation is of little significance as they are consistent between each model, and it is believed they will not affect the results or component interactions sufficiently enough for consideration.

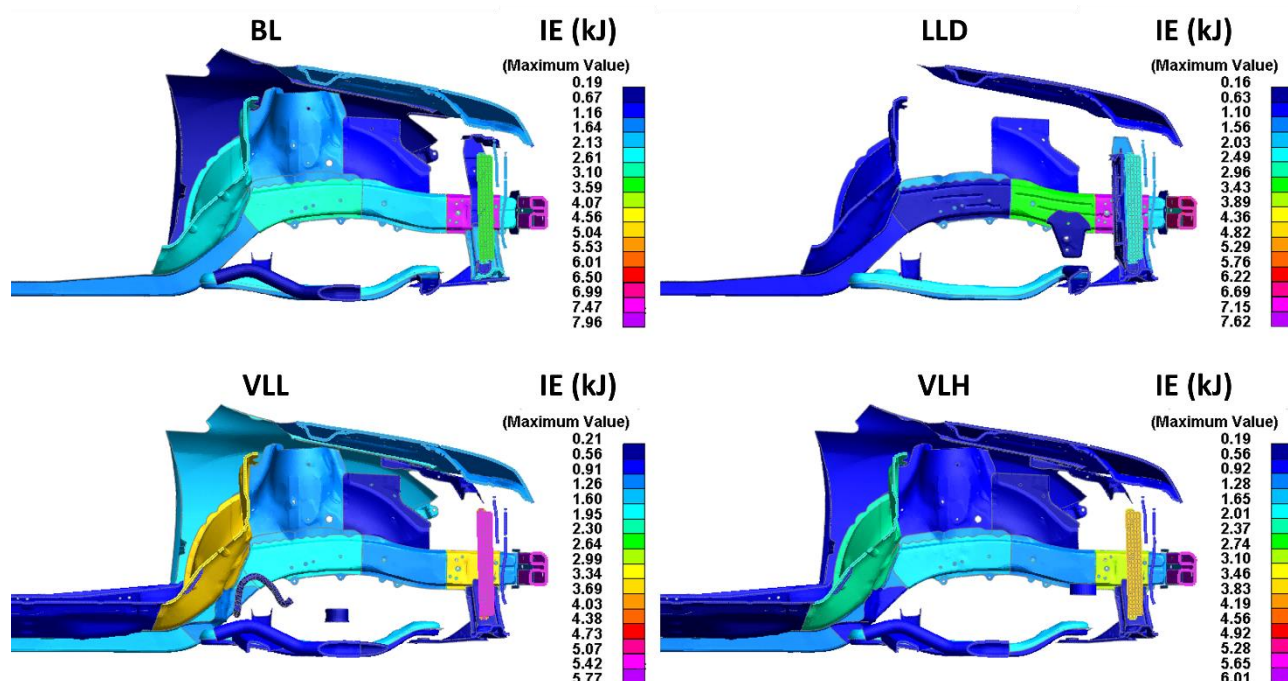


Figure 49. Venza Comparison of Leading Component IE (XZ)

Figure 49 shows that the front crash beam in each model absorbed the most energy for the respective vehicle. The LLD is the only model in which the IE absorbed by components decreases systematically throughout the progression of the vehicle crash structure (right to left). The systematic progression of IE through the collapse of the crash rail highlights the stiffness progression and effectiveness of the crash rail structure in absorbing the impact energy as the crush distance progresses. The crash beam and crash cans form the foremost part of the crash rails and in all models a high component IE is exhibited. Other than the LLD variation and excluding

the crash rails and crash cans, higher IE is exhibited in the mid-section of the crash rails than the foremost sub-component which is affixed behind the crash can. The higher IE exhibited in rearward components, combined with inconsistent IE reduction throughout the front crash rail, suggests that the sub-components that form the complete crash rail are less effective in absorbing and managing the impact energy. The greater engagement of rearward structures of the front crash rails is visibly identified in Figure 50, which shows that the occupant floor was minimally involved in energy absorption within the VLL and VLH variations.

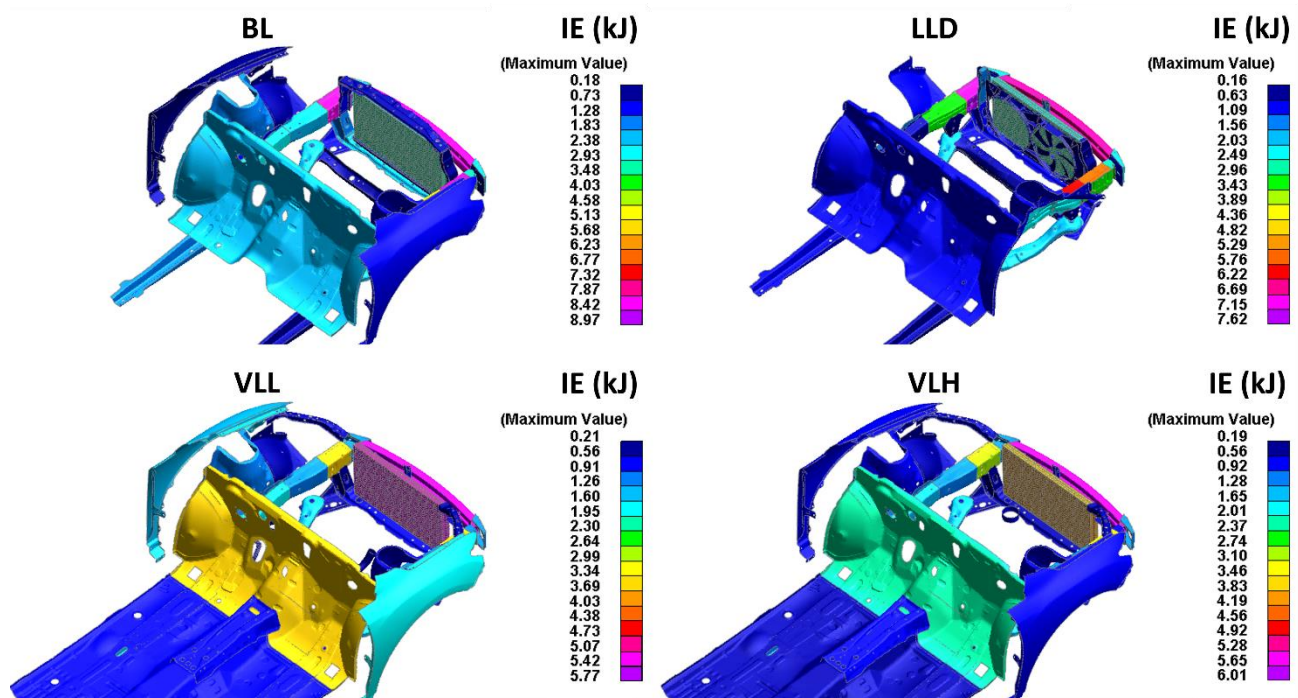


Figure 50. Venza Comparison of Leading Component IE (ISO)

In addition, BL and LLD variations show an asymmetric absorption between the two front rails, lending towards a greater energy absorption on one side of the vehicle. The BL provides evidence of the right side absorbing more KE than the left, but the opposite is present in the LLD model. Owing to the RMR process, the VLL and VLH models express equal absorption on both sides of the vehicle. Furthermore, the amount of energy absorbed by the components in VLL and VLH is less than that of the BL and LLD models. Therefore, the efficiency of KE absorption of the components shown in both, Figure 49 and Figure 50 are presented in Table 48.

Table 48. Venza Component Internal Energy Efficiency

Model	Initial KE (kJ)	Total IE (Global) (kJ)	Total KE into IE (%)	Amount of KE absorbed by components (%)	Component IE of global IE (%)	N°. of Components above 35kJ
BL	112.82	109.40	96.97	79.11	81.58	54
LLD	93.93	91.47	97.38	79.81	81.96	46
VLL	99.56	90.60	91.00	67.34	74.00	56
VLH	82.98	76.63	92.35	67.05	72.61	54

Table 48 provides the efficiency of the listed components in absorbing the KE of the vehicle model as well as the total percentage of the KE converted to IE. The results show that an approximate reduction of initial KE between the BL and VLH vehicle models is 30kJ whilst the LLD vehicle model provides an initial KE reduction of 19kJ which aligns with the vehicle mass reduction achieved by these model revisions. As identified through sections 2.3 and 2.4, the reduction of initial KE is fundamental in the achievement of improving inter-category crash-compatibility. The other factor to consider from the test case is the amount of KE converted to IE as this signifies the efficiency of the vehicle architecture to absorb loads effectively. Table 48 highlights that all vehicles achieved over 90% conversion of KE into IE. By analysing the amount of IE that the listed components provide of the complete vehicle, the LLD provides the greatest percentage and requires 8 fewer parts than the BL. The 'Front Bumper Cross Member' was responsible for the most energy absorption across each model. Through BL to VLH, the 'Front Bumper Cross Member' energy absorption constituted to 63%, 70%, 58% and 73% of the total absorbed. The key item to note here is that the energy absorbing efficiency of the 'Front Bumper Cross Member' increased. Furthermore, the VLH had achieved 3% more than LLD despite retaining the gauge thickness of BL. In contrast, the 'Front Bumper Cross Member' of the LLD possessed a gauge thickness of 3.6mm, nearly triple to that of the BL and VLH.

Figure 49 and Figure 50 show the components that exhibited high levels of IE throughout the crash duration. The BL and LLD models achieved an 80% absorption of KE with those components. In contrast, the VLL and

VLH achieve 13% less. This indicates that the load is distributed across other components of the vehicle model which were not initially designed for defensive structures. Another perspective is that the light-weighted components perform underwhelmingly against the rigid wall opposition, increasing the forces and intrusions experienced by the occupant cabin and not sufficiently reducing the impact acceleration. However, it should be noted that the rigid-wall test-case showcases the ability to overcome the forces provided by the test vehicle, therefore not representing a real scenario. This is factored into the assessment of the RMR within section 5.3.3 as the process aims to reduce the aggressivity and the efficiency of the frontal crash rails to improve inter-category crash-compatibility. Thus, it can be conjectured that the lower energy absorption by the components shown in Figure 49 and Figure 50 is beneficial for occupants of an L7e vehicle.

Crash Pulse and Velocity

The occupant compartment velocity was calculated by industry standard practises. The accelerometers were positioned at the base of the vehicle B-pillar to the side of the occupant and driver seating position.

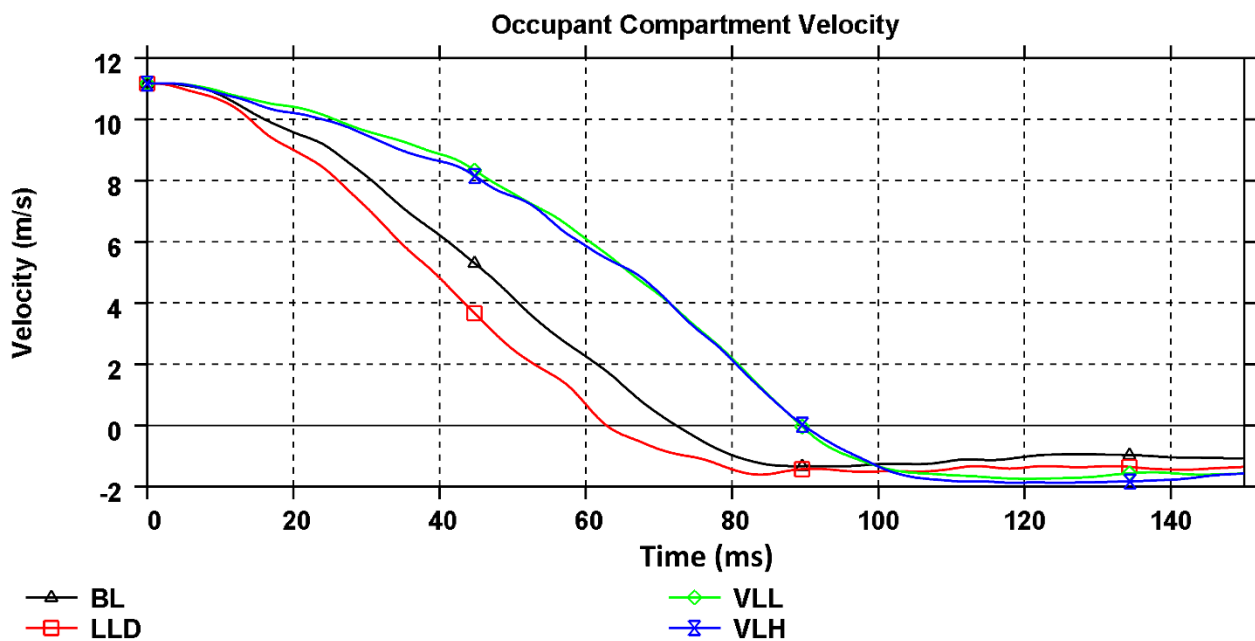


Figure 51. Driver Side Venza Occupant Compartment Velocity

Figure 51 displays the velocity recorded in the occupant compartment. The interception of the zero value on the y-axis signifies the time at which the vehicle stops and begins to bounce-back, caused by the inertial load

falling below threshold and allowing elastic unloading of the vehicle. This is known as the rebound phase and marks the time of maximum crush displacement. The time to zero velocity varies between each model. Table 49 provides the time to zero velocity of each revision for the driver's side. The passenger side has similar time to zero velocity for each revision, all being within 1 millisecond of the driver side counterpart, therefore they are not discussed individually. The passenger side velocity is provided in Appendix IV.

Table 49. Time to Zero Velocity of Venza Models

Vehicle Model Revision	Time to 0 Velocity (ms)	Time Difference to BL (ms)
BL	72.27	0
LLD	62.51	-9.75
VLL	89.39	+17.12
VLH	89.69	+17.42

The LLD vehicle model has the fastest time-to-zero velocity by 9.75ms in comparison to the BL. The VLL and VLH models provide similar results to one another but at 17.12ms and 17.42ms respectively. This difference can be seen in Figure 51 by a noticeably softer gradient of the velocity curve throughout the test duration. The velocity gradient observed by the BL and LLD, in the time interval of 40-75ms, is also displayed by the VLL and VLH, though 17ms later. The delay indicates that there is less resistance throughout the initial contact with the rigid wall before the stiffness and rate of energy absorption 'ramps up' to match that of BL and LLD.

The quicker the vehicle's time to zero velocity, the higher the risk of an occupant sustaining an injury. This is because the change in velocity (Delta-V) occurs within a shorter time frame through the entirety of the crash pulse. The acceleration in the occupant compartment of the Venza models, filtered through SAE C60, are shown in Figure 52. The acceleration of the LLD model is the largest and possesses the greatest rate of change after the time to zero velocity at 62ms. VLL and VLH models provide the same total deceleration over a longer period of time, thus reducing the average acceleration and therefore the injury risk to the occupant. The average deceleration of the BL model is 15.7G, the LLD model increased this by 2.4% whilst VLL and VLH reduce the average G by 2.7% and 2.9% respectively. Figure 52 presents the acceleration recorded for the occupant compartment in the longitudinal direction.

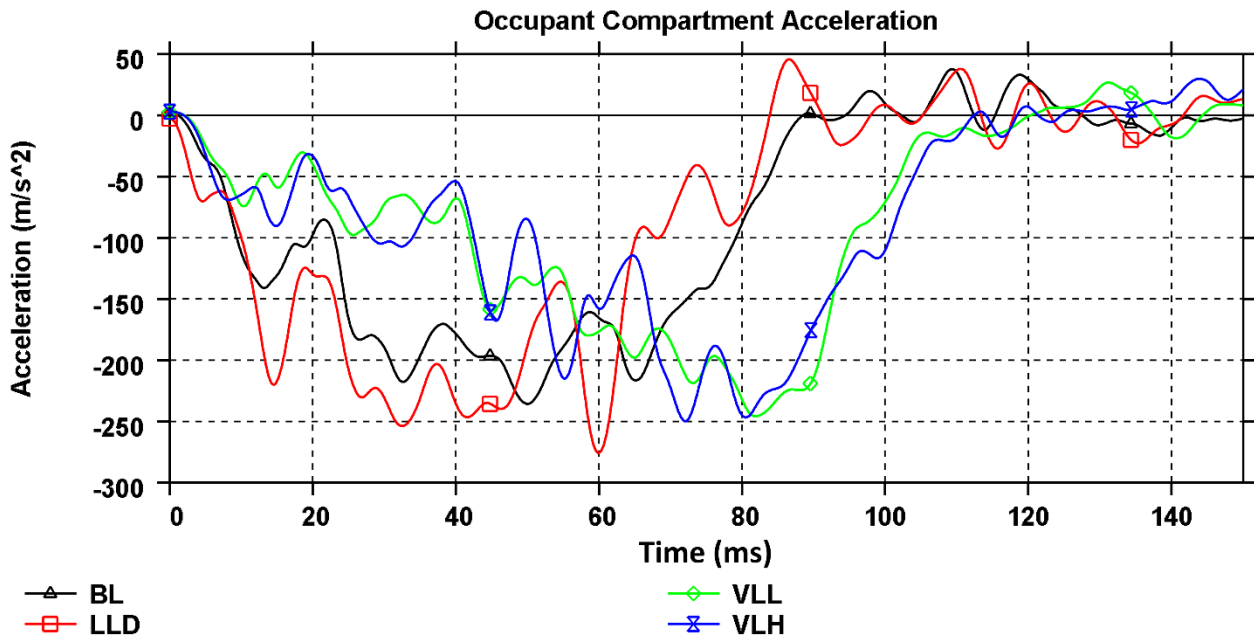


Figure 52. Venza Occupant Compartment Acceleration Comparison (x)

Although the rate of change of velocity for the impact phase is less for VLL and VLH in comparison to the BL and LLD, it could result in larger extrusions to the occupant cabin brought on by an extended crush length. Numerical calculation allows the crush length to be evaluated throughout the complete test-phase, known as the dynamic crush. The dynamic crush it is not reliant on the prediction of the coefficient of restitution of the vehicle structure.

Dynamic Crush

The dynamic crush is defined as the total deformation of the vehicle in a specified vector. The vector for the FFRW test case is along the longitudinal (x-direction) axis. Figure 53 presents the crush length of the vehicle throughout the impact of each Venza model.

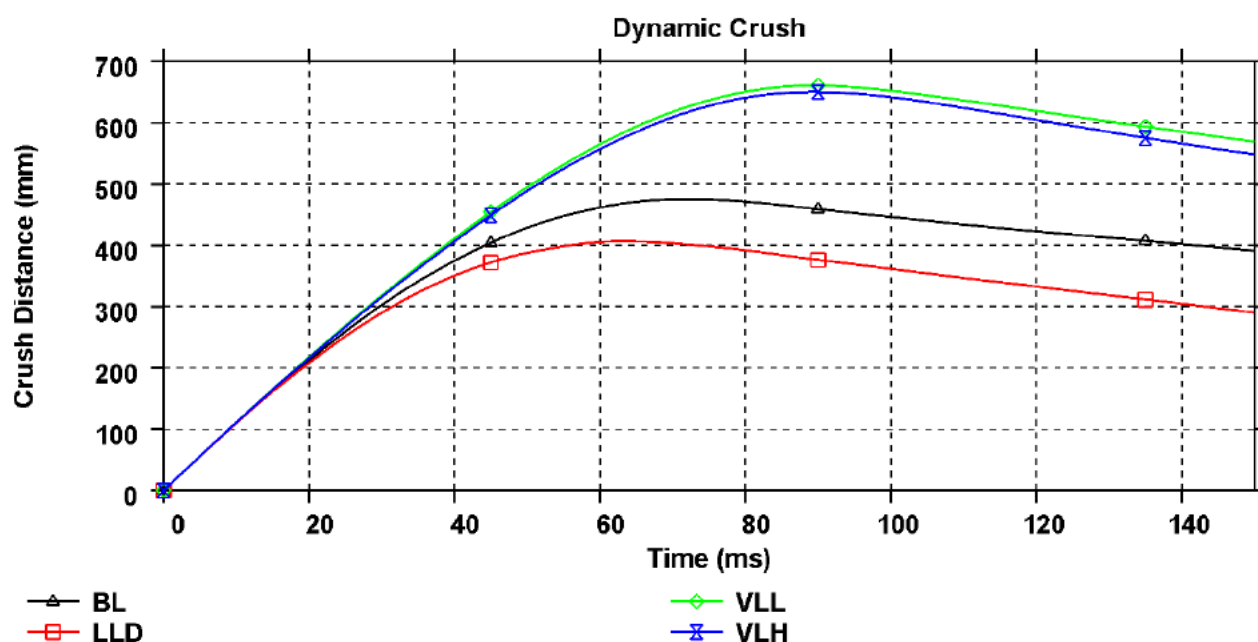


Figure 53. Venza Models Dynamic Crush Comparison

Figure 53 display the average crush length achieved between the left and right side of the vehicle. The Passenger side (right side) exhibits the same response with all values within 2% of the driver's side (maximum of 9mm difference).

Table 50. Driver Side Venza Revision Dynamic Crush

Model	Maximum Crush (mm)	$T_{\max \text{ disp}}$ (ms)	Crush Length of BL (%)
BL	476	72	0
LLD	407	63	85.5
VLL	661	89	138.8
VLH	650	89	136.5

Table 50 provides the maximum crush of the Venza vehicle model of all revisions as well as the percentage difference to the BL model for comparison. The VLH has a larger crush distance of 174mm in comparison to the BL, 243mm greater than the LLD. Despite the much longer crush distance, the deformation pattern of the LLD and VLH are comparable to the BL model. Figure 54 shows the kinematics of deformation of the frontal

structure for each model at the time of maximum intrusion. The general shape of the bonnet follows the same pattern between each model as well as the engagement of the frontal crash beam and crash cans. The crush distance reached by VLL and VLH models suggests a greater utilisation and reliance upon the vehicle tyres to transfer and absorb the forces of impact. This is largely due to the extended crush distance affecting the lower suspension cradle cross member and suspension control arms, as depicted in Figure 55.

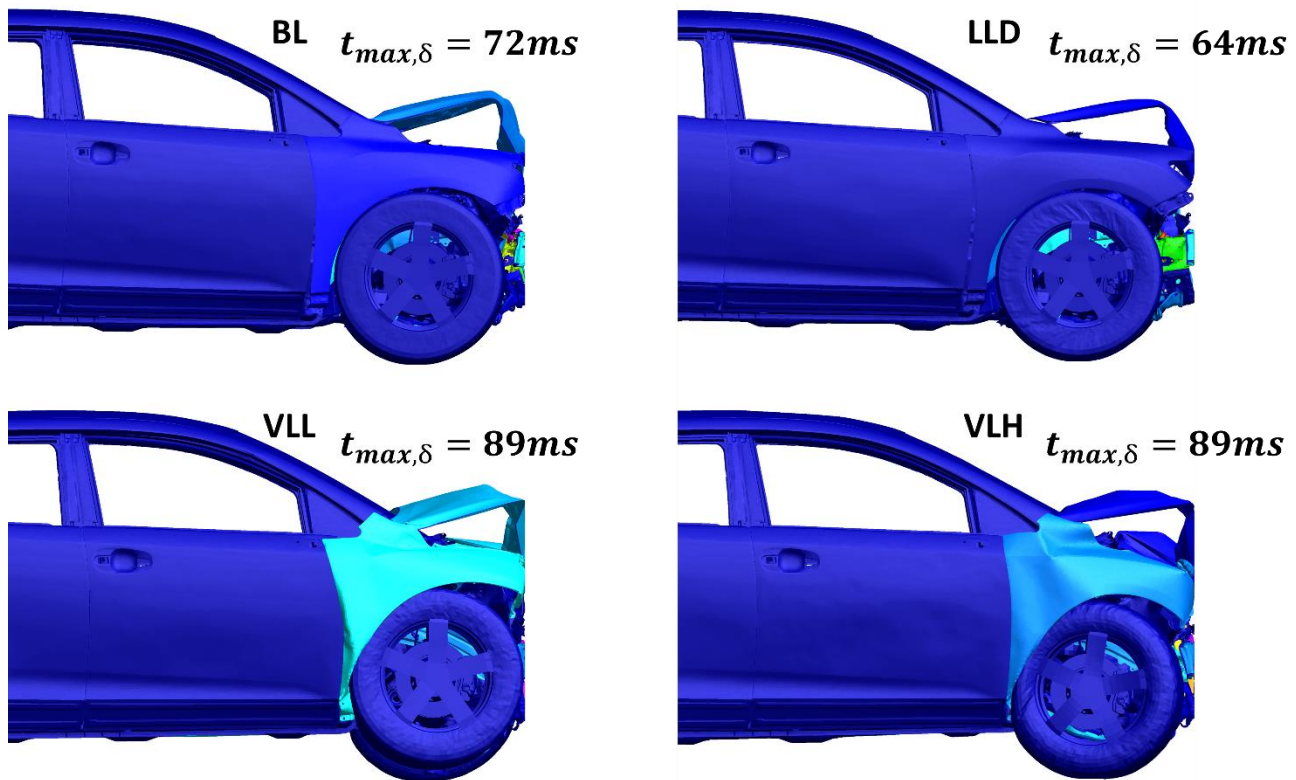


Figure 54. Venza Crash Deformation

Figure 55 shows the kinematics of the crush at the time of maximum crush distance for each model. The paler colours of blue through to yellow reflect the IE of the component. Interestingly, the undercarriage of BL, VLL and VLH demonstrate that the rear sections of the front crash-rails are engaged unsymmetrically across the vehicle, highlighting the effects of the engine block and the effect of the ‘pull’ from engine mounts onto the cradle side rails and suspension arms. Despite the crush length and interaction of the tyres from the VLL and VLH with the footwell panelling, the models exhibit no plastic deformation to the A-pillar beams located behind the front tyres, suggesting that the integrity of the occupant compartment is not compromised and thus possible to retain the occupant injury metrics of the BL model.

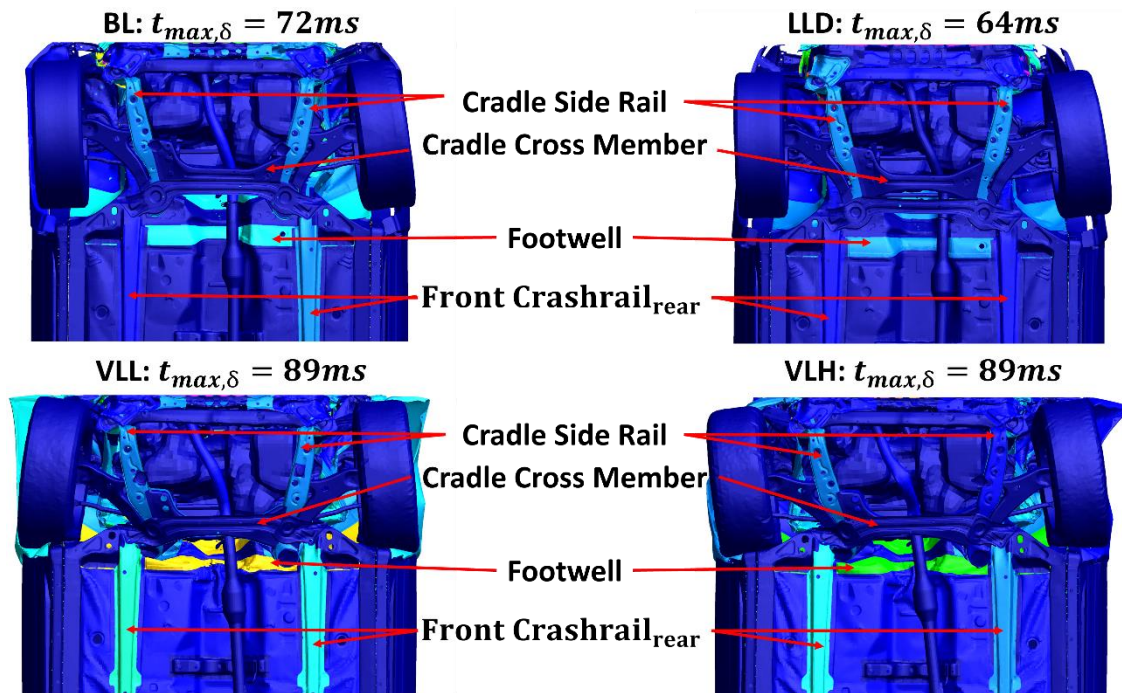


Figure 55. Venza Undercarriage Crush Deformation

Further examination of the crushing mode of the components identified in the section 'Crush Load-path' and Figure 55 reveals that a substantial portion of the crush length is constituted by the lateral distance attained by a buckling mode of the crash rails. Below, Figure 56 shows the components of higher IE for each model, as provided by Figure 49, at the time of maximum crush. The right-hand side of Figure 56 shows the crush kinematics of the various parts of the crash rail and the corresponding lateral displacement of the crash arm.

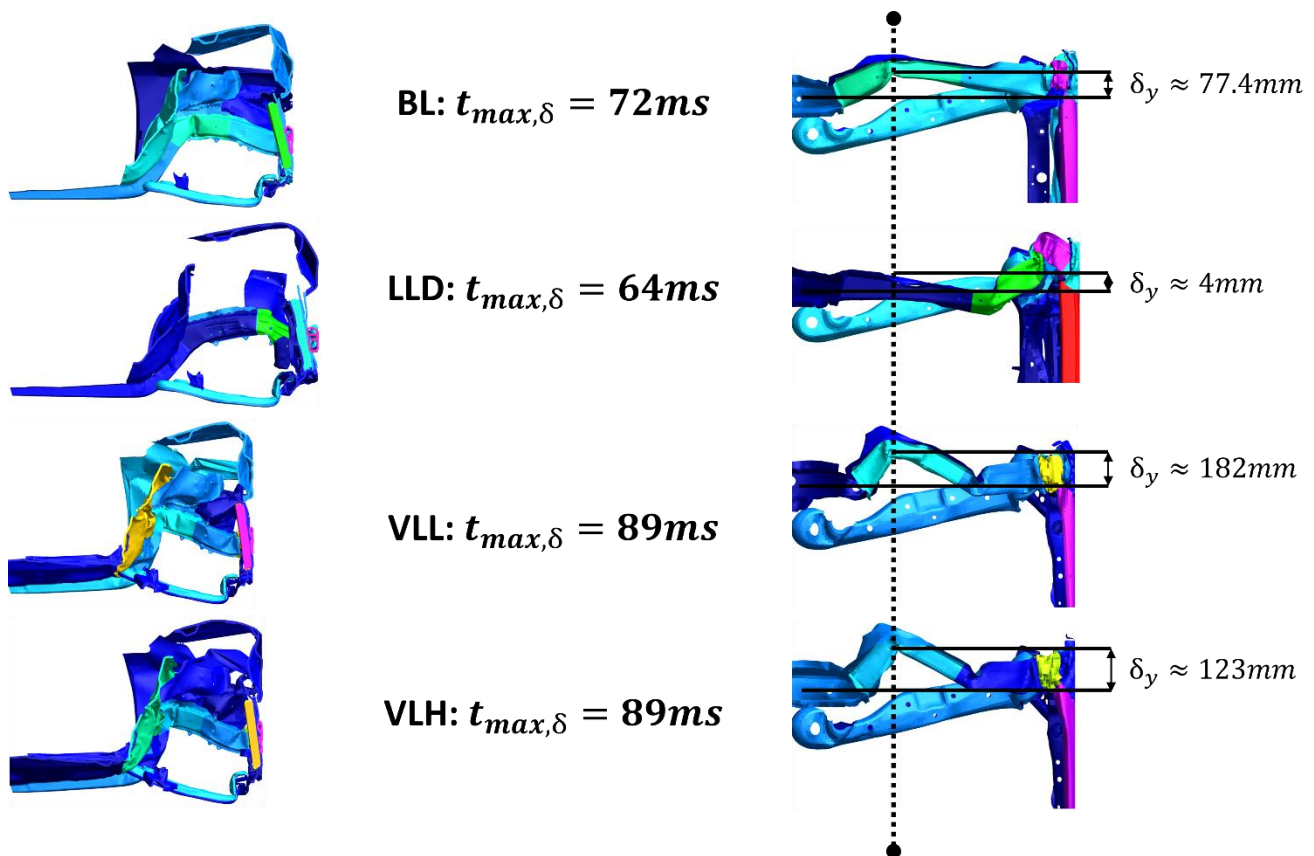


Figure 56. Venza Components Crush Kinematics

The foremost crash cans of the BL, VLL and VLH possessed a straight and good folding mechanism, however the crash rail behind had buckled in the same direction, therefore reducing the absorption capability. In contrast, the LLD crash cans also buckled, however the crash rail remained relatively undeformed. The lateral displacement of the induced buckling modes constitutes to a sizeable portion of the total crush length of the BL (16%), VLL (27%) and VLH (19%) models. Nonetheless, this establishes that the crushing kinematics of the BL are kept throughout the RMR process. Although, the magnitude of deformation for the VLL and VLH models appears to be greater with impact into a rigid wall. On the other hand, this suggests greater benefits to the occupants of L7e vehicles due to the reduced frontal strength and capability to counteract the entailed forces within the distance of the crash beam and front crash cans. The extended crush-length, however, could lead to a greater risk of the occupant sustaining an injury via compartment intrusions.

Occupant Compartment Intrusions

Intrusions and penetrations of the occupant compartment can be the cause of numerous injuries by blunt force trauma. For full frontal impact, the intrusion measurements of the pedal positions, footrest and the steering column are evaluated. Figure 57 annotates the measurement locations used. The IP-R represents the steering column, Footwell shall be called the footrest and the Toepans-L,-C and -R are the clutch, brake and accelerator pedals respectively.

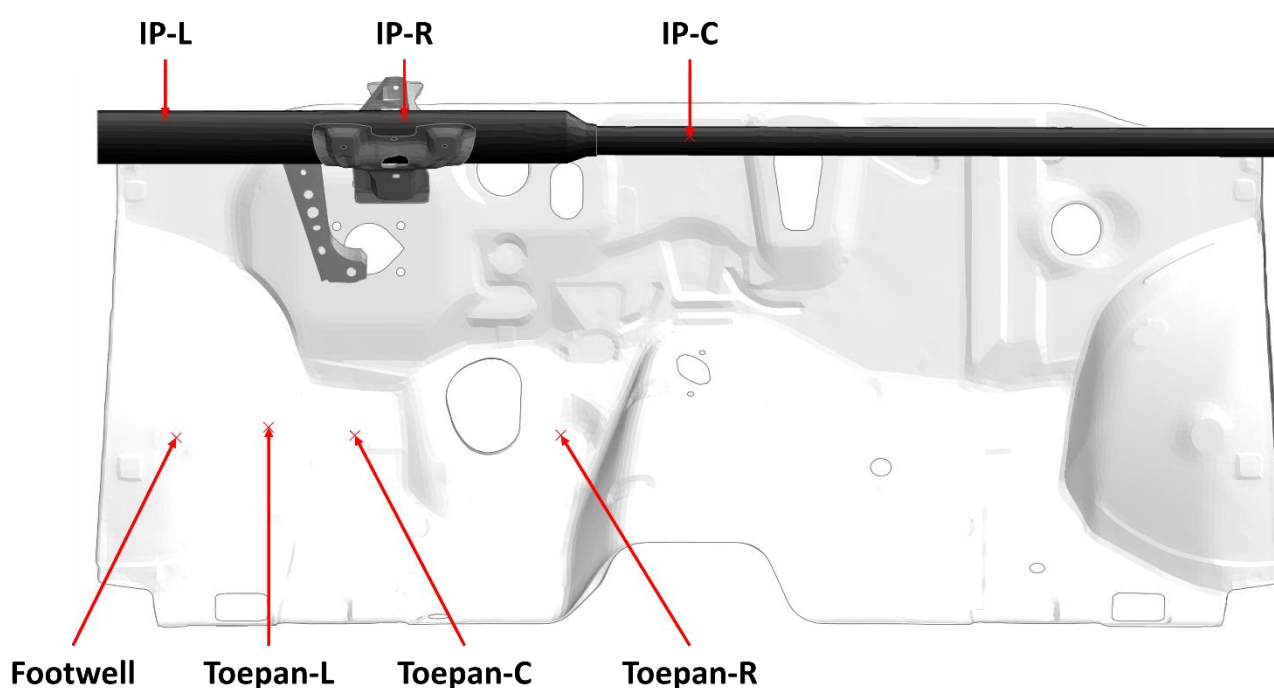


Figure 57. Venza Instrumental Panel and Footwell Panel Measurement Locations

The footrest and pedal locations were calculated by summing the longitudinal and vertical vectors with respect to the B-Pillar location. The Steering Column intrusion is calculated by the vector total of all axes as described in Euro NCAP's Full Width Frontal Impact Test Protocol (2015). Table 51 summarises the maximum intrusion ($Intrusion_{Max}$) calculated by the aforementioned method as well as the time of occurrence (t_{max}).

Table 51. Venza Intrusion Results

Sensor	Name	BL		LLD			VLL			VLH		
		Intrusion _{Max} (mm)	t _{max} (ms)	Intrusion _{Max} (mm)	t _{max} (ms)	Comparison to BL (%)	Intrusion _{Max} (mm)	t _{max} (ms)	Comparison to BL (%)	Intrusion _{Max} (mm)	t _{max} (ms)	Comparison to BL (%)
Footwell	Footrest	26	150	10	79	38	65	92	250	61	91	235
Toepan-L	Clutch Pedal	69	73	21	150	30	134	90	194	127	92	184
Toepan-C	Brake Pedal	78	150	36	150	46	158	91	203	147	91	188
Toepan-R	Accelerator Pedal	55	150	19	150	35	185	91	336	170	91	309
IP-R	Steering Column	26	150	15	150	58	38	92	146	44	93	169

It is shown by Table 51 that the intrusions recorded by the VLL and VLH models all exceed that of the BL whereas the LLD reduced the intrusions significantly. On average, the VLL increases the intrusion by 2.3 times and the VLH increases it on average by a factor of 2.2. In contrast, the LLD achieves an intrusion by a factor of 0.4 to the BL. A general trend across the Footwell panel of the VLL and VLH models is that the intrusion increases with each consecutive sensor from left to right, indicating that the tunnel strength of the Footwell panel had diminished through the RMR procedure. Additionally, the largest intrusions of the VLL and VLH are identified surrounding the time of maximum dynamic crush and time of zero velocity (shown in Table 49 and Table 50) however, the majority of the maximum intrusions of the BL and LLD models are obtained at the end of the test duration. This is visible in Figure 58 which graphically represents Table 51.

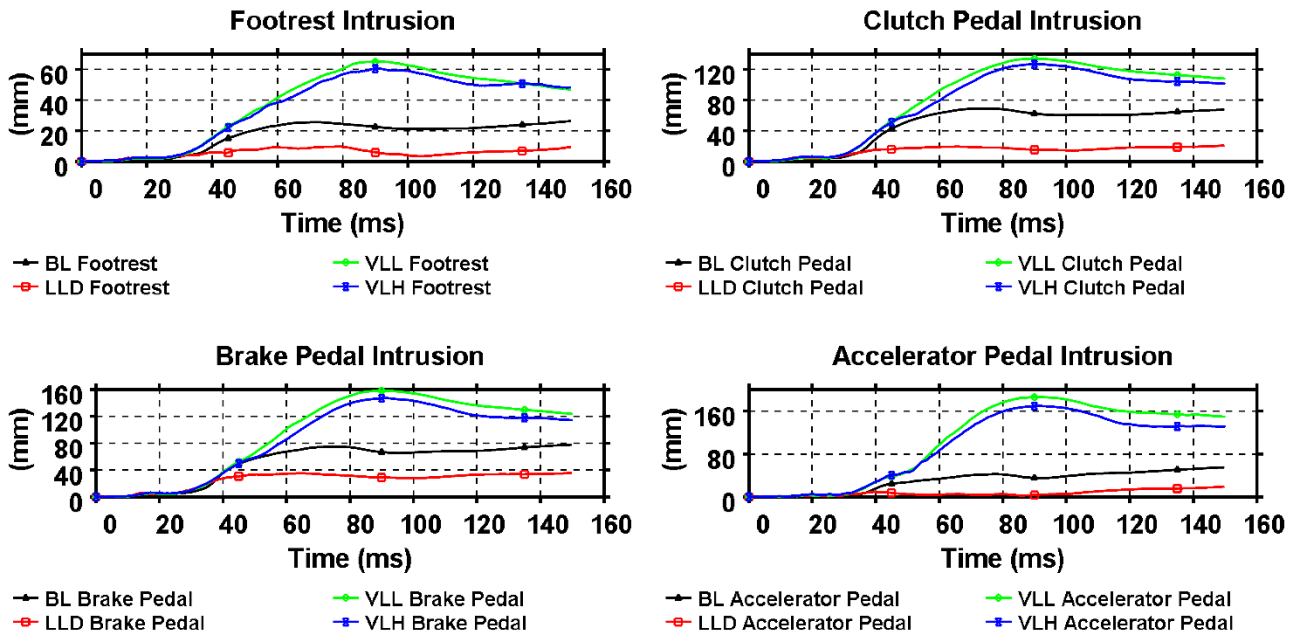


Figure 58. Venza Footwell Intrusions Comparison

VLL and VLH models recorded an intrusion over 3 times greater than the BL model. The sizeable difference is owed to the impact and influence of the engine block to the footwell panel and attached structures. The engine block extends 50mm further towards the occupant in the VLL and VLH models than the BL and LLD (Figure 118, Appendix IV). The engine block intrusion into the occupant space must be avoided otherwise crash safety performance is weakened. Therefore, the intrusion attained by the footwell panel was visually inspected and is provided in Figure 59.

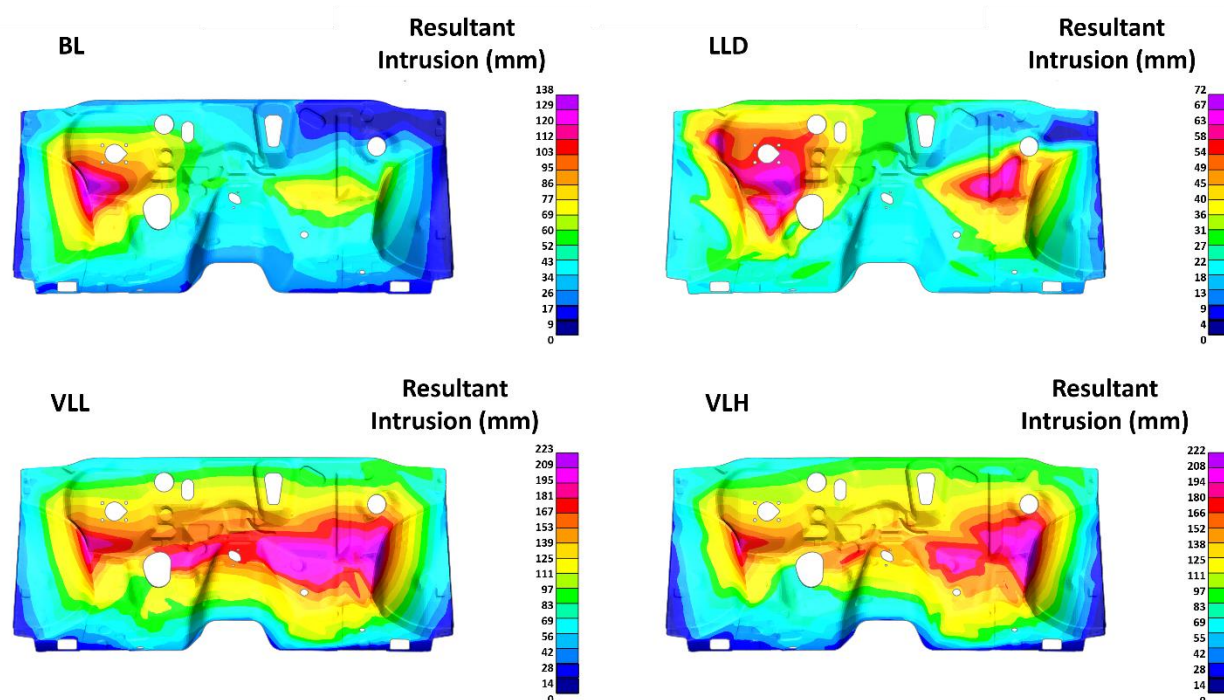


Figure 59. Footwell Panel Resultant Intrusion

Unlike the intrusion recordings, the intrusion plot of Figure 59 includes all directions of relative displacement to assess the compartment integrity. BL and LLD show larger intrusion upon the upper-left corner of the footwell panel, focused around the wheel-arch and panel bend. The two models also possess similar intrusion readings of approximately 70mm on the right side of the footwell panel, despite a total crush length difference of 69mm (Table 50). Similarly, VLL and VLH also share a localised high intrusion on the left hand of the footwell panel, though the right side extends to approximately 210mm. It is also apparent that the areas surrounding the tunnel (centre of the footwell panel) have a large relative displacement of approximately 115mm, approximately 3 times that of the BL. The majority of the intrusion surrounding the tunnel was vertical, thereby weakening the structure further and allowing greater longitudinal intrusion by the engine block located behind the right-hand side of the footwell. Despite the greater displacement of the engine block in the VLL and VLH models, there was no penetrations into the occupant cabin by this component. Nonetheless, Figure 59 implies that the passenger, in this case, may be at greater risk of sustaining an injury than the driver. Yet, the likely impact scenario would be into another vehicle's side structure, not a rigid wall. Therefore, the extended displacement of the engine block of the Venza, induced by the interactions of the front structure, are beneficial

to the occupant of the target vehicle due to the reduced influence of a heavy rigid mass. In addition to the footwell intrusions, the Instrumental Panel (IP) intrusions were examined. The steering column was assessed by the NCAP protocols and IIHS assessment methods (Euro NCAP 2015, IIHS 2016: 3). Similar to other intrusions, the VLL and VLH perform worse than the BL and LLD counterparts, but the difference is not as severe as with other intrusion measurements. The y-component between each revision has less than 12.5mm difference and is therefore not the major contributing factor to the difference in results. As expected, the longitudinal vector provided the greatest difference between revisions. Whilst the maximum longitudinal intrusion of the VLL and VLH models occurs at the approximate time of zero velocity (90 milliseconds), the BL and LLD have longitudinal intrusions that fluctuate around 10mm and 5mm throughout. The maximum intrusion of the BL and LLD is apparent at the end of the test phase alike other metrics, whereas the time of maximum intrusion for the VLL and VLH occurs at 90ms before reducing. The VLH intrusion begins to rise once again at 120ms in the same pattern as BL and LLD. However, the small fluctuations of millimetre changes may be the result of small bounces in components and movement of the vehicle as neither vehicle had come to rest by the end of the test duration.

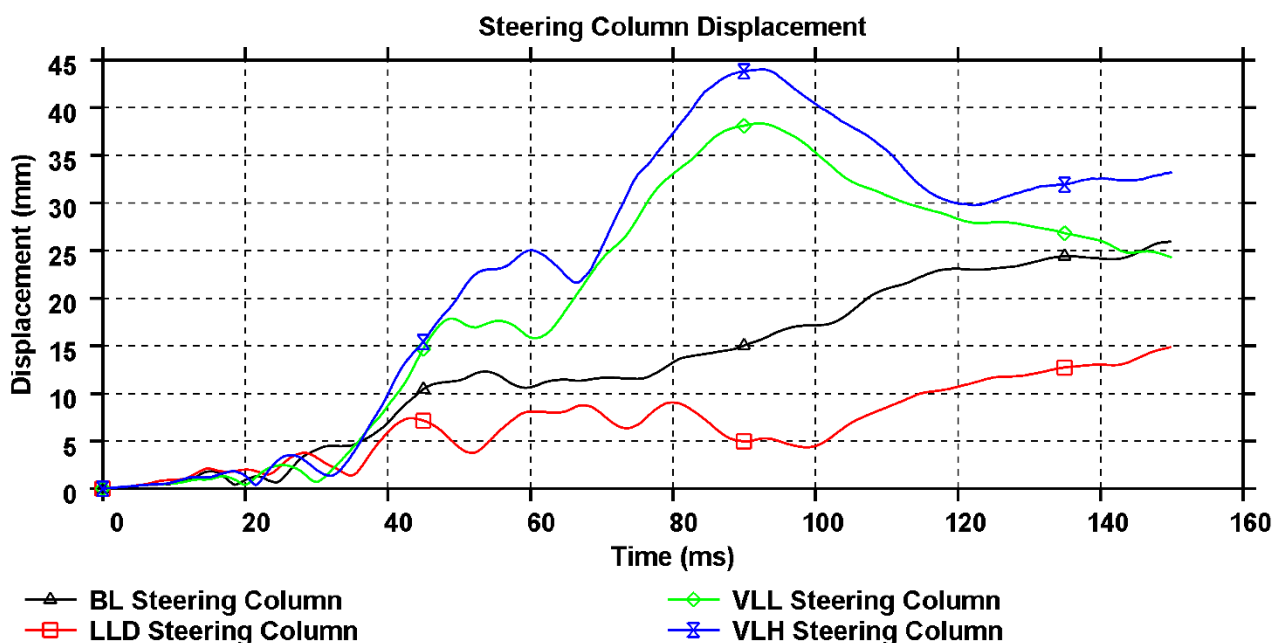


Figure 60. Steering Column Relative Displacement

Valuation by Consumer Testing

Consumer testing provides a rating for the crashworthiness performance of a vehicle, rather than a pass or fail assessment as discussed in section 2.3.1. Utilisation of the Moderate Overlap Structural Performance evaluation procedure provides bounds for the structural performance score of the Venza (IIHS 2016). Only the structural performance is assessed because there is lack of occupant data, restraint systems and seating positions. Moreover, the primary focus of the light-weighting study was to evaluate the feasibility of light-weighting a vehicle and maintaining crashworthiness performance. Table 52 presents the IIHS occupant compartment intrusion guidelines for rating the performance of the Venza. All bounds are measured in millimetres and ' i_v ' signifies the absolute sum of intrusion vectors recorded.

Table 52. IIHS Rating for Occupant Compartment Intrusion (2016: 3)

Parameter	Good	Acceptable	Marginal	Poor
Footrest	$0 \leq i_v \leq 150$	$150 < i_v \leq 225$	$225 < i_v \leq 300$	$300 < i_v$
Left Toepan	$0 \leq i_v \leq 150$	$150 < i_v \leq 225$	$225 < i_v \leq 300$	$300 < i_v$
Centre Toepan	$0 \leq i_v \leq 150$	$150 < i_v \leq 225$	$225 < i_v \leq 300$	$300 < i_v$
Right Toepan	$0 \leq i_v \leq 150$	$150 < i_v \leq 225$	$225 < i_v \leq 300$	$300 < i_v$
Steering Column	$0 \leq i_v \leq 50$	$50 < i_v \leq 100$	$100 < i_v \leq 150$	$150 < i_v$

The IIHS guidelines are applied to the resulting vectors of the footrest, pedals and steering column, the outcomes are shown in Table 53. The steering column results only utilised the x-direction (towards occupant seating) in accordance with IIHS (2016). Displacement of the steering column is measured in all axes but without an occupant model and safety system details, the other components of displacement have been omitted as it is unknown whether they could cause significant injuries or equipment malfunction.

Table 53. Intrusion Rating Performance of Venza

Vehicle Metric	Name	BL		LLD		VLL		VLH	
		i_v (mm)	Rating	i_v (mm)	Rating	i_v (mm)	Rating	i_v (mm)	Rating
Footwell	Footrest	26.4	Good	9.8	Good	65.1	Good	60.8	Good
Toepan-L	Clutch Pedal	69.2	Good	20.9	Good	134.1	Good	127.2	Good
Toepan-C	Brake Pedal	77.9	Good	35.8	Good	158.3	Acpt.	147.1	Good
Toepan-R	Accelerator Pedal	55.2	Good	19.2	Good	185.9	Acpt.	169.6	Acpt.
IP-R	Steering Column	10.4	Good	5.4	Good	33.9	Good	40.6	Good

Despite many of the VLH's intrusion metrics being larger than the BL, the majority had maintained the 'Good' rating, the worst result located at the right toepan, landing in the 'Acceptable' (Acpt.) category by 14.6mm. As discussed in the sub-section "Dynamic Crush", this is likely caused by the extended distance of the engine block and the yield-path of engine-mount components combined with the buckling mode of deformation of the mid and rear front rails.

5.3.3 Performance of RMR Conclusion

The RMR performance is evaluated on the ability to reduce vehicle mass at a component level toward a proposed favourable mass ratio for occupants of an L7e vehicle. The favourable mass ratio was identified in section 4.3 as a maximum of 3:1 bullet to target vehicle. The process and outcome of the light-weighting procedure is compared to the process and outcome of the in-depth Light-weighting study conducted by Lotus Engineering Inc. (2010). Lastly, the crashworthiness performance of the light-weighted vehicles are compared in the established test-scenario conducted by NCAC (2014a, 2014b). This is accomplished with the aid of IIHS and Euro NCAP evaluation protocols and criteria (IIHS 2016, Euro NCAP 2015). The results discussed throughout sections 5.3.1 and 5.3.2 are summarised in Table 54. The actual values of each criterion are provided as well as the percentage change to the BL vehicle.

Table 54. Venza Performance Overview

Criteria	Measures	Vehicle Model		
		BL	LLD	VLH
Vehicle Mass	Structural (kg)	1768.7	1458.9	1309.2
	Change (%)	0	-18	-26
Vehicle IE of KE	Actual (kJ)	97	97	92
	Change (%)	0	0	-5
Time to Zero Velocity	Actual (ms)	72	63	90
	Change (%)	0	-12.5	+25
Dynamic Crush Length	Actual (mm)	476	407	650
	Change (%)	0	-14	+36
Occupant Compartment Accel	Actual (G)	24	29	27
	Change (%)	0	+21	+13
Intrusion: Steering Column	Actual (mm)	26	15	44
	Change (%)	0	-42	+67
	IIHS Rating	Good	Good	Good
Intrusion: Clutch	Actual (mm)	69	21	127
	Change (%)	0	-67	+84
	IIHS Rating	Good	Good	Good
Intrusion: Brake	Actual (mm)	78	36	147
	Change (%)	0	-54	+88
	IIHS Rating	Good	Good	Good
Intrusion: Accelerator	Actual (mm)	55	19	170
	Change (%)	0	-65	+209
	IIHS Rating	Good	Good	Acceptable
Intrusion: Footrest	Actual (mm)	26	10	61
	Change (%)	0	-62	+134
	IIHS Rating	Good	Good	Good

The light-weighting procedure of the RMR is readily applicable to an existing vehicle design. The component exclusion method of the RMR helps develop greater fixtures to constraints. The RMR used in this study omitted glass panelling, drivetrain parts and components modelled by solids or spring and beam systems by use of string search function in the BOM. In contrast, the LLD version had no limitations, an example is provided by the reduction of engine mass from 235kg (used within the BL and VLH vehicle) to 188kg, making an initial saving of 47kg. The manual process adopted by Lotus Engineering Inc also allows tuning of systems and addition of components throughout the light-weighting procedure for driving performance. On the other hand, it is assumed that the labour intensity required to complete light-weighting procedure and material is heavy. In contrast, the RMR parameters and weighting criteria is quickly applicable to the complete vehicle

and is not labour intensive. This is further reduced if the vehicle manufacturer has already established a database of permitted materials and manufacturing techniques, else the labour intensity of material identification stage of the RMR is equivalent to the manual process adopted by Lotus Engineering Inc. In contrast, the manual method supports changes to vehicle architecture to maintain driver comfort, such as NVH. However, as outlined in the scope definition and operational boundaries of the RMR in section 5.1, the RMR procedure does not cater for driving comfort as the primary purpose of the RMR is to reduce the vehicle mass whilst maintaining crash-performance for specific load-cases; thereby increasing the crash efficiency of current and future vehicles.

Despite the limitations to the component and modelling type applied by the RMR, the VLH had achieved a mass target 26% less than the BL, 9% more than was achieved for the LLD. This results in the mass of the VLH equating to 2.9 times greater than an L7e vehicle (450kg), thus passing the target of a 3:1 mass ratio. The mass target was achieved by utilising just 49% of the original mass of the BL vehicle. Thereby, the 26% vehicle reduction is equal to 52.7% of the 'allowable components' as described in section 5.3.1 and Table 46. It can be deduced that the percentage of components that can be altered by the RMR process would increase with a more extensive material database. It can be reasoned that this would provide more favourable conditions for L7e vehicle and increase the feasibility of light-weighting larger M_1 vehicles to ascertain a mass ratio of 3:1 or less.

However, engineering judgement and individual examination of the BL vehicle to achieve the LLD version had proved more successful in retaining the structural crash performance. The LLD had achieved a reduction to the baseline in all intrusion recordings above 40%, retaining all intrusions under 40mm. In contrast, the VLH had achieved an increase of 85% to the BL for the brake and clutch pedals, and a 209% increase in the accelerator pedal. Despite the greater intrusion readings, all but the accelerator pedal remained within the 'Good' classification as highlighted in Table 52. Therefore, by intrusion assessment alone, the VLH had

managed to retain majority of the safety ratings for structural performance, but the LLD had superior performance. On the other hand, by design, the FFRW test-case is expected to increase the dynamic crush length of the VLH. The parameterisation of the RMR directs toward vehicle crash-compatibility and lateral impact safety, as defined in section 5.2. Thus, the VLH may reduce the risks to L7e occupants due to the reduced aggressivity of the vehicle, the reduced mass and the reduced stiffness of frontal crash structures reduces the risk of compromising the target vehicle's occupant compartment. However, the rigid wall within the FFRW does not represent a vehicle's side structure and does not provide a response representative of a two-vehicle collision. Therefore, the slower time to zero velocity, assuming safe intrusion measurements, is more beneficial as the instantaneous force applied to the opposing structure is weakened. This is reflected by the VLH in the time to zero velocity arriving 20ms later than that of BL and 30ms later than LLD. As each vehicle reached the same velocity in the later stages of impact, the decreased time to zero velocity of the VLH aided in accomplishing 2G less driver-seat acceleration than the LLD, though it was 3G more than the BL. The likely cause of the increased acceleration of the VLH is due to the 'ramping effect' caused by the original crash structure design tied with the RMR process to favour a stronger vehicle mid-section. This is displayed by Figure 52 which highlights the general linear progression of deceleration of the occupant cabin until approximately 80ms, narrowly preceding the time of maximum intrusion, before returning to constant velocity at the same rate as the BL. However, the sharp change in acceleration due to the engagement of multiple structures of the occupant cabin is not likely to happen due to the implementation of ADAS to vehicle fleets. As expressed in section 2.3.2: Advances in Crash Avoidance & Mitigation Technology, the impact severity and likelihood of a collision is substantially reduced for arrangements which are not 'blinded' or impaired by obstacles and road infrastructure. Therefore, the feasibility and performance of the RMR to existing vehicle geometries achieves mass reduction targets whilst maintaining sufficient structural performance. Despite this, it is unknown whether the occupant injury risks of an L7e vehicle have been reduced sufficiently enough for a variety of bullet vehicles that have more beneficial mass-ratio as well as targeted light-weighting by the RMR.

To identify the opportunities for inter-category vehicle compatibility between M₁ and L7e, research has been conducted for high-risk collision arrangements of different bullet vehicles into an L7e vehicle that have employed the RMR procedure.

6 Inter-Category Compatibility

The RMR was built and tested with the Venza vehicle model impacting a rigid wall, however this provides the reliance of the vehicle absorbing the total energy within its own crash structures. Thus, to increase the safety of occupants within the L7e and smaller vehicle categories better compatibility is required. The aim of this section is to assess the overall safety performance of the Microcab against larger vehicles before and after the RMR is applied to the bullet vehicle. By this method, the mass-ratios trends identified in section 4.3 would be targeted for a fair comparison, thus providing information regarding compatibility between impact location and vehicle mass-ratio via foremost assessment of occupant injuries sustained.

The research aims to provide new considerations for achieving better inter-category vehicle compatibility and to set a concept which could aid in reaching 'Vision 0'. This is accomplished by concentrating strength in the structures of modern day and near future crash scenarios and thereby maximising the efficiency of vehicle crash structures as a function of total vehicle mass. Additionally, the logic of application of the RMR procedure has the potential to aid in consumer perception and adoption rates of the Heavy-Quadricycle category. Thereby assisting the achievement of EU emissions targets by enhancing small electric vehicle uptake and reducing material use and weight, supplementing the overall drive efficiency of BEV.

The research is accomplished with two vehicles which are representative of extremes within the M_1 category. The same load-case as used in chapter 4 is adopted as this was identified in chapter 3 to pose the greatest risk and likelihood to an occupant of an L7e vehicle within a city environment. The research is defined through the scope of the project and the corresponding assumptions and limitations in section 6.1, the methodology to achieve the research is detailed in section 6.2, followed by detailed results and topical discussion in sections 6.3 and 6.4 respectively.

6.1 Inter-Category Compatibility Scope

The target of the project is to examine the crash behaviour and performance of bullet and target vehicles, in relation to occupant safety, via increased crash-efficiency as a function of vehicle masses. This is accomplished by targeted mass reductions of the bullet and target vehicle to achieve a favourable vehicle mass-ratio for the L7e occupant. The RMR procedure for weight reduction is adopted to achieve the targeted mass reduction of all vehicles, with focus to maintaining or reducing the injuries sustained in the target vehicle. Either vehicle will not receive architectural changes as this would change component interaction between revisions. The research is conducted assuming a lateral crash composition within an inner-city environment as described in chapter 3. The general collision details are summarised in section 6.2, Table 56. The extremes of bullet vehicle selection must provide substantially different mass and size to one another, enabling investigation of the effects of vehicle heights with two-vehicle mass ratios. The goals of the research can be summarised as:

- Evidence for the effectiveness of a partnered and zonal approach to light-weighting and occupant injuries sustained.
- Evidence of crash-efficiency increases of paired vehicles as a function of vehicle masses.
- Demonstration of the contributing factors required to achieve inter-category compatibility and crash safety harmonisation.

The three main goals of the research are realised with the management of assumptions and limitations that help define the research boundaries and practical application of the topic. These are listed and described in Table 55.

Table 55. The Scope Assumptions and Limitations of Compatibility as a Function of Mass

Assumptions of Scope	Description
A _{s1}	ADAS does not engage for a lateral impact. Neither vehicle nor driver takes evasive manoeuvres at any stage throughout the entire collision.
A _{s2}	Information provided in section 2.3.2 'Advances in Crash Avoidance & Mitigation Technology'; ADAS mitigates collisions of other arrangements sufficiently to yield no serious injuries within impact.
A _{s3}	Initial velocity of the bullet vehicle is maximum permitted within legal boundaries.
A _{s4}	The ground is new asphalt, the weather conditions are dry and vehicles tyres are in optimal condition to provide a constant coefficient of friction of 0.9 for tyre to ground contact (MFES 2007).
A _{s5}	Materials selected to form the 'Substitute Material Database' of stage 2 in the RMR process (Figure 38) are viable for all vehicles.
A _{s6}	No curtain airbags present for L7e occupant cabin due to packaging, weight and cost restrictions as described in section 2.2.1, sub-section 'L-Category Vehicles'. Only a simple 3-point restraint system is implemented.
A _{s7}	Occupant is a 50 th percentile male in a natural seating position.
Limitations of Scope	Description
L _{s1}	Only driver-side occupant injuries of the L7e are recorded.
L _{s2}	Bullet vehicle safety and performance is assessed by data recorded within the occupant compartment and sensor locations across the vehicle.
L _{s3}	Small range of validated material models for 'Substitute Material Database' (NCAC 2014b, 2014c).
L _{s4}	Passive crash-structures are designed and retained to the original vehicle model. No changes to geometrical structural design or component configurations are made.
L _{s5}	Limited vehicle pool to represent Heavy-Quadricycles (L7e category).
L _{s6}	Target vehicle is over mass targets of L7e category.
L _{s7}	Target vehicle is stationary to minimise effects of induced changes to rotational acceleration experienced by the occupant due to the overweight-target vehicle.

The assumptions and limitations of the project scope provided in Table 55 assist in forming the methodology and technique used to investigate inter-category crash compatibility as a function of mass. The experimental procedure is defined in section 6.2, in which the complete process is formed.

6.2 Inter-Category Compatibility Methodology

The experimental procedure follows the same impact arrangement as used in the Mass Relationship Exploration, chapter 4. The vehicle alignment matches the Euro NCAP Side Impact Protocol (2019) for purely lateral impact, as shown by Figure 11. This states that the bullet vehicle impacts the driver-side of the target

vehicle. The vehicle alignments are so the longitudinal centre lines of each vehicle are perpendicular to each other. The impact location aligns the central longitudinal-vertical plane of the bullet vehicle with the transverse-vertical plane of the H-Point of the target vehicle. An example of the alignment is shown in Figure 61. The red line represents the longitudinal and transverse vertical planes of the bullet and target vehicle respectively.

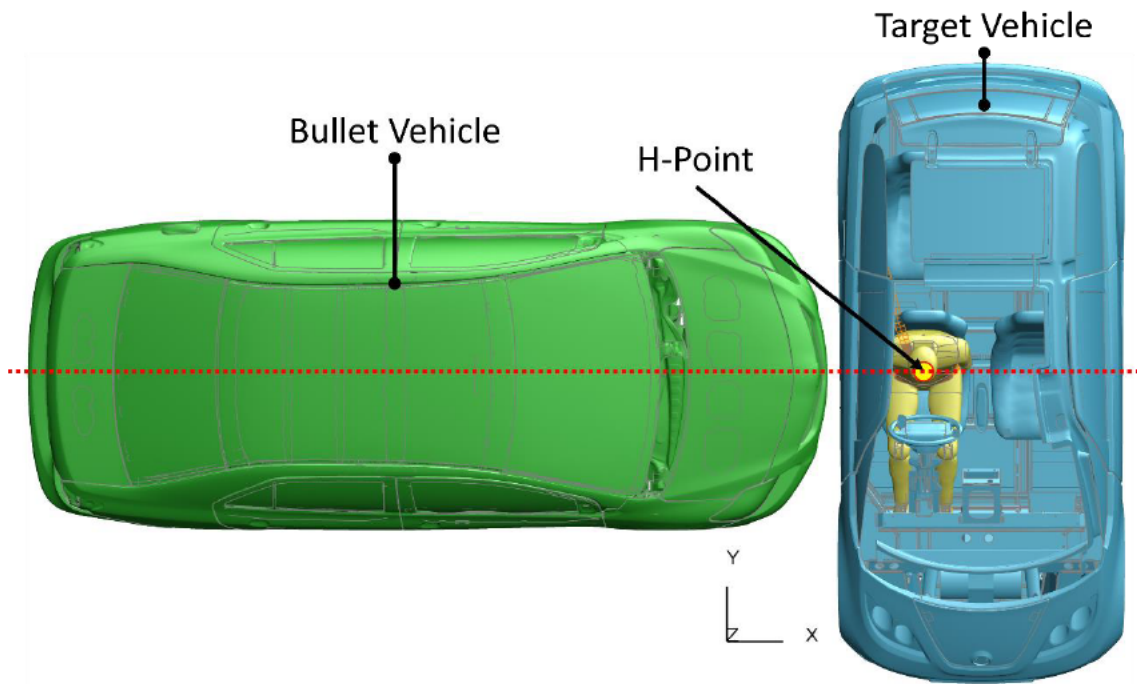


Figure 61. Vertical Plane Alignment of Bullet and Target Vehicle

All vehicle tyres contact the same horizontal plane. As the height of impact is not constrained, it allows the inclusion of the effects of vehicle height on the occupant injuries sustained in the inter-category compatibility research. A synopsis of the test format for the research regarding inter-vehicle compatibility and mass efficiency is provided in Table 56.

Table 56. Summary of Inter-Category Test-Case Arrangement

Vehicle Assignment	Vehicle Category	Number of Vehicles	Light-weight Revisions (per vehicle)	Initial Velocity (m/s)	Angle (degrees)	Occupant Model	Duration (ms)
Bullet	M ₁	2	1	13.4	0	None	200
Target	L7e	1	1	0	90	Driver	

To achieve the research goals of the compatibility study listed in section 6.1, two vehicles that represent the largest and smallest of the M_1 category have been selected. These are the 2014 Chevrolet Silverado and the 2010 Toyota Yaris (NHTSA 2017, 2010). The relevant attributes of the Silverado and Yaris are provided in Table 57. For the vehicles acting as bullet vehicles, the bonnet height is measured vertically down from the foremost divide between bumper and the bonnet. The crash rail measurements are taken from the centre point of the cross-sectional area straight down and across for the height and span measurements respectively. The $CofG_x$ is measured from the front of the vehicle longitudinally (driving direction is positive), $CofG_y$ is taken from the longitudinal centreline of the vehicle with positive direction to the left side of the vehicle (driver-side) and $CofG_z$ is measured from the ground upwards.

Table 57. Silverado and Yaris Variant Details Summary

Vehicle Model	Mass (kg)	Length (m)	Width (m)	Height (m)	Bonnet Height (m)	Crash Rail Height (mm)	Crash Rail Span (mm)	$CofG_x$ (mm)	$CofG_y$ (mm)	$CofG_z$ (mm)
Silverado	2518.5	5.85	2.03	1.91	1.16	512	812	-2590.3	0.9	733.8
Light-weight Silverado	1956.4							-2520.2	-1.0	727.8
Yaris	1253.6	4.29	1.69	1.47	0.82	466	959	-1883.1	-2.4	548.1
Light-weight Yaris	1022.9							-1851.8	-5.9	522.8

Table 57 presents a 'Light-weight' variant of the Silverado and Yaris vehicle models. The light-weight versions have been accomplished by the RMR procedure. The same process as detailed throughout section 5.2 was adopted. The same weighting criteria detailed in 5.2.2 was used.

The light-weight variants of the Silverado and Yaris allow comparisons to be made to the occupant injury metrics recorded within the target vehicle. The different structures of the vehicles allow examination and investigation of other factors, such as height or structure positioning, which influence inter-category crash-compatibility and assists in identifying the next steps towards crash-safety harmonisation. In addition to this, the light-weight variants, in comparison to their original counterparts, provide evidence of crash-safety

efficiency as a function of total vehicle mass. Lastly, by applying the RMR to the target vehicle and assessing the performance to each variant of the bullet vehicle, an indication to the crash-efficiency of pairing vehicles with the safety orientated light-weighting procedure is shown. The relevant specifications of the Microcab for the compatibility research is provided in Table 58, the measurements are taken by the same reference locations as specified for Table 57. Although, the crash beam span references the length of the crash beams along the side of the Microcab (across the bullet vehicle) and the crash beams are defined as the protective structures within the internal door panelling (used for door height) of the Microcab.

Table 58. Microcab Variant Details Summary

Vehicle Model	Mass (kg)	Length (m)	Width (m)	Height (m)	Door Height (m)	Crash Beam Heights (mm)	Crash Beam Span (mm)	CofG _x (mm)	CofG _y (mm)	CofG _z (mm)
Microcab	935.9	3.39	1.55	1.65	1.06	787/490	940	-32.3	23.76	524.9
Light-weight Microcab	766.7							-37.5	27.9	516.9

Each light-weight variant of the vehicles listed in Table 57 and Table 58 achieve a mass reduction of 22.3%, 18.4% and 18% for the Silverado, Yaris and Microcab respectively. The combination of assessments between the light-weight models and original designs offers a combination of mass ratios that highlight the potential for inter-category safety. In addition, the differences in height and span of the bullet vehicle will assist in identifying further requirements of inter-category compatibility and methods of maximising crash efficiency within vehicle-to-vehicle collisions. A summary of each test case for the research and the associated mass ratios are provided in Table 59.

Table 59. Compatibility Test-case Assignments

Group	Study Identification	Bullet Vehicle	Target Vehicle	Bullet to Target Mass Ratio
S	S1	Silverado	Microcab	2.69
	S2	Silverado	Light-weight Microcab	3.28
	S3	Light-weight Silverado	Microcab	2.09
	S4	Light-weight Silverado	Light-weight Microcab	2.55
Y	Y1	Yaris	Microcab	1.34
	Y2	Yaris	Light-weight Microcab	1.64
	Y3	Light-weight Yaris	Microcab	1.09
	Y4	Light-weight Yaris	Light-weight Microcab	1.33

The bullet to target vehicle mass-ratios presented in Table 59 have a range of approximately 1.1:1 up to 3.3:1. The systematic approach ensures that each bullet vehicle impacts the target vehicle without any changes, thereby acting as the control for that group. Following this, the results from study 2 of each group (signified by group letter and number) pose an increase to the vehicle mass-ratio due to the light-weighted target vehicle. In study two, maintenance of original injury metrics and vehicle integrity shows improvement in the overall safety-efficiency as a function of mass of the target vehicle. An increase in efficiency also presents itself if the increase to injury metrics recorded between study 1 and study 2, increase by a factor less than the prediction identified in section 4.4, within the 'Mass Relationship Exploration' study.

Following this, the partner protection of the bullet vehicle is investigated in study 3. Alike study 2, the safety efficiency as a function of vehicle mass is examined. As the RMR focuses on reducing the aggressivity of the bullet vehicle to the target vehicle, an increase in efficiency and compatibility is evident with lower occupant injury metrics and better vehicle integrity of the target vehicle. Furthermore, an improvement to crash-safety efficiency is revealed should the occupant injuries sustained reduce at a greater rate than predicted (in relation to the mass-ratio) and that crush-distance of the bullet vehicle is greater. The trade-off of the bullet vehicle

integrity to boost partner protection is detrimental if the bullet vehicle intrusions and accelerations increase to receive poor ratings (Table 52).

Lastly, study 4 is investigated for crash-safety harmonisation between the bullet and target vehicles after undergoing the mass-reduction procedure for occupant safety. In both groups, the mass-ratio of study-4 to study-1 are nearly equivalent (differences of 0.14 and 0.01). This enables fair comparisons to be made between the two studies in regard to inter-category compatibility and partnered passive crashworthiness efficiency. The partnered crashworthiness efficiency can be defined as the frontal aggressivity of the bullet vehicle in relation to the protection of the target vehicle.

The geometrical differences of the bullet vehicles between test groups helps inform further requirements to enhance inter-category compatibility and identification of a relationship between impacting height, protective coverage (by area) and occupant injuries.

6.3 Inter-Category Compatibility Results

For each group shown in Table 59, the passive crashworthiness performance of the bullet and target vehicle is examined as well as the occupant injury metrics. The injury criterion, sensors and methods used to attain the injury results are detailed in section 4.2.2. The bullet vehicle metrics are recorded by the same technique used as industry practise as described in section 5.3.2 (IIHS 2016, Euro NCAP 2021, 2020c). Cross-sections across the target were implemented to record force transmission and localisation.

6.3.1 Occupant Results

The results of the Inter-category compatibility and efficiency of mass study are separated into the respective groups and assessment metrics. Namely, the regions and types of occupant metrics. The occupant metrics recorded were separated into regions and form of data. The occupant head metrics are presented first, followed by the accelerations recorded by the WSID50 sensors at the T12 and Pelvis. The accelerometer locations within the WSID50 are shown in Figure 19. The thoracic metrics are presented after the head, the lateral accelerations for the T4, T12 and Pelvis were recorded. For assessment guideline purposes, the absolute

3-dimensional acceleration of the Pelvis was also recorded (Insurance Institute for Highway Safety 2014, Schram 2017: 16, Euro NCAP 2020c: 21). Occupant rib deflections and rate thereof are presented within the sub-section 'Thorax Metrics' which also submits the results following the injury criteria calculations for the VC and TTI, Equations Equation 5 and Equation 6 respectively.

Where applicable, the results are highlighted to correspond with a combination of IIHS and Euro NCAP rating classification that is utilised for lateral impact evaluations (Euro NCAP 2020c, Insurance Institute for Highway Safety 2014). This provides a basis for a comparative assessment across each study within the group. The criteria boundaries suggest the possible risk and severity of injury sustained by the occupant. The boundaries of the occupant scoring used are presented in Table 60. The blank cells represent that the rating information is not applicable or available to the corresponding criteria.

Table 60. Criteria Bounds for Occupant Protection (Euro NCAP 2020c, Insurance Institute for Highway Safety 2014)

Occupant Criteria	Unit	IIHS				Euro NCAP	
		Good	Acceptable	Poor	Limit	High	Low
HIC ₁₅	Score	623	779	935	1000	500	700
Resultant Acceleration, 3ms Exceedance	G					88	72
Shoulder Compression	mm					60	80
Average Rib Compression ^a	mm	34	42	50			
Worst Rib Compression ^b	mm	51	55	δ > 55			
Chest Rib Compression ^c	mm					28	50
Abdominal Rib Compression ^c	mm					47	65
Rib Compression Rate	m/s	8.2	9.84	11.48			
Viscous Criterion	m/s	1	1.2	1.4		0.32	1
Thoracic Trauma Index	G					90	
Absolute Pelvic Acceleration	G					130	

- a) The criterion is only applied if the peak rib compression does not exceed 50mm else,
- b) The evaluation only considers the worst rib compression rating boundaries.
- c) The rib compression scoring is only based on the worst performing rib (highest compression).

The tabulated results throughout section 6.3.1 utilise a colour coding system to represent the boundary the results classify into. The boundaries are colour coded as illustrated in Table 61 below.

Table 61. Colour Key for Boundaries of Occupant Safety Rating

Consumer Protection Program	Rating	Colour
IIHS	Good	Green
	Acceptable	Yellow
	Poor	Red
	Limit	Dark Red
Euro NCAP	High	Light Blue
	Low	Purple

The IIHS ratings have priority in the colour ranking system due to the extended number of bounds in comparison to the Euro NCAP. Additionally, the 'Poor' rating shown in Table 60 permits a greater extension to the data recorded than the 'Low' rating of Euro NCAP.

Occupant Accelerations

Head Acceleration

Figure 62 shows the time-history plot of the head acceleration recorded for Group-S with application of CFC180 filter. The filter was used for better visualisation of the head acceleration through time as a large and sharp spike is observed in S1 which reaches 4777m/s^2 (487G). The filter reduced the accelerations of S2 to S4 from their serviceable values slightly, but the shape and time of the peaks remained the same for all studies. Nonetheless, the data obtained for the head acceleration for Group-S is provided in Table 62 and the discussion utilises the data required by evaluation procedures that were defined in Table 21

Table 21. The head acceleration plot with the CFC1000 applied can be found in Appendix V, Figure 119.

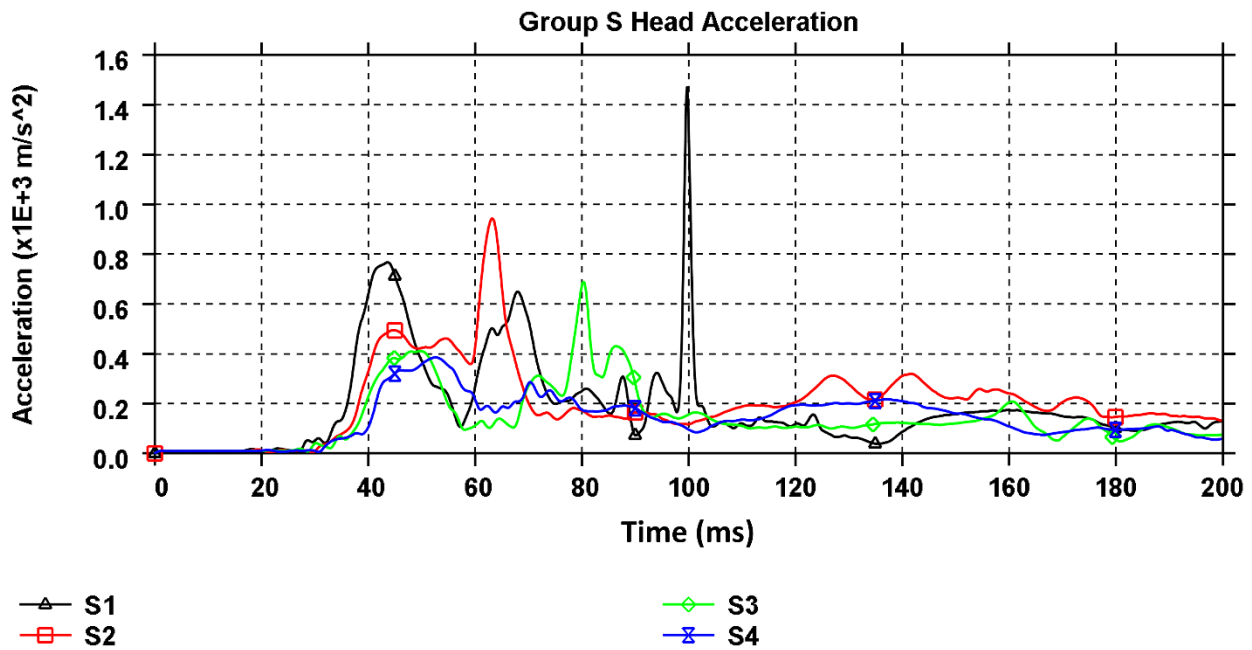


Figure 62. Group-S Resultant Head Acceleration (CFC 180)

The large peak exhibited by S1 raises from 103m/s^2 to 4777m/s^2 and returns down to 245m/s^2 within 0.9ms. Visual examination of the occupant response shown that the head had reached the maximum displacement, in relation to the torso, and had impacted with the shoulder. Additionally, a large constitute of the peak was from the lateral and vertical displacement of the target vehicle. The time that the bullet and target vehicle disconnected at the upper section of the door coincides with the time of S1 peak acceleration. The rotation and vertical movement of the target vehicle opposing the head's vector of movement is a likely cause for the sudden and sharp increase. Despite the magnitude of the acceleration, the HIC_{15} of S1 remains below 1000 and the maximum acceleration in 3ms exceedance remained in limits due to the small timeframe of 0.9ms, underlining the importance of lower sustained head acceleration for occupant injury predictions. Table 62 provides the maximum acceleration, 3ms exceedance and HIC_{15} results.

The Head acceleration recorded by Group-Y shown initial strong peaks of acceleration in the Y1 and Y3 studies. However, the secondary peak exhibited by Y2 had provided 20m/s^2 more peak acceleration than Y1. In contrast, Y4 had a small increase in head acceleration at 70ms, and the largest peak was realised at 100ms

with a value of 347m/s^2 , nearly 17G less than Y1 which has the same mass ratio. The plot of head acceleration is provided in Figure 63.

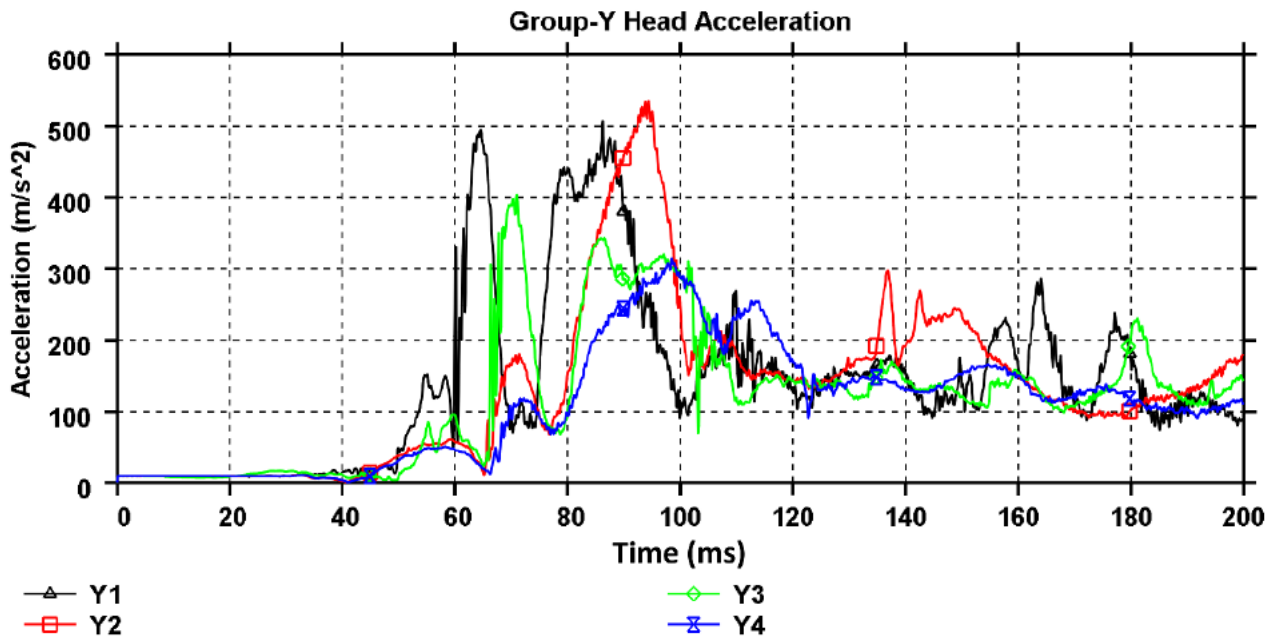


Figure 63. Group-Y Head Acceleration

The small fluctuations noticeable after 120ms are caused by the vehicle movement throughout the impact phase. The head did not contact any vehicle surface in any study of Group-Y. The head criteria for Group-Y is shown in Table 62.

Table 62. Head Acceleration Metrics

Model	Mass Ratio	Maximum Acceleration:			HIC ₁₅ :		
		Value (m/s ²)	Time (ms)	3ms exceedance (G)	Score	t ₁ (ms)	t ₂ (ms)
S1	2.69	4722	99.6	66.4	984	99.5	99.9
S2	3.28	966	63.4	78.6	418	51.4	66.4
S3	2.09	796	80.4	47.5	171	77.1	90.1
S4	2.55	383	55.7	37.1	90	44.9	59.9
Y1	1.34	512	86	47	200	76.8	91.8
Y2	1.64	582	94	55	224	84.5	99.5
Y3	1.09	403	71	35	82.7	83.5	98.5
Y4	1.33	347	99	34	77.6	91.1	106.1

The largest acceleration exceeding 3ms is presented by S2, in which only the target vehicle had undergone RMR. This coincides with the largest vehicle mass-ratio presented throughout Group-S of 3.28 and suggests

that the bullet vehicle's aggressivity overcame the integrity of the occupant compartment. However, S3 provides a significant improvement to S2 with approximate improvements of 20, 40 and 60% in peak acceleration, acceleration of 3ms exceedance and the HIC_{15} . The improvements insinuate that reductions to the bullet vehicle provide the greatest improvement to occupant safety protection. However, the partnered light-weighted vehicles in S4 provided further improvements to S3 by reducing the peak and sustained head acceleration by 42G and 10G respectively. In addition, the S4 pairing reduced the HIC_{15} by 47% in comparison to S3.

The results of Group-Y all retain performance of the higher limit for Euro NCAP evaluations. Study Y4 provided a HIC_{15} result 61.2% lower than Y1. The results of Group-Y also indicate that it is more impactful to reduce the mass of the bullet vehicle to increase occupant safety of the target vehicle. In a similar fashion, by collaborating efforts to maximise compatibility and safety as a function of mass, Y4 provides the best occupant results and reductions.

Table 62 also shows that despite the large mass differences, there is only 3.6G difference between the maximum acceleration of S4 and Y4. Further, S4 displayed a maximum acceleration lower than Y3, despite the 2.5:1 mass ratio, whilst managing to score 3ms exceedance and a HIC_{15} score within 6% and 14% respectively. Using the regression formulae provided for the HIC_{15} in Table 33, the differences between the mass-ratios should result in an achieved HIC_{15} of 188 (a factor of 2.43 times greater), in which less than half of that was obtained.

T12 Acceleration

The T12 acceleration is used for the calculation of the TTI as detailed in Equation 6. The occupant criteria do not have a limiting value assigned specifically to the T12 vertebrae, but the response was examined to identify potential variance in TTI results between tests 1-4 of Group-S and Group-Y.

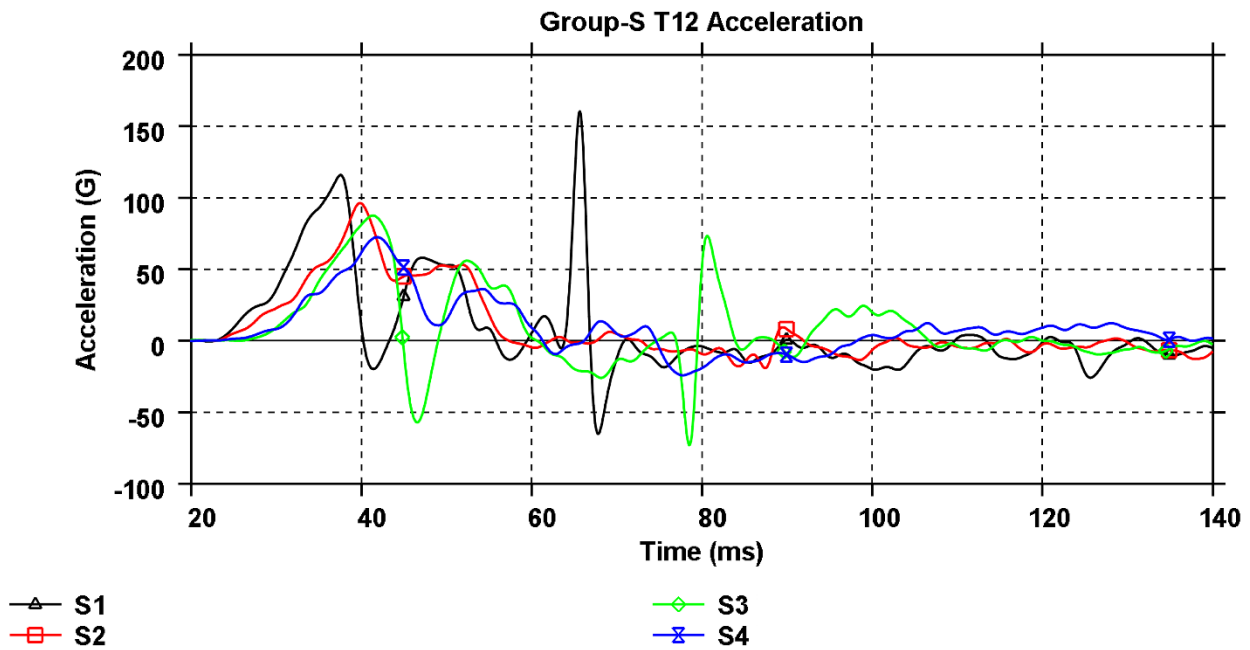


Figure 64. Group-S T12 Lateral Acceleration

Figure 64 presents the lateral acceleration recorded at the T12 vertebrae for Group-S in units of gravity. No acceleration was recorded until after 20ms and fluctuates near 0G after 140ms. It can be seen in Figure 64 that the gradient of acceleration is less severe for tests S3 and S4 which are home to the light-weight Silverado. Table 63 presents the T12 lateral acceleration for Group-S.

The lateral acceleration of Group-Y also came to a near rest after 140ms. In contrast to Group-S, the initial peak of Y1 occurred 10ms later than Y2, although the sharp spike still occurred approximately 25ms after the initial rise. In Group-Y the studies of Y1 and Y2 possessed the largest gradient to the initial peak, reaching it within 10ms. In contrast, Y3 and Y4 took 25ms and 15ms respectively. With the exception of Y3, the magnitude of initial peak of each study was within 13% of each other. However, Y2 possessed the largest mass-ratio of Group-Y. The magnitude consistency of initial peaks, shown in Figure 65, suggests that the crash rail height of the bullet vehicle (466mm) is a predominant factor in the injuries sustained due to the ride height of the Microcab.

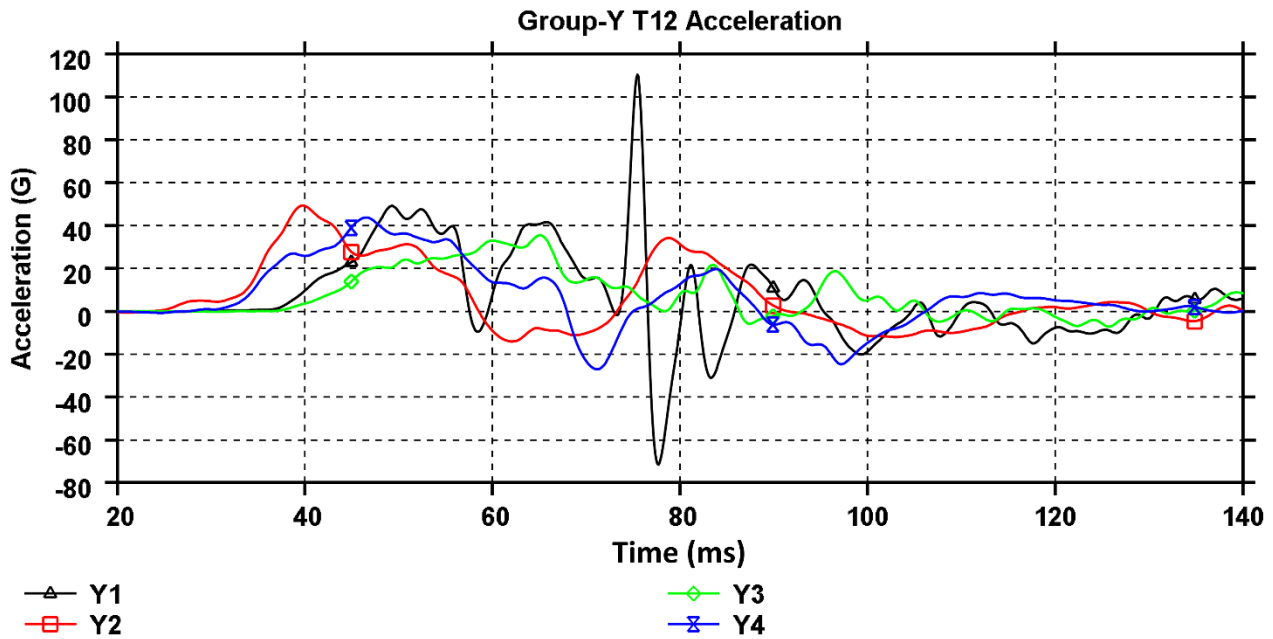


Figure 65. Group-Y T12 Lateral Acceleration

The H-point is 710mm high the T12 sensor location is 890mm upwards from the ground. Therefore, the frontal crash rails of Group-Y have a clearance of 424mm from the T12 acceleration but do engage well with the lower protective door beam of the target vehicle. Furthermore, the 820mm bonnet height of the bullet vehicle in group-Y does not provide enough height to engage with the target vehicle components, and therefore the major intrusions and loading forces travel under the occupant and cause the occupant door to buckle outwards. This is not apparent with the 1.16m bonnet height of Group-S which surpasses the height of the door panelling.

Table 63. T12 Acceleration

Model	Peak Lateral Acceleration (m/s ²)	Peak Lateral Acceleration (G)	Time of Peak Acceleration (ms)
S1	1576	161	66
S2	945	96	40
S3	860	88	41
S4	712	73	42
Y1	1083	110	75
Y2	348	36	65
Y3	392	40	54
Y4	342	35	66

The T12 acceleration results of S1 possessed the largest peak acceleration of all studies despite S2 presenting a larger mass ratio (3.28:1) in comparison to S1 (2.69:1). The T12 acceleration of S2 was 40% less than S1. The peak acceleration of S1 was witnessed at 66ms and is the cause for the larger acceleration difference between S1 and S2. At 66ms the maximum penetration into the occupant compartment of the Microcab was reached and the Silverado begins to push the Microcab along the ground. The large penetration and sharp secondary acceleration response recorded in S1 indicates poor crash compatibility in mass and geometry, as described and highlighted in section 2.3.2: 'Heavy Quadricycle Crashworthiness Performance'. Study S4 provided the best results for T12 acceleration within Group-S, possessing the lowest peak acceleration and smallest gradient of acceleration change. In addition, with only a 0.14 mass ratio difference, a 55% reduction between S1 and S4 was recorded. The proximity of mass ratios between the two studies with such a substantial reduction in acceleration highlights the compatibility and structural efficiency attainable for occupant injuries despite differences in vehicle masses.

Crash incompatibility was also highlighted by the door deformation of Group-Y. The reduced impact area of the Toyota Yaris (in comparison to the Silverado) is what likely helped maintain a low acceleration yield throughout the collision but at a cost of increased intrusion. In addition, the structure and outer panels of the Yaris missed the protective panels and pillars of the Microcab throughout the crash duration, whereas the Silverado engaged with a larger amount of Microcab panelling and structures as the impact progressed. The

responses of the door deformation between Group-S and Group-Y are shown in Figure 66. The contour plots given are of nodal x-displacement (direction of bullet vehicle) from the global centre. Figure 66 indicates that the seat-base of Group-Y had buckled under impact from the bullet vehicle and the lower section of the door progressed through the occupant compartment and caused the seat to begin to rotate anticlockwise about the mounting location towards the bullet vehicle direction. The entire rotation of the occupant reduces the acceleration-based injury scores due to the frame of reference to the occupant body. Although, the severity of door deformation and partial ejection of occupant limbs would result in a poor score by Euro NCAP procedures. A similar mode of deformation was observed in their Heavy-Quadricycle tests described in section 2.3.2, 'Heavy Quadricycle Crashworthiness Performance'. In contrast, the door deformation displayed in the Group-S study is less severe. The bottom section of the door still slides underneath the occupant compartment as the crash rail ground clearance of 512mm is underneath the seat-mount height. However, the height of the Silverado's bonnet reduced the folding deformation of the Microcab's door and provides a more distributed load across the bullet vehicle width in comparison to the Yaris.

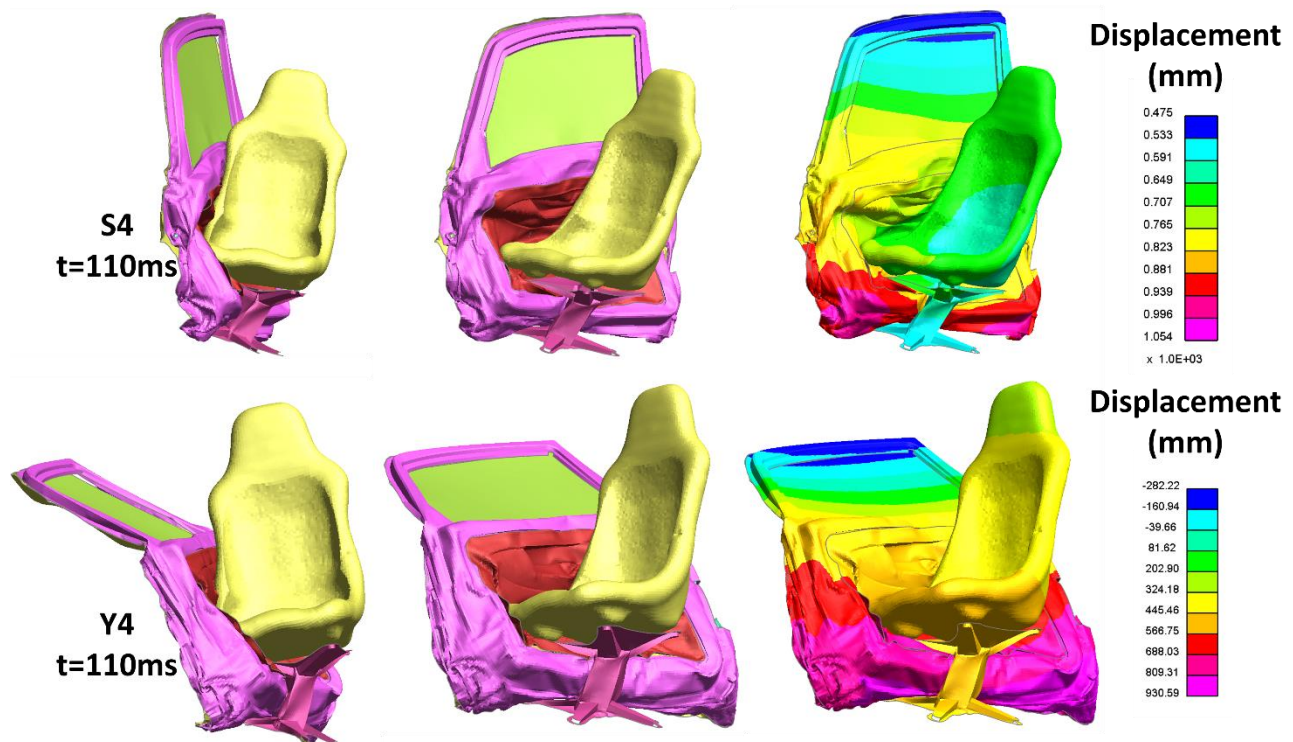


Figure 66. Door Response to Groups S and Y

Pelvic Acceleration

As part of the condition of the TTI scoring, the peak resultant pelvic acceleration must remain below 130G. However, to provide information on the load distribution to the occupant the lateral pelvic acceleration through time has been provided in Figure 67 for Group-S and Figure 69 for Group-Y.

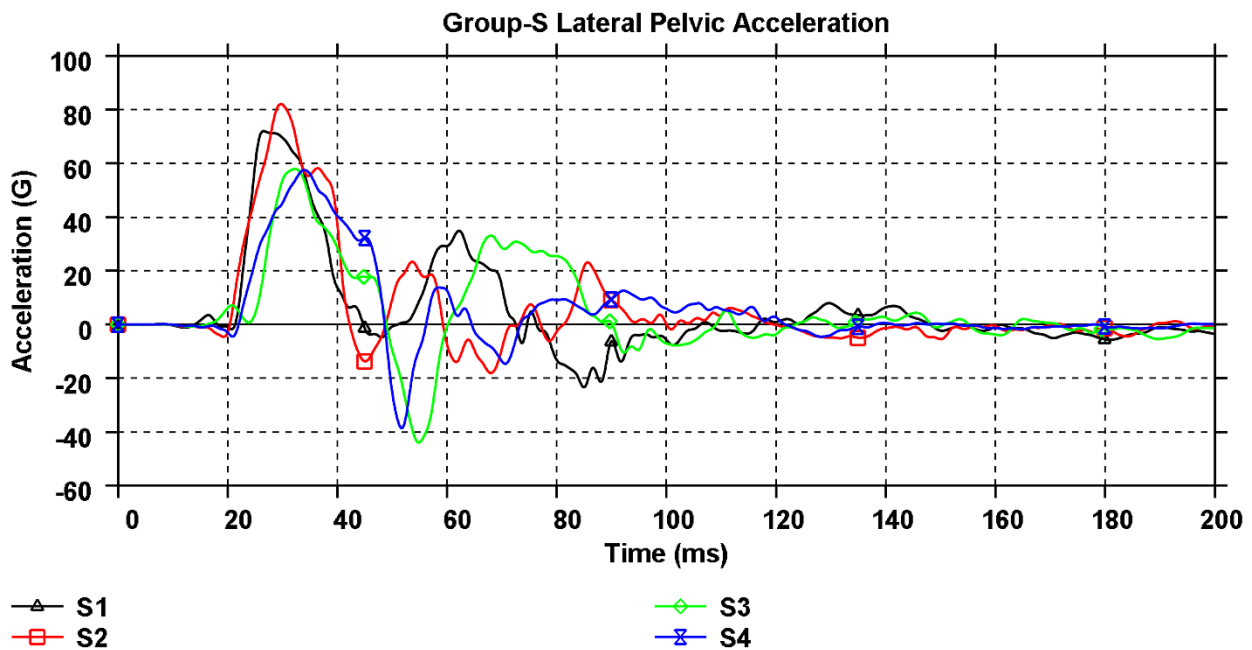


Figure 67. Group-S Lateral Pelvis Acceleration

The lateral acceleration experienced by the occupants of S1 and S2 occur fractionally earlier and with greater magnitude than S3 and S4. The greater acceleration recorded in S2 suggests the stiffness of the light-weight Microcab was insufficient to deal with the frontal crash-rails of the Silverado. Additionally, the vertical location of the crash-rails aligns between the main protective structures of the Microcab, as detailed in Table 57 and Table 58. Consequently, the bullet vehicles with greater aggressivity and lower partner protection (S1 and S2) pose a significantly higher risk to occupants of the target vehicle as the efficacy of protective structures is lessened with misalignment.

The response of the target vehicle to an impact causes accelerations in other directions, the resultant pelvic acceleration highlights other vectors of acceleration that effect the occupant. The resultant pelvic acceleration plot for Group-S is presented in Figure 68.

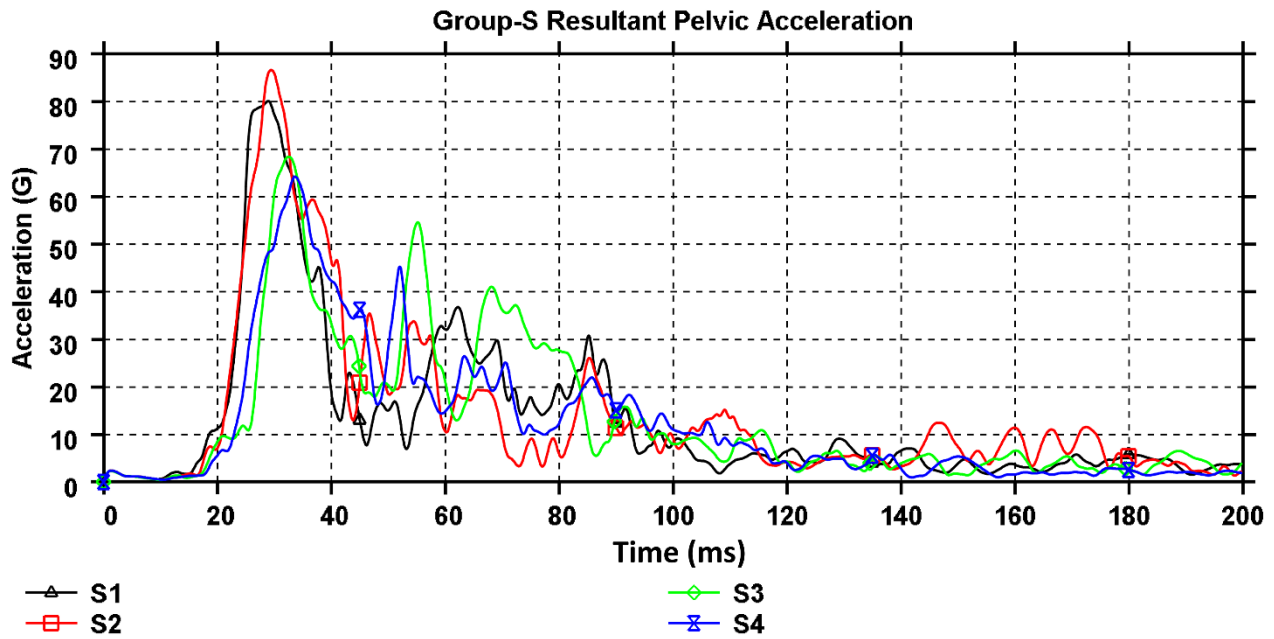


Figure 68. Group-S Resultant Pelvic Acceleration

The pelvic acceleration witnessed in Group-Y were lower than the Group-S counterpart by approximately 20G for the corresponding study, except for S2 to Y2. Figure 69 shows the pelvic lateral acceleration for Group-Y.

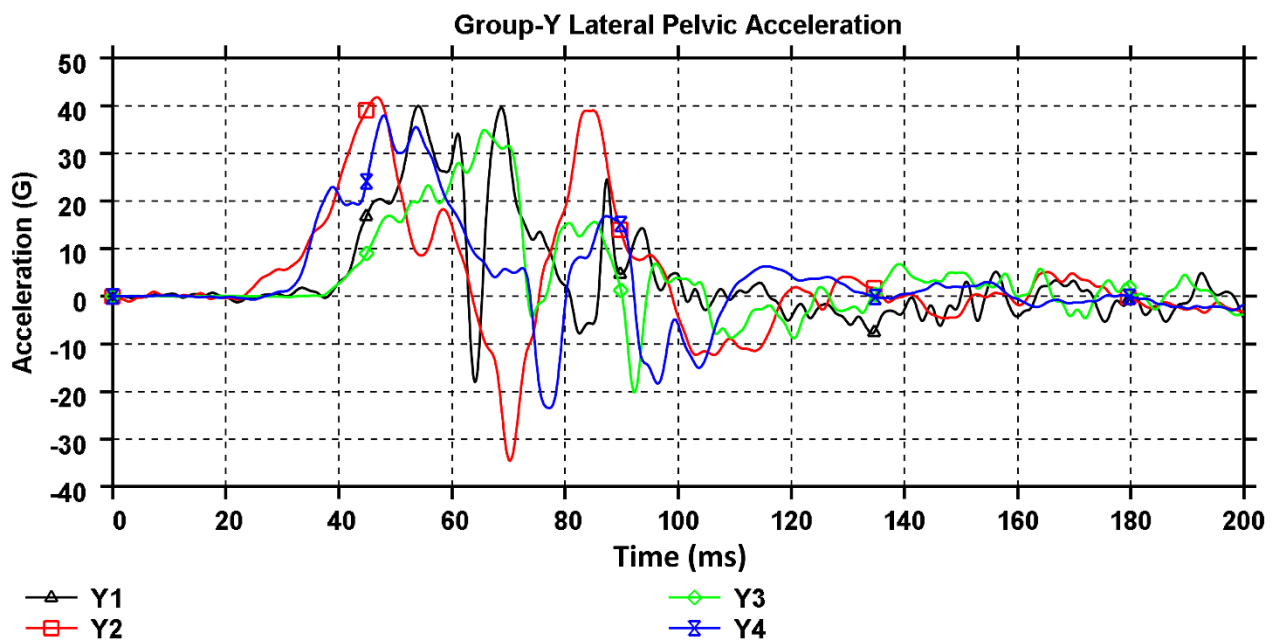


Figure 69. Group-Y Lateral Pelvic Acceleration

The initial acceleration peaks had occurred in the same order as T12. The greatest magnitude of change occurred in the Y2 study at 45ms to 70ms. The greatest rate of change from peak to trough is apparent in Y1

with a 16ms timeframe. Study Y3 shows a gradual progression of acceleration to reach the first peak followed by a sudden drop in acceleration once the target vehicle is 'pushed' by the bullet vehicle at a near constant velocity. The negative acceleration spikes presented in Y1, Y2 and Y4 are caused by the anticlockwise rotation of the seat mount as previously shown in Figure 66. The rate in which the pelvic acceleration changes in Group-Y is indicative of the target vehicle's structural rigidity to oppose the bullet vehicle. The faster the acceleration change, the easier the bullet vehicle invaded the occupant compartment. Correspondingly, the study Y3 provided the best results in both magnitude of acceleration and rate of change of acceleration.

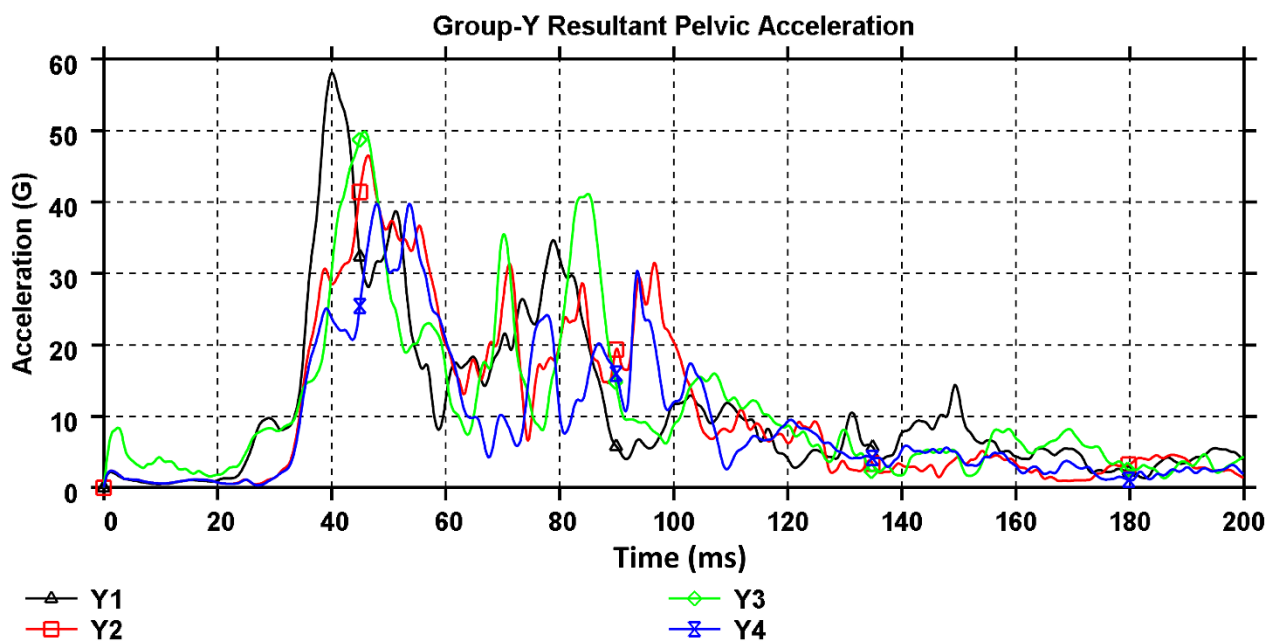


Figure 70. Group-Y Resultant Acceleration

Although Y3 presented the lowest lateral acceleration, the vertical and longitudinal components of acceleration result in Y3 performing the second worst. The resultant pelvic acceleration plot is given in Figure 70. Similarly to S4, Y4 has minimal acceleration induced by other vectors. Only a 2G increase was recorded from the lateral to resultant acceleration. In addition, the order of initial acceleration peaks had altered, resulting in Y1 and Y3 reaching the peak before Y2 and Y4. The lateral and resultant pelvic acceleration results are tabulated in Table 64.

Table 64. Pelvic Acceleration

Model	Lateral			Resultant		
	Peak Acceleration (m/s ²)	Peak Acceleration (G)	Time of Peak Acceleration (ms)	Peak Acceleration (m/s ²)	Peak Acceleration (G)	Time of Peak Acceleration (ms)
S1	704	72	26	785	80	29
S2	807	82	30	850	87	29
S3	569	58	32	670	68	32
S4	565	58	34	630	64	33
Y1	392	40	54	570	58	40
Y2	412	42	47	455	46	46
Y3	343	35	66	489	50	46
Y4	373	38	48	390	40	54

Table 64 shows that all studies passed required acceleration limit of 130G. The range of obtained accelerations in Group-S were less than Group-Y. Comparing the two groups, Group-Y achieved pelvic acceleration reductions of 27%, 53%, 74% and 63% for the corresponding study number of Group-S. Additionally, Group-Y reduced the resultant pelvic acceleration by 18G between Y1 and Y4, 2G better achieved by Group-S. On the other hand, the larger coverage of the bullet vehicle in Group-S (due to the rail width, height and bonnet height) against the side of the bullet vehicle allowed a greater lateral acceleration saving to be made by Group-S against Group-Y, totalling a 14G reduction from S1 to S4 as opposed to 12G by Group-Y.

Thorax Metrics

The investigated thorax metrics are the rib compressions and rate thereof as well as the VC and TTI. The scoring mechanism described in Table 60 and the corresponding colours from Table 61 are employed.

Rib Compression

Rib compression is measured by the peak displacement in the lateral direction and is not time dependant. In addition to the individual compression value attained by a single rib, a similar compression across the ribs throughout the shoulder, thorax and abdominal regions is better as it indicates that the load upon the occupant is distributed well. The results from the rib-springs of the WSID50 were filtered through a CFC600

filter and were double differentiated to calculate the acceleration. The rib compression is measured in millimetres and are presented in Table 65.

Table 65. Peak Rib Compression (mm)

Rib Location	S1	S2	S3	S4	Y1	Y2	Y3	Y4
Shoulder	66.0	71.5	51.0	56.6	4.6	5.0	3.0	11.7
Upper Thorax	54.4	51.2	39.3	41.4	2.0	5.3	7.7	12.5
Middle Thorax	58.5	47.6	36.2	35.8	3.7	3.6	2.6	7.5
Lower Thorax	53.0	52.5	39.2	40.8	1.6	4.1	6.9	11.5
Upper Abdominal	52.7	52.6	37.1	40.3	4.6	5.0	3.0	11.7
Lower Abdominal	50.5	50.9	43.0	44.9	2.0	5.3	7.7	12.5

The IIHS shoulder limit is 60mm, this value was exceeded by S1 and S2 which would result in the reduction of the vehicle rating by one category. Nonetheless, the shoulder compression is evaluated separately to the ribs within the chest and abdominal regions which facilitates a 'Good' score for S3 and S4. For IIHS ranking, the ribs within the thorax and abdominal regions are evaluated together. The average rib compression method of scoring is only available should none of the compressions exceed 50mm. The results exhibited by S1 and S2 exceed 50mm and are therefore rated by the worst peak compression method as defined in Table 60. However, S3 and S4 would be evaluated by the average rib compression methodology, scoring an 'Acceptable' rating overall. However, the abdominal ribs of S3 and S4 score highly for the Euro NCAP scoring as they achieve less than 47mm deflection. Using the same scoring method as NCAP, only the thoracic ribs of S3 and S4 would align between high and low ratings as the maximum limit is 50mm.

The larger rotation induced by the bullet vehicle of Group-Y to the target vehicle door panelling and occupant seat mounts (Figure 66) aided in the rib compressions of Group-Y all accomplishing a Euro NCAP score of high. This resulted in the alignment of the occupant torso to the inner-door packaging for Y1 and Y2. The lower height of the bullet vehicle intrusion and the mode of door collapse in Group-Y studies resulted in the inner-door panelling striking the underside of the occupant seat. Therefore, the inner-door panelling did not directly engage with the occupant as shown in Group-S.

In each Group-S model, the shoulder compression was over 11mm greater than the other ribs. The larger deflection for this rib is due to the door height in relation to the occupant seating position. Models S1 and S4 show the largest deviance from the average of the torso ribs (excluding the shoulder) with 5mm difference at the middle thoracic rib. S2 and S3 show a maximum of 3mm difference at the same rib location, in which the inner-door panelling made first contact with the occupant.

In addition to the injury risks incurred by the peak deflection of the ribs, the rate in which they occur is an important factor. The compression rate, in metres per second, is evaluated by IIHS scoring methods. However, Euro NCAP only score the compression rate by its inclusion in the VC formula (Equation 5).

Rib Compression rate

The deflection rate is a time dependant quantity for risk of injury. A deflection rate of 8.2m/s signifies a 5% risk of sustaining AIS4+ (severe) thoracic injury. The deflection rates of each rib are provided in Table 66.

Table 66. Group-S Peak Rib Deflection Rate (m/s)

Rib Location	S1	S2	S3	S4	Y1	Y2	Y3	Y4
Shoulder	8.3	8.7	6.3	8.1	0.9	2.5	3.0	2.8
Upper Thorax	6.1	5.3	3.6	5.0	1.5	1.1	1.2	1.6
Middle Thorax	7.0	4.4	6.0	3.3	0.7	1.6	1.7	2.2
Lower Thorax	6.3	4.8	5.2	4.6	0.9	1.2	1.0	1.7
Upper Abdominal	6.2	4.7	4.6	4.2	0.9	2.5	3.0	2.8
Lower Abdominal	6.8	5.6	5.6	4.9	1.5	1.1	1.2	1.6

Each model receives a 'Good' IIHS rating for rib deflection rate with the exception of the shoulder rib for S1 and S2, the models with the original Silverado. The average deflection rate is also higher for S1 (6.8m/s) than S2 (5.6m/s) but this is overshadowed by S3 and S4 with average rates of 5.2m/s and 5m/s respectively. The lower deflection rate of S3 and S4 in comparison to S1 and S2 implies that inter-category compatibility is more reliant on the changes to the bullet vehicle than the target vehicle, unless the structures and safety boundaries are designed accordingly of the L7e vehicle, further enhancing the partnered compatibility. The responses of Group-Y had an overall increase in comparison to Y1. However, the lower compression rates of Y1 and Y2

signify the lack of structural engagement of the target vehicle's protective structure. By this reasoning it can be argued that Y3 and Y4 performed better despite the higher rib compression rates.

The compression rate and compression distance of each rib are substituted into Equation 5 to attain the time-dependant VC rating. The VC is evaluated by IIHS and NCAP, however the boundary of the 'Good' ranking of IIHS coincides with the low limit of Euro NCAP of 1m/s. A VC of 1m/s represents a 5% risk of the occupant sustaining an AIS4+ injury. The compression rate of the upper and lower thoracic ribs are also differentiated to obtain the acceleration before conversion into units of gravity. The worst performing rib of the upper or lower thorax is used in Equation 6 with the T12 acceleration (in G) to calculate the TTI. As described in section 4.3.3, the TTI is heavily influenced by internal compartment packaging, arm positioning and predominant impact location. Therefore, the TTI is a good indicator to the effects of impact location and vehicle packaging, in relation to occupant safety performance. This is more prominent due to the architectural differences of the bullet vehicles between Group-S and Group-Y as well as the structural design of the target vehicle.

Viscous Criterion and Thoracic Trauma Index

Table 67 presents the VC attained by each rib of each study within Group-S as well as the associated TTI for that model. The TTI is not scored by boundaries, but has a limit of 90G established by FMVSS 214 (NHTSA 2012).

Table 67. Group-S VC and TTI Metrics

Study	VC (m/s)						TTI (G)
	Shoulder Rib	Upper Thoracic Rib	Middle Thoracic Rib	Lower Thoracic Rib	Upper Abdominal Rib	Lower Abdominal Rib	
S1	1.574	1.17	1.462	1.212	1.194	1.365	167.8
S2	1.598	0.845	0.983	1.022	1.019	1.071	135.3
S3	1.064	0.560	0.796	0.755	0.577	1.046	112.8
S4	1.266	0.448	0.344	0.599	0.581	0.900	103.6
Y1	0.035	0.105	0.134	0.116	0.150	0.604	77
Y2	0.082	0.042	0.037	0.055	0.134	0.404	40
Y3	0.009	0.055	0.071	0.092	0.124	0.362	57
Y4	0.039	0.039	0.025	0.041	0.076	0.258	41

Table 67 shows that all models within Group-S exceed the limit of TTI, although improvements from the original vehicles in S1 are present. The TTI percentage reduction against S1 demonstrated by S2, S3 and S4 are 20%, 33% and 38% respectively. This exemplifies the crash compatibility and crash efficiency as a function of total vehicle mass in each model, given their respective mass-ratios (Table 59). In contrast, Group-Y all achieved the limiting value of TTI. The TTI was lowest in the two studies (Y2 and Y4) which applied the light-weighting procedure to the target vehicle. Correspondingly, the studies of Y2 and Y4 experienced the lowest T12 acceleration but were first to reach the initial peak, as described in Table 63. Considering the overall rib compression and compression rate, the Y4 arguably performed the best as the acceleration induced loading caused by the impact was not heavily localised to a specific rib. This is indicative of better component interaction and engagement of the target vehicle structure to resist the loading.

Additionally, the VC shows substantial improvement between S1 and S4 in scoring IIHS 'Good' in all chest and abdominal ribs. Comparably, S3 once again highlights that an M_1 categorised vehicle with frontal crash structures orientated towards compatibility provide greater benefits to occupant safety than altering the lower-mass vehicle. However, despite the vehicle mass ratio of 3.28 in S2, it had outperformed the original vehicles of S1. On average, the S3 improved the VC by 0.29 in relation to S2, which is further reduced by 0.11 by S4. The average reduction in comparison to S2 is 0.4m/s across each rib, constituting to 40% of the high limit of Euro NCAP's VC scoring.

6.4 Inter-Category Compatibility Conclusion

The results detailed throughout section 6.3 investigate the feasibility of inter-category compatibility with the perspective of occupant injury metrics. The occupant injury metrics sustained between each group of study followed the same general trend despite the differences in bullet vehicle height and width. An overview of the performance, by test group, is given in Table 68. The values given are provided as a percentage of the compared studies. Therefore, a value less than 1 signifies a lower value was achieved and vice versa. The value

corresponds to the percentage of the compared study. For example, a value of 0.6 of 'x to y' signifies that 'y' is 60% of 'x'.

Table 68. Change to Metrics by Study Comparison

Group	Relative Study Comparison	Metrics							
		HIC ₁₅	Acceleration			Rib compression:		VC	TTI
			3ms exceedance	T12	Pelvis	Value	Rate		
S	S2 to S1	0.42	1.18	0.60	1.09	0.97	0.82	0.82	0.81
	S3 to S2	0.41	0.60	0.92	0.78	0.75	0.93	0.73	0.83
	S3 to S1	0.72	0.17	0.55	0.85	0.73	0.77	0.60	0.67
	S4 to S3	0.53	0.78	0.83	0.94	1.06	0.96	0.86	0.92
	S4 to S2	0.22	0.47	0.76	0.74	0.80	0.90	0.63	0.77
	S4 to S1	0.09	0.56	0.45	0.80	0.78	0.74	0.52	0.62
Y	Y2 to Y1	1.12	1.17	0.33	0.79	1.53	1.56	0.66	0.52
	Y3 to Y2	0.37	0.64	1.11	1.09	1.09	1.11	0.95	1.43
	Y3 to Y1	0.74	0.41	0.36	0.86	1.67	1.73	0.62	0.74
	Y4 to Y3	0.94	0.97	0.88	0.80	2.18	1.14	0.67	0.72
	Y4 to Y2	0.35	0.62	0.97	0.87	2.38	1.27	0.63	1.03
	Y4 to Y1	0.39	0.72	0.32	0.69	3.64	1.98	0.42	0.53

Of the studies presented in Table 68, evidenced through Y2:Y1 and S2:S1, study-2 of each group performed the worst in their respective group. The light-weighting procedure was applied to the target vehicle and had increased the vehicle mass ratio by 22%, thereby increasing the bullet vehicle aggressivity and reducing partner protection. Despite this, study-2 managed to reduce 6 of the 8 occupant metrics recorded in Group-S, and 3 within Group-Y. Of those which increased, the maximum acceleration rise was identified in the 3ms exceedance criterion of 18% and 17% for Group-S and Group-Y respectively.

A substantial reduction was observed for each time dependant metric in Group-S from the S4. In comparison to S1, the mass-ratio of S4 is 5.2% less yet achieved a 55% reduction in T12 acceleration and an average reduction of 35% across the thorax metrics. In Group-Y, Y4 also provided reductions comparable to those accomplished in Group-S. An average of 60% reduction was achieved for thoracic metrics utilising acceleration. Despite the reduction in crash pulse experienced within the occupant cabin, each study in group-Y obtained a

greater rib compression. However, the maximum rib compression of study Y1 was less than 5mm, resulting in a 1mm change totalling a 20% difference.

Within each group, study-4 provided the best reductions overall. S4 presented the best results for all occupant metrics except rib compression in Group-S. Similarly, all best reductions were obtained by Y4 for Group-Y, except for the rib compression and rate of rib compression. For each group, the second-best performing models were S3 and Y3 for their corresponding group. The mass ratio difference between study 1 and study 4 gave the closest approximation to an equal vehicle mass-ratio for the corresponding group. The bullet to target vehicle mass ratio difference between S1 and S4 is 0.14, and only 0.01 between Y1 and Y4.

The efficacy of inter-category compatibility is demonstrated by the performance of S4 and Y4. Discounting the rib metrics due to sensitivity of Y4, both S4 and Y4 achieved 51% of the metrics recorded for S1 and Y1. Moreover, the results obtained by S1 had provided 11 poor or marginal performances for thoracic injury metrics, whereas S4 had managed to reduce this to 2. Studies S3 and Y3 achieved a similar performance as S4 and Y4, but the reductions were 8% and 11% worse respectively.

In conclusion, having applied the RMR procedure to the bullet vehicle, the aggressivity was reduced and partner protection had improved by approximately 40%. Though, once the same procedure was applied to the target vehicle, the performance improved by a further 10% irrespective of differences in bullet vehicle geometry. The crash safety efficiency as a function of vehicle mass had also increased as shown by S2 and Y2. The overall occupant injury metrics were improved by 15% (S2) and 4% (Y2) despite the increase of bullet to target vehicle mass ratio, effectively increasing the aggressivity of the bullet vehicle.

7 Discussion

The research undertaken in this thesis explored a new approach to improving automotive inter-category compatibility for occupant safety. The results indicate that crashworthiness efficiency as a function of vehicle mass can be improved by prioritisation of vehicle regions through a light-weighting procedure. Additionally, the data obtained supports the hypothesis that inter-category crash compatibility can be improved. The outcomes had also shown that the improvements made to crash-efficiency and inter-category compatibility were further enhanced by adopting a partnered approach to crash safety (section 6.3).

The outcome of the research was achieved by a multi-phase approach. The initial investigation had explored the effects of bullet to target vehicle mass-ratios (see chapter 4) upon occupant injuries sustained within an L7e vehicle. Although the target vehicle used to represent the Heavy-Quadricycle was the Microcab, which does not meet the weight requirements of an L7e classification; the height, width, length, and structure met the requirements for L7e classification. Additionally, the seating position and general body shape of the Microcab are representative of current Heavy-Quadricycles on the market. Thus, the validity of the results and methodology adopted for the 'Mass Relationship Exploration' remain in-tact. Furthermore, the procedure adopted for the 'Mass Relationship Exploration' study mitigated influencing factors which were often prevalent or overlooked by previous literature. Namely variations of bullet vehicle geometry and stiffness, occupant positioning and stance and the impact location in relation to protective structures (Tolouei, Maher, and Titheridge 2013, Padmanaban 2003, Sadeghipour 2017, Kelley et al. 2019). The management and restriction of influencing factors provided generalisability of the study for all vehicles of L7e categorisation.

The results of the 'Mass Relationship Exploration' study inferred possible correlations between bullet and vehicle mass-ratio and occupant injury metrics. However, the limited number of experiments means that a definitive relationship could not be truly established. As such, the formula for the lines of regression should not be taken as a definitive function. Nonetheless, the outcome supported the hypothesis that an ideal vehicular mass-ratio between an M_1 and L7e vehicle does exist, although likely for a specific occupant metric

and injury form. This is exemplified by the sensitivity of the HIC_{15} and VC of the thorax and abdominal regions to the changes in vehicle mass-ratio.

Interestingly, occupant injury metrics displayed signs of plateauing towards their respective maximum values at a common mass ratio of bullet to target vehicle of 3:1. The results obtained indicate that a maximum injury result (commonly recorded at a 4:1 vehicle mass ratio) is easily attainable by an occupant of a L7e vehicle. This is due to the average mass of a M_1 vehicle being 1397kg, which is above the 3:1 mass ratio. This is a significant factor to consider as the difference in mass between the M_1 vehicle category and L7e category is likely to increase due to vehicle market trends (as discussed in section 2.2.1) and various government initiatives encouraging the uptake of BEVs, which could add an additional 230kg of battery weight to vehicles of the M_1 category, resulting in an average vehicle mass over 3.6 times greater than the L7e category allowance (Tostengard 2015, DIRECTIVE 2008/50/EC 2015, REGULATION (EU) 2019/631 2019).

To lessen the risk and severity of injuries sustained by an occupant of an L7e vehicle, a novel approach to vehicle light-weighting was developed. The unique methodology named the RMR was presented throughout chapter 5. The RMR successfully demonstrated, through a case study of the Toyota Venza, a mass reduction of 26%, a 9% further reduction in comparison to a labour intensive manual approach conducted by Lotus Engineering Inc. (2010). The first aim of the RMR was to reduce the mass of an M_1 vehicle enough to provide a more favourable mass-ratio for occupants of L7e vehicles. The 26% reduction of the Toyota Venza resulted in a mass-ratio reduction from 3.9 to 2.9 against the maximum weight of a Heavy-Quadricycle, therefore achieving a more favourable mass-ratio, albeit only slightly. Secondly, the vehicular scores for passive crashworthiness were largely maintained after application of the RMR procedure. The intrusion ratings all remained 'Good' except for the accelerator pedal which achieved an 'Acceptable' score. Overall, the RMR achieved the aims set out by this study by reducing the mass whilst maintaining sufficient crashworthiness performance.

However, intrusion and crush distances ascertained by the RMR process still increased. The maximum crush extended by 174mm and the maximum intrusion of the footwell increased by 115mm. However, this was expected due to the parameterisation and ranking of regions across the vehicle prioritising L7e occupant protection. Thus, the aggressivity of the Venza was accordingly reduced by the RMR changes as it was assumed the Venza was the bullet vehicle. This approach sanctioned larger crush distances to be achieved by the weakened frontal structures, inducing a 'ramping up' effect with deformation progression. Thereby increasing partner protection whilst not sacrificing self-protection.

The RMR process is universally applicable to M₁ passenger vehicles and Heavy-Quadricycles due to the new approach to mass reduction and inter-category compatibility. The parameterisation of component CofG, component gauge thickness and material function, in relation to occupant positioning and vehicle protective structures, ensures applicability to pre-existing vehicle designs. However, as this system provides a new approach to component management and identification, certain aspects could be refined. For instance, acceptance of rigid-bodies and solids to the ranking process would allow more accurate predictions to be made but were out of scope for this study. Furthermore, the NVH and general driving performance were not accounted for throughout the process, as it was found that clever placement of vibration isolators or dampers can sufficiently mitigate any undesired effects (Mallick 2021).

The RMR procedure was applied to numerous vehicles to investigate the feasibility of improving inter-category compatibility in relation to occupant injury metrics. The results from the Inter-Category Compatibility (section 6.3) studies shown that overall occupant injury metrics were lowered by 50% and specific, key injury indicators were reduced by 58%. The systemic method of investigating bullet vehicle aggressivity, target vehicle protectivity and partnered protection provided evidence towards crashworthiness efficiency as a function of mass and confirmed the hypothesis that inter-category compatibility is possible by achieving favourable mass ratios with focus on critical structure regions.

The 4th variation of tests in each respective group provided the best results for occupant safety of the target vehicle. Despite the differences in mass-ratio and impacting geometry provided by the Silverado and Yaris against the Microcab, a similar overall reduction to occupant injuries were observed when the thoracic rib compressions and deflections were not considered (due to sensitivity of percentile variation). Secondly, the results displayed evidence that by only reducing the aggressivity of the bullet vehicle that injury metrics recorded follow the same trend as the partnered approach, though 10% less effective. The results of study 2 in each group revealed that focusing target vehicle mass on localised areas of impact increases the overall crash efficiency of the vehicle with regard to mass and impacting mass-ratio. However, the results highlight that despite the increased efficiency, no distinguishable improvements to occupant metrics were noticeable, therefore no decrease to occupant injury risk was established for study 2.

Nonetheless, the procedure to investigate compatibility by a partnered approach to crash efficiency shown definitive benefits. The approach differed from previous studies which typically focus on one vehicle and engagement of protective structures for compatibility improvements (Acierno et al. 2004, Baker et al. 2008). To this end, the results of inter-category compatibility had not shown the geometrical influencers for performance assessment. Despite this, the target vehicle deformation and state of integrity was consistent through each examination which allowed a fair comparison and assessment to be made for the effects of inter-category compatibility.

8 Conclusions

The thesis has addressed the problem statement in section 3.1 which refers to the increased risk to occupants of Heavy-Quadricycles by providing evidence that supports the hypothesis given in section 3.3, which states:

“A relationship between occupant injury metrics and vehicle mass-ratios can be determined to provide an ideal vehicular mass-ratio between bullet and target vehicle, allowing for objective light-weighting procedures targeting occupant safety and bodily regions thereof. Improvements to crash efficiency can be made by identification of critical structural regions for defined impact scenarios, providing better inter-category compatibility.”

The research successfully explored all factors of the research hypothesis, accomplishing the necessary aims of each study. The evidence satisfied the hypothesis, though further explorations are required to determine the broader validity across more parameters, metrics and vehicles.

The first study followed a systematic approach of increasing bullet vehicle mass to achieve the range of mass-ratios that an L7e vehicle would encounter on public roads. The use of the ‘Advanced European Mobile Deformable Barrier’ provided a constant frontal stiffness that was representative of the average M_1 vehicle fleet throughout each simulation. The ‘total mass’ procedure applied to the rigid carriage allowed management of the barrier’s inertial properties whilst not affecting the stiffness of the barrier face. Therefore, the AE-MDB remained representative of an M_1 vehicle throughout each test. Current and conceptual designs of Heavy-Quadricycles have a large variance in structural designs. The initial contact location of the bullet to target vehicle was carefully selected to minimise the effects of differing structural designs on occupant injuries sustained. This method provided greater applicability of results across the L7e category.

The first study showed that injury metrics plateaued to a maximum value despite further increases of vehicle mass-ratios. The study revealed that HIC_{15} and VC were more responsive to changes in vehicle mass ratios of

1:1 to 3:1. Interestingly, the results demonstrated that there is a maximum value of occupant injury metrics recorded due to vehicle mass-ratio. The outcome suggested a possible correlation of percentage change between mass-ratio and occupant metrics. However, further data is required to establish a definitive function. Further research could be accomplished to confirm the ratio relationship and define the mathematical function. Nonetheless, a pattern was observable and the completion of the aim to identify a beneficial mass-ratio for occupant injury metrics was not impeded. The most favourable mass-ratio for occupant injuries of an L7e vehicle was identified as 5:2. Furthermore, a ratio of 3:1 was recognised as the limiting ratio of bullet to target vehicle mass in which the injury metrics began to plateau and achieve their maximum results.

The method of light-weighting conducted in the research to achieve favourable vehicle mass ratios adopted a unique perspective to achieve the target. Investigation of the effectiveness of collision mitigation technology and advanced driving assistance systems by a scholarly review conducted within section 2.3.2: 'Advances in Crash Avoidance & Mitigation Technology' revealed that the efficacy of the technologies could drastically reduce at junctions of European roads due to lack of visibility and predictable driver behaviour. It was therefore deduced that the likelihood of a lateral impact, in comparison to other collision arrangements, would increase in the perceivable future. Furthermore, the lateral arrangement would pose the greatest risk to occupants of L7e vehicles due to the limited packaging space for protective structures and the occupant proximity to the vehicle door. Consideration of these two factors showed the necessity to achieve greater inter-category compatibility and formed the basis of the novel ranked mass reduction (RMR) procedure. Information gathered of the range of M_1 geometry, in reference to the L7e occupant seating position, was used to define the limiting factors of the RMR to ensure applicability and effectiveness for all passenger vehicles. The identification and utilisation of vehicle regions, and not individual components, is a unique concept for light-weighting and crash compatibility development. The application of ranked and weighted parameters, corresponding to component location, gauge thickness and material selection showcased a 26%

total mass reduction (53% of structural parts) whilst maintaining good self-protection and vehicle integrity scores for a rigid wall impact by IIHS evaluation systems.

The employment of a zonal mass reduction procedure as a technique to achieve greater inter-category compatibility proved successful and addressed the concerns of occupant safety for the more vulnerable road users of the L7e category. The partnered approach to light-weighting by zonal prioritisation demonstrated the best performance. The results show that the time dependant injury metrics were reduced by 50% across both test groups despite measurable differences in the bullet vehicle's impacting height, area and alignment with the target vehicle's protective structures.

This thesis has addressed a potential safety concern for emerging vehicles on the roadmap to achieving battery powered and connected and autonomous vehicles. The research considered the efficacy of advanced driving assistance systems and collision mitigation systems within an inner-city environment and how that would affect collision rates and arrangements. The thesis investigated a probable collision arrangement which poses the greatest risk to occupants of Heavy-Quadracycles. The results of the thesis have shown that inter-category compatibility can be improved by adopting a partnered and zonal method of mass reduction to maximise the relationship of reduced aggressivity and increased self-protection of opposing vehicles. The 50% exhibited by the partnered vehicles lays a good foundation for methods of achieving 'Vision 0'.

9 References

- ACEA (2019) *Vehicles in Use Europe 2019* [online] available from <https://www.acea.auto/files/ACEA_Report_Vehicles_in_use-Europe_2019-1.pdf>
- Acierno, S., Kaufman, R., Rivara, F.P., Grossman, D.C., and Mock, C. (2004) 'Vehicle Mismatch: Injury Patterns and Severity'. in *Accident Analysis & Prevention* [online] vol. 36 (5). 761–772. available from <<http://www.sciencedirect.com/science/article/pii/S000145750300099X>>
- Addendum 13: UN Regulation No. 14 (2020) [online] United Nations member states. available from <Regulation No. 014 - Rev.6 - Safety-Belt Anchorages>
- Addendum 15: UN Regulation No. 16 (2020) [online] E/ECE/324/Rev.1/Add.15/Rev.10–E/ECE/TRANS/505/Rev.1/Add.15/Rev.10. United Nation member states. available from <<https://unece.org/fileadmin/DAM/trans/main/wp29/wp29regs/2020/R016r10e.pdf>>
- Addendum 24–Regulation No.25 (2015) ECE/TRANS/WP.29/2014/72
- Addendum 42: Regulation No. 43 (2020)
- Addendum 94: Regulation No. 95 (2014) [online] Addendum 94: Regulation No. 95. United Nations. available from <<https://unece.org/fileadmin/DAM/trans/main/wp29/wp29regs/2015/R095r2e.pdf>>
- Ahmad Mujahid, A.Z., Lang, G.L., and Ahmad Firdaus, A.Z. (2010) *Numerical Simulation Study on Lateral Collapse of Kenaf-Foam Composite Filled in Cylindrical Tube Subjected to Dynamic Loading*. 97–110
- Amsterdam Roundtable Foundation and McKinsey & Company (2014) *Electric Vehicles in Europe: Gearing up for a New Phase?* [online] 60. available from <https://www.mckinsey.com/~media/McKinsey/Locations/Europe_and_Middle_East/Netherlands/Our_Insights/Electric_vehicles_in_Europe_Gearing_up_for_a_new_phase/Electric_vehicles_in_Europe_Gearing_up_for_a_new_phase.pdf>
- An, X., Gao, Y., Fang, J., Sun, G., and Li, Q. (2015) 'Crashworthiness Design for Foam-Filled Thin-Walled Structures with Functionally Lateral Graded Thickness Sheets'. *Thin-Walled Structures* 91, 63–71
- Ansys (2020) *Granta EduPack*. Ansys
- Asanjarani, A., Dibajian, S.H., and Mahdian, A. (2017) 'Multi-Objective Crashworthiness Optimization of Tapered Thin-Walled Square Tubes with Indentations'. *Thin-Walled Structures* [online] 116, 26–36. available from <<https://www.sciencedirect.com/science/article/pii/S0263823116304165>>
- Automobiledimensions (n.d.) *Automobile Dimensions and Sizes of All Makes* [online] available from <<https://www.automobiledimension.com/mid-size-suv.php>> [5 September 2020]
- Baker, B.C., Nolan, J.M., O'Neill, B., and Genetos, A.P. (2008) 'Crash Compatibility between Cars and Light Trucks: Benefits of Lowering Front-End Energy-Absorbing Structure in SUVs and Pickups'. in *Accident*

- Analysis & Prevention* [online] vol. 40 (1). 116–125. available from <<http://www.sciencedirect.com/science/article/pii/S0001457507000796>>
- Bastien, C., Blundell, M. V., and Neal-Sturgess, C. (2017) 'A Study into the Kinematic Response for Unbelted Human Occupants during Emergency Braking'. *International Journal of Crashworthiness* [online] 22 (6), 689–703. available from <<http://dx.doi.org/10.1080/13588265.2017.1301080>>
- BMW (2020) *Economic Affairs Ministry Launches Call for Proposals to Make Electric Mobility More Competitive and to Integrate It into the Energy System* [online] available from <<https://www.bmw.de/Redaktion/EN/Pressemitteilungen/2020/20200702-economic-affairs-ministry-launches-call-for-proposals-to-make-electric-mobility-more-competitive.html>> [11 June 2021]
- Burgess, M. (2016) 'Electric Cars to Be Allowed in Bus Lanes'. *BBC News* [online] 25 January. available from <<https://www.bbc.com/news/uk-england-35399212>>
- Cano, Z.P., Banham, D., Ye, S., Hintennach, A., Lu, J., Fowler, M., and Chen, Z. (2018) 'Batteries and Fuel Cells for Emerging Electric Vehicle Markets'. *Nature Energy* 3 (4), 279–289
- carhs.training (2021) *Crash- Regulations : Europe , United Nations , USA , China and India*. Safetywissen, 1. available from <<https://www.safetywissen.com/object/B04/B04.fl4737823wsk3tx0vib475752wysa963747868375/safetywissen?prev=%2Frequirement%2F.1107349076x2q7fqycw67591b69dvq63495945991%2F>>
- carhs (2021) *Applicability of Selected UN Regulations on the Classification of Vehicles*. Safetywissen, 1
- Catapult (2016) *Driverless Pods - Catapult Catapult* -. available from <<https://ts.catapult.org.uk/innovation-centre/cav/cav-projects-at-the-tsc/self-driving-pods/>>
- Christ, D. (2020) 'Simulating the Relative Influence of Tire, Vehicle and Driver Factors on Forward Collision Accident Rates'. *Journal of Safety Research* 73, 253–262
- Cicchino, J.B. (2017) 'Effectiveness of Forward Collision Warning and Autonomous Emergency Braking Systems in Reducing Front-to-Rear Crash Rates'. *Accident Analysis and Prevention* 99, 142–152
- Council of the European Union (2017) '8666/1/17 REV 1 TRANS 158'. in *Council Conclusions on Road Safety - Endorsing the Valletta Declaration of March 2017 - Council Conclusions (8 June 2017)* [online] held 2017 at Brussels. 1–8. available from <<https://data.consilium.europa.eu/doc/document/ST-9994-2017-INIT/en/pdf>>
- Daimler (n.d.) *Technical Data - Daimler Global Media Site* [online] available from <<https://media.daimler.com/marsMediaSite/en/instance/ko/Technical-data.xhtml?oid=40311855>> [20 June 2021]
- Davies, H., Bastien, C., Nieuwenhuis, P., and Bailey, S. (2016a) *Challenges and Opportunities for Improving the Safety of Lightweight Vehicles — Coventry University*. in [online] held 2016. available from <<https://pureportal.coventry.ac.uk/en/publications/challenges-and-opportunities-for-improving-the>>

safety-of-lightwei>

- Davies, H., Santos, G., Faye, I., Kroon, R., and Weken, H. (2016b) 'Establishing the Transferability of Best Practice in EV Policy across EU Borders'. *Transportation Research Procedia* [online] 14, 2574–2583. available from <<http://dx.doi.org/10.1016/j.trpro.2016.05.350>>
- Delannoy, P., Faure, J., Coulombier, D., Zeitouni, R., and Martin, T. (2004) 'New Barrier Test and Assessment Protocol to Control Compatibility'. in *SAE 2004 World Congress & Exhibition* [online] held 2004. SAE International, 11. available from <<https://www.sae.org/publications/technical-papers/content/2004-01-1171/>>
- Department for Transport (2021) *Reported Road Casualties Great Britain : 2010 Annual Report* [online] available from <<https://www.gov.uk/government/statistics/reported-road-casualties-great-britain-annual-report-2020/reported-road-casualties-great-britain-annual-report-2020#contact-details>>
- Department for Transport and Hammond, S. (2013) 'Thirty Years of Seatbelt Safety'. *Press Release, Seat Belts* [online] 31 January. available from <<https://www.gov.uk/government/news/thirty-years-of-seatbelt-safety>>
- Dhani, A. (2019) *Reported Road Casualties in Great Britain: Quarterly Provisional Estimates Year Ending June 2018* [online] available from <https://assets.publishing.service.gov.uk/government/uploads/system/uploads/attachment_data/file/848485/road-casualties-year-ending-june-2019.pdf>
- Diaz, S., Mock, P., Bernard, Y., Bieker, G., Pniewska, I., Ragon, P.-L., Rodriguez, F., Tietge, U., and Wappelhorst, S. (2021) *European Vehicle Market Statistics 2020/21*. 1–55. available from <<http://eupocketbook.theicct.org>>
- DIRECTIVE 2008/50/EC (2015) [online] Belgium. available from <<https://eur-lex.europa.eu/legal-content/EN/TXT/PDF/?uri=CELEX:02008L0050-20150918&from=EN>>
- Directive 2014/94/EU on the Deployment of Alternative Fuels Infrastructure (2020) [online] European Parliament. available from <<https://eur-lex.europa.eu/legal-content/EN/TXT/PDF/?uri=CELEX:02014L0094-20200524&from=EN>>
- Dixit, V. V., Chand, S., and Nair, D.J. (2016) *Autonomous Vehicles: Disengagements, Accidents and Reaction Times*. vol. <http://journals.plos.org/plosone/article?id=10.1371/journal.pone.0168054> PLoS ONE, 29/07/2018. available from <<http://journals.plos.org/plosone/article?id=10.1371/journal.pone.0168054>>
- Doll, S. (2021) 'China Claims Title of Having World's Largest EV Charging Network'. *Electrek* [online] 29 October. available from <<https://electrek.co/2021/10/29/china-claims-title-of-having-worlds-largest-ev-charging-network/>>
- DVSA (2019) 'History of Road Safety, The Highway Code and the Driving Test - GOV.UK'. in *History of Road Safety, The Highway Code and the Driving Test* [online] available from

<<https://www.gov.uk/government/publications/history-of-road-safety-and-the-driving-test/history-of-road-safety-the-highway-code-and-the-driving-test>>

Edwards, M., Seidl, M., Carroll, J., and Nathanson, A. (2014) *Provision of Information and Services to Perform an Initial Assessment of Additional Functional Safety and Vehicle Construction Requirements for L7e-A Heavy on-Road Quads* [online] vol. 1326718. Transport Research Laboratory. available from <<http://ec.europa.eu/DocsRoom/documents/5466/attachments/1/translations/en/renditions/native>>

Ellway, J. (2013) *AE-MDB Specification* [online] available from <<https://cdn.euroncap.com/media/1369/tb-014-ae-mdb-specification-v10-0-deedc4d5-0b92-470c-b7da-e99fcdaff93.pdf>>

EU-LIVE (n.d.) *Design Contest Winners Announcement* [online] available from <<https://eu-live.eu/winners/>> [16 June 2021a]

EU-LIVE (n.d.) *Modular Vehicle Concepts for the Future* [online] available from <<https://eu-live.eu/>> [16 June 2021b]

EUCAR (2019) *Battery Requirements for Future Automotive Applications EG BEV&FCEV* [online] available from <<https://www.dke.de/resource/blob/933404/fa7a24099c84ef613d8e7afd2c860a39/kompendum-li-ionen->>>

Euro NCAP (2021) 'ASSESSMENT PROTOCOL – SAFETY ASSIST'. *EUROPEAN NEW CAR ASSESSMENT PROGRAMME - Protocols* [online] (v9.0.4), 35. available from <<http://www.euroncap.com/en>>

Euro NCAP (2020a) *Euro NCAP | Offset-Deformable Barrier - ODB*. available from <<https://www.euroncap.com/en/vehicle-safety/the-ratings-explained/adult-occupant-protection/previous-tests/offset-deformable-barrier/>>

Euro NCAP (2020b) *EUROPEAN NEW CAR ASSESSMENT PROGRAMME (Euro NCAP) SIDE IMPACT MOBILE DEFORMABLE BARRIER TESTING PROTOCOL* [online] vol. June. available from <<https://cdn.euroncap.com/media/58234/euro-ncap-side-protocol-ae-mdb-v812.pdf>>

Euro NCAP (2020c) *ASSESSMENT PROTOCOL – ADULT OCCUPANT PROTECTION* [online] Euro NCAP. available from <<https://www.euroncap.com/en/for-engineers/protocols/adult-occupant-protection/>>

Euro NCAP (2016a) *Euro NCAP | 2016 Quadricycles' Tests*. Euro NCAP. available from <<https://www.euroncap.com/en/vehicle-safety/safety-campaigns/2016-quadricycles-tests/>>

Euro NCAP (2016b) *TEST RESULTS Aixam Crossover GTR* [online] available from <https://cdn.euroncap.com/media/22126/aixam_crossover_gtr_2016_datasheet.pdf>

Euro NCAP (2016c) *TEST RESULTS Bajaj Qute* [online] available from <https://cdn.euroncap.com/media/22124/bajaj_qute_2016_datasheet.pdf>

Euro NCAP (2016d) *TEST RESULTS Microcar M.GO Family* [online] available from <https://cdn.euroncap.com/media/22203/microcar_mgo_family_2016_datasheet.pdf>

Euro NCAP (2016e) *TEST RESULTS Chatenet CH30* [online] available from

- <https://cdn.euroncap.com/media/22123/chatenet_ch30_2016_datasheet.pdf>
- Euro NCAP (2015) 'FULL WIDTH FRONTAL IMPACT TESTING PROTOCOL'. *Euro NCAP Testing Protocols* [online] 1.0.2 (April), 1–29. available from <<https://cdn.euroncap.com/media/20872/full-width-frontal-impact-test-protocol-v102.pdf>>
- Euro NCAP (2014a) *L7e Full Width Frontal Barrier Impact Protocol* [online] available from <<https://cdn.euroncap.com/media/1563/heavy-quadricycles-side-test-and-assessment-v-11.pdf>>
- Euro NCAP (2014b) *L7e Side Impact Testing Protocol* [online] available from <<https://cdn.euroncap.com/media/1563/heavy-quadricycles-side-test-and-assessment-v-11.pdf>>
- Euro NCAP (2014c) *TEST RESULTS Tazzari ZERO* [online] available from <<https://cdn.euroncap.com/media/1694/euro-ncap-test-on-heavy-quadricycles-tazzari.pdf>>
- Euro NCAP (2014d) *TEST RESULTS Renault Twizy 80* [online] available from <<https://cdn.euroncap.com/media/1691/euro-ncap-test-on-heavy-quadricycles-renault.pdf>>
- Euro NCAP (2014e) *TEST RESULTS Club Car Villager 2+2 LSV* [online] available from <<https://cdn.euroncap.com/media/1693/euro-ncap-test-on-heavy-quadricycles-clubcar.pdf>>
- Euro NCAP (2014f) *TEST RESULTS Ligier IXO JS LINE 4 Places* [online] available from <<https://cdn.euroncap.com/media/1692/euro-ncap-test-on-heavy-quadricycles-ligier.pdf>>
- Euro NCAP (n.d.) *Euro NCAP | Euro NCAP - Members and Test Facilities* [online] available from <<https://www.euroncap.com/en/about-euro-ncap/members-and-test-facilities/>> [23 June 2021]
- European Commission (2021a) *Collision Avoidance Systems | Mobility and Transport* [online] available from <https://ec.europa.eu/transport/road_safety/specialist/knowledge/esave/esafety_measures_unknown_safety_effects/collision_avoidance_systems_en> [23 June 2021]
- European Commission (2021b) *Junctions | Mobility and Transport* [online] available from <https://ec.europa.eu/transport/road_safety/specialist/knowledge/road/getting_initial_safety_design_principles_right/junctions_en> [25 July 2021]
- European Commission (2019) 'EU Road Safety Policy Framework 2021-2030 - Next Steps towards "Vision Zero"'. *COMMISSION STAFF WORKING DOCUMENT* [online] (283), 1–33. available from <https://ec.europa.eu/transport/road_safety/sites/default/files/move-2019-01178-01-00-en-tra-00_3.pdf>
- European Commission (2018) 'Sustainable Mobility for Europe: Safe, Connected, and Clean'. *COMMUNICATION FROM THE COMMISSION TO THE EUROPEAN PARLIAMENT, THE COUNCIL, THE EUROPEAN ECONOMIC AND SOCIAL COMMITTEE AND THE COMMITTEE OF THE REGIONS* [online] 14. available from <https://eur-lex.europa.eu/resource.html?uri=cellar:0e8b694e-59b5-11e8-ab41-01aa75ed71a1.0003.02/DOC_1&format=PDF>
- European Commission (2016) *COMMISSION STAFF WORKING DOCUMENT Accompanying the Document*

- COMMUNICATION FROM THE COMMISSION TO THE EUROPEAN PARLIAMENT, THE COUNCIL, THE EUROPEAN ECONOMIC AND SOCIAL COMMITTEE AND THE COMMITTEE OF THE REGIONS [online] Brussels. available from <<https://eur-lex.europa.eu/legal-content/EN/TXT/PDF/?uri=CELEX:52016SC0244&from=EN>>
- European Commission (n.d.) *Vehicle Categories* [online] available from <https://ec.europa.eu/growth/sectors/automotive/vehicle-categories_en> [14 June 2021]
- Fang, J., Sun, G., Qiu, N., Steven, G.P., and Li, Q. (2017) 'Topology Optimization of Multicell Tubes Under Out-of-Plane Crushing Using a Modified Artificial Bee Colony Algorithm'. *Journal of Mechanical Design, Transactions of the ASME* 139 (7), 1–16
- Favaro, F., Nader, N., Eurich, S., Tripp, M., and Varadaraju, N. (2017) *Examining Accident Reports Involving Autonomous Vehicles in California* [online] vol. 12. PLoS ONE. available from <<http://journals.plos.org/plosone/article?id=10.1371/journal.pone.0184952>>
- Favarò, F.M., Nader, N., Eurich, S.O., Tripp, M., and Varadaraju, N. (2017) 'Examining Accident Reports Involving Autonomous Vehicles in California'. *PLoS ONE* 12 (9), 1–20
- Feucht, M., Haufe, A., and Pietsch, G. (2007) 'Modelling of Adhesive Bonding in Crash Simulation'. in *LSDYNA-Forum* [online] 6th edn. Frankenthal: DYNAmore, 1–56. available from <<https://www.dynamore.de/de/download/papers/forum07/forum07/keynote/modelling-of-adhesive-bonding-in-crash-simulation>>
- Fildes, B., Keall, M., Bos, N., Lie, A., Page, Y., Pastor, C., Pennisi, L., Rizzi, M., Thomas, P., and Tingvall, C. (2015) 'Effectiveness of Low Speed Autonomous Emergency Braking in Real-World Rear-End Crashes'. *Accident Analysis and Prevention* [online] 81, 24–29. available from <<http://dx.doi.org/10.1016/j.aap.2015.03.029>>
- Fujimura, T. (2015) *Simulation and Optimization Analysis of Small Vehicle Deceleration to Reduce Occupant Injury at Frontal Collision* [online] available from <<https://www.sae.org/publications/technical-papers/content/2015-32-0705/>>
- Gandikota, I., Rais-Rohani, M., Dormohammadi, S., and Kiani, M. (2015) 'Multilevel Vehicle-Dummy Design Optimization for Mass and Injury Criteria Minimization'. *Proceedings of the Institution of Mechanical Engineers, Part D: Journal of Automobile Engineering* 229 (3), 283–295
- Gao, Q., Wang, L., Wang, Y., and Wang, C. (2016) 'Crushing Analysis and Multiobjective Crashworthiness Optimization of Foam-Filled Ellipse Tubes under Oblique Impact Loading'. *Thin-Walled Structures* 100, 105–112
- Gaylor, L., Junge, M., and Abanteriba, S. (2017) 'Efficacy of Seat-Mounted Thoracic Side Airbags in the German Vehicle Fleet'. *Traffic Injury Prevention* [online] 18 (8), 852–858. available from <<https://doi.org/10.1080/15389588.2017.1316843>>

- Gierczycka, D., Watson, B., and Cronin, D. (2015) 'Investigation of Occupant Arm Position and Door Properties on Thorax Kinematics in Side Impact Crash Scenarios-Comparison of ATD and Human Models'. *International Journal of Crashworthiness* [online] 20 (3), 242–269. available from <<http://dx.doi.org/10.1080/13588265.2014.998000>>
- Gitlin, J. (2018) 'This Volvo Concept Could Replace Planes and Trains with the Automobile'. *Ars Technica* [online] 14 September. available from <<https://arstechnica.com/cars/2018/09/volvo-gets-optimistic-about-the-future-with-the-360c-driverless-concept/>>
- Gromer, A., Stahlschmidt, S., and D'Souza, R. (2009) *Development of the PDB WorldSID 50th Model with the German Automotive Industry*. Stuttgart
- GTAI (2020) 'The Automotive Industry in Germany'. in *Germany Trade & Invest* [online] vol. 7 (2020/2021). 1–16. available from <<https://www.gtai.de/resource/blob/64100/817a53ea3398a88b83173d5b800123f9/industry-overview-automotive-industry-en-data.pdf>>
- Hagenzieker, M.P., Commandeur, J.J.F., and Bijleveld, F.D. (2014) 'The History of Road Safety Research: A Quantitative Approach'. *Transportation Research Part F: Traffic Psychology and Behaviour* [online] 25 (PART B), 150–162. available from <<https://www.sciencedirect.com/science/article/pii/S1369847813001009?via%3Dihub>>
- Hakkert, A.S. and Gitelman, V. (2014) 'Thinking about the History of Road Safety Research: Past Achievements and Future Challenges'. *Transportation Research Part F: Traffic Psychology and Behaviour* [online] 25 (PART B), 137–149. available from <<https://www.sciencedirect.com/science/article/pii/S1369847814000187>>
- Harald, K., Stefan, K., Ernst, T., Heinz, H., Peter, L., and Wolfgang, S. (2016) 'Prospective Evaluation of the Collision Severity L7e Vehicles Considering a Collision Mitigation System'. in *Transport Research Arena TRA2016* [online] vol. 14. 3877–3885. available from <<http://www.sciencedirect.com/science/article/pii/S2352146516304811>>
- Harrison, A., Christensen, J., Bastien, C., and Kanarachos, S. (2020) 'Crashworthy Structures for Future Vehicle Architecture of Autonomous Pods and Heavy Quadricycles on Public Roads: A Review'. *Proceedings of the Institution of Mechanical Engineers, Part D: Journal of Automobile Engineering* 234 (1)
- Hirst, D., Winnett, J., and Hinson, S. (2020) 'Electric Vehicles and Infrastructure'. *House of Commons Library* [online] (December), 295–314. available from <<https://researchbriefings.files.parliament.uk/documents/CBP-7480/CBP-7480.pdf>>
- Hou, S., Shu, C., Zhao, S., Liu, T., Han, X., and Li, Q. (2015) 'Experimental and Numerical Studies on Multi-Layered Corrugated Sandwich Panels under Crushing Loading'. *Composite Structures* 126, 371–385
- Hughes, B.P., Anund, A., and Falkmer, T. (2015) 'System Theory and Safety Models in Swedish, UK, Dutch and

- Australian Road Safety Strategies'. *Accident Analysis and Prevention* [online] 74, 271–278. available from <<https://www.sciencedirect.com/science/article/pii/S0001457514002206>>
- Humanetics Innovative Solutions (2018) *WorldSID 50th User Manual* [online] Farmington Hills. available from <https://humanetics.humaneticsgroup.com/sites/default/files/2020-11/um-w50m_rev_k.pdf>
- ICCT (2019) *EUROPEAN VEHICLE MARKET STATISTICS* [online] Berlin. available from <<http://eupocketbook.theicct.org>>
- IDEO (n.d.) *IDEO · The Future of Automobility* [online] available from <<https://automobility.ideo.com/preface/intro>> [12 December 2017]
- IIHS (2017) *Frontal Crash Tests: About Our Tests* [online] available from <<http://www.iihs.org/iihs/ratings/ratings-info/frontal-crash-tests>>
- IIHS (2016) 'Moderate Overlap Frontal Crashworthiness Evaluation - Guidelines for Rating Structural Performance'. *Insurance Institute for Highway Safety* [online] 2 (December), 4. available from <https://www.iihs.org/media/8c0e4bd7-c953-4d6a-99f5-2713b5f1d048/UweT0w/Ratings/Protocols/archive/structural_1116.pdf>
- IIHS HLDI (2020) *Self-Driving Vehicles Could Struggle to Eliminate Most Crashes* [online] available from <<https://www.iihs.org/news/detail/self-driving-vehicles-could-struggle-to-eliminate-most-crashes>> [2 July 2020]
- Insurance Institue for Highway Safety (2014) *Side Impact Crashworthiness. Evaluation Guidelines for Rating Injury Measures (Version III)* [online] available from <https://www.iihs.org/media/ba19c647-c2e7-4341-8f12-fe84b0e68a21/9mhzGw/Ratings/Protocols/current/measures_side.pdf>
- International Transport Forum (2020a) *Road Safety Report, United Kingdom* [online] available from <<https://www.itf-oecd.org/sites/default/files/united-kingdom-road-safety.pdf>>
- International Transport Forum (2020b) *Road Safety Report, Germany* [online] available from <<https://www.itf-oecd.org/sites/default/files/germany-road-safety.pdf>>
- International Transport Forum (2020c) *Road Safety Report, France* [online] available from <<https://www.itf-oecd.org/sites/default/files/france-road-safety.pdf>>
- International Transport Forum (2020d) *ROAD SAFETY ANNUAL REPORT 2020* [online] International Transport Forum. available from <https://www.itf-oecd.org/sites/default/files/docs/irtad-road-safety-annual-report-2020_0.pdf>
- Irlle, R. (2021) *EV-Volumes - The Electric Vehicle World Sales Database* [online] available from <<https://www.ev-volumes.com/>> [12 June 2021]
- Ito, D., Yokoi, Y., and Mizuno, K. (2014) 'Crash Pulse Optimization for Occupant Protection at Various Impact Velocities'. *Traffic Injury Prevention* [online] 16 (3), 260–267. available from <<http://www.tandfonline.com/doi/abs/10.1080/15389588.2014.937805?journalCode=gcpi20>>

- Jaroszweski, D. and McNamara, T. (2014) 'The Influence of Rainfall on Road Accidents in Urban Areas: A Weather Radar Approach'. *Travel Behaviour and Society* 1 (1), 15–21
- Jeong, G., Park, H.K., Lee, K.S., Ko, S. hoon, Choo, H., and Lee, H.B. (2017) 'Development of a Driver-Side Airbag Considering Autonomous Emergency Braking'. in *25th International Technical Conference on the Enhanced Safety of Vehicles (ESV)* [online] held 2017 at Detroit Michigan, United States. National Highway Traffic Safety Administration. available from <<https://trid.trb.org/view/1490115>>
- Jurewicz, C., Sobhani, A., Woolley, J., Dutschke, J., and Corben, B. (2016) 'Exploration of Vehicle Impact Speed - Injury Severity Relationships for Application in Safer Road Design'. *Transportation Research Procedia* [online] 14, 4247–4256. available from <<http://dx.doi.org/10.1016/j.trpro.2016.05.396>>
- Kahane, C.J. (2003) *Vehicle Weight, Fatality Risk and Crash Compatibility of Model Year 1991-99 Passenger Cars and Light Trucks* [online] available from <<https://crashstats.nhtsa.dot.gov/Api/Public/ViewPublication/809662>>
- Kamran, M., Xue, P., Ahmed, N., Zahran, M.S., and Hanif, A.A.G. (2017) 'Axial Crushing of Uni-Sectional Bi-Tubular Inner Tubes with Multiple Outer Cross-Sections'. *Latin American Journal of Solids and Structures* 14 (12), 2198–2220
- Kane, M. (2021) 'China Now Has Over 1 Million Public Charging Points'. *InsideEVs* [online] November. available from <<https://insideevs.com/news/544573/china-1million-public-charging-points/>>
- Kelley, M.E., Talton, J.W., Weaver, A.A., Usoro, A.O., Barnard, E.R., and Miller, A.N. (2019) 'Associations between Upper Extremity Injury Patterns in Side Impact Motor Vehicle Collisions with Occupant and Crash Characteristics'. in *Accident Analysis & Prevention* [online] vol. 122. 1–7. available from <<http://www.sciencedirect.com/science/article/pii/S0001457518306997>>
- Kohar, C.P., Mohammadi, M., Mishra, R.K., and Inal, K. (2015) 'Effects of Elastic-Plastic Behaviour on the Axial Crush Response of Square Tubes'. *Thin-Walled Structures* 93, 64–87
- Kohar, C.P., Zhumagulov, A., Brahme, A., Worswick, M.J., Mishra, R.K., and Inal, K. (2016) 'Development of High Crush Efficient, Extrudable Aluminium Front Rails for Vehicle Lightweighting'. *International Journal of Impact Engineering* 95, 17–34
- KPMG (2015) 'Connected and Autonomous Vehicles – The UK Economic Opportunity'. *KPMG International* (March), 1–24
- KPMG International (2019) *2019 Autonomous Vehicles Readiness Index* [online] available from <<https://assets.kpmg/content/dam/kpmg/xx/pdf/2019/02/2019-autonomous-vehicles-readiness-index.pdf>>
- Krebs, J. and Bhalsod, D. (2012) *Advanced European Movable Deformable Barrier*. Livermore Software Technology Corporation
- Kuppa, S. (2004) 'Injury Criteria for Side Impact Dummies'. *National Transportation Biomechanics Research*

Centre National Highway Traffic Safety Administration 1–67

- Lai, X., Ma, C., Hu, J., and Zhou, Q. (2012) 'Impact Direction Effect on Serious-to-Fatal Injuries among Drivers in near-Side Collisions According to Impact Location: Focus on Thoracic Injuries'. in *Intelligent Speed Adaptation + Construction Projects* [online] vol. 48. 442–450. available from <<http://www.sciencedirect.com/science/article/pii/S0001457512000899>>
- Lee, J.E., Kim, G.E., and Kim, B.W. (2019) 'Study on the Improvement of a Collision Avoidance System for Curves'. *Applied Sciences (Switzerland)* 9 (24)
- Lee, Y. and Park, G.-J. (2017) 'Non-Linear Dynamic Response Structural Optimization for Frontal-Impact and Side-Impact Crash Tests'. *Proc IMechE Part D: J Automobile Engineering* 231 (5), 600–614
- Li, J. (2020) 'Charging Chinese Future: The Roadmap of China's Policy for New Energy Automotive Industry'. *International Journal of Hydrogen Energy* 45 (20), 11409–11423
- Li, Z., Duan, L., Chen, T., and Hu, Z. (2018) 'Crashworthiness Analysis and Multi-Objective Design Optimization of a Novel Lotus Root Filled Tube (LFT)'. *Structural and Multidisciplinary Optimization* 57 (2), 865–875
- Ligier Group (2013) *PRESS Info IAA* 2013. 1–35. available from <<https://www.ligiergroup.de/presse/files/Dokumente/Downloads/PressINFOUK.pdf>>
- Lotus Engineering Incorporation (2010) *An Assessment of Mass Reduction Opportunities for a 2017 – 2020 Model Year Vehicle Program*. vol. Rev 006A
- Lowne, R. (2001) *RECOMMENDATIONS FOR A REVISED SPECIFICATION FOR THE EEVC MOBILE DEFORMABLE BARRIER FACE R* Lowne [online] available from <<https://unece.org/DAM/trans/main/wp29/wp29wgs/wp29grsp/grspinf/30/30inf02.pdf>>
- Ma, C.C., Lan, F.C., Chen, J.Q., Liu, J., and Zeng, F.B. (2015) 'Automobile Crashworthiness Improvement by Energy-Absorbing Characterisation of Aluminium Foam Porosity'. *Materials Research Innovations* 19, S1109–S1112
- Mallick, P.K. (2021) 'Designing Lightweight Vehicle Body'. *Materials, Design and Manufacturing for Lightweight Vehicles* [online] 2, 405–432. available from <<http://dx.doi.org/10.1016/B978-0-12-818712-8.00010-0>>
- Mercedes-Benz (2020) *EQC SUV*. vol. Electric I. Stuttgart
- Mercedes-Benz (2019) '360° Environmental Check Mercedes-Benz EQC'. in *Brochure* [online] Stuttgart: Daimler Communications, 1–16. available from <<https://www.daimler.com/documents/sustainability/product/daimler-environmental-check-mb-eqc-class-org.pdf>>
- Mercedes-Benz AG (2019) 'GLE Coupé'. in *Preisliste Gültig Ab 22. November 2019* [online] Berlin: Mercedes-Benz AG, 1–67. available from <<https://www.mercedes-benz.de/content/dam/germany/passengercars/Passenger-Cars/Preislisten/glc-gle-gls/Mercedes-Benz-Preisliste-GLE-Coupe-C167.pdf>>

- MFES (2007) 'Skidding Friction: A Review of Recent Research'. [online] available from <<http://mfes.com/friction.html>>
- Mikusova, M. (2017) 'Crash Avoidance Systems and Collision Safety Devices for Vehicle Occupants'. in *MATEC Web of Conferences* [online] held 2017. EDP Sciences, 24. available from <https://www.matec-conferences.org/articles/mateconf/abs/2017/21/mateconf_dyn2017_00024/mateconf_dyn2017_00024.html>
- Mock, P. (2019) *European Vehicle Market Statistics 2018/2019*. 1–64. available from <<http://eupocketbook.theicct.org>>
- Nagel, G. (2005) *(TEZ) Impact and Energy Absorption of Straight and Tapered Rectangular Tubes* [online] Queensland University of Technology. available from <<https://core.ac.uk/download/pdf/10884696.pdf>>
- NCAC (2014a) *2010 Toyota Venza (Baseline BL) FE Model Validation , Trend & Robustness Study* [online] available from <<https://www.nhtsa.gov/crash-simulation-vehicle-models>>
- NCAC (2014b) *2010 Toyota Venza (LO) FE Model Trend & Robustness Study* [online] available from <<https://www.nhtsa.gov/crash-simulation-vehicle-models>>
- NCAC (2014c) *2010 Toyota Venza (HO) FE Model Trend & Robustness Study* [online] available from <<https://www.nhtsa.gov/crash-simulation-vehicle-models>>
- NCAP, E. (2019) *Side Impact Mobile Deformable Barrier Testing Protocol - For 2020 Implementation* [online] vol. Version 8. Euro NCAP. available from <<https://cdn.euroncap.com/media/55859/euro-ncap-side-protocol-ae-mdb-v811.pdf>>
- NHTSA (2020) 'NHTSA Announces 2020 Update on AEB Installation by 20 Automakers | NHTSA'. *NHTSA Media* [online] 17 December. available from <<https://www.nhtsa.gov/press-releases/nhtsa-announces-2020-update-aeb-installation-20-automakers>>
- NHTSA (2017) *2014 Chevrolet Silverado*. U.S Department of Transportation. available from <<https://www.nhtsa.gov/node/34676>>
- NHTSA (2015) *Critical Reasons for Crashes Investigated in the National Motor Vehicle Crash Causation Survey*.
- NHTSA (2014a) *Crash Simulation Vehicle Models | NHTSA* [online] available from <<https://www.nhtsa.gov/crash-simulation-vehicle-models>> [2 October 2020]
- NHTSA (2014b) *Toyota Venza Baseline*. United States Department of Transportation. available from <[http://www-nrd.nhtsa.dot.gov/Departments/Crashworthiness/Crashworthiness by vehicle Models/LS DYNA_FE_MODELS/VENZA_BASELINE/VenzaBL.tar.gz](http://www-nrd.nhtsa.dot.gov/Departments/Crashworthiness/Crashworthiness%20by%20vehicle%20Models/LS DYNA_FE_MODELS/VENZA_BASELINE/VenzaBL.tar.gz)>
- NHTSA (2014c) *Toyota Venza Low Option*. United States Department of Transportation. available from <[http://www-nrd.nhtsa.dot.gov/Departments/Crashworthiness/Crashworthiness by vehicle Models/LS DYNA_FE_MODELS/VENZA_LOW_OPTION/VenzaLO.tar.gz](http://www-nrd.nhtsa.dot.gov/Departments/Crashworthiness/Crashworthiness%20by%20vehicle%20Models/LS DYNA_FE_MODELS/VENZA_LOW_OPTION/VenzaLO.tar.gz)>
- NHTSA (2012) *LABORATORY TEST PROCEDURE FOR FMVSS No. 214, DYNAMIC SIDE IMPACT PROTECTION*

- Moving Deformable Barrier Test Requirements Using Advanced Test Dummies*. [online] (September), 45. available from <<https://www.nhtsa.gov/sites/nhtsa.dot.gov/files/tp214d-09.pdf>>
- NHTSA (2010) *2010 Toyota Yaris*. 1. United States Department of Transportation. available from <[http://www-nrd.nhtsa.dot.gov/Departments/Crashworthiness/Crashworthiness](http://www-nrd.nhtsa.dot.gov/Departments/Crashworthiness/Crashworthiness%20by%20vehicle%20Models/LSDYNA_FE_MODELS/YARIS/Yaris.tar.gz) by vehicle Models/LSDYNA_FE_MODELS/YARIS/Yaris.tar.gz>
- NHTSA (2006) *NATIONAL HIGHWAY TRAFFIC SAFETY ADMINISTRATION LABORATORY TEST PROCEDURE FOR FMVSS 216 Roof Crush Resistance* [online] available from <[https://www.nhtsa.gov/sites/nhtsa.gov/files/tp-216-05.pdf#:~:text=FMVSS 216%2C Roof Crush Resistance,of 2722 kilograms or less.&text=3 by means that require no action by passenger car occupants.>](https://www.nhtsa.gov/sites/nhtsa.gov/files/tp-216-05.pdf#:~:text=FMVSS%20216%2C%20Roof%20Crush%20Resistance,of%202722%20kilograms%20or%20less.&text=3%20by%20means%20that%20require%20no%20action%20by%20passenger%20car%20occupants.>)>
- NHTSA (n.d.) 'Car Safety Ratings | Vehicles, Car Seats, Tires | NHTSA'. in *NHTSA* [online] available from <<https://www.nhtsa.gov/ratings#25196>>
- Nia, A.A. and Chahardoli, S. (2016) 'Mechanical Behavior of Nested Multi-Tubular Structures under Quasi-Static Axial Load'. *Thin-Walled Structures* 106, 376–389
- Noversa, M. and Peixinho, N. (2013) 'Numerical Simulation of Impact Behaviour of Structures with Internal Pressurization for Crash-Adaptive Concept'. *Engineering Transactions* 61 (3), 185–195
- Oasys (n.d.) *Oasys Suite Version 17.0 Released - LS-DYNA*. available from <<https://www.oasys-software.com/dyna/news/oasys-suite-17-0-released/>>
- Omer, K., ten Kortenaar, L., Butcher, C., Worswick, M., Malcolm, S., and Detwiler, D. (2017) 'Testing of a Hot Stamped Axial Crush Member with Tailored Properties – Experiments and Models'. *International Journal of Impact Engineering* 103, 12–28
- Padmanaban, J. (2003) 'Influences of Vehicle Size and Mass and Selected Driver Factors on Odds of Driver Fatality.' *Annual Proceedings / Association for the Advancement of Automotive Medicine. Association for the Advancement of Automotive Medicine* [online] 47, 507–524. available from <[/pmc/articles/PMC3217563/](https://pubmed.ncbi.nlm.nih.gov/127563/)>
- Plötz, P., Gnann, T., and Sprei, F. (2016) 'Can Policy Measures Foster Plug-in Electric Vehicle Market Diffusion?' *EVS 2016 - 29th International Electric Vehicle Symposium* 8 (2010), 789–797
- PMR (2019) *Europe Motorized Quadricycles Market Is Set Grow at a CAGR of ~5% between 2019 and 2029* [online] available from <<https://www.prnewswire.co.uk/news-releases/europe-motorized-quadricycles-market-is-set-grow-at-a-cagr-of-5-between-2019-and-2029-pmr-892294445.html>> [7 June 2021]
- Qiu, N., Gao, Y., Fang, J., Feng, Z., Sun, G., and Li, Q. (2015) 'Crashworthiness Analysis and Design of Multi-Cell Hexagonal Columns under Multiple Loading Cases'. *Finite Elements in Analysis and Design* 104, 89–101
- Reddy, S., Abbasi, M., and Fard, M. (2015) 'Multi-Cornered Thin-Walled Sheet Metal Members for Enhanced

Crashworthiness and Occupant Protection'. *Thin-Walled Structures* 94, 56–66

Reddy, T.J., Rao, Y. V.D., and Narayanamurthy, V. (2018) 'Thin-Walled Structural Configurations for Enhanced Crashworthiness'. *International Journal of Crashworthiness* [online] 23 (1), 57–73. available from <<https://doi.org/10.1080/13588265.2017.1306824>>

Regulation (EC) No 715/2007 (2007, Official Journal of the European Union) [online] (EC) No 715/2007. Europe: European Union. available from <<https://eur-lex.europa.eu/legal-content/EN/TXT/PDF/?uri=CELEX:32007R0715&from=EN>>

Regulation (EU) 2018/ 858 (2018, Official Journal of the European Union) [online] Europe: European Union. available from <<https://eur-lex.europa.eu/legal-content/EN/TXT/PDF/?uri=CELEX:32018R0858&from=EN>>

Regulation (EU) 2019/129 (2019, Official Journal of the European Union) [online] (EU) 2019/129. Europe: European Union. available from <<https://eur-lex.europa.eu/legal-content/EN/TXT/PDF/?uri=CELEX:32019R0129&from=EN>>

Regulation (EU) 2019/2144 (2019, Official Journal of the European Union) [online] (EU) 2019/2144. Europe: European Union. available from <https://ec.europa.eu/transport/road_safety/sites/roadsafety/files/vademecum_2018.pdf>

REGULATION (EU) 2019/631 (2019, Official Journal of the European Union) [online] 2019/631. EU Members: European Parliament and of the Council. available from <<https://eur-lex.europa.eu/legal-content/EN/TXT/PDF/?uri=CELEX:32019R0631&from=EN>>

Regulation (EU) 2020/239 (2020, Official Journal of the European Union) [online] (EU) 2020/239. Europe: European Union. available from <<https://eur-lex.europa.eu/legal-content/EN/TXT/PDF/?uri=CELEX:32020R0239&from=EN>>

Regulation (EU) No 168/2013 (2013, Official Journal of the European Union) [online] (EU) No 168/2013. Brussels, Europe: The European Parliament and of the Council. available from <<https://eur-lex.europa.eu/legal-content/EN/TXT/PDF/?uri=CELEX:32013R0168&from=EN>>

Regulation (EU) No 901/2014 of 18 July 2014 Implementing Regulation (EU) No 168/2013 (2014, Official Journal of the European Union) [online] EU No 901/2014. Brussels, Europe: European Union. available from <<https://eur-lex.europa.eu/legal-content/EN/TXT/PDF/?uri=CELEX:32014R0901&from=EN>>

Regulation No. 100 (2013, World Forum for Harmonization of Vehicle Regulations) United Nations

Reichert, R., Kan, S., Arnold-Keifer, S., and Mueller, B. (2018) 'IIHS Side Impact Parametric Study Using LS-DYNA'. in *15th International LS-DYNA Users Conference* [online] held 2018. IIHS, 1–12. available from <<https://www.dynalook.com/conferences/15th-international-ls-dyna-conference/occupant-protection/iihs-side-impact-parametric-study-using-ls-dyna-r>>

Sadeghipour, E. (2017) *A New Approach to Assess and Optimize the Frontal Crash Compatibility of Vehicle*

- Structures with Focus on the European Fleet of Passenger Cars*. Munich, 1–169. available from <https://www.researchgate.net/publication/321038492_A_New_Approach_to_Assess_and_Optimize_the_Frontal_Crash_Compatibility_of_Vehicle_Structures>
- Sanchez, M. (n.d.) *Smart Car Dimensions & Specifications* [online] available from <<https://itstillruns.com/differences-toyota-avalon-models-5335779.html>>
- Sankaran, V. (2021) 'Tesla to Be Served Search Warrant over Crash as Elon Musk Denies Autopilot Was Used | The Independent'. *Independant Online* [online] 20 April. available from <<https://www.independent.co.uk/news/world/americas/tesla-crash-autopilot-elon-musk-b1834205.html>>
- Santucci, M., Pieve, M., and Pierini, M. (2016) 'Electric L-Category Vehicles for Smart Urban Mobility'. in *Transport Research Arena TRA2016* [online] vol. 14. 3651–3660. available from <<http://www.sciencedirect.com/science/article/pii/S2352146516304409>>
- Schlosser, J., Schneider, R., Rimkus, W., Kelsch, R., Gerstner, F., Harrison, D.K., and Grant, R.J. (2017) 'Materials and Simulation Modelling of a Crash-Beam Performance - A Comparison Study Showing the Potential for Weight Saving Using Warm-Formed Ultra-High Strength Aluminium Alloys'. *Journal of Physics: Conference Series* 896 (1)
- Schram, R. (2017) *Technical Bulletin: Data Format and Injury Criteria Calculation* [online] available from <<https://cdn.euroncap.com/media/27044/tb-021-data-acquisition-and-injury-calculation-v20.pdf>>
- smart (2021) 'Smart EQ Fortwo and Forfour. The Price List.' in *Brochure* [online] held 2021. Mercedes-Benz, 1–30. available from <<https://tools.mercedes-benz.co.uk/current/smart/pricelists/smart-electric-drive.pdf>>
- Stahlschmidt, S. and Gromer, A. (2010) 'WorldSID 50th vs. ES-2. A Comparison Based on Simulations.' *11th International LS- ...* [online] 2, 13–32. available from <<http://www.dynamore.de/de/download/papers/forum10/papers/D-I-02.pdf>>
- Subit, D., Vezin, P., Laporte, S., and Sandoz, B. (2017) 'Will Automated Driving Technologies Make Today's Effective Restraint Systems Obsolete?' *American Journal of Public Health* 107 (10), 1590–1592
- Sun, G., Pang, T., Fang, J., Li, G., and Li, Q. (2017a) 'Parameterization of Criss-Cross Configurations for Multiobjective Crashworthiness Optimization'. *International Journal of Mechanical Sciences* 124–125, 145–157
- Sun, G., Pang, T., Xu, C., Zheng, G., and Song, J. (2017b) 'Energy Absorption Mechanics for Variable Thickness Thin-Walled Structures'. *Thin-Walled Structures* 118, 214–228
- Sun, G., Zhang, H., Wang, R., Lv, X., and Li, Q. (2017c) 'Multiobjective Reliability-Based Optimization for Crashworthy Structures Coupled with Metal Forming Process'. *Structural and Multidisciplinary Optimization* 56 (6), 1571–1587

- Svensson, M.Y., D'Addetta, G.A., Carlsson, A., Ewald, C., Luttenberger, P., Mayer, C., Strandroth, J., Tomasch, E., Gutsche, A., and Wismans, J. (2014) 'Future Accident Scenarios Involving Small Electric Vehicles'. in *IRC-14-13* [online] held 2014 at IRCOBi Conference 2014. International Research Council on Biomechanics of Injury, 51–52. available from <http://www.ircobi.org/wordpress/downloads/irc14/pdf_files/13.pdf>
- Syed, M.H. and Abadin, Z.U. (2020) 'A Pattern for Autonomous Vehicle Platoon'. *ACM International Conference Proceeding Series* [online] 7. available from <<https://dl.acm.org/doi/pdf/10.1145/3424771.3424813>>
- Templeton, B. (2020) 'Tesla In Taiwan Crashes Directly Into Overturned Truck, Ignores Pedestrian, With Autopilot On'. *Forbes Online* [online] June. available from <<https://www.forbes.com/sites/bradtempleton/2020/06/02/tesla-in-taiwan-crashes-directly-into-overturned-truck-ignores-pedestrian-with-autopilot-on/?sh=2dd0c52758e5>>
- Tencer, A.F., Kaufman, R., Mack, C., and Mock, C. (2005) 'Factors Affecting Pelvic and Thoracic Forces in Near-Side Impact Crashes: A Study of US-NCAP, NASS, and CIREN Data'. in *Accident Analysis & Prevention* [online] vol. 37 (2). 287–293. available from <<http://www.sciencedirect.com/science/article/pii/S0001457504000934>>
- Tolouei, R., Maher, M., and Titheridge, H. (2013) 'Vehicle Mass and Injury Risk in Two-Car Crashes: A Novel Methodology'. in *Accident Analysis & Prevention* [online] vol. 50. 155–166. available from <<http://www.sciencedirect.com/science/article/pii/S0001457512001388>>
- Tostengard, A. (2015) *50 KWh Bosch EV Battery Will Soon Weigh Just 190 Kilograms - The Green Optimistic* [online] available from <<https://www.greenoptimistic.com/bosch-electric-vehicle-battery-kg/>>
- U.S Department of Energy (n.d.) *Alternative Fuels Data Center: How Do All-Electric Cars Work?* available from <<https://afdc.energy.gov/vehicles/how-do-all-electric-cars-work>>
- U.S Department of Energy (n.d.) *Alternative Fuels Data Center: How Do Hybrid Electric Cars Work?* available from <<https://afdc.energy.gov/vehicles/how-do-hybrid-electric-cars-work>>
- UN Addendum - Regulation 137 (2016, E/ECE/324/Rev.2/Add.136 –E/ECE/TRANS/505/Rev.2/Add.136) [online] Addendum 136 – Regulation No. 137. United Nation member states: United Nations. available from <<https://unece.org/fileadmin/DAM/trans/main/wp29/wp29regs/2016/R137e.pdf>>
- UN Addendum 134 - Regulation No. 135 (2015) [online] E/ECE/324/Rev.2/Add.134 –E/ECE/TRANS/505/Rev.2/Add.134. United Nation member states. available from <<https://unece.org/fileadmin/DAM/trans/main/wp29/wp29regs/2015/R135e.pdf>>
- UN Regulation 14 (2013, Global Registry) [online] ECE/TRANS/180/Add.14. Geneva: United Nations. available from <<https://unece.org/fileadmin/DAM/trans/doc/2014/wp29grsp/ECE-TRANS-180a14e.pdf>>
- Viano, D.C., Patel, M., and Ciccone, M.A. (1989) 'Patterns of Arm Position during Normal Driving'. *Human Factors* [online] 31 (6), 715–720. available from <<https://www.scopus.com/inward/record.uri?eid=2-s2.0-0024954494&partnerID=40&md5=94be4eb6d098b3063c047362a0fbca40>>

- Volvo, A.B. (2021) *360c | A New Way to Travel | Volvo Cars*. available from <<https://www.volvocars.com/intl/cars/concepts/360c>>
- Wappelhorst, S., Hall, D., Nicholas, M., and Ltsey, N. (2020) 'Analyzing Policies To Grow the Electric Vehicle Market in European Cities'. *ICCT White Paper* [online] (February), 1–43. available from <https://theicct.org/sites/default/files/publications/EV_city_policies_white_paper_fv_20200224.pdf>
- Wegman, F., Aarts, L., and Bax, C. (2008) 'Advancing Sustainable Safety. National Road Safety Outlook for The Netherlands for 2005-2020'. *Safety Science* [online] 46 (2), 323–343. available from <<https://www.sciencedirect.com/science/article/pii/S092575350700094X>>
- Westfield Technology Group (2022) *Westfield POD - Westfield Autonomous Vehicles* [online] available from <<https://westfieldavs.com/westfield-pod/>>
- Xu, P., Yang, C., Peng, Y., Yao, S., Zhang, D., and Li, B. (2016) 'Crash Performance and Multi-Objective Optimization of a Gradual Energy-Absorbing Structure for Subway Vehicles'. *International Journal of Mechanical Sciences* 107, 1–12
- Yin, H., Fang, H., Wen, G., Wang, Q., and Xiao, Y. (2016) 'An Adaptive RBF-Based Multi-Objective Optimization Method for Crashworthiness Design of Functionally Graded Multi-Cell Tube'. *Structural and Multidisciplinary Optimization* 53 (1), 129–144
- Yong, T. and Park, C. (2017) 'A Qualitative Comparative Analysis on Factors Affecting the Deployment of Electric Vehicles'. *Energy Procedia* [online] 128, 497–503. available from <<https://doi.org/10.1016/j.egypro.2017.09.066>>
- Zahran, M.S., Xue, P., Esa, M.S., and Abdelwahab, M.M. (2018) 'A Novel Tailor-Made Technique for Enhancing the Crashworthiness by Multi-Stage Tubular Square Tubes'. *Thin-Walled Structures* [online] 122, 64–82. available from <<https://www.sciencedirect.com/science/article/pii/S0263823117303579?via%3Dihub>>
- Zeng, Q., Wen, H., and Huang, H. (2016) 'The Interactive Effect on Injury Severity of Driver-Vehicle Units in Two-Vehicle Crashes'. in *Journal of Safety Research* [online] vol. 59. 105–111. available from <<http://www.sciencedirect.com/science/article/pii/S0022437516303280>>
- Zhang, L., Bai, Z., and Bai, F. (2018) 'Crashworthiness Design for Bio-Inspired Multi-Cell Tubes with Quadrilateral, Hexagonal and Octagonal Sections'. *Thin-Walled Structures* 122, 42–51
- Zhang, X., Wen, Z., and Zhang, H. (2014) 'Axial Crushing and Optimal Design of Square Tubes with Graded Thickness'. *Thin-Walled Structures* [online] 84, 263–274. available from <<https://www.sciencedirect.com/science/article/pii/S0263823114002158>>
- Zhu, G., Wang, Z., Cheng, A., and Li, G. (2017) 'Design Optimisation of Composite Bumper Beam with Variable Cross-Sections for Automotive Vehicle'. *International Journal of Crashworthiness* [online] 22 (4), 365–376. available from <<http://dx.doi.org/10.1080/13588265.2016.1267552>>

10 Appendices

Appendix I

Table 69. Detailed L6e and L7e Classification Criteria

Cat.	L6e			L7e					
Cat. Name	Light Quadricycle			Heavy Quadricycle					
Sub-Cat.	L6e-A	L6e-B		L7e-A		L7e-B		L7e-C	
Sub-Cat. Name	Light on-road quad	Light quadri-mobile		Heavy on-road quad		Heavy all terrain quad		Heavy quadri-mobile	
Sub-Sub-Cat.	N/A	L6e-BP	L6e-BU	L7e-A1	L7e-A2	L7e-S1	L7e-S2	L7e-CP	L7e-CU
Sub-Sub-Cat. Name	N/A	Light quadri-mobile for passenger transport	Light quadri-mobile for utility purposes	A1 heavy on-road quad	A2 heavy on-road quad	All terrain quad	Side-by-side buggy	Heavy quadri-mobile for passenger transport	Heavy quadri-mobile for utility purposes
N° Wheels	4								
Max. Length	4m	3m		4m				3.7m	
Max. Width	2m	1.5m		2m				1.5m	
Max. Height	2.5m								
Max. Mass	425 kg			450 kg					600 kg
Max. Speed	45 km/h			NR		90 km/h	NR	90 km/h	
Max. Power	4kW	6kW		15kW		NR	15kW		
Tran. Type	Passenger		Utility	Passenger					Utility
Max. N° Seats	2						3	4	2
Seat Type	NR			Straddle	Non-Straddle	Straddle	Non-Straddle		
Enclosed	NR	Y		NR				Y	
Accessibility	NR	Max. 3 sides		NR				Max. 3 sides	
Steering System	NR			Handlebar	NR	Handlebar	NR		
GC	NR					≥180 mm		NR	
WB to GC Ratio	NR					≤6	≤8		
Loading Bed ¹	N		Y	N					Y

Where:

NR = Not Restricted, WB = Wheelbase, GC = Ground Clearance, N = No, Y = Yes, N° = Number of, Max. = Maximum, Cat. = Category, Tran. = Transport

¹Criteria of loading bed for L6e-BU and L7e-CU:

- Loading bed area clearly separated by rigid partition between occupants and loading bed
- Loading bed must be able to carry minimum volume represented by 600mm cube
- Loading bed calculation methods:
 - a) length of loading bed × width of loading bed ≥ 0,3 × Length of vehicle × Width of vehicle.
 - b) an equivalent loading bed area as defined above in order to install machines and/or equipment.

Appendix II

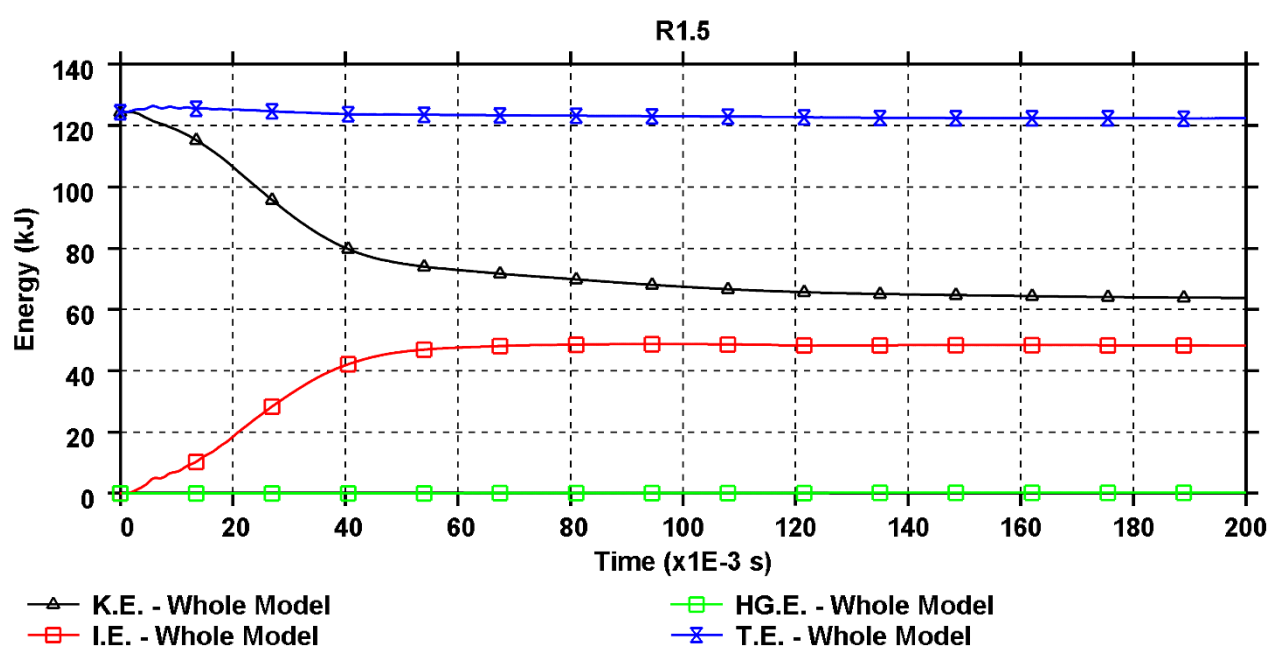


Figure 71. R1.5 Energy Curve

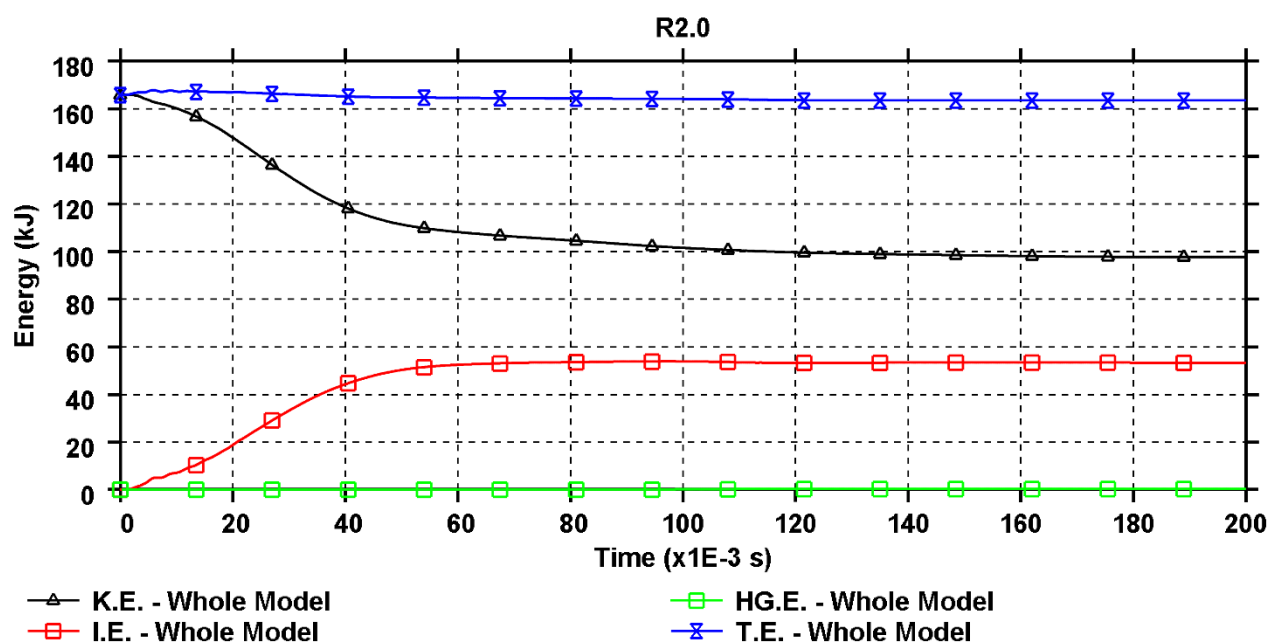


Figure 72. R2.0 Energy Curve

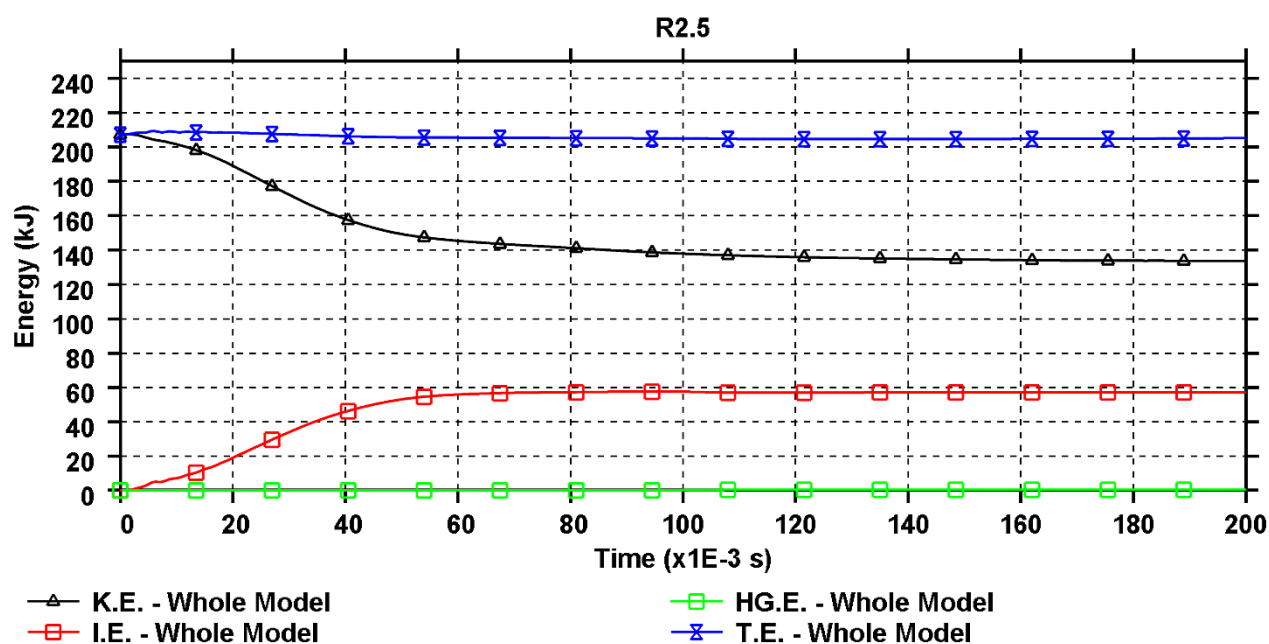


Figure 73. R2.5 Energy Curve

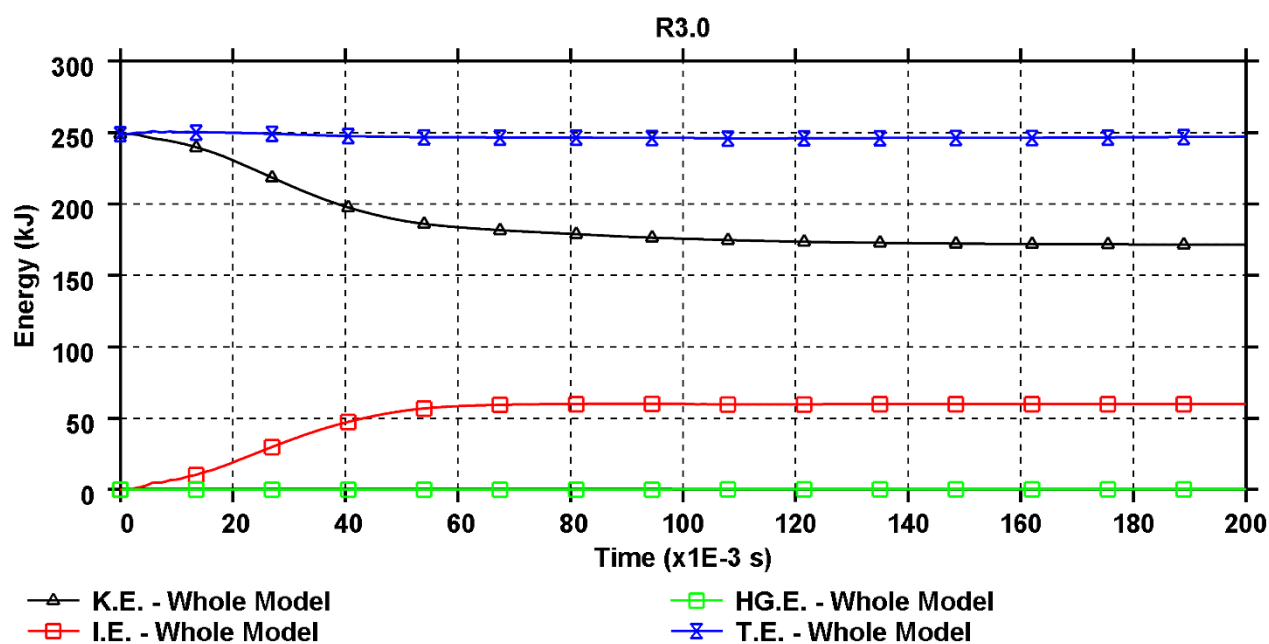


Figure 74. R3.0 Energy Curve

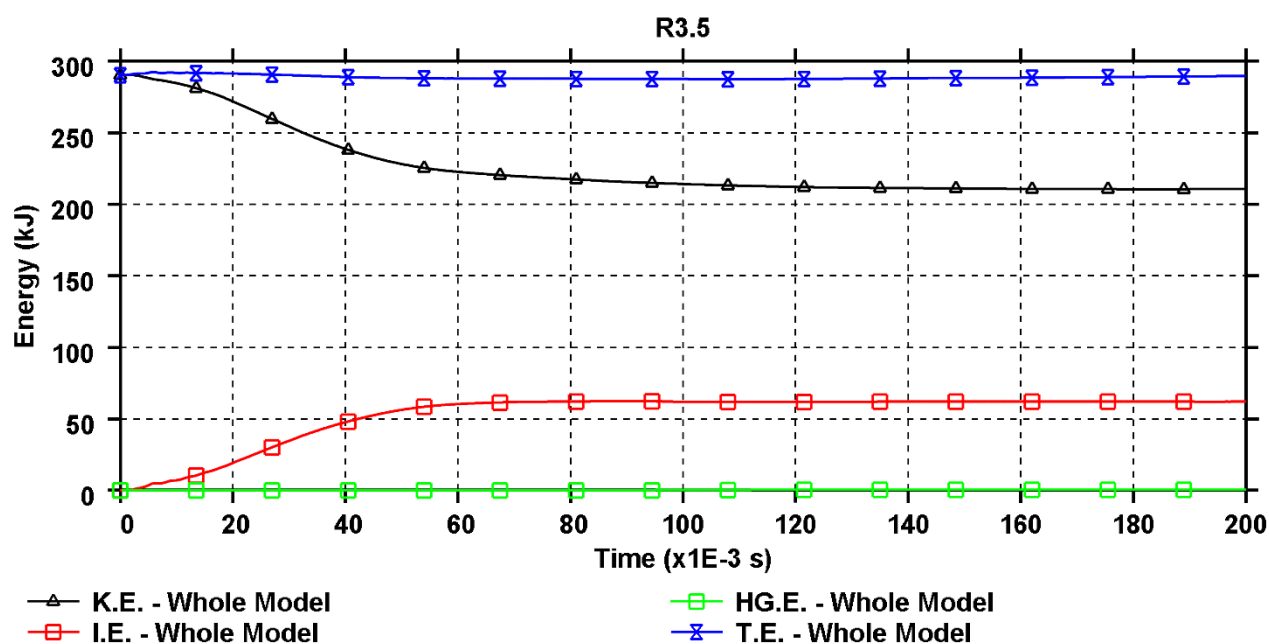


Figure 75. R3.5 Energy Curve

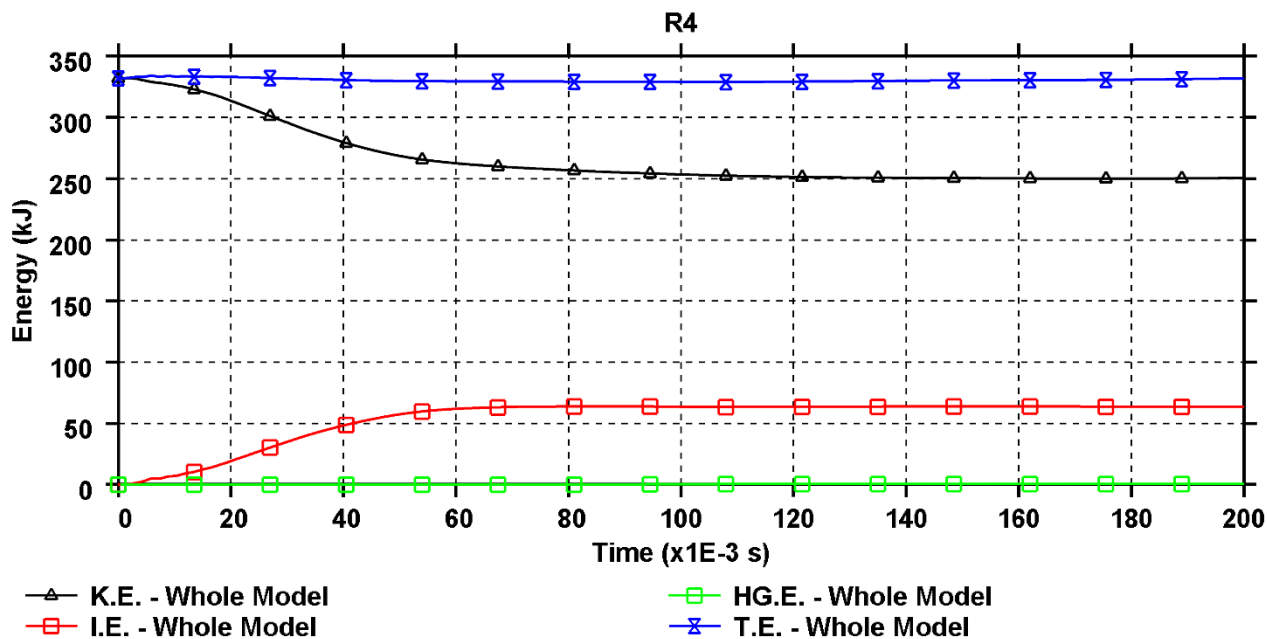


Figure 76. Energy Curve

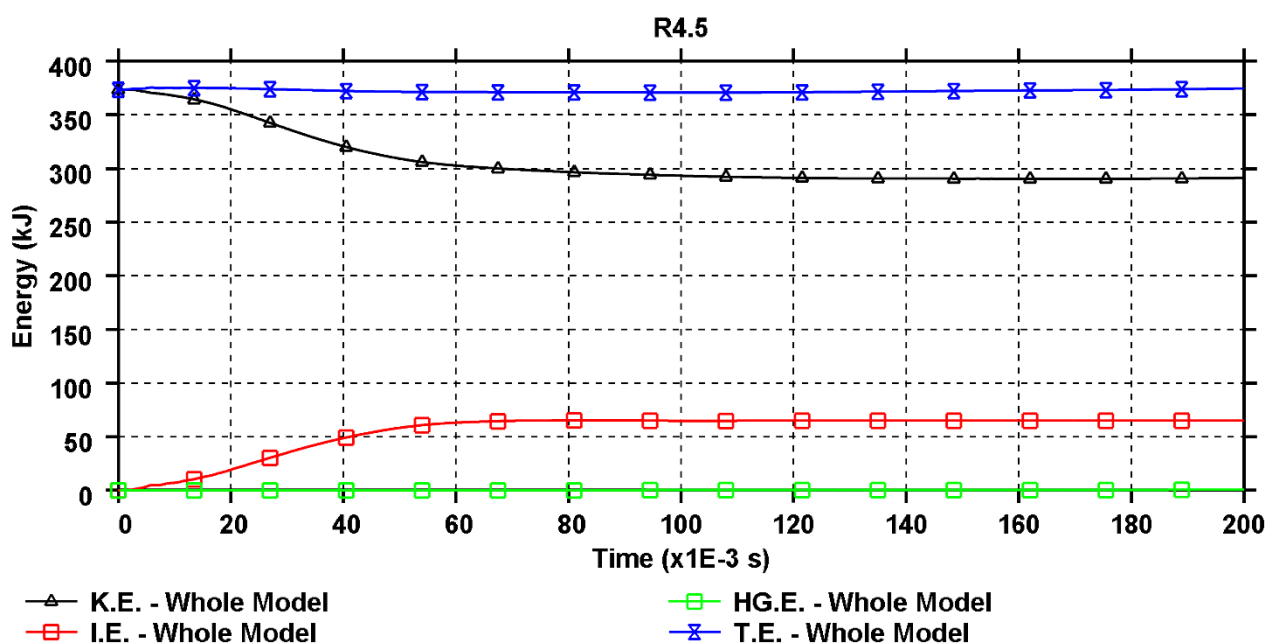


Figure 77. R4.5 Energy Curve

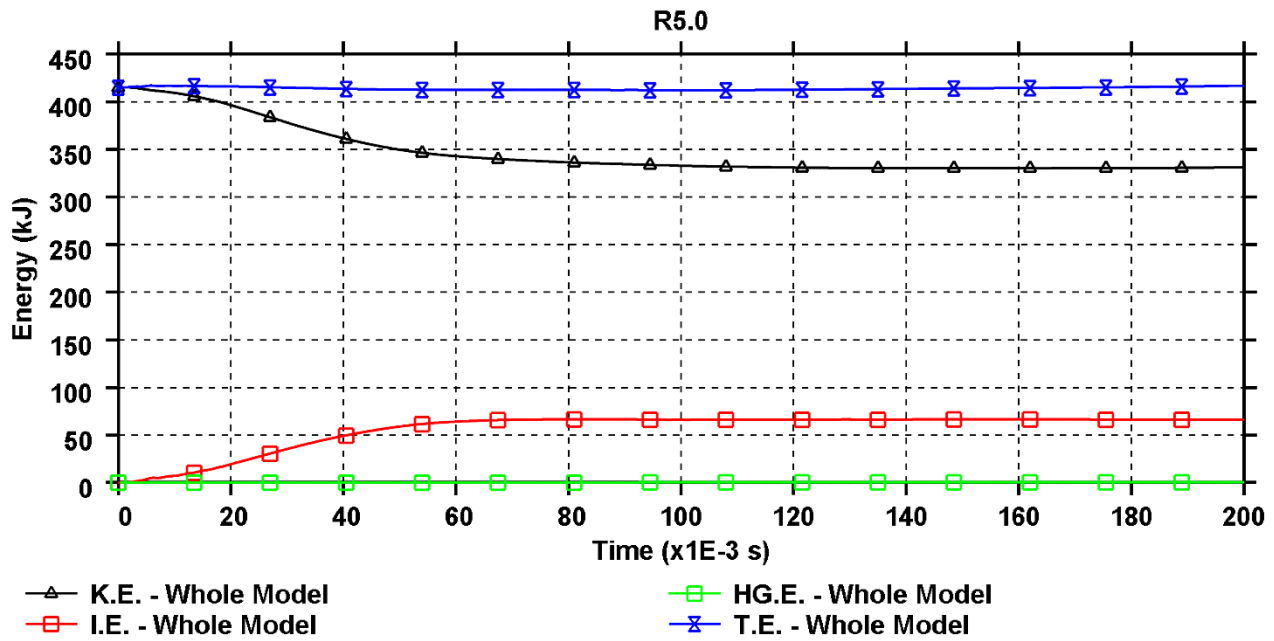


Figure 78. R5.0 Energy Curve

Table 70. Body Accelerations (G) for Mass-Ratios

Sensor Location	R1.0	R1.5	R2.0	R2.5	R3.0	R3.5	R4.0	R4.5	R5.0
T4 (g)	45.01	45.93	53.95	46.88	48.24	52.61	51.21	54.15	53.87
T12 (g)	31.18	38.48	46.65	45.36	47.40	47.50	51.75	50.72	50.25
Pelvis (g)	19.58	24.30	29.18	30.28	29.66	30.40	32.35	33.72	33.52

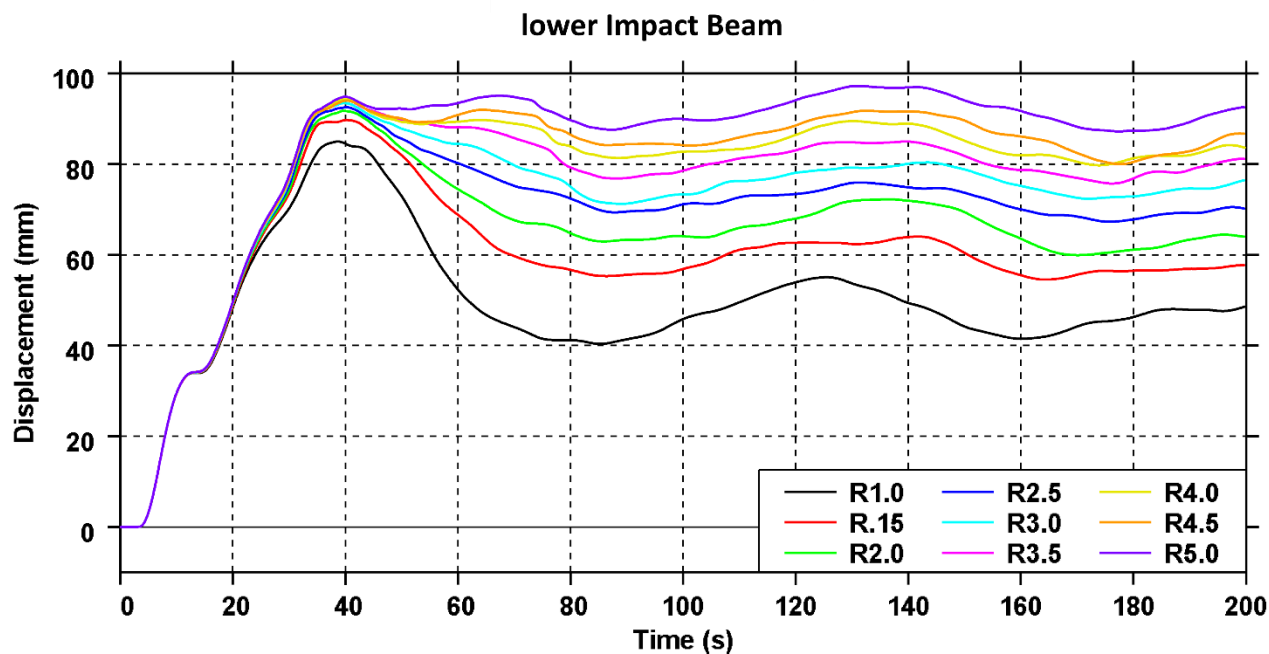


Figure 79. Intrusion of Lower Impact Beam

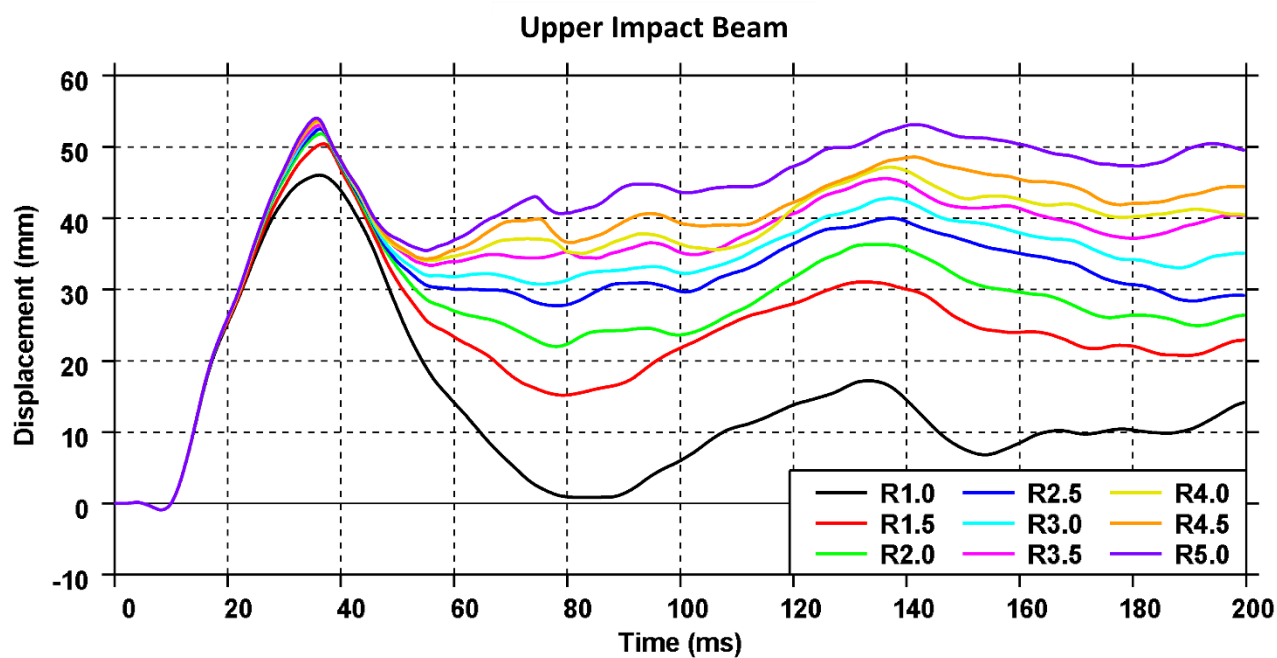


Figure 80. Intrusion of Upper Impact Beam

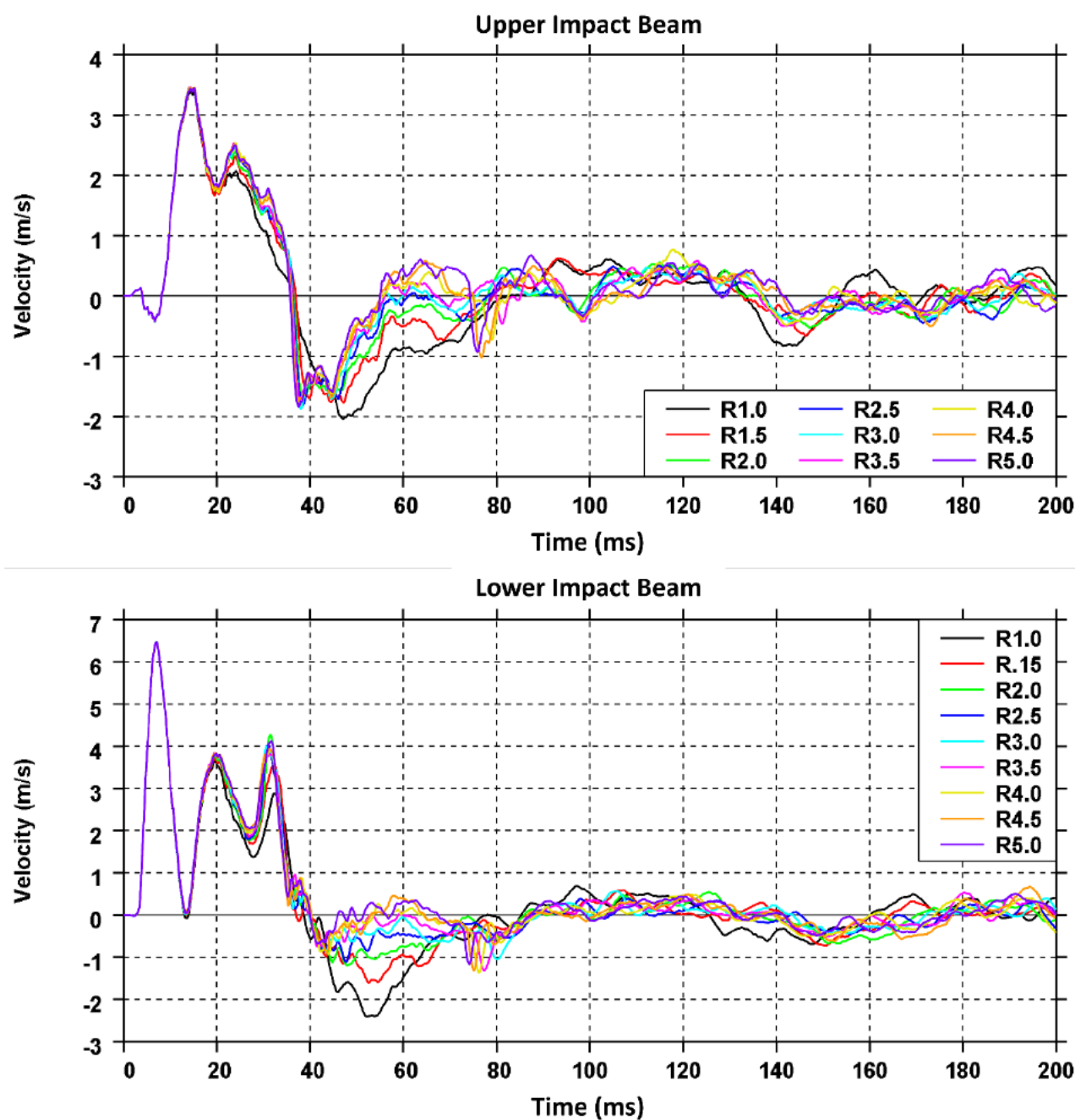


Figure 81. Door Intrusion Rates for Mass Relationship Exploration

Table 71. Rib Data from Mass Exploration Experiments

R1.0	Compression (mm)			Velocity (m/s)			Acceleration (m/s ²)			
	Max	Min	Max. Mag.	Max	Min	Max. Mag.	Max	Min	Max. Mag.	Mag (g)
Shoulder Rib	0.84	-20.37	20.37	0.91	-1.40	1.40	382.51	-207.78	382.51	38.99

Upper T-Rib	1.03	-21.87	21.87	1.67	-1.47	1.67	479.62	-340.28	479.62	48.89
Middle T-Rib	1.05	-23.15	23.15	1.97	-1.81	1.97	617.98	-388.78	617.98	62.99
Lower T-Rib	0.45	-20.08	20.08	1.61	-1.47	1.61	402.24	-484.71	484.71	49.41
Upper A-Rib	2.95	-21.58	21.58	1.51	-1.13	1.51	426.27	-242.94	426.27	43.45
Lower A-Rib	1.00	-31.62	31.62	1.90	-1.59	1.90	477.90	-386.27	477.90	48.72
R1.5	Compression (mm)			Velocity (m/s)			Acceleration (m/s ²)			
	Max	Min	Max. Mag.	Max	Min	Max. Mag.	Max	Min	Max. Mag.	Mag (g)
Shoulder Rib	0.84	-22.19	22.19	1.17	-1.72	1.72	393.40	-281.52	393.40	40.10
Upper T-Rib	1.04	-27.50	27.50	1.86	-1.83	1.86	534.00	-412.50	534.00	54.43
Middle T-Rib	1.08	-31.78	31.78	2.29	-2.55	2.55	587.29	-442.60	587.29	59.87
Lower T-Rib	0.49	-29.02	29.02	2.31	-2.04	2.31	729.87	-523.85	729.87	74.40
Upper A-Rib	1.74	-29.03	29.03	2.01	-1.51	2.01	526.78	-412.83	526.78	53.70
Lower A-Rib	0.91	-44.04	44.04	3.22	-2.07	3.22	619.30	-574.36	619.30	63.13
R2.0	Compression (mm)			Velocity (m/s)			Acceleration (m/s ²)			
	Max	Min	Max. Mag.	Max	Min	Max. Mag.	Max	Min	Max. Mag.	Mag (g)
Shoulder Rib	0.83	-21.65	21.65	1.12	-2.12	2.12	517.99	-445.44	517.99	52.80
Upper T-Rib	1.05	-28.92	28.92	2.07	-2.07	2.07	561.82	-445.66	561.82	57.27
Middle T-Rib	1.08	-34.97	34.97	2.51	-2.96	2.96	676.18	-584.53	676.18	68.93
Lower T-Rib	0.49	-32.59	32.59	2.04	-2.64	2.64	725.58	-567.55	725.58	73.96
Upper A-Rib	2.15	-30.89	30.89	2.35	-1.68	2.35	502.03	-483.48	502.03	51.18
Lower A-Rib	3.08	-48.01	48.01	3.57	-2.32	3.57	647.01	-638.33	647.01	65.95
R2.5	Compression (mm)			Velocity (m/s)			Acceleration (m/s ²)			
	Max	Min	Max. Mag.	Max	Min	Max. Mag.	Max	Min	Max. Mag.	Mag (g)
Shoulder Rib	0.84	-21.84	21.84	1.03	-2.15	2.15	345.52	-501.43	501.43	51.11
Upper T-Rib	1.04	-30.10	30.10	2.04	-2.26	2.26	586.41	-366.17	586.41	59.78
Middle	1.09	-37.51	37.51	2.88	-3.19	3.19	821.44	-716.94	821.44	83.74

T-Rib										
Lower T-Rib	0.49	-35.04	35.04	2.37	-2.72	2.72	784.17	-688.09	784.17	79.94
Upper A-Rib	4.04	-33.47	33.47	2.53	-1.80	2.53	523.99	-443.14	523.99	53.41
Lower A-Rib	3.35	-51.34	51.34	4.29	-2.48	4.29	938.32	-811.95	938.32	95.65
R3.0	Compression (mm)			Velocity (m/s)			Acceleration (m/s ²)			
	Max	Min	Max. Mag.	Max	Min	Max. Mag.	Max	Min	Max. Mag.	Mag (g)
Shoulder Rib	0.85	-21.66	21.66	1.22	-2.20	2.20	373.93	-540.67	540.67	55.11
Upper T-Rib	1.05	-30.52	30.52	2.06	-2.26	2.26	602.94	-414.89	602.94	61.46
Middle T-Rib	1.11	-39.18	39.18	3.15	-3.46	3.46	652.89	-677.02	677.02	69.01
Lower T-Rib	1.60	-37.02	37.02	2.36	-2.89	2.89	1094.2 3	-644.56	1094.2 3	111.54
Upper A-Rib	4.14	-34.68	34.68	2.62	-1.95	2.62	635.45	-481.76	635.45	64.78
Lower A-Rib	3.58	-52.95	52.95	4.51	-2.63	4.51	1127.0 4	-1002.79	1127.0 4	114.89
R3.5	Compression (mm)			Velocity (m/s)			Acceleration (m/s ²)			
	Max	Min	Max. Mag.	Max	Min	Max. Mag.	Max	Min	Max. Mag.	Mag (g)
Shoulder Rib	0.83	-21.13	21.13	1.13	-2.05	2.05	437.11	-458.34	458.34	46.72
Upper T-Rib	1.05	-30.73	30.73	1.95	-2.27	2.27	536.82	-634.97	634.97	64.73
Middle T-Rib	1.10	-40.29	40.29	3.19	-3.29	3.29	643.55	-825.05	825.05	84.10
Lower T-Rib	1.10	-38.17	38.17	2.55	-2.90	2.90	850.26	-804.99	850.26	86.67
Upper A-Rib	2.55	-35.07	35.07	2.82	-1.90	2.82	615.64	-588.54	615.64	62.76
Lower A-Rib	1.93	-53.18	53.18	4.40	-2.58	4.40	769.54	-1077.74	1077.7 4	109.86
R4.0	Compression (mm)			Velocity (m/s)			Acceleration (m/s ²)			
	Max	Min	Max. Mag.	Max	Min	Max. Mag.	Max	Min	Max. Mag.	Mag (g)
Shoulder Rib	0.86	-20.85	20.85	0.98	-2.09	2.09	422.50	-564.26	564.26	57.52
Upper T-Rib	1.05	-31.12	31.12	1.80	-2.32	2.32	479.62	-674.45	674.45	68.75
Middle T-Rib	1.10	-41.03	41.03	3.01	-3.52	3.52	752.94	-645.00	752.94	76.75
Lower T-Rib	0.49	-38.94	38.94	2.30	-3.05	3.05	882.93	-847.46	882.93	90.00

Upper A-Rib	2.46	-36.02	36.02	2.82	-1.98	2.82	762.07	-483.79	762.07	77.68
Lower A-Rib	2.04	-54.66	54.66	4.32	-2.67	4.32	784.31	-798.70	798.70	81.42
R4.5	Compression (mm)			Velocity (m/s)			Acceleration (m/s ²)			
	Max	Min	Max. Mag.	Max	Min	Max. Mag.	Max	Min	Max. Mag.	Mag (g)
Shoulder Rib	0.83	-20.34	20.34	0.93	-2.09	2.09	442.12	-513.65	513.65	52.36
Upper T-Rib	1.05	-30.16	30.16	1.82	-2.41	2.41	538.36	-500.56	538.36	54.88
Middle T-Rib	1.11	-41.13	41.13	2.89	-3.72	3.72	673.33	-772.17	772.17	78.71
Lower T-Rib	0.51	-38.39	38.39	2.43	-3.28	3.28	770.41	-763.36	770.41	78.53
Upper A-Rib	0.38	-35.94	35.94	2.49	-2.04	2.49	611.94	-571.09	611.94	62.38
Lower A-Rib	0.00	-54.70	54.70	4.40	-2.80	4.40	737.56	-859.64	859.64	87.63
R5.0	Compression (mm)			Velocity (m/s)			Acceleration (m/s ²)			
	Max	Min	Max. Mag.	Max	Min	Max. Mag.	Max	Min	Max. Mag.	Mag (g)
Shoulder Rib	0.84	-20.18	20.18	0.82	-2.01	2.01	408.18	-584.51	584.51	59.58
Upper T-Rib	1.05	-30.33	30.33	1.80	-2.44	2.44	486.74	-605.99	605.99	61.77
Middle T-Rib	1.10	-41.58	41.58	3.11	-3.64	3.64	738.52	-738.78	738.78	75.31
Lower T-Rib	0.50	-39.41	39.41	2.48	-3.34	3.34	1023.0 7	-608.35	1023.0 7	104.29
Upper A-Rib	1.28	-36.57	36.57	2.66	-2.00	2.66	676.56	-612.99	676.56	68.97
Lower A-Rib	0.06	-55.61	55.61	4.52	-2.77	4.52	1071.1 4	- 1148.57	1148.5 7	117.08

Table 72. Viscous Criterion of Mass-Ratio Exploration

WSID50 Rib	R1.0	R1.5	R2.0	R2.5	R3.0	R3.5	R4.0	R4.5	R5.0
Shoulder Rib	0.17	0.22	0.27	0.28	0.28	0.26	0.26	0.25	0.24
Upper Thorax Rib	0.22	0.30	0.35	0.40	0.41	0.41	0.42	0.43	0.43
Middle Thorax Rib	0.27	0.48	0.61	0.70	0.80	0.78	0.85	0.90	0.89
Lower Thorax Rib	0.19	0.39	0.51	0.56	0.63	0.65	0.70	0.74	0.78
Upper Abdominal Rib	0.19	0.34	0.43	0.50	0.53	0.58	0.60	0.53	0.57
Lower Abdominal Rib	0.35	0.83	1.01	1.30	1.40	1.38	1.39	1.42	1.48

Appendix III

Table 73. Omitted Materials in Venza Light-weighting

FE Material name
11900 MAT20 MAT_RIGID
ALUMINUM 7000 SERIES 253 MPa
Radiator fan module
Steel_suspension-high strength
Steel_Elastic
SF 570/640
Q&T 5160 523MPa
steel-lingage 273 Mpa
pass_frt_tread
driver_rr_sidewall
Al_alloy_wheel
BH 280-400
10014 BIW_structural_adhesive-MSC457B-High_Strength_Epoxy
MS 1250-1500
Fuel tank strap
Exhaust
Exhaust muffler STEEL 120KSI
Exhaust pipe Steel-25KSI
BH 260-370
Steel-coil spring
Windshield_Backlite_Glass
Adhesive Glass
Rigid_Accels
Dummy_Mass_support_spring_NONLINEAR_SPRING_SHOULDER
Dummy_Mass_support_spring_NONLINEAR_SPRING_LAP
Dummy_Belt_Spring_8kN_LINEAR_SPRING
exhaust springs

Appendix IV

Table 74. List of parts within LLD with high Hourglass Energy

Part title
11202_Radiator_Support_Side_Inner_LH
11252_Radiator_Support_Side_Inner_LH

11260_Radiator_Support_Side_Inner_Front_Mid_Bracket_LH
11302_Front_Bumper_pedpro_Cross_Member_Upper
11303_Front_Bumper_pedpro_Cross_Member_Side_Outer_LH
11304_Front_Bumper_pedpro_Cross_Member_Side_Inner_LH
11353_Front_Bumper_pedpro_Cross_Member_Side_Outer_LH
11354_Front_Bumper_pedpro_Cross_Member_Side_Inner_RH
11801_Cowl_Top_Side_Connection_Panel_Lower_LH
Body SPOTWELDS_PSOLID_Property
12111_A-Pillar_(Front_Hinge_Pillar)_Outer_Reinf
12112_A-Pillar_(Front_Hinge_Pillar)_Outer_Reinf
12122_A-Pillar_(Front_Hinge_Pillar)_Inner_reinf
12123_A-Pillar_(Front_Hinge_Pillar)_Inner_reinf
12124_A-Pillar_(Front_Hinge_Pillar)_Inner_reinf
12161_A-Pillar_(Front_Hinge_Pillar)_Outer_Reinf
12162_A-Pillar_(Front_Hinge_Pillar)_Outer_Reinf
12172_A-Pillar_(Front_Hinge_Pillar)_Inner_reinf
12173_A-Pillar_(Front_Hinge_Pillar)_Inner_reinf
12174_A-Pillar_(Front_Hinge_Pillar)_Inner_reinf
13203_BIW_B-Pillar_Middle_Panel_Bottom
13204_BIW_B-Pillar_Middle_Panel_Reinforcement_LH
13220_BIW_B-Pillar_Middle_Panel_Inside_Reinforcement_LH
13253_BIW_B-Pillar_Middle_Panel_Bottom
13254_BIW_B-Pillar_Middle_Panel_Reinforcement_LH
13270_BIW_B-Pillar_Middle_Panel_Inside_Reinforcement_LH
16201_Roof_Side_Rail_Inner_LH
16202_Roof_Side_Rail_Inner_Reinf
16203_Roof_Side_Rail_Inner_Inside_LH
16251_Roof_Side_Rail_Inner_LH
16252_Roof_Side_Rail_Inner_Reinf
16253_Roof_Side_Rail_Inner_Inside_LH
17803_Rear_Front_Floor_Cross_Member_Ending_Member_LH
17804_Front_Front_Floor_Cross_Member_LH
17805_Front_Front_Floor_Cross_Member_Ending_Member_LH
17853_Rear_Front_Floor_Cross_Member_Ending_Member_LH
17855_Front_Front_Floor_Cross_Member_Ending_Member_LH
17901_Dash_Panel
fan
Left_front_wheel_core
Left_front_wheel_core
Lift Gate SPOT WELD 4.0 mm SOLID Property

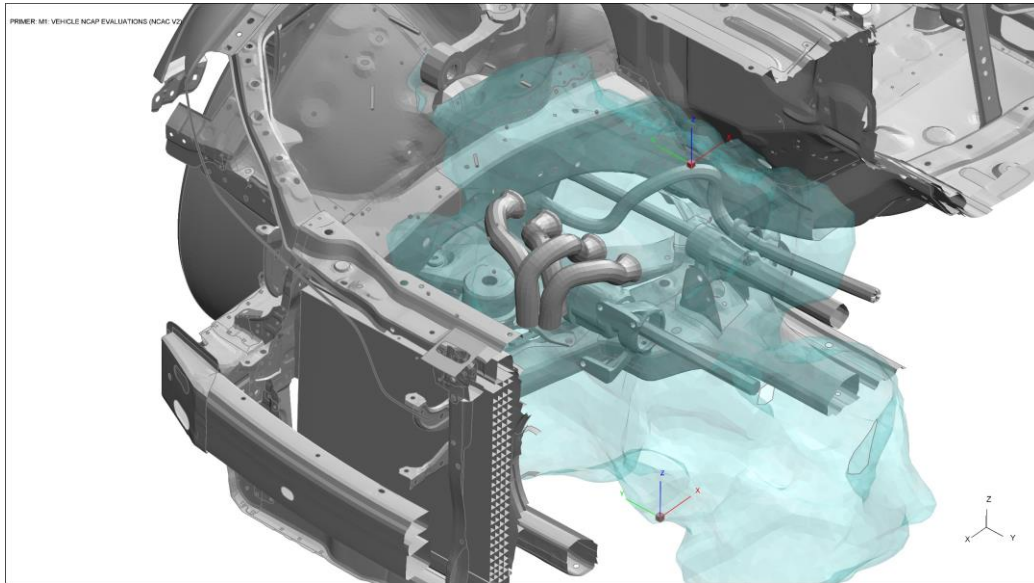


Figure 82. Engine Sensor Locations

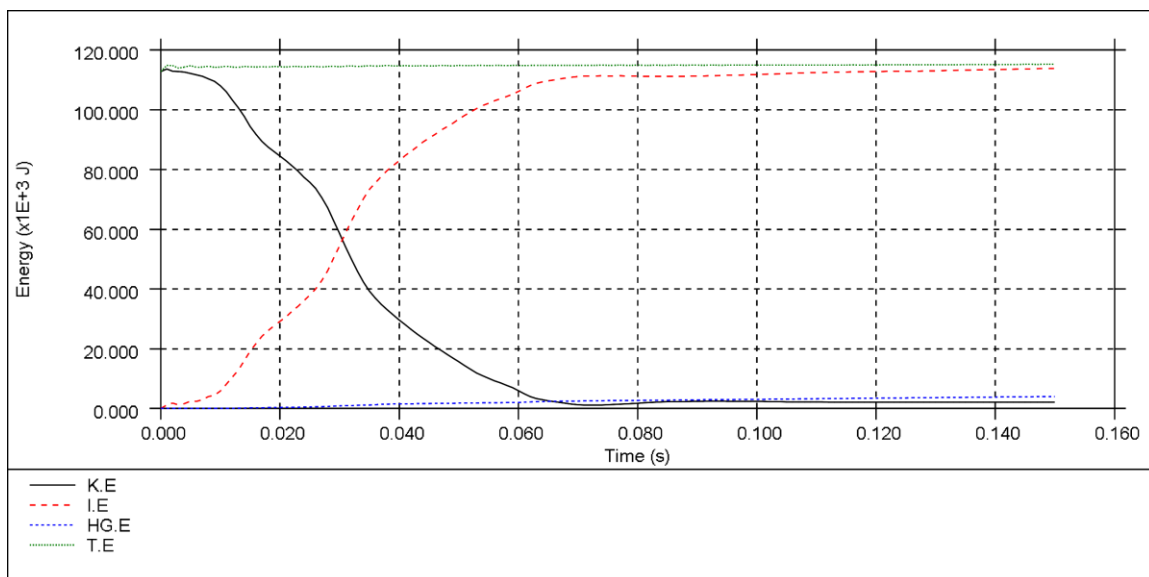


Figure 83. Baseline Venza Energy Curve (25mph)

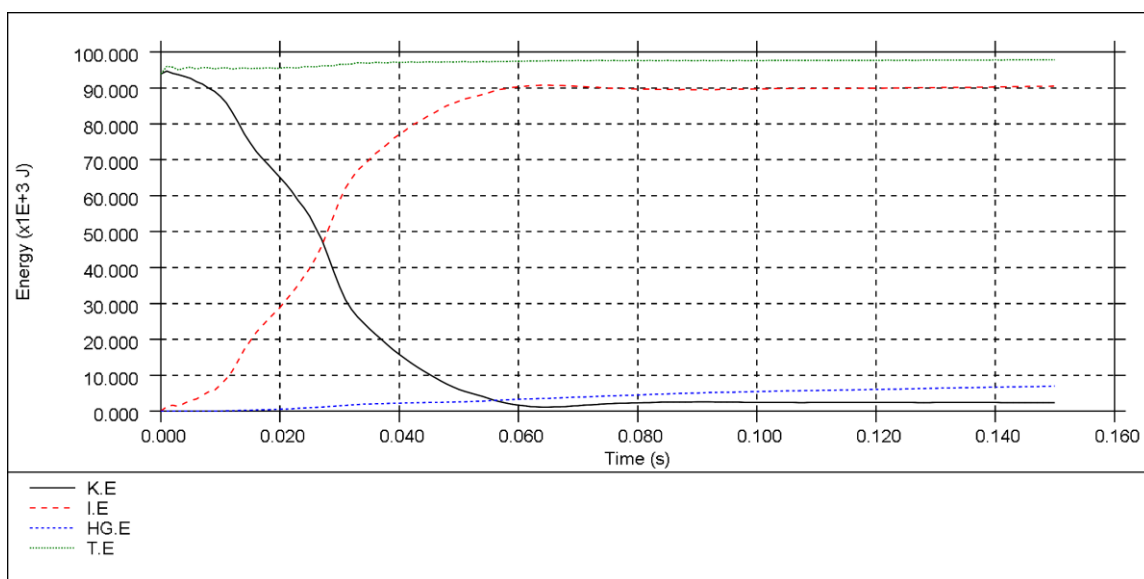


Figure 84. LLD Venza Energy Curve

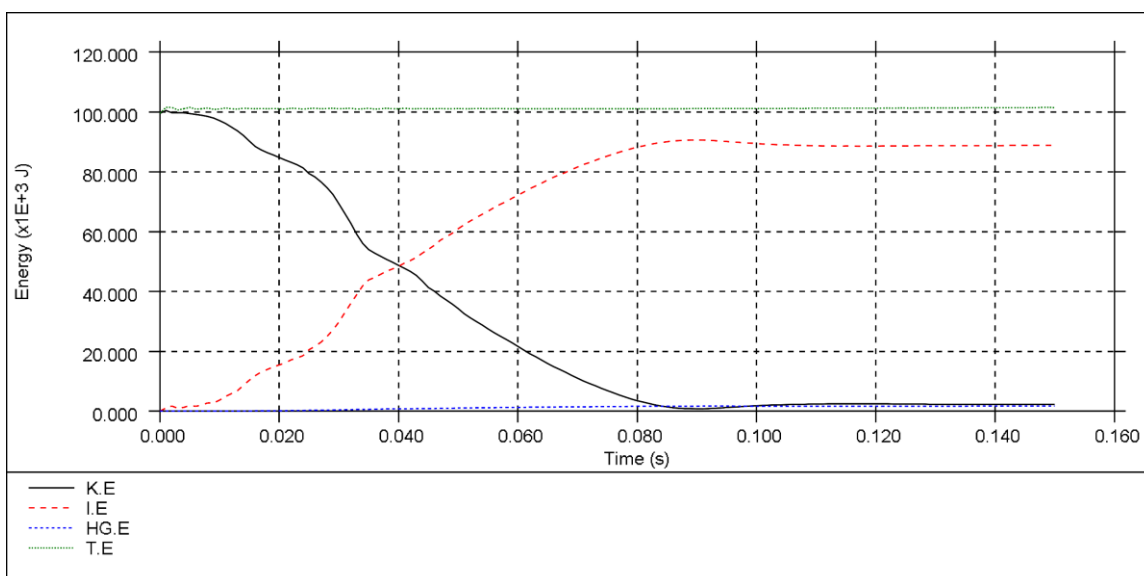


Figure 85. VLL Venza Energy Curve

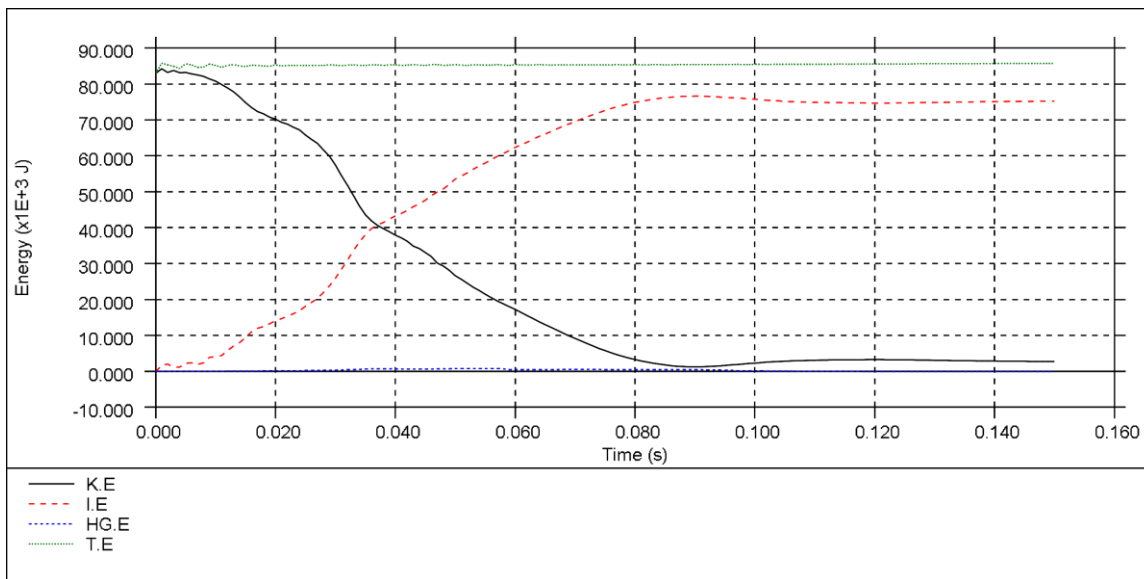


Figure 86. VLH Venza Energy Curve

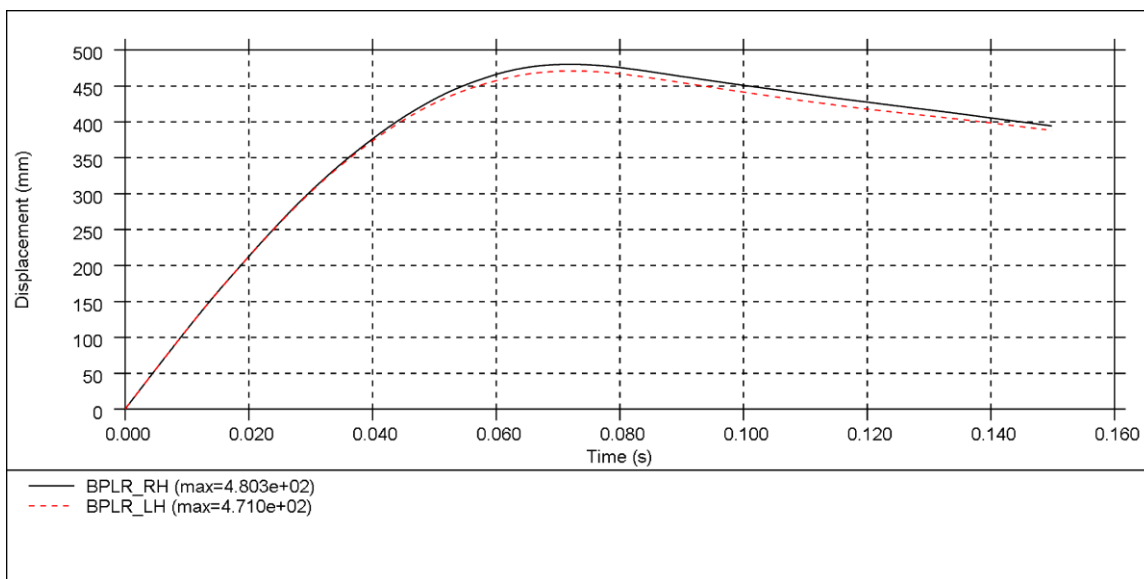


Figure 87. BL Dynamic Crush

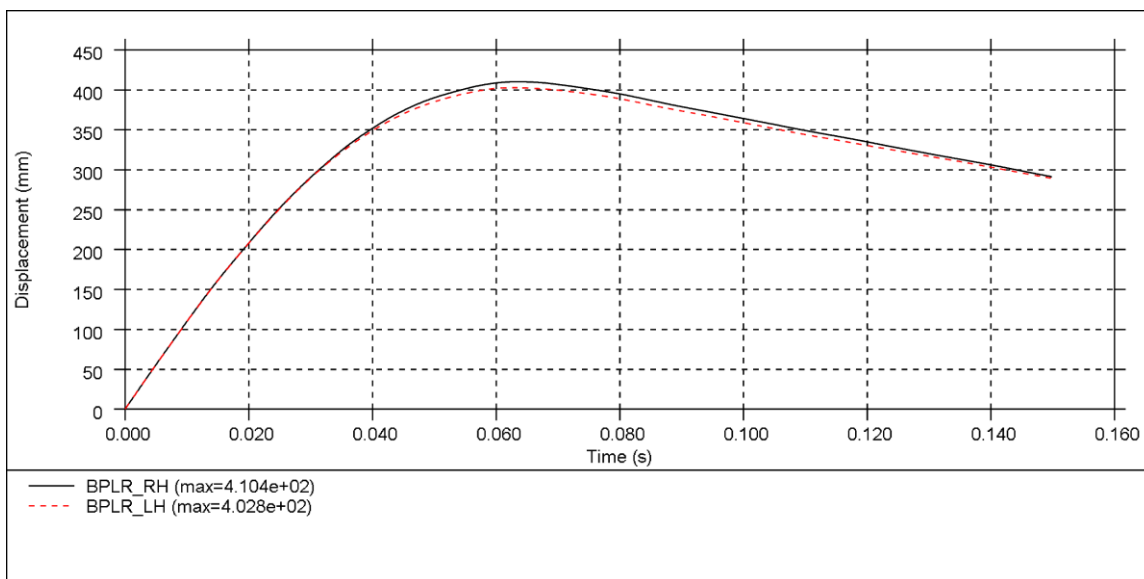


Figure 88. LLD Venza Dynamic Crush

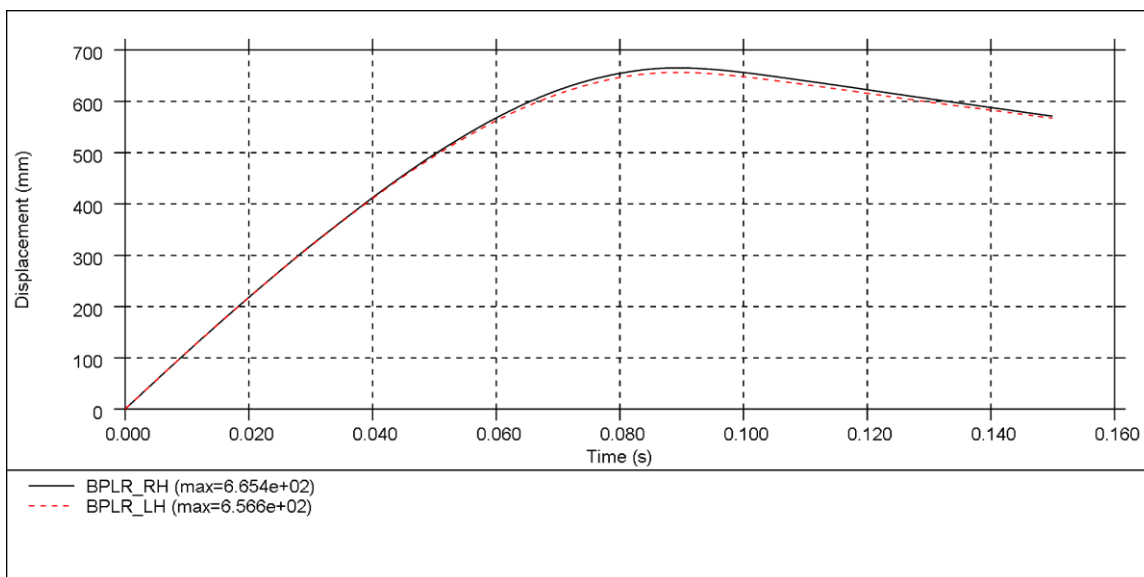


Figure 89. VLL Venza Dynamic Crush

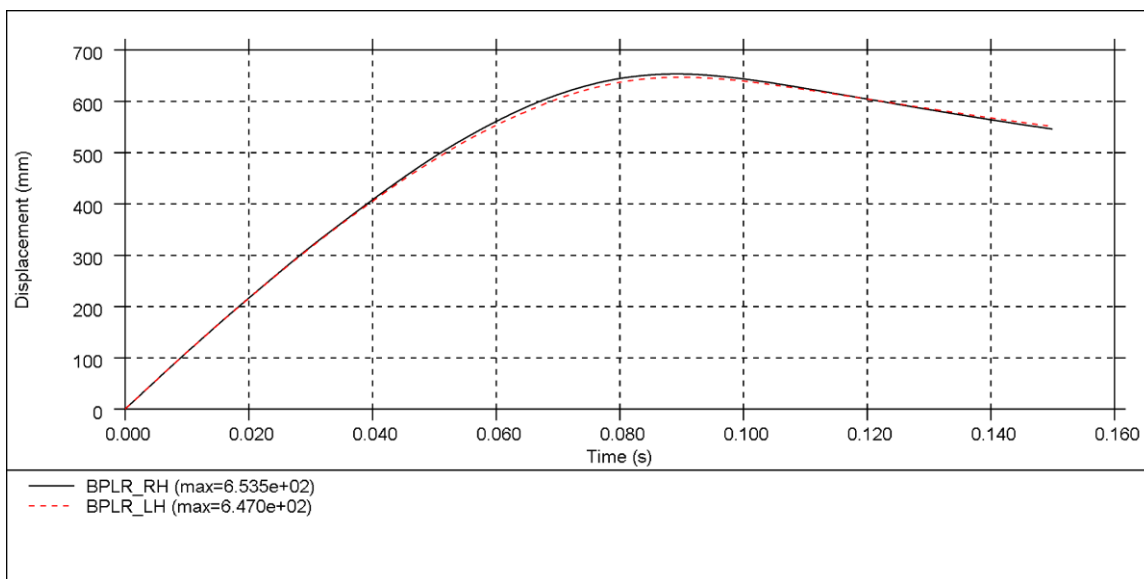


Figure 90. VLH Venza Dynamic Crush

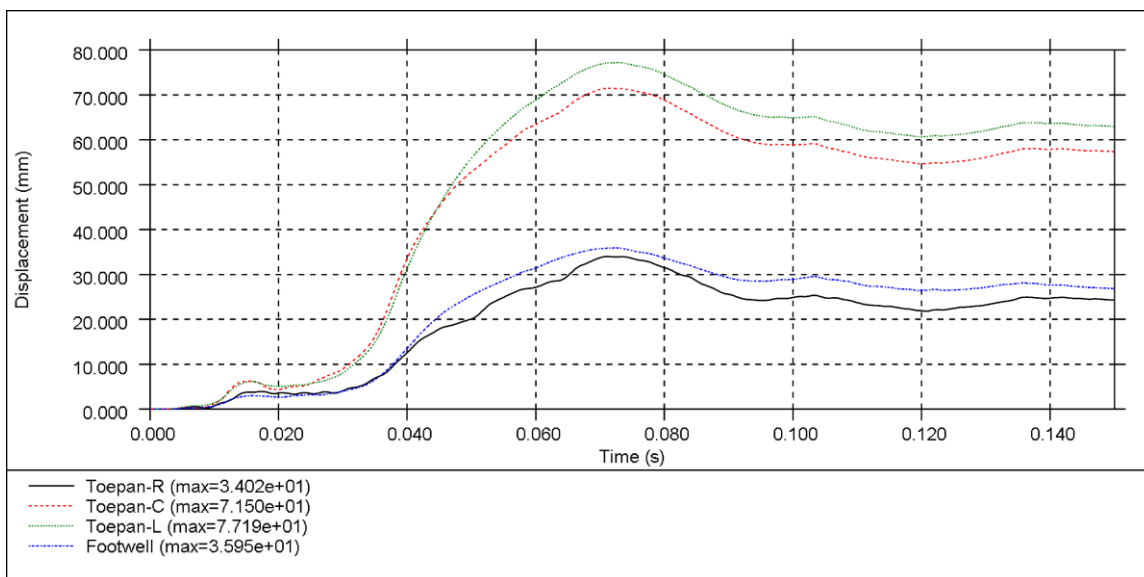


Figure 91. BL Occupant Compartment Intrusion

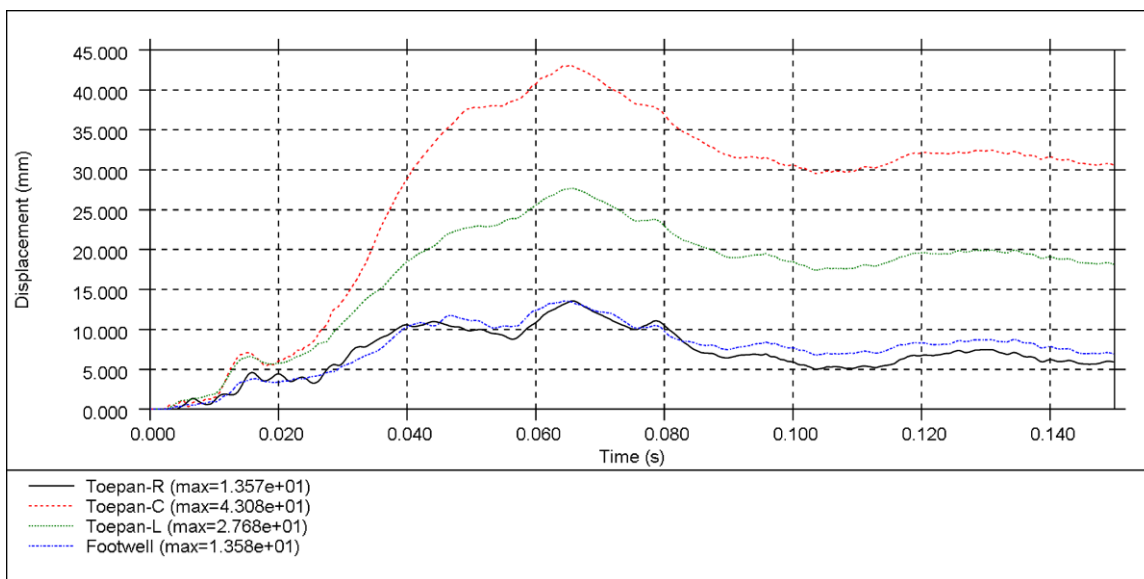


Figure 92. LLD Venza Occupant Compartment Intrusion

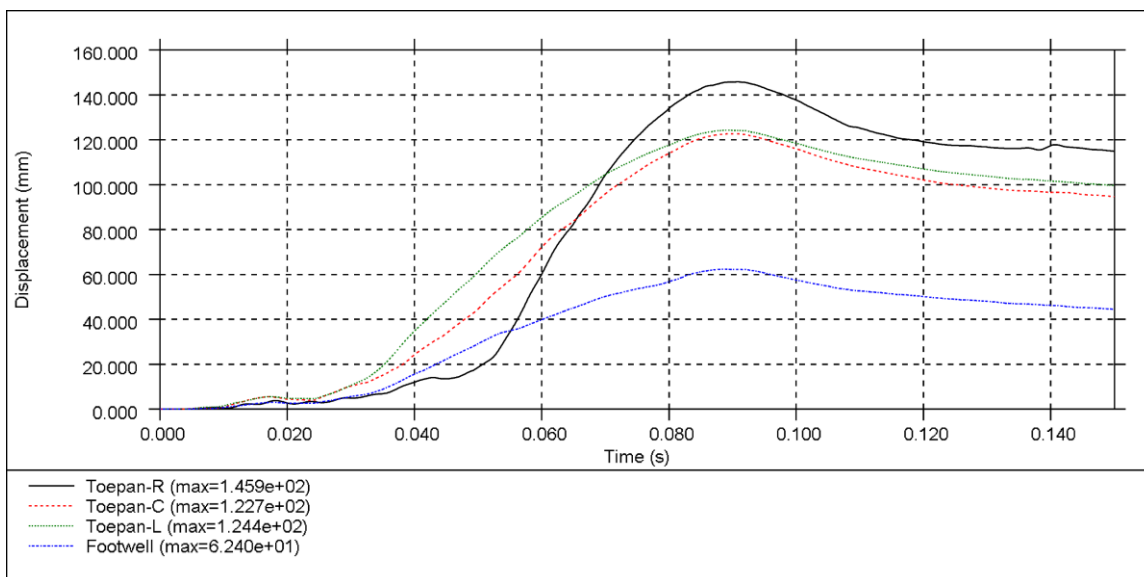


Figure 93. VLL Occupant Compartment Intrusion

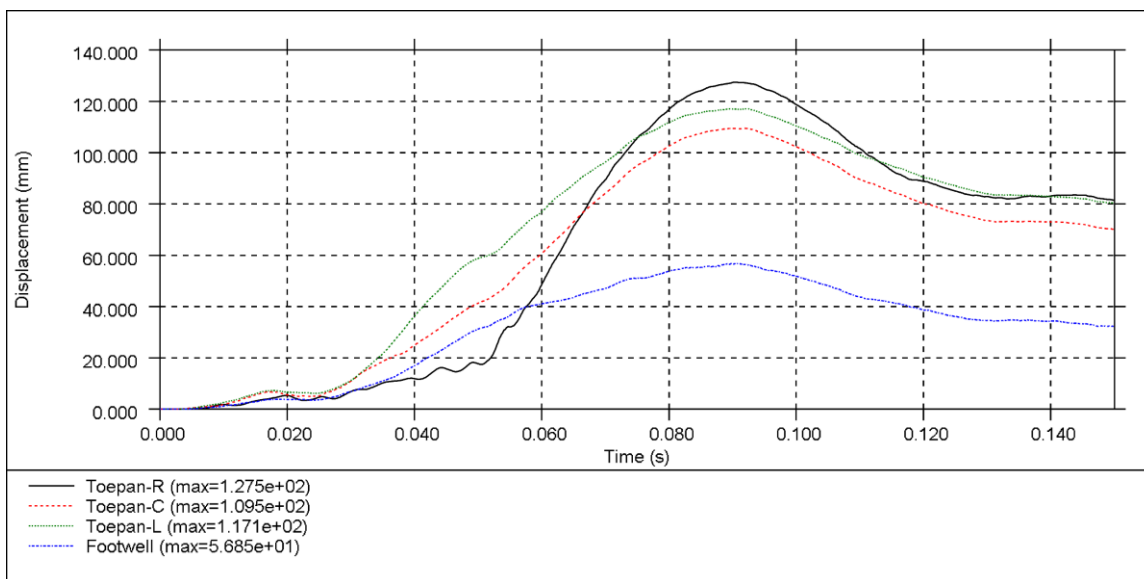


Figure 94. VLH Venza Occupant Compartment Intrusion

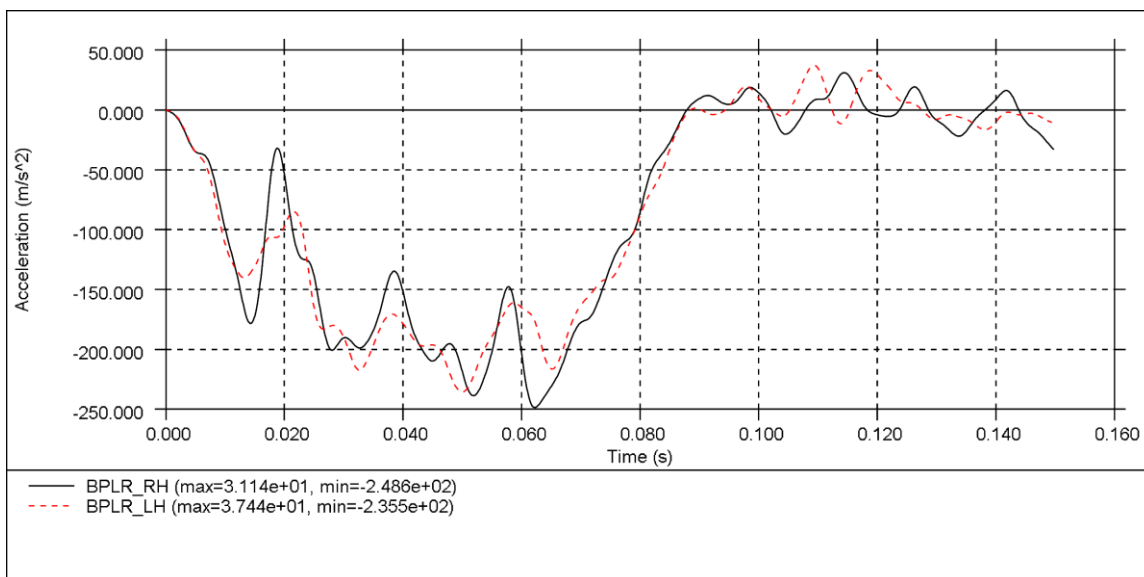


Figure 95. Baseline Venza Occupant Compartment Acceleration

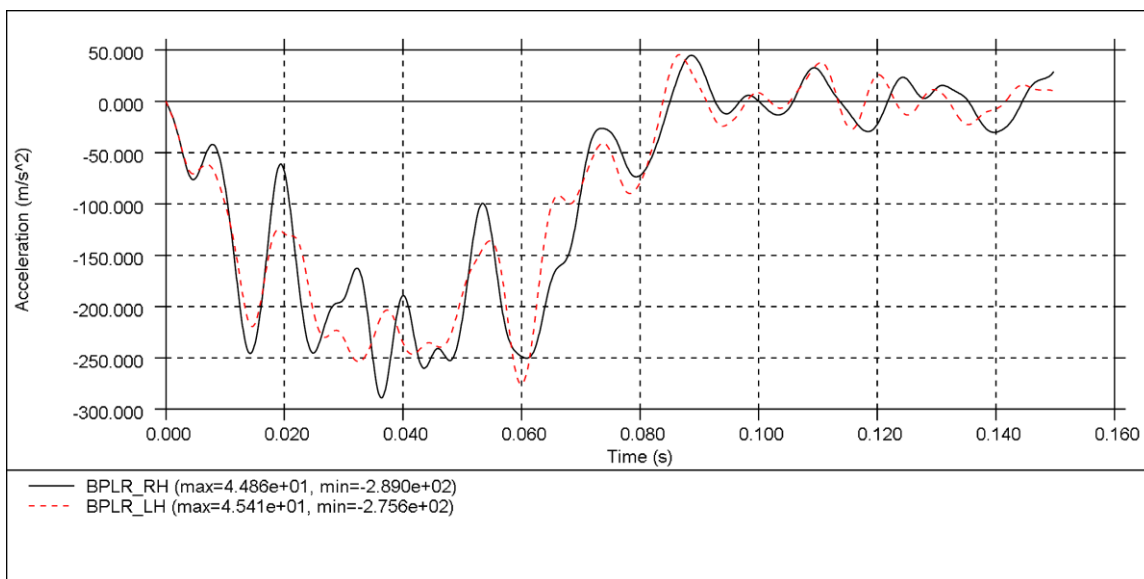


Figure 96. LLD Venza Occupant Compartment Acceleration

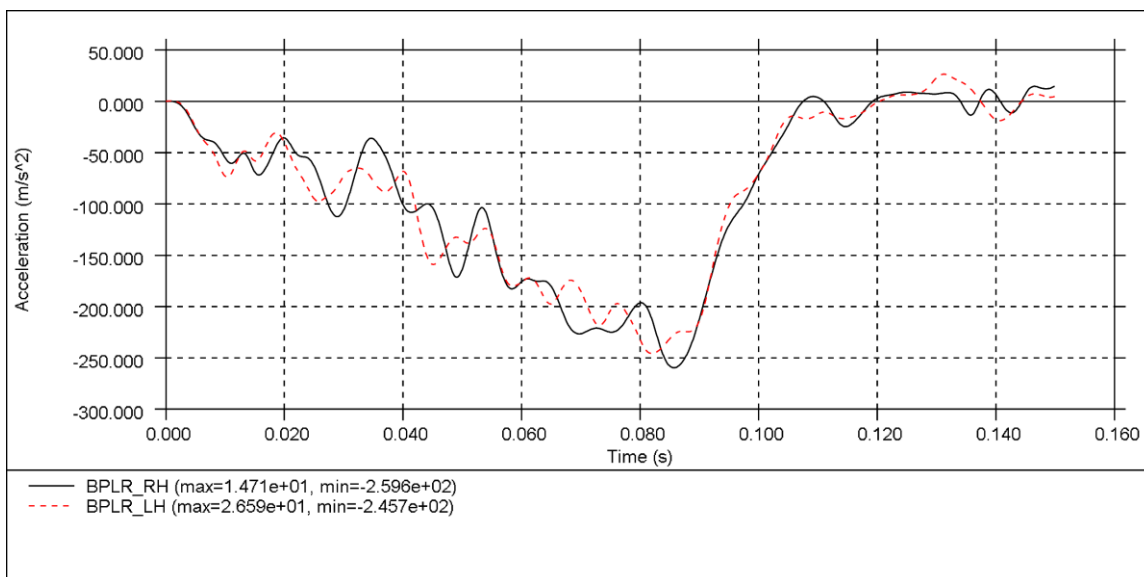


Figure 97. VLL Venza Occupant Compartment Acceleration

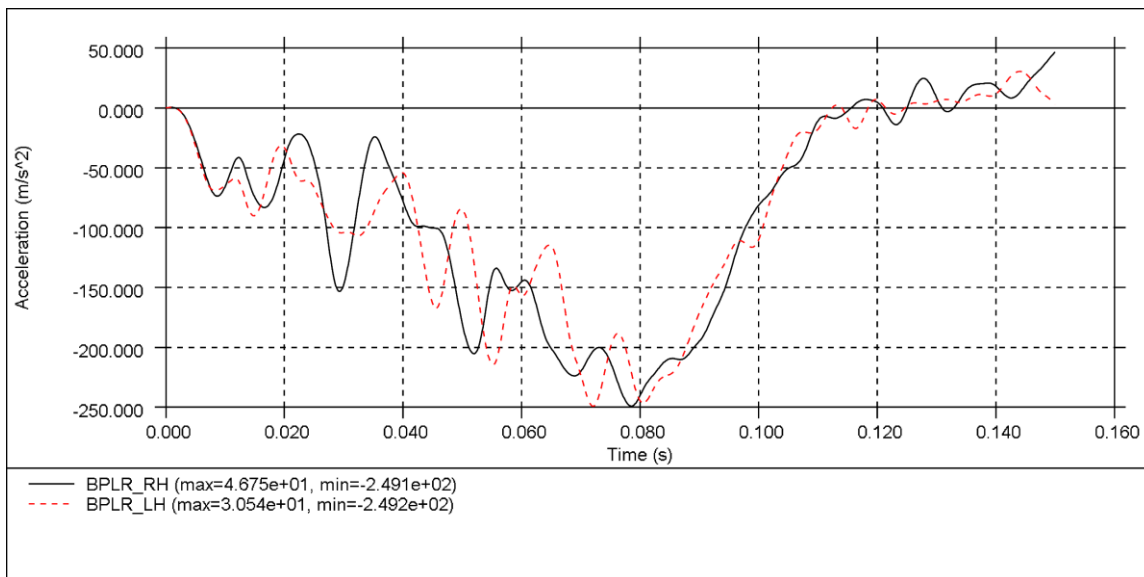


Figure 98. Rev2 Venza Occupant Compartment Acceleration

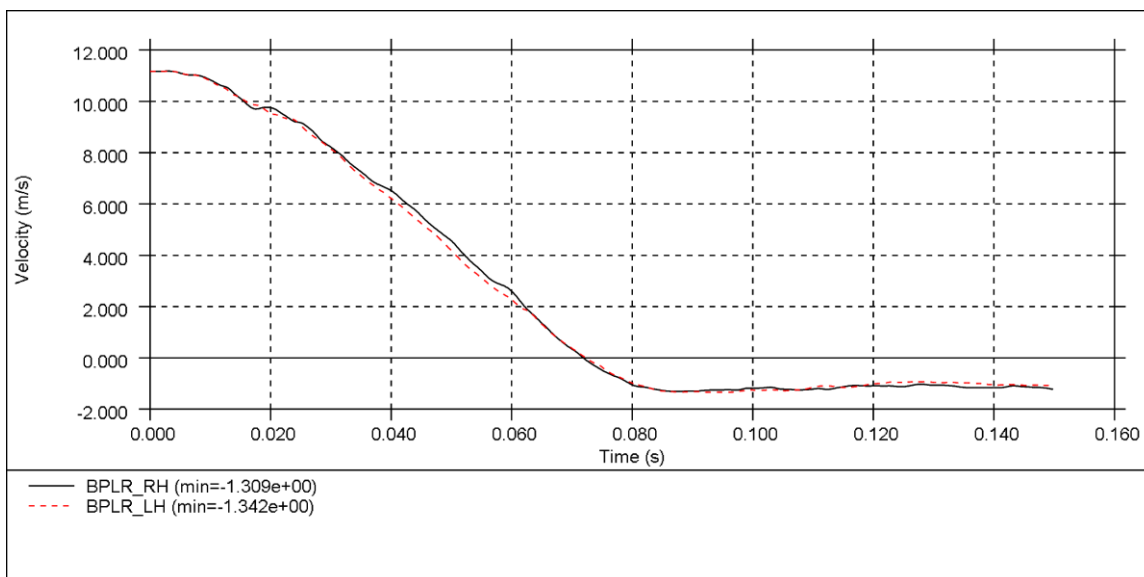


Figure 99. Baseline Venza Occupant Compartment Velocity

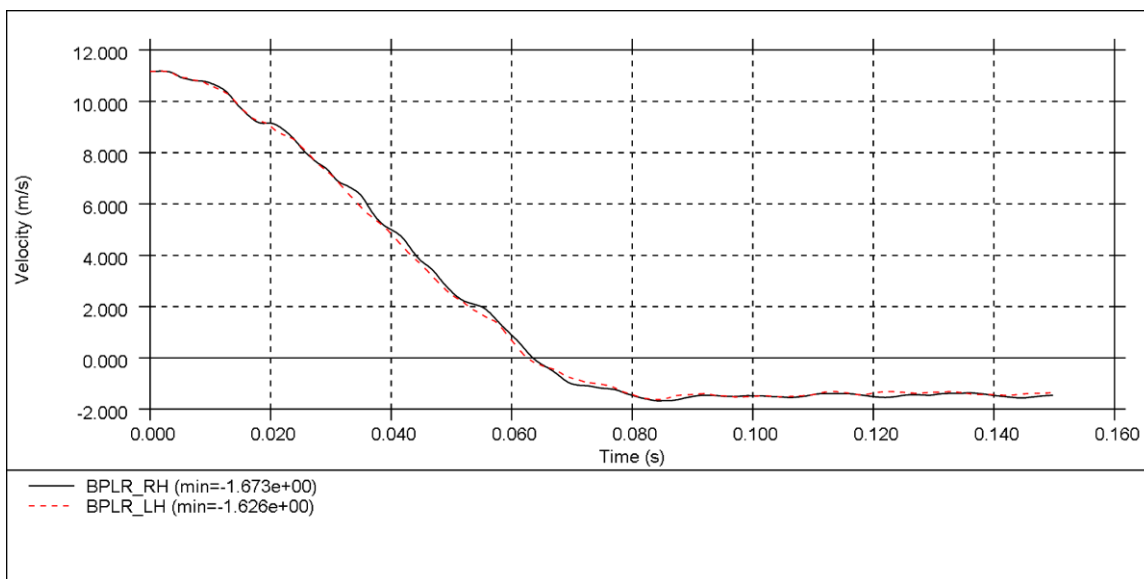


Figure 100. LLD Venza Occupant Compartment Velocity

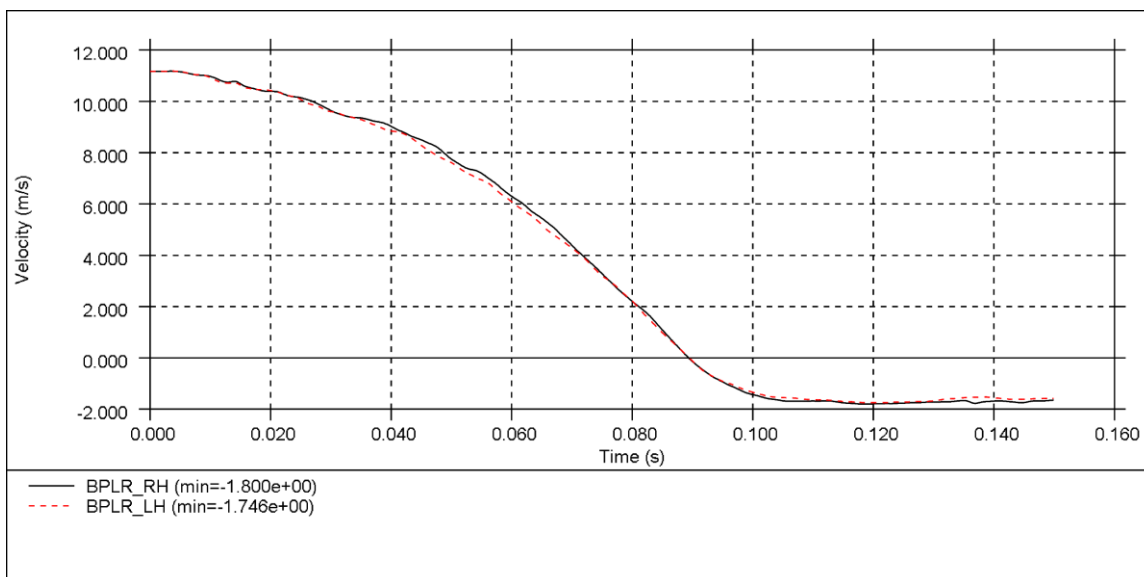


Figure 101. VLL Venza Occupant Compartment Velocity

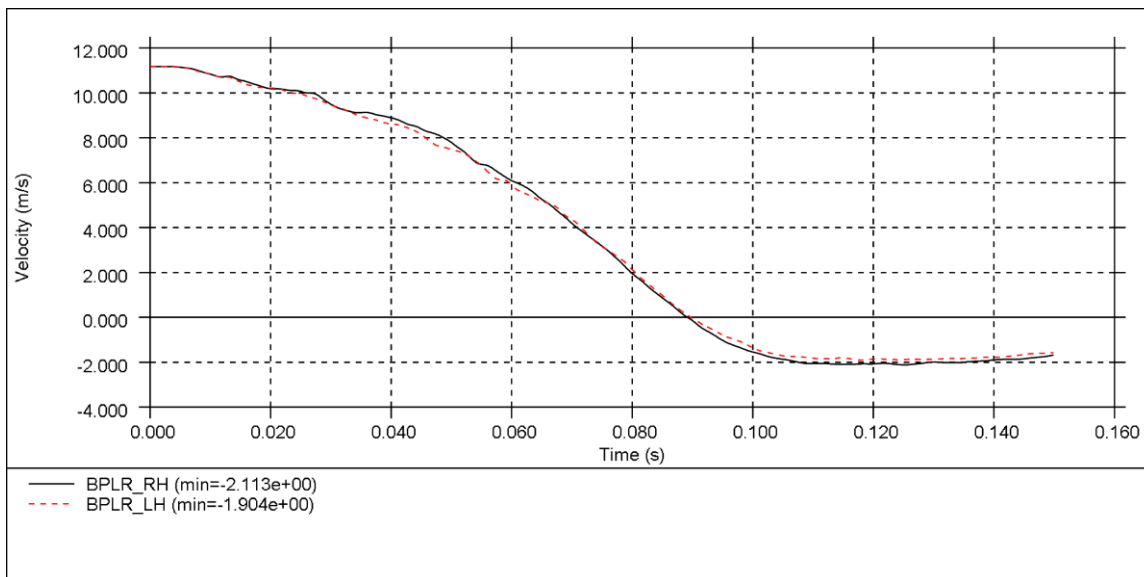


Figure 102. VLH Venza Occupant Compartment Velocity

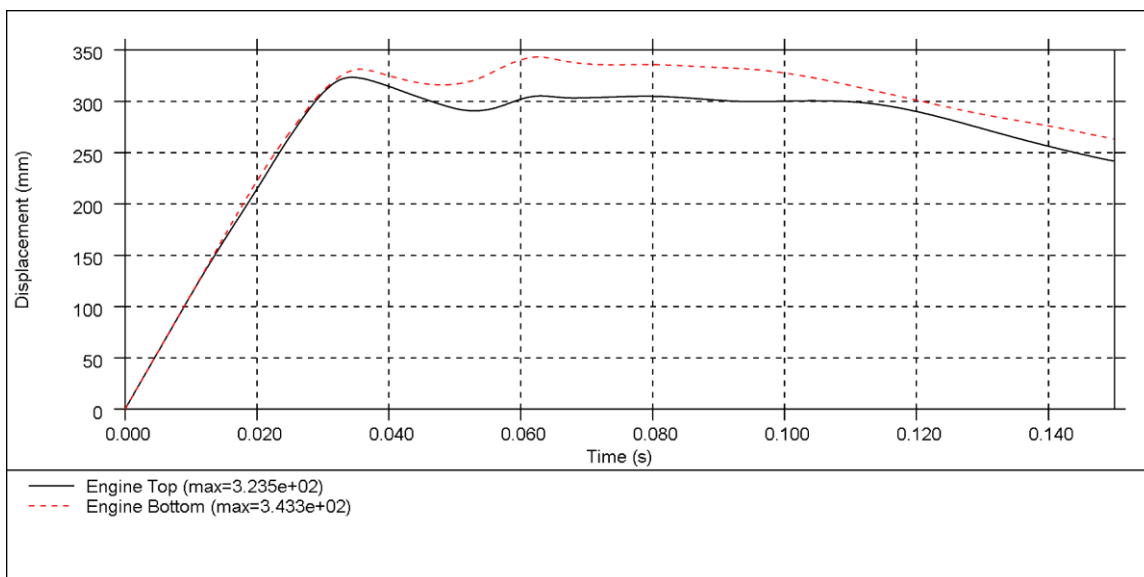


Figure 103. Baseline Venza Longitudinal Engine Displacement

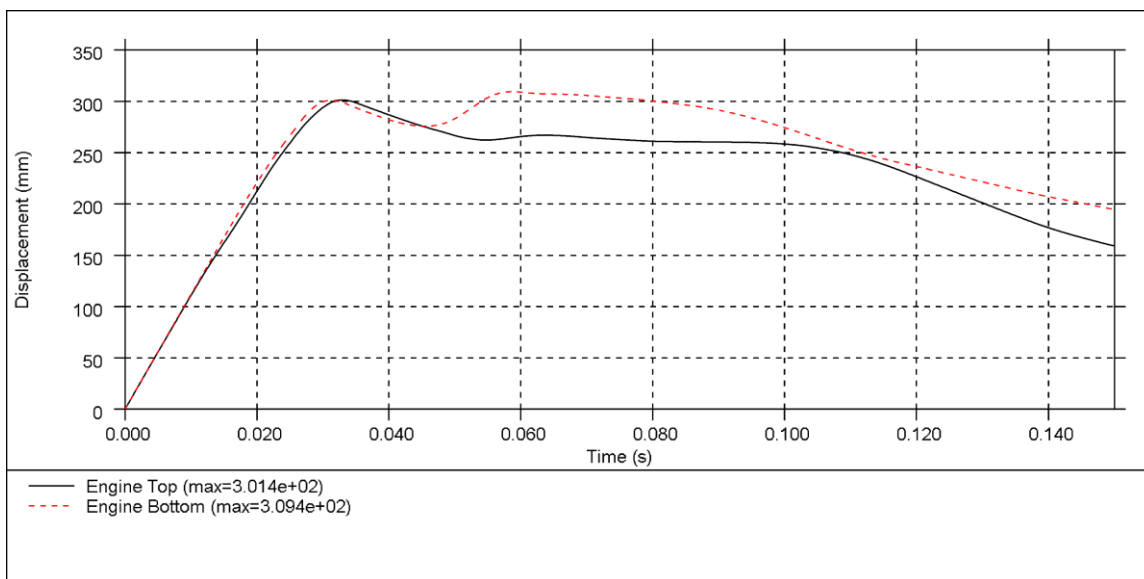


Figure 104. LLD Venza Longitudinal Engine Displacement

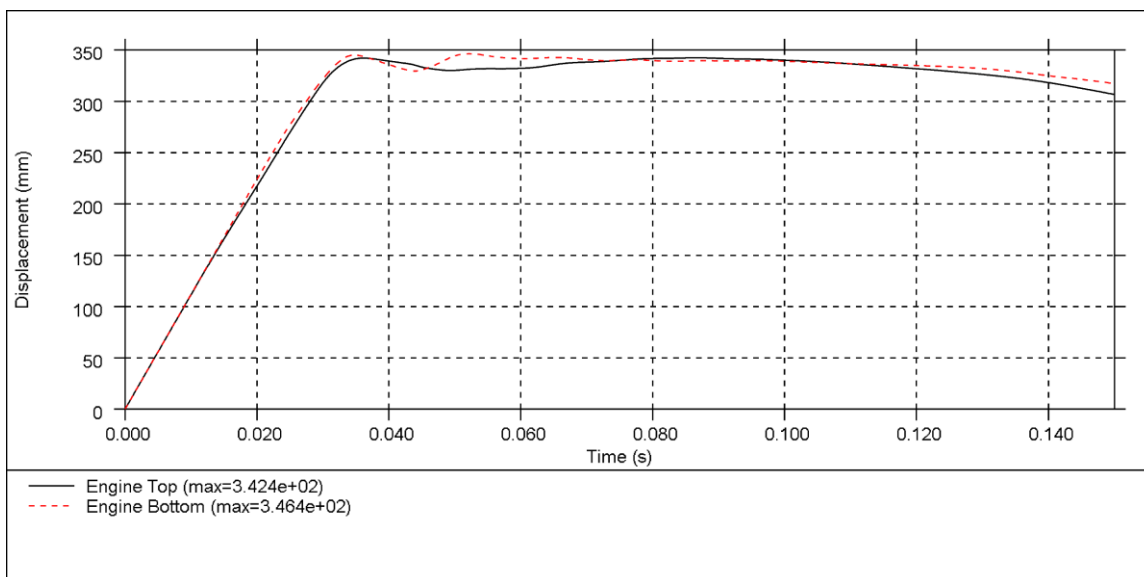


Figure 105. VLL Venza Longitudinal Engine Displacement

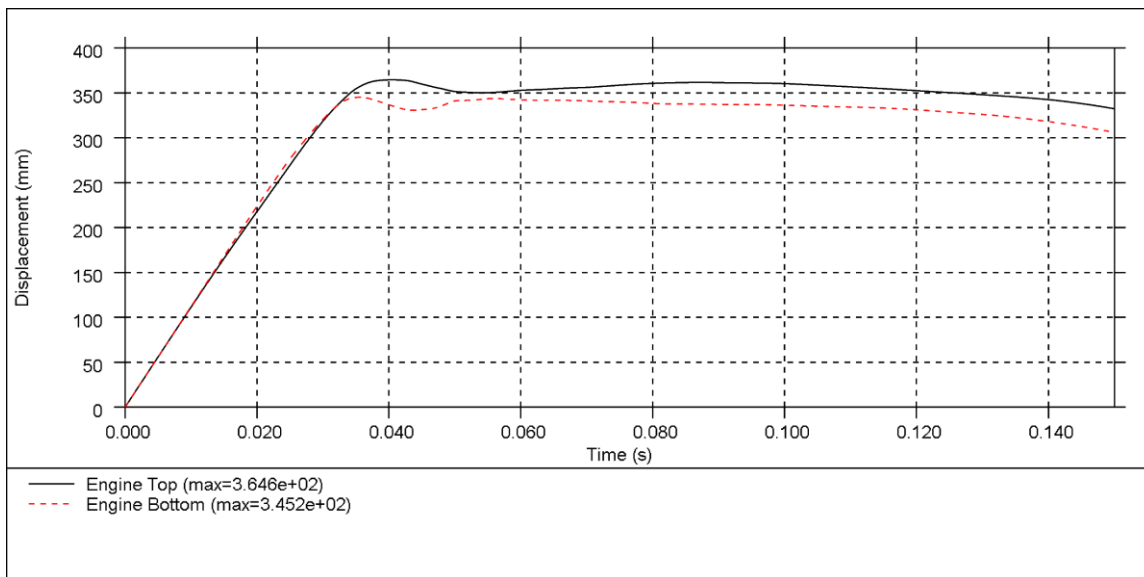


Figure 106. VLH Venza Longitudinal Engine Displacement

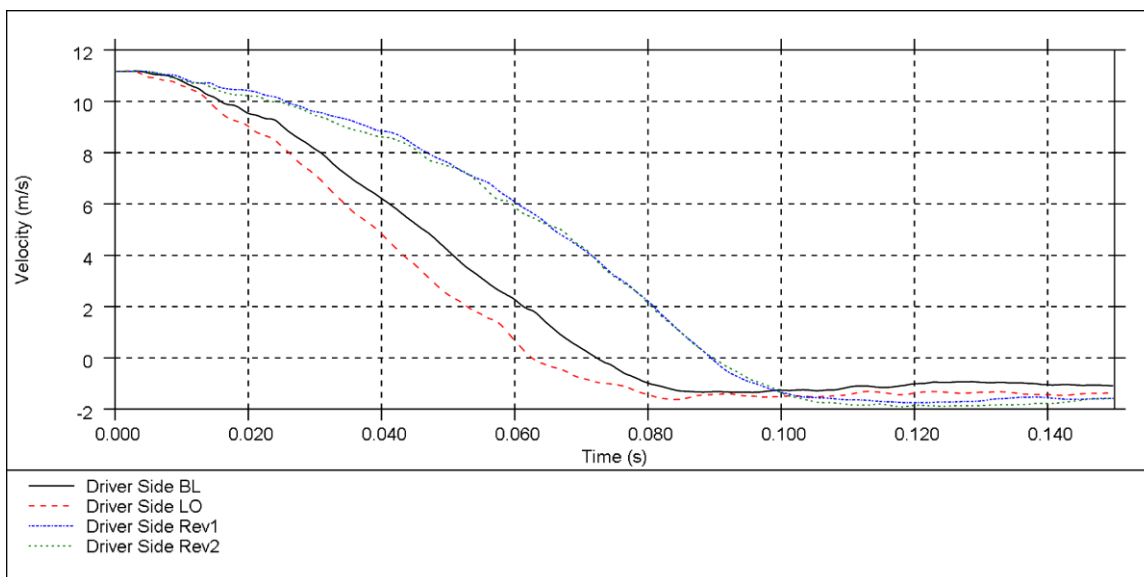


Figure 107. Venza Driver Velocity Comparison

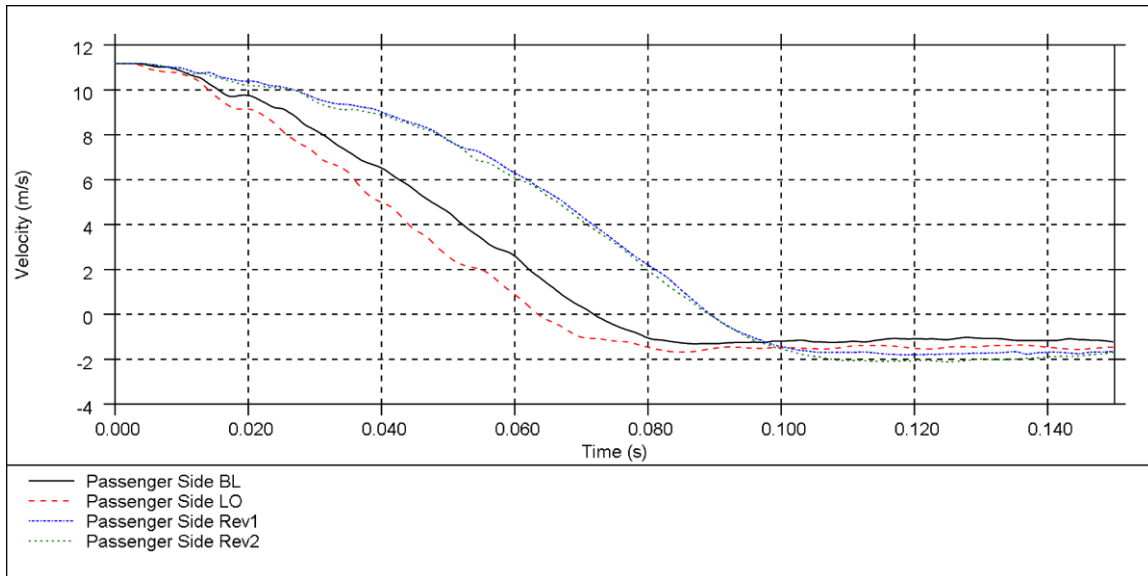


Figure 108. Venza Passenger Velocity Comparison

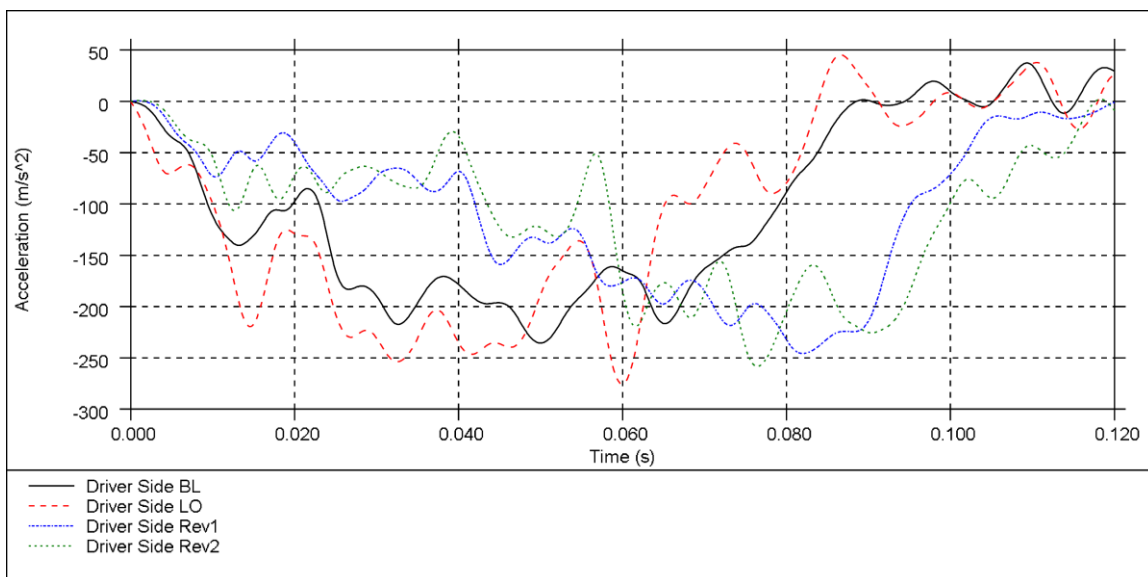


Figure 109. Venza Driver Acceleration Comparison

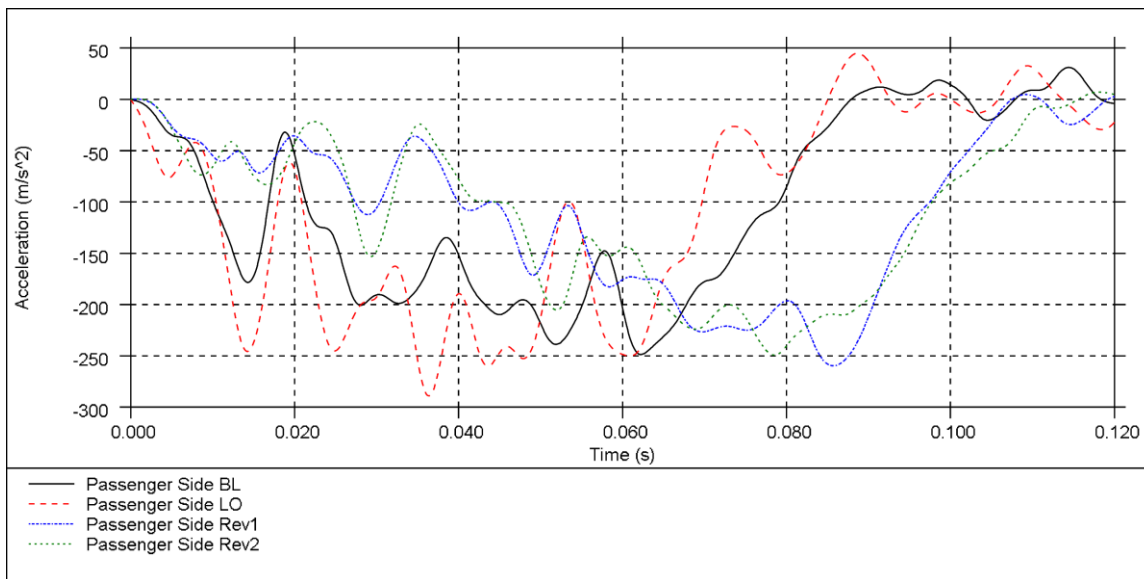


Figure 110. Venza Passenger Acceleration Comparison

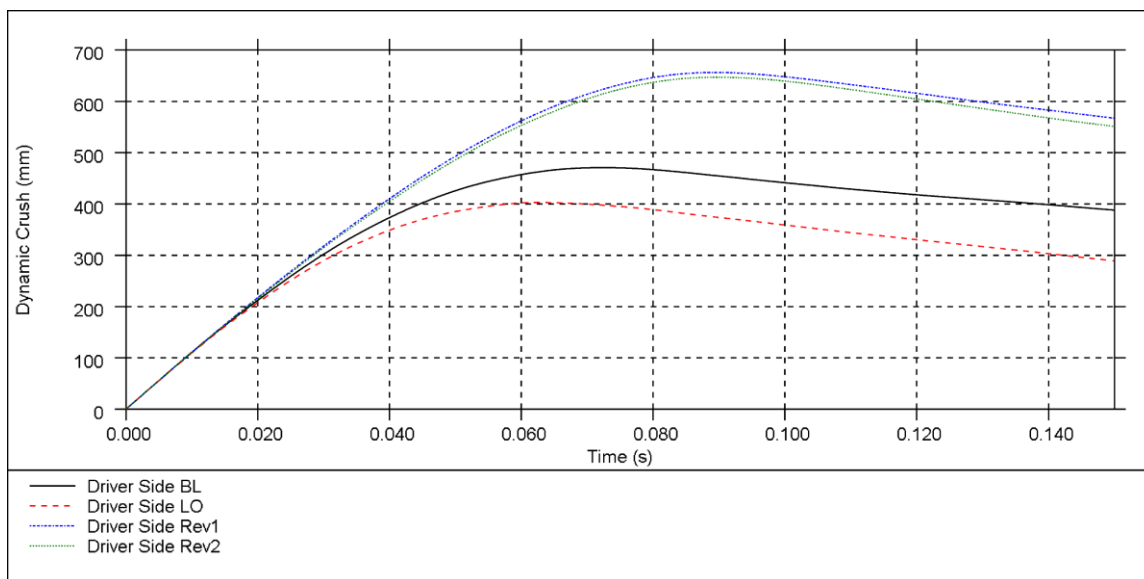


Figure 111. Venza Driver Dynamic Crush Comparison

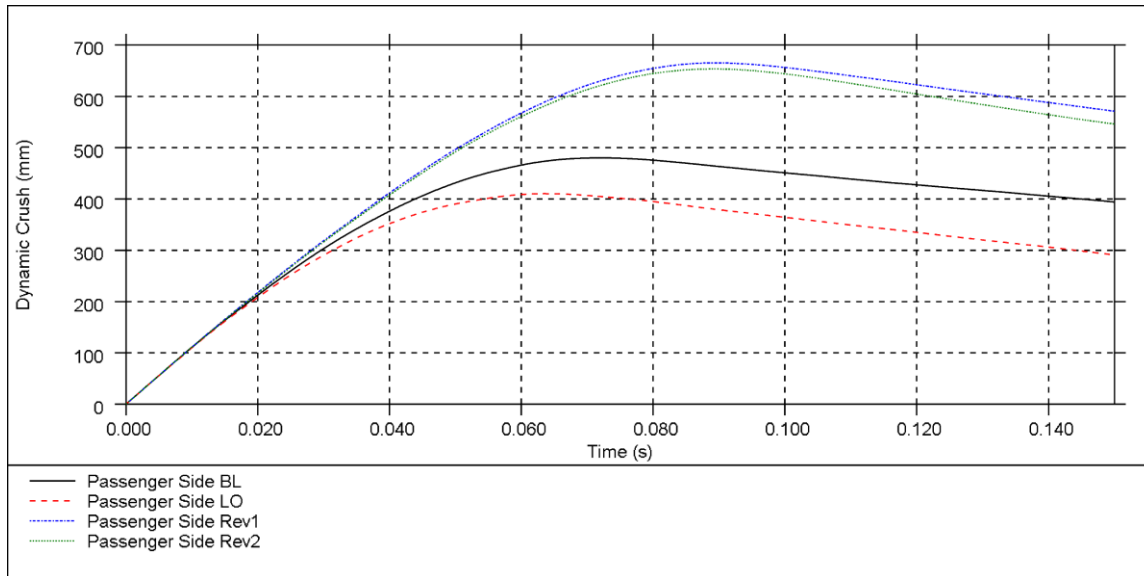


Figure 112. Venza Passenger Dynamic Crush Comparison

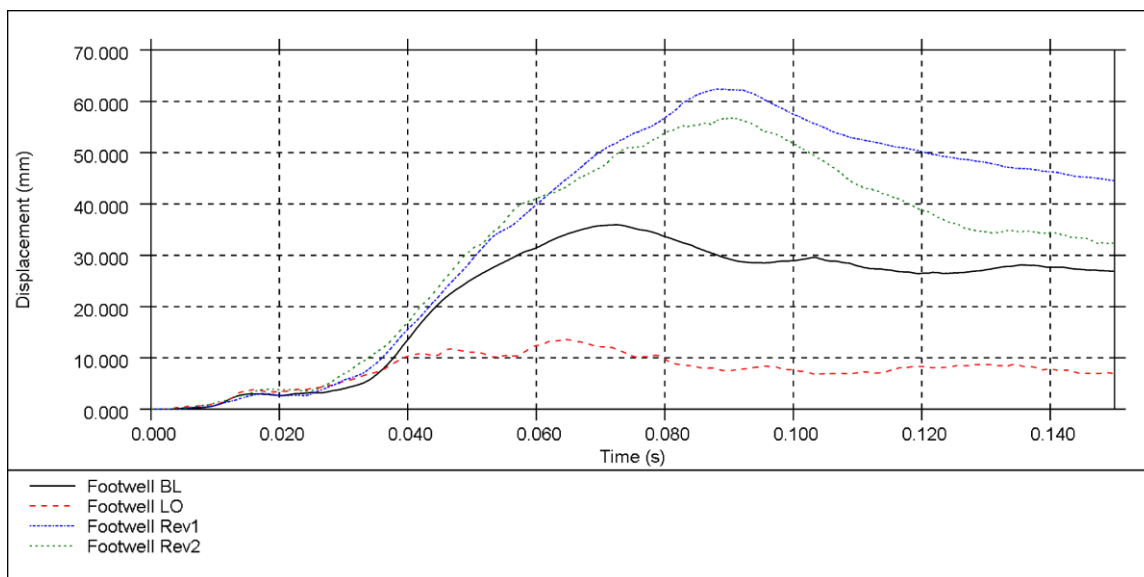


Figure 113. Venza Driver Footwell Intrusion Comparison

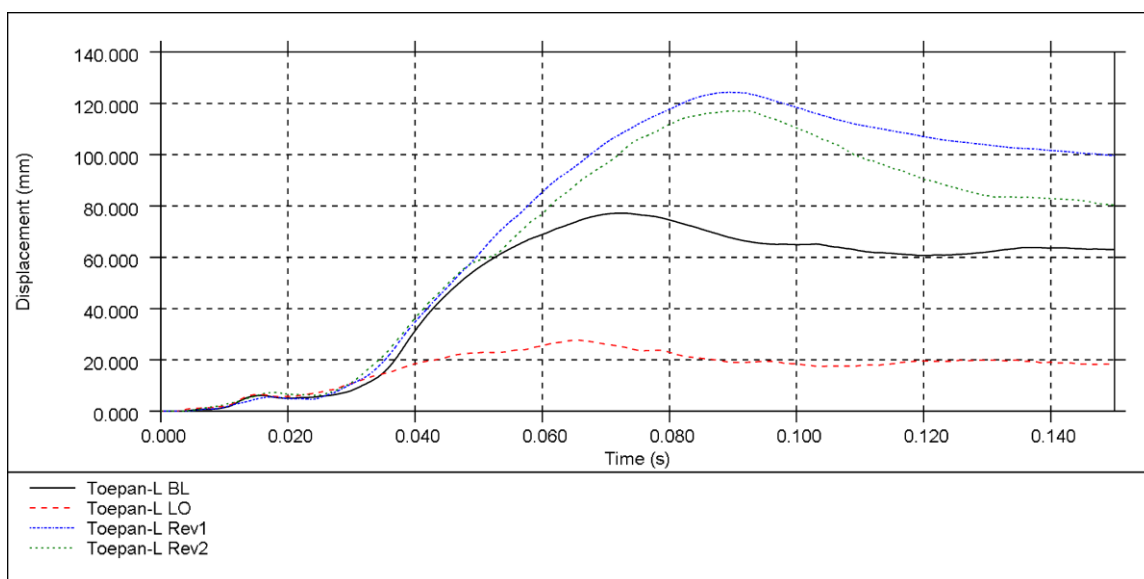


Figure 114. Venza Driver Toe-pan Intrusion Comparison

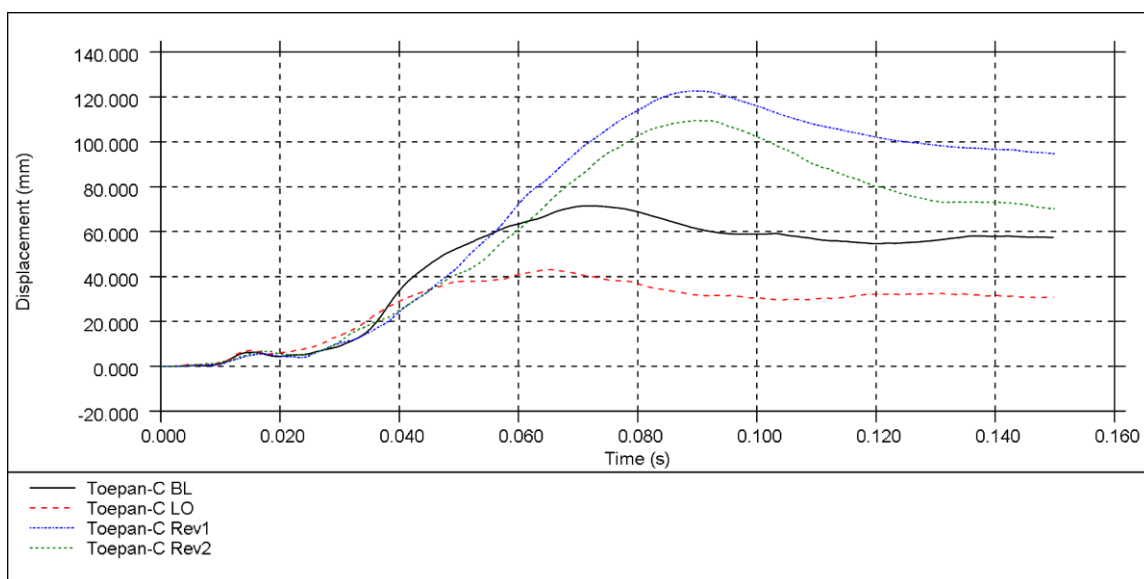


Figure 115. Venza Toe-pan Centre Intrusion Comparison

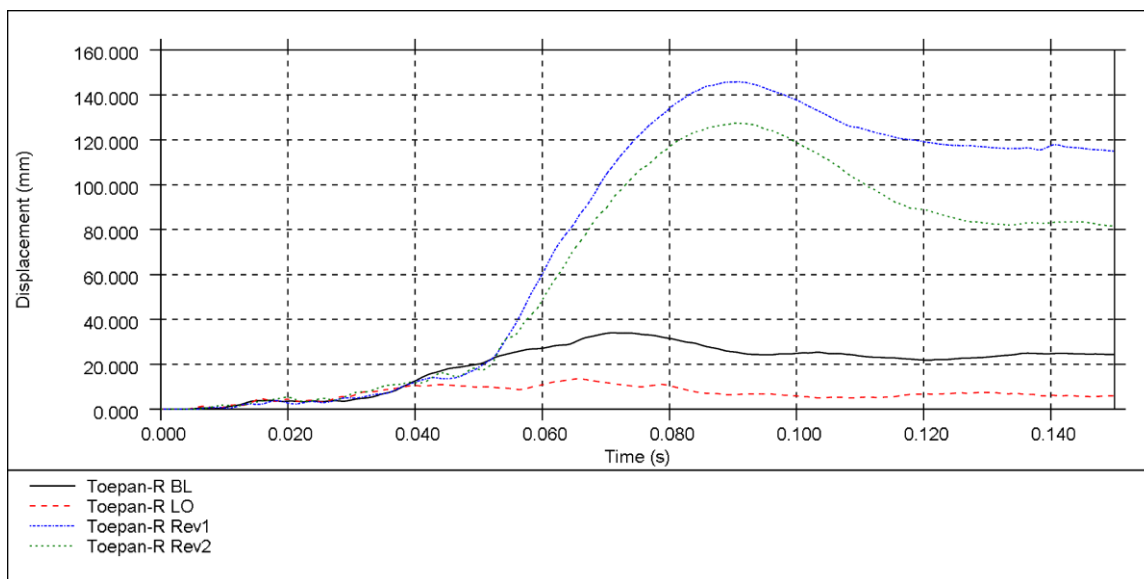


Figure 116. Venza Passenger Toe-pan Intrusion Comparison

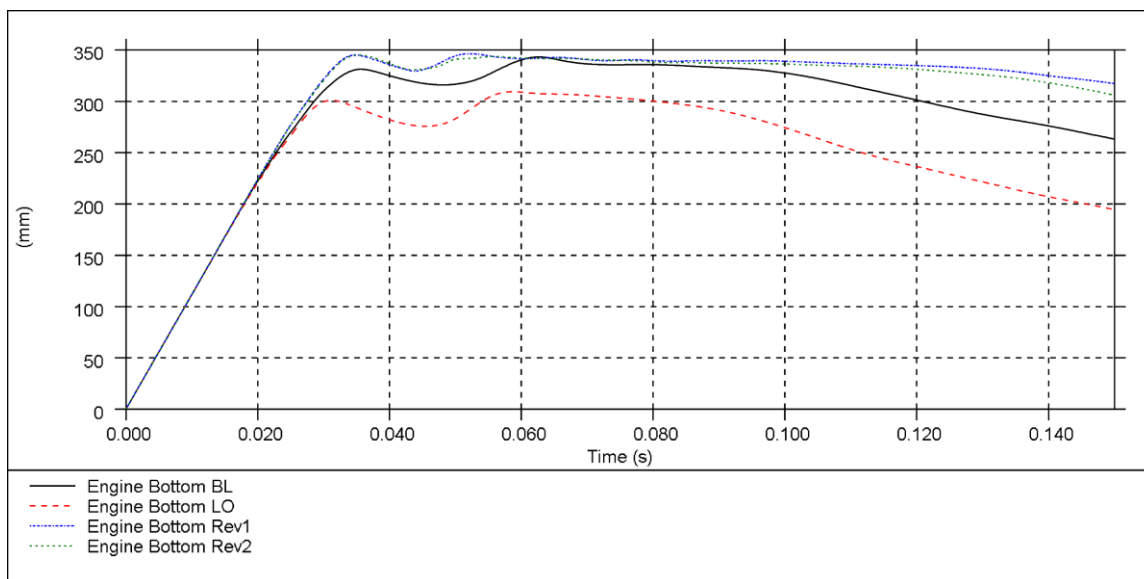


Figure 117. Venza Engine 'Bottom' Displacement Comparison

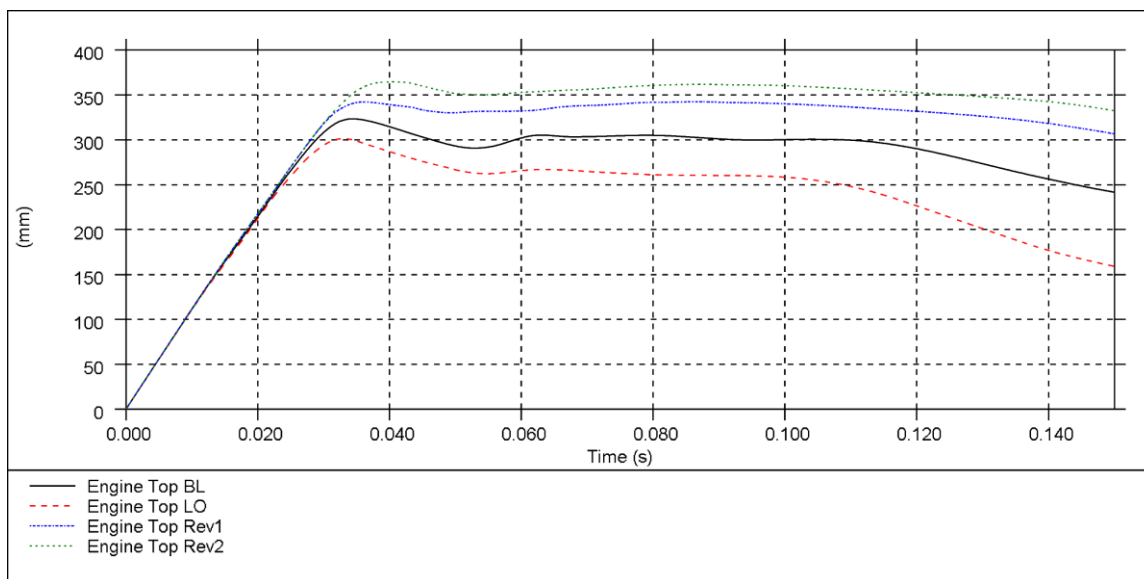


Figure 118. Venza Engine 'Top Displacement Comparison

Appendix V

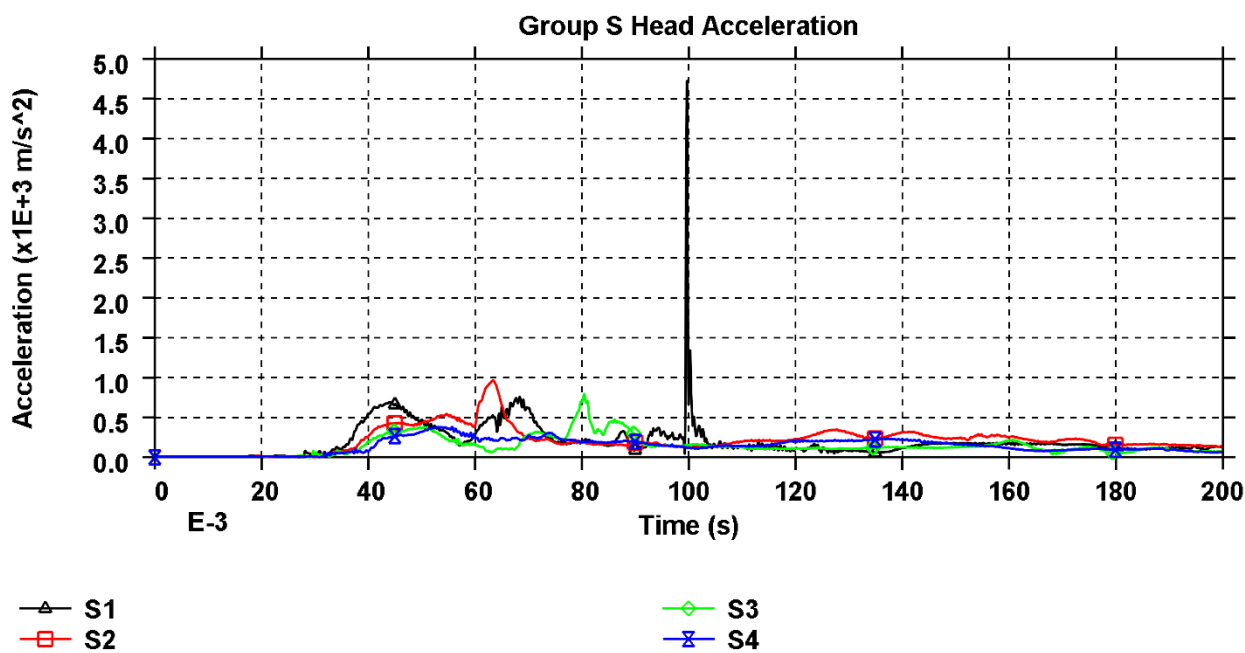


Figure 119. Group-S Head Acceleration (CFC1000)

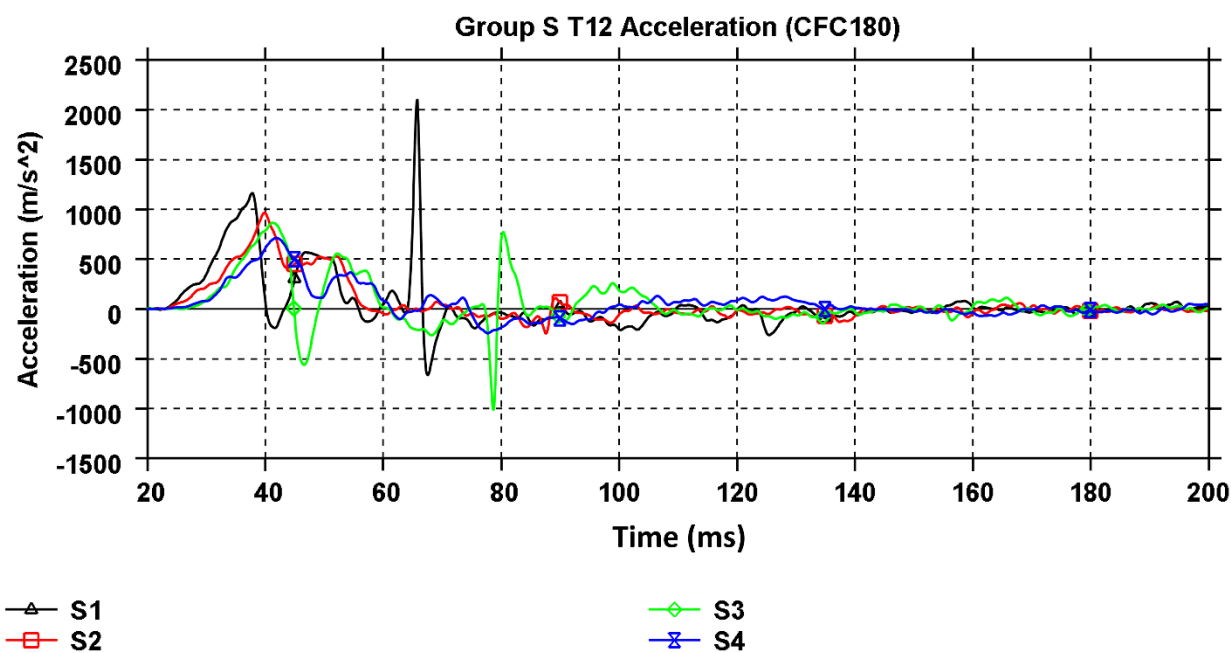


Figure 120. Group-S T12 Lateral Acceleration

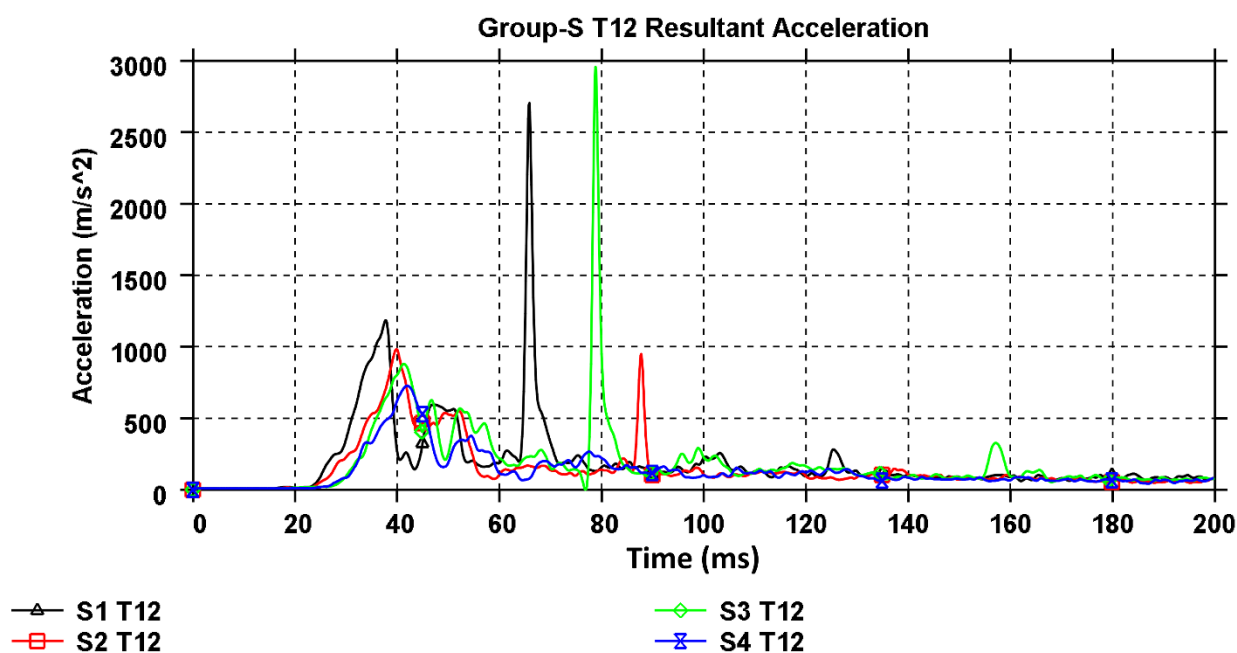


Figure 121. Group-S T12 Resultant Acceleration

Appendix VI – Ethic Documents



Certificate of Ethical Approval

Applicant:

Andrew Harrison

Project Title:

Minimalizing Occupant Injury and Vehicle Mass by Time-History Based Optimisation:
An Analytical Relationship of Vehicle Parameters and Occupant Injury Scores for
Heavy Quadricycles with Autonomous Driving Assisted Systems

This is to certify that the above named applicant has completed the Coventry University Ethical Approval process and their project has been confirmed and approved as Low Risk

Date of approval:

13 June 2019

Project Reference Number:

P92400



Certificate of Ethical Approval

Applicant:

Andrew Harrison

Project Title:

Adaptive Vehicle Crash Structures to Reduce Crash Impulse Severity

This is to certify that the above named applicant has completed the Coventry University Ethical Approval process and their project has been confirmed and approved as Low Risk

Date of approval:

01 December 2017

Project Reference Number:

P62134